ABSTRACT

Title: THE ASSIMILATION OF HYPERSPECTRAL SATELLITE RADIANCES IN GLOBAL NUMERICAL WEATHER PREDICTION

James Alan Jung, Ph.D 2008

Directed By: Dr. Eugenia Kalnay, Department of Atmospheric and Oceanic Sciences, University of Maryland

Hyperspectral infrared radiance data present opportunities for significant improvements in data assimilation and Numerical Weather Prediction (NWP). The increase in spectral resolution available from the Atmospheric Infrared Sounder (AIRS) sensor, for example, will make it possible to improve the accuracy of temperature and moisture fields. Improved accuracy of the NWP analyses and forecasts should result. In this thesis we incorporate these hyperspectral data, using new assimilation methods, into the National Centers for Environmental Prediction's (NCEP) operational Global Data Assimilation System/Global Forecast System (GDAS/GFS) and investigate their impact on the weather analysis and forecasts.

The spatial and spectral resolution of AIRS data used by NWP centers was initially based on theoretical calculations. Synthetic data were used to determine channel selection and spatial density for real time data assimilation. Several problems were previously not fully addressed. These areas include: cloud contamination, surface related issues, dust, and temperature inversions.

In this study, several improvements were made to the methods used for assimilation. Spatial resolution was increased to examine every field of view, instead of one in nine or eighteen fields of view. Improved selection criteria were developed to find the best profile for assimilation from a larger sample. New cloud and inversion tests were used to help identify the best profiles to be assimilated in the analysis. The spectral resolution was also increased from 152 to 251 channels. The channels added were mainly near the surface, in the water vapor absorption band, and in the shortwave region.

The GFS was run at or near operational resolution and contained all observations available to the operational system. For each experiment the operational version of the GFS was used during that time.

The use of full spatial and enhanced spectral resolution data resulted in the first demonstration of significant impact of the AIRS data in both the Northern and Southern Hemisphere. Experiments were performed to show the contribution to the improvements in global weather forecasts from the increase in spatial and spectral resolution. Both spatial and spectral resolution increases were shown to make significant contributions to forecast skill. New methods were also developed to check for clouds, inversions and for estimating surface emissivity. Overall, an improved methodology for assimilating hyperspectral AIRS data was achieved.

THE ASSIMILATION OF HYPERSPECTRAL SATELLITE RADIANCES IN GLOBAL NUMERICAL WEATHER PREDICTION.

By

James Alan Jung

Dissertation submitted to the Faculty of the Graduate School of the
University of Maryland, College Park, in partial fulfillment
of the requirements for the degree of
Doctor of Philosophy
2008

Advisory Committee:
Dr. Eugenia Kalnay, Chair
Dr. John F. Le Marshall, Co-Chair
Dr. William Smith Sr.
Dr. Rachel Pinker
Dr. James Carton
Dr. Robert Hudson
Dr. Eric Kasischke

Acknowledgements

I wish to express my gratitude to Dr. John Le Marshall and Dr. Eugenia Kalnay, my advisors, for their guidance and support with my academics and this research. I wish to thank my committee, Dr. William Smith Sr., Dr. Rachel Pinker, Dr. James Carton, Dr. Robert Hudson, and Dr. Eric Kasischke for their comments and suggestions in completing this research. I wish to also thank Dr. W. Paul Menzel, Dr. Tom Zapotocny and Mr. Timothy Schmit for their encouragement and support.

Thanks are also due to:

The AIRS Science Team headed by Dr. Moustafa Chahine and the NASA Jet Propulsion Laboratory provided the high spatial and spectral resolution AIRS datasets used as the observing system in this study.

Dennis Keyser and Stacie Bender of the National Center for Environmental Prediction assisted in decoding and processing the high spectral and spatial AIRS datasets.

The National Centers for Environmental Prediction provided the operational Global Data Assimilation System/Global Forecast System for use as the analysis / forecast system and computer resources used in this research.

This work was supported in part by a grant of computer time from the Department of Defense High Performance Computing Modernization Program at the John C. Stennis Space Center, Mississippi.

Walter Wolf who assisted in the preparation and distribution of the AIRS data sets used in this research.

This research was supported under National Oceanographic and Atmospheric Administration (NOAA) grant NA06NES4400002 and The Joint Center for Satellite Data Assimilation (JCSDA).

Table of Contents

List of Tables

List of Figures

Chapter 1: Introduction

The National Aeronautics and Space Administration (NASA) Atmospheric Infrared Sounder (AIRS) is the first of the new generation of meteorological advanced sounders for operational and research use. It is part of a large international investment to upgrade the operational meteorological satellite systems. The new systems include the National Oceanic and Atmospheric Administration (NOAA) Cross-track Infrared Sounder (CrIS) and the European Organization for the Exploitation of Meteorological Satellites (EUMETSAT) Infrared Atmospheric Sounding Interferometer (IASI) on the U.S. and European operational polar-orbiting satellites.

A subset of 324 channels selected from the 2378 AIRS channel spectrum which contained one sounding location out of 18 used for limited spatial resolution studies was generated by NOAA/ National Environmental Satellite, Data and Information Service (NESDIS). This limited dataset was distributed to all of the numerical weather prediction centers interested in assimilating AIRS data.

Demonstration of the beneficial impact of this significant technological investment on NWP has been a high priority. Here, for the first time are data-assimilation studies with the NCEP GFS using full spatial resolution hyperspectral radiances, available in real time from AIRS.

Our assimilation trials show, for the first time, significant improvements in forecast skill in both the Northern and Southern hemispheres, compared to identical forecast simulations only without AIRS data. This magnitude of improvement would normally take several years to achieve at an operational weather center. Because the experiments presented here were designed to be feasible for operational applications (e.g. using the

subset of AIRS channels chosen for operational distribution), the AIRS data are now used within the NCEP operational NWP suite. Improvements which were incorporated into the NCEP operational AIRS assimilation include; modifications to the dataset used to distribute every field of view and improvements to the data selection criteria used by the thinning routine. A modified warmest field of view dataset is also being distributed internationally by NESDIS.

1.1 Previous Studies

A number of numerical weather prediction centers have tested the assimilation of AIRS data showing limited benefit. The European Center for Medium Range Forecast (ECMWF) conducted assimilation experiments from 10 December 2002 to 19 March 2003 to determine impact of AIRS data in their global 4D-VAR system (McNally et al. 2003). McNally et al. (2003) used assimilation techniques similar to those used to assimilate HIRS and AMSU-A radiances over land and ocean. The average impact of the 100 cases used by McNally et al. (2003) was positive but small. Similar AIRS assimilation studies conducted with the Meteo-France numerical weather prediction model also produced small positive results (Auligne et al. 2003). A different time period (1 Aug to 19 Aug 2003) with a clear/cloudy scheme developed by Goldberg et al. (2003) was also tested with very similar positive but small impact.

An AIRS targeting study was conducted by Lacy Holland and Zoltan Toth (personal communication 2003) (http://wwt.emc.ncep.noaa.gov/gmb/ens/training.html). This study was part of the Winter Storm Reconnaissance Program (WSRP). The WSRP goal was to identify which areas have the greatest potential for observations to have an impact. The AIRS data for these experiments were distributed by NESDIS as a 281

channel spectral subset and were thinned to 1 of 18 FOVs. The AIRS data were added to the data already used by the GFS which included all of the operational data plus dropsondes released for the WSRP. In this study a total of 7 cases were studied during 2003. Temperature, vector wind, and humidity between 1000 – 25 hPa and surface pressure were investigated for impact. It was determined that the surface pressure and vector wind forecast were degraded, temperature forecasts had a neutral impact, and specific humidity forecasts were improved. The authors concluded that "AIRS has no overall benefit".

1.2 Thesis

Chapters 2 and 3 outline the history of the United States' meteorological satellite program. *Chapter 2* starts with the first satellite experiments developed by Verne Suomi and Robert Parent and gives a brief history and future direction of the operational polar and geosynchronous environmental satellites. *Chapter 3* gives a description of the various sensors on board the NASA Earth Observing System (EOS) Aqua spacecraft, including AIRS, the observing system highlighted in these experiments.

Chapter 4 outlines the history of satellite temperature and moisture retrievals developed for use by NWP. Strengths and weaknesses of the statistical and physical methods used operationally to derive temperature and moisture retrievals by the National Environmental Satellite Service (now known as the NESDIS) are discussed. Some impact studies from using the temperature and moisture retrievals, conducted with NWP models are discussed along with studies conducted using the latest techniques of radiance assimilation.

The Global Forecast System and data used for these experiments are summarized in *Chapters 5 and 6*. An overview of the forecast model, the assimilation system, data pre-processing, verification techniques and the observational database are discussed in *Chapter 5*. *Chapter 6* discusses the AIRS database used in these studies including channel selection and tuning parameters required by this assimilation system.

Chapters 7 – 9 describe the AIRS assimilation experiments. These chapters include the methodology of experiments and the results of increasing the spatial and spectral resolution of the AIRS data in combination and individually. *Chapter 10* outlines the procedures used to improve cloud detection and calculate surface emissivity directly using AIRS data.

Chapter 11 summarizes the results and conclusions of the present research. This chapter also describes possible future research based on the new perspective achieved through these studies.

Chapter 2: The Meteorological Satellite Program

The first meteorological satellite experiment flew on the Explorer VII satellite, launched 13 October 1959. The experiment was devised by Vern Suomi and Robert Parent to provide the most basic of meteorological measurements. It was to measure the balance between the radiation input to the atmosphere from the sun and the radiation from the earth exiting the atmosphere as a result of the reflection and emission processes. The spatial distribution of the radiation imbalances between incoming and outgoing radiation (the net radiation) is the primary driving force of atmospheric circulations. The solar input had already been measured from ground based and balloon borne platforms. Suomi's experiment was the first to measure the energy exiting to space.

Suomi's radiometer consisted of two heat sensing detectors, one painted black to absorb radiation at all wavelengths and the other painted white to reflect the sun's shortwave energy and thereby absorb only radiation emitted by the earth. Thus, Suomi was able to differentiate between the energy leaving the earth's atmosphere due to reflected sunlight (provided by the difference between the radiation sensed by the black and white sensors) and that emitted by the earth and atmosphere (the radiation measured by the white sensor). These first experiments led to the development of satellite instruments which measure environmental conditions.

2.1 The Polar Orbiting Environmental Satellites

The first satellite dedicated entirely to satellite meteorology was launched on 1 April 1960 and was called the Television and Infrared Observational Satellite (TIROS-1). Although crude by today's standards, TIROS-1 images generated immense excitement.

For the first time one could view the Earth and its weather systems as a whole. Global weather observations were realized immediately and the operational meteorological satellite program evolved rapidly thereafter. Nearly 23,000 images were returned in the 79-day lifetime of TIROS-1. As a result, a total of 10 TIROS satellites were launched from 1 April 1960 to 2 July 1965. Several technological improvements were introduced in the TIROS series. TIROS-2 introduced a scanning radiometer, the Medium Resolution Infrared Radiometer (MRIR), which was similar to today's imaging instruments. TIROS-8 introduced Automatic Picture Transmission (APT). APT was a Vidicon camera system which provided daytime visible imaging and had passive infrared radiometers for sensing radiation during both day and night. The data were immediately broadcast to the Earth. The slow transmission rate allowed inexpensive ground receivers to obtain and display the images in real time.

The experimental TIROS series gave way to the Environmental Science Services Administration (ESSA) satellites (9 in all from 1966 to 1969) which exploited the TIROS developments on a fully operational basis. In 1970 ESSA became NOAA. Subsequent operational satellites were given the designation NOAA.

The NIMBUS research satellite series started in 1964, testing remote sensing concepts and instruments. With the successful creation of a global picture of the earth's surface and atmosphere accomplished in 1964, the emphasis shifted towards measuring the vertical distribution of temperature and moisture in the atmosphere to enable more accurate initialization of global NWP models.

Another very important event occurred in 1969 with the launch of NIMBUS-3. It carried two instruments designed to provide the ability to generate atmospheric soundings

from satellite observations. The Satellite Infrared Spectrometer (SIRS) made measurements in the 15μm portion of the spectrum. The second instrument, the Infrared Interferometer Spectrometer (IRIS), measured spectra in the infrared from 6-25μm. These were the forerunners of today's operational sounding instruments.

Accurate temperature retrievals were accomplished with the 8-channel SIRS (Wark and Hilleary, 1969). Comparison with radiosonde observed profiles showed the satellite derived temperature profile to be representative. Due to the lack of vertical resolution, detailed vertical features were smoothed. The major problems with the early SIRS observations were induced by clouds which usually existed within the instrument's 225 km field of view. Also, the SIRS observed only along the suborbital track and, consequently, there were large gaps in the data between orbits.

In spite of its problems, the SIRS data showed promise of improving the current weather analysis/forecast systems. SIRS retrievals were put into operational use on 24 May 1969, barely a month after launch. The first numerical forecast impact experiment (Smith et al. 1970) , conducted for a meteorological situation on 24 June, 1969, revealed that the inclusion of SIRS data in the analysis of 500 hPa height over the Pacific Ocean was considerably different from that excluding the data. Namely, the SIRS data indicated a cut-off low with an intense jet to the north instead of a diffusely defined tough. Extended range (72 hr.) forecasts for North America displayed maximum errors based on the analysis with SIRS of only half the magnitude of those resulting without the use of the data.

NIMBUS-5 carried the first microwave sounding device, the NIMBUS Experimental Microwave Spectrometer (NEMS), a nadir viewing, 5-channel instrument. The NEMS demonstrated the capability to probe through clouds, even dense overcast.

Inter-comparison of the Infrared Temperature Profile Radiometer (ITPR) (also on NIMBUS-5), NEMS and radiosonde data found that the best results were achieved from a combination of infrared and microwave radiance data in the temperature profile inversion process (Waters et al. 1975). This provided the maximum available thermal information, regardless of cloud condition.

In 1972 the Vertical Temperature Profile Radiometer (VTPR) instrument, an eight-channel infrared filter wheel radiometer, was also included on the operational NOAA Improved TIROS Operational System (ITOS) series of satellites. The VTPR provided operational sounding capability over the entire globe. The ITOS also carried the Very High Resolution Radiometer (VHRR). This high resolution visible and infrared radiometer provided multi-channel, 1 km resolution infrared and visible imagery, enabling accurate estimation of sea surface temperatures and other applications.

From the available studies conducted in the early 1970s, it was recognized that the optimum temperature sounding could be achieved by taking advantage of the unique characteristics offered by the 4.3μm, 15μm and 0.5cm atmospheric absorption bands. As a consequence, the NIMBUS-6 High Resolution Infrared Sounder instrument was designed to accommodate channels in both the 4.3μm and 15μm regions and these were complemented by the 0.5 cm microwave wavelength oxygen (O_2) channels of the Scanning Microwave Spectrometer (SCAMS). The HIRS also was designed with passively cooled detectors to allow for complete cross-track scanning. The SCAMS also scanned, but with lower spatial resolution. The HIRS instrument successfully demonstrated an improved sounding capability in the lower troposphere due to the inclusion of the 4.3μm observations.

The operational implementation of infrared and microwave instruments was achieved on the TIROS-N/NOAA- A to D series spacecraft, which started in 1978. The vertical temperature sensitivity of the infrared channels (the weighting functions) was carefully selected to cover the depth of the atmosphere. Infrared soundings of 30 km horizontal resolution were complimented with microwave soundings of 150 km horizontal resolution. During the operational life span of this series, the VHRR was upgraded to the Advanced Very High Resolution Radiometer (AVHRR), the SCAMS was upgraded to the Microwave Sounding Unit (MSU) and the HIRS was upgraded to the HIRS/2. The complement of infrared and microwave instruments aboard these polar orbiting spacecraft provided complete global coverage of vertical temperature and moisture profile data every 12 hours.

The next series of polar orbiting satellites known as the Advanced TIROS-N (ATN)/NOAA-E to J started in 1983. New systems were added incrementally starting with NOAA-8 (NOAA-E) which carried the Search and Rescue (SAR) system. The Earth Radiation Budget Experiment (ERBE) was added to NOAA-9 and NOAA-10. The Solar Backscatter UltraViolet (SBUV) radiometer was also added to NOAA-9.

The current series of polar orbiting satellite are known as the NOAA-K, L, and M series. These are follow-on satellites to the highly successful series of NOAA satellites ending with NOAA-14. The first one in this series (NOAA-K) was launched in 1998. These satellites carry an advanced instrument complement including improved versions of existing instruments along with new microwave instruments. These instruments are intended to measure atmospheric temperature and humidity with improved accuracy. More passive microwave channels have been added with the Advanced Microwave Sounding

Units (AMSU-A1, AMSU-A2 and AMSU-B). The AMSU instruments have better spatial resolution and upper atmospheric sounding capabilities than the previous MSU instruments. The AMSU-A units provide a total of 15 microwave channels for temperature soundings, while the AMSU-B provides 5 channels for sensing moisture. The new AVHRR (AVHRR/3) has gain improvements to the visible channels that will allow better low energy/light detection. It also adds a sixth visible channel for greater spectral measurements. This new channel at 1.6μm, called 3A, improves snow and ice discrimination and is time-shared with the standard 3.7μm channel now called 3B. The other instruments (HIRS/3, SBUV/2) on board these satellites have modest changes to improve performance and increase instrument life.

The next generation polar orbiting satellites will be known as the National Polar-orbiting Operational Environmental Satellite System (NPOESS). This system consolidates expertise and resources of the current NOAA, NASA, and Department of Defense (DOD) environmental satellite programs to produce a substantially improved next-generation operational system. There will be several new environmental sensors on board each NPOESS satellite; a Visible/Infrared Imager/Radiometer Suite (VIIRS) which will collect high resolution visible and infrared radiometric data of the Earth's atmosphere, ocean, and land surfaces (Miller et al. 2006) which will replace the AVHRR/3, an Advanced Technology Microwave Sounder (ATMS) used to derive temperature and moisture profiles of the atmosphere (replacing AMSU) which will be used in conjunction with a Crosstrack Infrared sounder (CrIS) (Muth et al. 2004) (replacing HIRS/4), an Ozone Mapping and Profiler Suite (OMPS) will replace the SBUV/2 and a Conical Microwave Imager/Sounder (CMIS). These new instruments will measure various environmental parameters including

atmospheric vertical temperature and moisture profiles, sea surface winds and soil moisture (Kunkee, 2002). The first NPOESS era satellite is scheduled to be launched in 2008.

2.2 The Geosynchronous Orbiting Environmental Satellites

Instantaneous hemispheric viewing of the atmosphere was first accomplished with the Application Technology Satellites (ATS) which were launched into geostationary orbit, starting 7 December 1967 with ATS-1. These satellites carried the Spin Scan Cloud-cover Camera (SSCC), developed by Vern Suomi and Robert Parent at the University of Wisconsin. The SSCC enabled continuous half-hourly hemispheric images of the Earth during daylight hours. This began the era of our ability to temporally observe weather patterns. The ATS-6 was the first geostationary satellite to carry the meteorological sensor Geosynchronous Very High Resolution Radiometer (GVHRR). It was a two channel radiometer scanning in the visible (0.55 – 0.75μm) and infrared (10.5 – 12.5μm) range.

The success of the ATS geostationary satellites led to the development by NASA of an operational spacecraft designed specifically for meteorology starting in 1974. Five spacecraft were built for this series, two Synchronous Meteorological Satellites (SMS) operated by NASA and three Geostationary Operational Environmental Satellites (GOES) operated by NOAA. These spacecraft provided continuous coverage from locations over the Equator. The principal instrument was the Visible Infrared Spin Scan Radiometer (VISSR).

In 1980 five additional GOES spacecraft were procured by NOAA to support operational meteorological requirements through the 1980s. This was called the GOES-D to H series and carried the new VISSR Atmospheric Sounder (VAS). A solar X-ray sensor was also on board these satellites called the Space Environment Monitor (SEM). The SEM

was a magnetometer which detected activity in the 0.5 to 3.0 angstroms region. The magnetometer was designed to study solar activity and the Earth's magnetic field.

The VAS was an infrared sensor with 12 spectral bands between 3.9 and 15μm. Time continuous 3-dimensional probing of the atmosphere was accomplished using 12 infrared spectral bands in an imaging or a sounding mode. A filter wheel in front of the detector package was used to achieve the spectral selection. Two of the VAS radiometer channels observed upwelling radiation in the 4.0 and 11μm windows, three channels observed radiation in the water vapor region, and seven channels measured radiation in the 4.3μm and 15μm carbon dioxide absorption regions.

Designed for multi-purpose applications, the VAS could be operated in three different modes:

a) a backup mode or VISSR
b) a Multi-Spectral Imaging (MSI) mode, and
c) a Dwell Sounding (DS) mode.

Within each mode of operation, there were a wide range of options regarding spatial resolution (7 km or 14 km), spectral channels, spatial coverage, and the time frequency of observation. The mode of operation was programmed into an onboard processor from the ground through 39 processor parameters.

The VAS was capable of vertically sounding the atmosphere from a geostationary altitude with approximately the same accuracy as that achieved by infrared sounders on the TIROS-N/NOAA series of polar orbiting spacecraft of the time. Initial results from the VAS vertical sounding demonstrated a capability to sense the temporal variations in atmospheric temperature and moisture, as well as the small-scale horizontal features (Le Marshall, 2006).

The first of the current GOES series (GOES-I to M) was launched 13 April 1994. These satellites are now 3-axis stabilized which means the instruments are always pointed toward the Earth. Other improvements include better pointing accuracy and the routine capability to track stars for navigational purposes. The VAS instrument combined imaging and sounding in one instrument, which meant that imaging must be abandoned while soundings are being made. The imager and sounder on GOES-I to M are separate instruments capable of independent, simultaneous operation.

The Imager has one visible channel and four infrared channels similar to the AVHRR instrument on the NOAA polar satellites. The exception is the 6.75μm water vapor channel on the imager replaced the 0.9μm visible channel on AVHRR. The Imager has a much more flexible scan pattern than the VAS. It is possible to suspend a full-disk scan, perform a rapid scan of a small area, then resume the full-disk scan.

The Sounder has 19 channels including a visible channel for cloud detection and is similar to the HIRS/2 instrument. A rotating filter wheel provides channel selection. Four scan spots, on four successive scan lines, are simultaneously sampled during each rotation of the filter wheel. A significant improvement to retrieve atmospheric parameters by the sounder over the VAS comes from the extra channels. The sounder has 3 more surface-sensing channels (6 versus 3) and 3 more channels in the water vapor sensitive shortwave infrared (6 versus 3). These improvements allow the Sounder to measure surface, moisture and temperature effects in greater detail.

The next generation GOES series, GOES-R and beyond, is scheduled to be launched in 2012 (Gurka and Dittberner, 2001). Both the Imager and Sounder will be replaced by an Advanced Baseline Imager (ABI) and a Hyperspectral Environmental

Sounder (HES) respectively. Other potential instruments on the GOES-R series include: a solar imaging suite, a GOES lightning mapper, and a search and rescue receiver (Gurka and Schmit, 2004). The ABI will be used for a wide range of qualitative and quantitative weather and oceanographic, climate and environmental applications and will have a higher resolution, more spectral bands and be able to scan a full disk image every 15 minutes (Schmit et al. 2005b). The increased spectral, temporal and spatial resolutions of the HES on GOES-R and beyond will provide a substantial increase in the quantity and quality of the products. Applications include: climate, atmosphere, clouds, land, ocean, hazards, and trace gases (Schmit et al. 2005a).

Chapter 3: The EOS Aqua Spacecraft

3.1 Background

On 4 May 2002, NASA's Aqua spacecraft was launched from Vandenberg Air Force Base in California, carrying on board six sophisticated instruments to observe and monitor the earth system and changes in it. The satellite, Aqua, is in a sun-synchronous orbit at an altitude of 705 km, with a track that takes it north across the equator at 1:30 P.M. and south across the equator at 1:30 A.M. A key component of the international, NASA-led EOS, the Aqua mission has a particular emphasis on water as it exists throughout the atmosphere (King and Greenstone 1999, King et al. 1999). The Aqua satellite's distinct earth-observing instruments measure numerous aspects of the earth's atmosphere, land, oceans, biosphere, and cryosphere, with a concentration on water in the earth system.

Three of the six Aqua instruments, the AIRS, AMSU, and Humidity Sensor for Brazil (HSB) formed the most sophisticated sounding system ever launched into space. The AIRS spectrometer and the microwave instruments, AMSU-A and HSB, are designed to operate in synchronism. AIRS, AMSU, and HSB form an integrated cross-track-scanning temperature and humidity sounding system on the EOS Aqua spacecraft. The simultaneous use of the data from these three instruments provides both new and improved measurements of cloud properties, atmospheric temperature and humidity, and land and ocean skin temperatures, with the accuracy, resolution, and coverage required by numerical weather prediction and climate models (Aumann et al. 2003). The AIRS was provided by the United States and is the centerpiece of the sounding group. The AMSU, also provided

by the United States and the HSB, provided by Brazil's National Institute of Space Research (INPE) completes the triplet. The AIRS/AMSU/HSB sounding system is designed to meet both NASA's research goals and the operational requirements of the National Oceanic and Atmospheric Administration (NOAA). The infrared and microwave observations are integrated in a way to allow retrieval of temperature and humidity profiles with rawinsonde accuracy. Profiles can be calculated with fields of view having 0% to 80% cloud coverage. Surface temperatures, cloud properties, and information on trace gas constituents of the atmosphere are also obtained from the AIRS/AMSU/HSB instruments.

Also on board Aqua is an Advanced Microwave Scanning Radiometer for EOS (AMSR-E), provided by Japan's National Space Development Agency (NASDA). AMSR-E obtains finer spatial resolution and has a broader range of microwave frequencies than was the case with previous satellite passive-microwave instruments, broadening the applicability of the AMSR-E datasets. The AMSR-E data are being used to derive global, all-weather information on such surface variables as temperature, sea-ice, snow cover, and soil moisture, plus information on water vapor, rainfall, and sea surface wind speed.

The last two instruments on Aqua are also on Aqua's complement EOS satellite, Terra. These are the Clouds and the Earth's Radiant Energy System (CERES) broadband scanning radiometer and a Moderate Resolution Imaging Spectroradiometer (MODIS), provided by the United States. CERES science is focused on the large-scale energy budget of the earth and on climate change. MODIS science is mostly focused on a large variety of physical biological elements and processes in the earth system. MODIS is the highest spatial resolution instrument on the Aqua platform, with products generated at 250 m, 500 m and 1 km resolutions.

3.2 Advanced Microwave Sounding Unit

The AMSU-A sensor is a 15 channel microwave sounder implemented as two independently operated modules. Module 1 has 12 channels in the 50-58 GHz oxygen absorption band that provides the primary temperature sounding capabilities and one channel at 89 GHz that provides surface and moisture information. Module 2 has two channels at 23.8 and 31.4 GHz which provide information about the surface and low level moisture and is particularly useful over ocean.

AMSU-A is primarily a temperature sounder. Its most important function is to provide atmospheric information in the presence of clouds. AMSU-A is a cross track scanner with a resolution of 40 km at nadir and is a direct descendant of the MSU, a component in the original TOVS system and is explained in NOAA (2005).

3.3 Humidity Sensor for Brazil

The HSB is primarily a humidity sounder. Its function was to provide supplementary liquid water and vapor data. It is also used with AMSU-A data to detect precipitation and provide rain rate estimates. This instrument is similar to the NOAA AMSU-B instrument. The HSB is a 4 channel microwave moisture sounder implemented as a single module. The HSB is also a cross-track scanner, and every channel has an identical field of view (1.1^o, or 14 km) to AIRS. Unlike AIRS, which has a sharply defined beam typical of optical systems, HSB has a beam typical of microwave systems. The HSB beam has a Gaussian-like profile in which the width is defined as the field of view which corresponds to the half-power points on the beam profile. HSB collects about 75% of its energy from the 1.1^o field of view and about 95% from the "main beam", an area of about 2.8^o in diameter. Unlike AMSU-A, the HSB is a continuously slewing scanner, and

samples are taken during the scan motion. The beams are therefore somewhat motion smeared in the scan direction. Details of the HSB sensor are explained in detail by Lambrigtsen (2003) and Lambrigtsen and Calheiros (2003).

3.4 Clouds and the Earth's Radiant Energy System

The two CERES instruments are improved versions of the ERBE radiometers. The CERES sensors on board Aqua are broadband scanning radiometers that measure the Earth's radiation balance and provide cloud property estimates to assess their role in radiative fluxes from the surface to the top of the atmosphere. CERES is a broadband scanning thermistor bolometer package with extremely high radiometric measurement precision and accuracy. The Aqua spacecraft carries two identical instruments: one operates in a cross-track scan mode and the other in a biaxial scan mode.

Each CERES instrument has three channels, a shortwave channel for measuring reflected sunlight, a longwave channel for measuring Earth-emitted thermal radiation, and a broadband channel for measuring the total radiation. The shortwave channel measures the solar radiation reflected from the earth/atmosphere system in the wavelength band 0.3-5.0μm. The longwave channel measures top of the atmosphere radiation emitted in the 8-12μm atmospheric window. The broadband channel measures top of the atmosphere total reflected and emitted radiative energy in a band from 0.3μm to greater than 100μm. Subtraction of the shortwave measurements from the 0.3-100μm measurement yields a measure of the broadband thermal emitted radiation, so that CERES isolates both the shortwave and longwave broadband components of the earth's radiation budget. Onboard calibration hardware includes a solar diffuser, a tungsten lamp system with a stability

monitor, and a pair of blackbody sources. Details of the CERES sensor are explained in Wielicki et al. (1996).

3.5 Moderate Resolution Imaging Spetroradiometer

MODIS is a cross-track scanning radiometer with 36 channels measuring visible and infrared spectral bands in the wavelength range 0.4-14.4μm with spatial resolutions of 250 m (two bands), 500 m (five bands), and 1000 m (29 bands). It is based on heritage sensors such as the AVHRR, Landsat Thematic Mapper (TM), HIRS, and the NIMBUS-7 Coastal Zone Color Scanner (CZCS). MODIS is the instrument on Aqua focused on biological and physical measurements of the earth/atmosphere system. The MODIS channels have been selected to enable advanced studies of land, ocean, and atmospheric properties. The atmospheric channels are used to derive atmospheric profiles, aerosol properties, total precipitable water and cloud properties. The land channels are used to derive surface temperature, surface emissivity and aerosol properties. The ocean channels primary functions include ocean color, phytoplankton and biogeochemistry properties. Barnes et al. (1998) provides a detailed description of MODIS.

3.6 Advanced Microwave Scanning Radiometer for EOS

The AMSR-E sensor was provided to the Aqua program by NASDA and is explained in Kawanishi et al. (2003). It is a 12 channel conically scanning passive microwave radiometer measuring vertically and horizontally polarized radiation at the microwave frequencies of 6.9, 10.7, 18.7 23.8, 36.5 and 89.0 GHz. The multi-frequency measurements are realized by multiple feed-horn antennas. AMSR-E conically scans at 40 revolutions/minute and observes the Earth's surface with a constant incidence of 55^{o}. This

instrument builds on the heritage of previous satellite passive microwave instruments including the NIMBUS-7 Scanning Multichannel Microwave Radiometer (SMMR), the Defense Meteorological Satellite Program (DMSP) Special Sensor Microwave/Imager (SSM/I), the Marine Observation Satellite Microwave Scanning Radiometers (MSRs), and the Tropical Rainfall Measurement Mission (TRMM) Microwave Imager (TMI). The AMSR-E provides improved spatial resolutions over the earlier satellite passive microwave instruments, and its 6.9 and 10.7 GHz channels allow soil moisture , sea ice temperature, and sea surface temperature measurements that are not obtainable with the SSM/I.

Several of the variables measured by AMSR-E, such as sea ice, snow cover, and sea surface temperature, are also measured by MODIS. The advantage of AMSR-E for these variables is the ability of the microwave instrument to obtain surface data even in the presence of a substantial cloud cover. This is possible through the inclusion on AMSR-E of several channels measuring at wavelengths where there is little atmospheric interference with the signal. This means that the AMSR-E provides Aqua with an all-weather, capability even for surface variables. This capability complements the finer spatial resolution of the MODIS data and greatly enhances the value of the Aqua mission for climate studies.

3.7 Atmospheric Infrared Sounder

AIRS is a 2382 channel high spectral resolution sounder, with 2378 channels measuring infrared radiation and four measuring visible and near-infrared radiation. The AIRS instrument provides infrared spectral coverage in the 3.74-4.61μm, 6.20-8.22μm, and 8.8-15.4μm infrared wavebands at a nominal spectral resolution of $\lambda/\Delta\lambda = 1200$. The AIRS characteristics are summarized in Table 3.1. The primary purpose of AIRS is to obtain

atmospheric temperature and humidity profiles from the surface upward to an altitude of 40 km. It was expected to provide substantial improvements, especially in the temperature measurements, over any previous space-borne instrument. Its infrared measurements have horizontal spatial resolutions of 13.5 km at nadir. The 2378 infrared channels on AIRS are radiometrically calibrated to standards of the National Institute of Standards and Technology. AIRS is the Aqua instrument with the most substantial technological advances of the six on-board the satellite.

Table 3.1 The AIRS channel characteristics.

Spectral Range	Vis: 0.40 – 0.94 μm IR: 3.74 – 4.61 μm 6.20 – 8.22 μm 8.80 – 15.4 μm
Spatial Resolution	Vis : 2.3 km sub-satellite IR : 13.5 km sub-satellite
Channels	Vis: 4 IR: 2378
$\Delta\lambda/\lambda$	1200
Noise (NEdT)	.0076 - .678

The AIRS instrument also includes four visible/near-infrared channels between 0.40 and 0.94μm with a horizontal spatial resolution of 2.3 km at nadir (Aumann et al. 2003). The primary purpose of the four visible and near-infrared channels is to provide diagnostic support for the infrared retrievals, principally through higher spatial resolution cloud and land data (Gautier et al. 2003). The secondary purpose centers on research products, including surface solar radiation flux and the height of low-level clouds.

In addition to supporting NASA's activities in process study and climate research, AIRS is the first hyperspectral IR radiometer designed to support NOAA/NCEP's operational requirements for numerical weather forecasting during its expected seven year

lifetime. AIRS, together with the AMSU microwave radiometer, achieved a global retrieval accuracy of 1°K/km in the lower troposphere under clear and partly cloudy conditions. Based on the excellent radiometric and spectral performance demonstrated by AIRS during the on-orbit testing, we expect the assimilation of AIRS data into the forecast to result in significant forecast improvement (Aumann et al. 2003). Details of the AIRS radiometric, spectral and spatial calibration are discussed by Pagano et al. (2003), Strow et al. (2003), Gaiser et al. (2003), and Hagan and Minnett (2003).

3.8 Aqua Sounding Suite: AIRS/AMSU/HSB

Together the AIRS/AMSU/HSB combination is regarded as the most advanced sounding system ever deployed in space. It incorporates the advances of the NOAA AMSU-A and AMSU-B microwave instruments plus the new advances provided by the AIRS. Its primary purpose centers on accurate temperature and humidity profiles, but its data are also being used to obtain information about several atmospheric trace gases, precipitable water, cloud liquid-water content, the heights of the tropopause and stratopause, cloud properties, sea and land surface temperature, surface spectral emissivity, and shortwave and longwave radiative fluxes (Parkinson and Greenstone 2000).

The alignment and synchronization of the AQUA instrument suite are essential to the ability to achieve the required 1°K/km retrieval accuracy in the presence of clouds. The HSB, which was similar to the AMSU-B, does not have the 89 GHz channel. The HSB does have an identical footprint to AIRS. AMSU-A is comprised of two separate sensor units, AMSU-A1 and AMSU-A2, with co-aligned, synchronized, and equal sized field of views (FOVs). The AMSU-A footprint is three times wider than the AIRS and HSB footprint and covers a cluster of nine AIRS/HSB footprints. The scan geometries of AIRS

and HSB, both with 1.1^{o} footprints, relative to the AMSU-A, with a 3.3^{o} footprint are illustrated in Fig. 3.1 (Aumann et al. 2003).

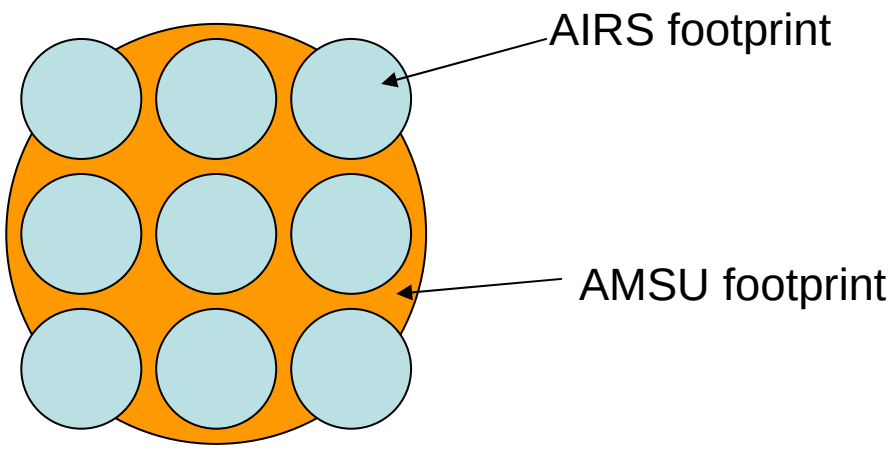

Figure 3.1 Relative size of the AIRS and AMSU footprints. AIRS footprint is ~14 km, AMSU footprint is ~40 km.

Chapter 4: Soundings from Satellites

Today, one of the most important productss from satellite measurements is the atmospheric sounding or retrieval. The concept of determining the state of an atmosphere from spectral measurements is not new. Atmospheric soundings have their roots back to 1905 when Schuster first conceived the radiative transfer equation (Kidder and Vonder Haar, 1995). King (1958) made a general statement regarding the possibility of applying satellite measurements to the integral form of the radiative transfer equation to determine vertical profiles of atmospheric parameters. If the atmosphere is observed at a number of carefully chosen wavelengths, whose weighting functions sample the atmosphere in the vertical, it is possible to retrieve temperature as a function of height. Kaplan (1959) made a more specific proposal to measure the atmospheric radiance. He proposed to measure ten narrow spectral intervals in the 15μm band of carbon dioxide (CO_2), and, by the inversion of the radiative transfer equation, determine the vertical temperature profile of the atmosphere.

Several methods of determining the atmospheric state from satellite observations were developed over the years. Early methods were statistically based, requiring collocated radiosondes and satellite observations to derive their relationships between satellite radiances and temperature. A statistical solution to the satellite sounding problem has been provided by Smith et al. (1970). As satellite instruments improved and computers became faster, deriving satellite soundings became more complex and accurate. Physical techniques slowly replaced various aspects of the statistical models, these methods were considered “hybrid”. A review of the hybrid methods is given by Fritz et al. (1972). Full

physical retrieval methods (e.g. Smith (1970), Chahine (1970) and Eyre et al. 1993) were eventually developed and replaced hybrid methods.

NWP has been the prominent user of satellite retrievals and has played a major part in their evolution and improvement. Since the first statistical retrievals were produced operationally by the National Environmental Satellite Service (NESS), NWP has been a user and has also helped in determining the quality of the satellite retrievals as a part of the assimilation process. In the 1990's, difficulties were experienced in using satellite sounding data in NWP from independently retrieved temperature and humidity profiles. Attention then focused on methods through which the information in the radiance measurements could be assimilated more directly into the NWP system. NWP has subsequently made inversion of the radiative transfer equation a part of the data assimilation process (e.g. Derber and Wu 1998).

4.1 Radiative Transfer

Radiative transfer serves as a mechanism for exchanging energy between different layers of the atmosphere and between the atmosphere and the surface. Infrared radiation emitted by the surface and atmosphere which is intercepted by satellite sensors is the basis for remote sensing of atmospheric temperature and moisture profiles.

The radiance leaving the earth-atmosphere system which can be sensed by a satellite borne radiometer is the sum of radiation emissions from the earth surface and each atmospheric level that are transmitted to the top of the atmosphere. For a given wavenumber v, the up-welling radiance I_v, is given by the Radiative Transfer Equation (RTE):

$$I_\nu = B_\nu(T_s)\tau_\nu(p_s) + \int_{p_s}^{0} B_\nu(T(p))\frac{\tau_\nu(p)}{dp}dp \qquad (4.1)$$

where $B_\nu(T)$, the Planck function, representing black body emission at wavenumber ν, a temperature profile $T(p)$, the atmospheric transmittance between pressure level p and the top of the atmosphere $\tau(p)$ and the surface temperature T_s. The first term is the spectral radiance emitted by the surface and attenuated by the atmosphere. The second term is the spectral radiance emitted to space by the atmosphere.

The basis of deriving atmospheric soundings from meteorological satellites is the solution of the RTE. In the RTE, the upwelling radiance at the top of the atmosphere comes from a combination of the Planck function, the spectral transmittance and the weighting function. Thus, the observed radiance from satellites can be physically related to the temperature field and the absorbing gas density.

If measurements are made in absorbing regions of the spectra, such as those associated with water vapour (H_2O) or ozone (O_3), and if temperature values are known, the transmittance profile may be inferred, just as the temperature profile may be recovered when the spectral transmittance is given. However, the density values are hidden in the exponent of an interval which is further complicated by the spectral integration over an instrument response function. Because of these complications, retrieval of the gaseous density profile is difficult, and no simple algorithm can be followed in deriving the density values.

4.2 Temperature Profile Inversion

Inference of an atmospheric temperature profile from satellite observations of thermal infrared emission was first suggested by King (1958). In his paper, King (1958)

pointed out that the angular radiance (intensity) distribution is the Laplace transform of the Planck intensity distribution as a function of the optical depth, and illustrated the feasibility of deriving the temperature profile from the satellite intensity scan measurements.

Kaplan (1959) advanced the sounding concepts by demonstrating that the vertical resolution of the temperature field could be inferred from the spectral distribution of atmospheric emission. Kaplan (1959) pointed out that the observations in the wings of a spectral band sense deeper into the atmosphere, whereas observation in the centre of the band see only the very top layer of the atmosphere since the radiation mean free path is small. Thus, by properly selecting a set of different sounding spectral channels, the observed radiances could be used to make an interpretation of the vertical temperature distribution in the atmosphere.

There is no unique solution for the detailed vertical profile of temperature or an absorbing constituent. The outgoing radiances arise from relatively deep layers of the atmosphere. The radiances observed within various spectral channels come from overlapping layers of the atmosphere and are not vertically independent of each other. Also, measurements of outgoing radiances possess measurement errors. As a consequence, there are a large number of statistical and physical approaches to the profile retrieval problem. The approaches differ in the procedures for solving the set of spectrally independent RTEs and in the type of ancillary data used to constrain the solution to ensure a meteorologically accurate and near optimal result.

4.3 Statistical Solutions for the Inversion of the RTE

In statistical methods, the radiative transfer equation is not directly used. This method assumes that the instrument has been designed so that the channel's weighting

functions will vertically sample the atmosphere. A set of radiosonde soundings that are nearly collocated in time and space with the satellite soundings is compiled. This training data set is used to calculate a statistical relationship between observed radiances and atmospheric temperatures. These relationships are then applied to other observed radiances to retrieve temperatures.

Acquiring a representative training data set is vital to the success of the statistical method. Some of the requirements for these data sets are:

a) data sets must be large to ensure that the retrieval matrix will be stable.
b) data sets must be collected for each satellite because of differences in the instruments.
c) data sets must be updated frequently to cover the different synoptic states such as winter and summer and to allow for changes in the satellite calibration.
d) data sets need to be divided into similar regions (desert, ice, ocean, etc.).

An advantage to statistical retrievals is that a statistical picture of the structure of the atmosphere is an integral part of the method. The retrieved temperatures cannot deviate too far from those which have actually been observed. This method also does not require information about the transmittances or require use of the RTE for its solution, thus making the retrievals computationally simple.

There are several problems with the statistical technique. One problem is that no filtering of input temperature or radiance noise is done. As a result the transformation matrix from radiances to temperature can be unstable. Small radiance errors can produce large errors in retrieved temperatures. Another problem is that representative errors are embedded in the statistics and are not easily changed. Relatively few radiosondes are available over elevated terrain, making it extremely difficult to construct training data representative of elevated terrain. A similar argument can be made over oceans and high

latitudes. Statistical retrieval solutions also trend towards the mean value but the extreme cases are usually of the most interest.

4.3.1 Statistical Least Squares Regression

Consider a statistical ensemble of simultaneously observed radiances and temperature profiles which have a relationship:

$$T = CR \tag{4.2}$$

where T and R are the matrix notations of temperature and radiances respectively and C is the matrix of solution coefficients. Using a statistical ensemble of co-located rawinsonde temperature profiles and satellite observed radiances a least squares regression can be used to derive C. For an ensemble of L soundings (where L>>M; L>>N) the matrices T and R have dimensions MxL and NxL respectively. The least squares regression solution is derived from

$(T-CR)^t(T-CR)$ or

$$\varphi = \sum_{l=1}^{L} (T_l - CR_l)^2 \tag{4.3}$$

where C is the slope which minimizes the sum of squared deviations of the data points in the regression line. This is done by solving

$$\partial\varphi/\partial C = 0 \tag{4.4}$$

which leads to

$$0 = -2TR^t + 2C\left(RR^t\right) \tag{4.5}$$

Solving for C,

$$C = TR^t\left(RR^t\right)^{-1} \tag{4.6}$$

The least squares regression solution was used for the operational production of soundings from the very first sounding spectrometer data (Smith, 1970).

The advantages of the least squares regression method over other methods are:

a) it uses real radiance and rawinsonde data comparisons to form the statistical sample and does not require knowledge of the weighting functions or the observation errors
b) the instrument need not be calibrated in an absolute sense
c) the regression is numerically stable

Some shortcomings of the regression method are:

a) it disregards the physical properties of the RTE in that the solution is linear whereas the exact solution is non-linear because the weighting function W and consequently the solution coefficients A are functions of temperature
b) the solution uses the same operator matrix for a range of radiances depending upon how the sample is stratified
c) rawinsonde data are required so that the satellite sounding is dependent on more than just surface data.

4.3.2 Statistical Regularization

To make explicit use of the physics of the RTE in a statistical method, one can express the radiances (R) for the statistical ensemble of temperature profiles (T) as

$$R = KT + E \tag{4.7}$$

where E is a matrix of the unknown observational errors and K is the matrix of solution coefficients. Solving for the observational covariance matrix (A) with the least squares approach, yields

$$A = \left(KTT^tK^t + EE^t\right)^{-1}TT^tK^t \tag{4.8}$$

where the covariance between observation error and temperatures (E^tT) are assumed to be uncorrelated and equal to zero. The covariance matrices can be written as

$$S_t = \frac{1}{(N-1)}TT^t \quad \text{and} \quad S_\varepsilon = \frac{1}{(N-1)}EE^t \tag{4.9}$$

where S_t is the signal covariance and S_ε is the noise covariance and N is the sample size, then

$$A = \left(KS_t K^t + S_\varepsilon\right)^{-1} S_t K^t \tag{4.10}$$

solving for temperature, we have

$$\begin{aligned} T &= AR \\ &= \left(S_t K^t\right)\left(KS_t K^t + S_\varepsilon\right)^{-1} R \end{aligned} \tag{4.11}$$

This form of solution was independently formulated by Strand and Westwater (1968) and Rodgers (1970).

Many of the shortcomings of the least squares regression technique do not apply to a solution by statistical regularization:

a) the temperature dependence of the K matrix can be taken into account through iteration;
b) the solution coefficients are evaluated for each new temperature profile retrieved;
c) there is no need for coincident rawinsonde and satellite observations and we can use a historical sample to define S_T. We may, however, need coincident rawinsonde and satellite observations to calculate biases and to empirically correct the solution for differences between observed and calculated radiances.

Two advantages of the least squares regression scheme are lost with statistical regularisation:

a) the satellite instrument needs to be calibrated accurately in an absolute sense;
b) the weighting functions must be known to high precision.

4.3.3 Minimum Information Solution

Another method of retrieving temperature profiles from observed radiances using the RTE is the Minimum Information Retrieval Technique (Twomey, 1963). In this solution, the retrieved temperature profile represents an optimal perturbation of a guess condition, such as a numerical forecast. Here T denotes the difference between the true

profile and the first guess and R denotes the difference between the observed and calculated radiance from the first guess temperature profile S_t as a covariance matrix of errors for the guess profile and S_ε is a covariance matrix of observational error.

If we assume that errors in the guess are uncorrelated from level to level and that the observed radiance errors are uncorrelated (random) from channel to channel, then

$$S_t = \sigma_t^2 I \qquad \text{and} \qquad S_\varepsilon = \sigma_\varepsilon^2 I \tag{4.12}$$

where σ_t^2 is the expected variance of the errors in the guess and σ_ε^2 the expected variance of errors in the observed radiances and I is the identity matrix. With these assumptions and, using the solution derived above, we find

$$T = \left(K^t K + \gamma I\right)^{-1} K^t R \tag{4.13}$$

where γ is given by

$$\gamma = \sigma_\varepsilon^2 / \sigma_t^2$$

In practice, use of this form of solution only requires knowledge of the observational error and an estimate of the error in the first guess profile. The solution may typically be obtained using $\gamma = 10^{-3}$ and iterating until the mean square difference between observed and measured brightness temperature is less than σ_ε^2, i.e.

$$\frac{1}{M} \sum_{i=1}^{M} \left(\delta R_i\right)^2 \leq \sigma_\varepsilon^2 \tag{4.14}$$

where δR_i represents the difference between observed and computed brightness temperature of channel i for M channels. Smith et al. (1972) used a numerical weather prediction model with this technique to provide temperature data from both the SIRS-B and VTPR instruments. In this case the temperature profile variance (σ_t^2) is the variance of

the numerical weather prediction model and not a natural atmospheric profile variance.

4.4 Physical Solutions for the Inversion of the RTE

In solving the retrieval problem, most physical retrieval schemes use a temperature profile and calculate the corresponding radiance. This is typically called the forward problem. With physical solutions to the RTE, the first guess profile is generally important. The closer the first guess profile is to the actual profile, the better the solution is likely to be. The first guess profile tends to be less important as the number of satellite channels used increases such as in the case of hyperspectral sounders. Many of the first retrieval schemes used climatology for a first guess profile. Model first guess or regression methods were determined by Le Marshall et al. (1985) to be a better choice than climatology. Two very early examples of methods which adjusted the temperature profile are Chahine (1970) and Smith (1970). The Chahine (1970) method retrieves temperature for as many levels as there are channels, assuming there are only a few independent channels. The Smith (1970) scheme for adjusting temperature profiles is similar to Chahine (1970) but relaxes the requirement that the temperature be retrieved at only the weighting function peaks. Classification schemes were also developed which used the satellite radiances themselves to choose an appropriate first guess profile (Uddstrom and Wark, 1985; Thompson et al., 1985; McMillin, 1986). Eventually soundings generated by numerical weather prediction models were used as a first guess.

As with the statistical method, there are advantages and disadvantages to the physical methods. Some advantages to physical retrievals are that physical processes are used at each stage of the retrieval and a large data base of coincident radiosondes is not necessary. However, some matching of radiosonde or analysis fields with satellite

observations is necessary to empirically adjust the forward radiative transfer models. The disadvantages include being computationally expensive and the final retrieval accuracy is highly dependent on the first guess profile for many second generation instruments.

The major problems with the Chahine (1970) method are: (a) the profile is not usually well represented by a series of line segments between pressure levels where the weighting functions peak, particularly for a small number of channels (levels), (b) the iteration and hence the solution can become unstable since one is attempting to extract M distinct pieces of information from M non-independent observations.

While the Smith (1970) method does avoid the problems of the Chahine method (no interpolation is required for a temperature at any pressure level and the solution is stable in the averaging scheme), it does have the main disadvantage that the averaging process can prevent obtaining a solution that satisfies the observations to within their measurement error levels. There is no guarantee that the solution converges to one which satisfies the radiances by this criterion.

4.4.1 The Chahine Relaxation Method

Chahine (1970) developed a method to retrieve temperature for various levels using the channel weighting function peaks. The difficulty in reconstructing the temperature profile from radiances at several selected wavelengths is due to the fact that the Fredholm equation, with fixed limits, may not always have a solution for an arbitrary function. Since the radiances are obtained from measurements which are only approximate, the reduction of this problem to a linear system is mathematically improper, and a nonlinear approach to the solution of the full RTE appears to become necessary. The basic RTE is:

$$I_\nu = B_\nu(T_s)\tau_\nu(p_s) + \int_{p_s}^{0} B_\nu(T(p))\frac{d\tau_\nu(p)}{dp}dp \tag{4.15}$$

Since the weighting function reaches a strong maximum at different pressure levels for different spectral channels, the actual upwelling radiance observed by the satellite, R, can be approximated through the use of the mean value theorem, by

$$R_\nu = B_\nu(T_S)\tau_\nu(p_S) + B_\nu(T(p_\nu))\left[\frac{d\tau_\nu(p)}{d\ln p}\right]_{p_\nu} \Delta_\nu \ln p \tag{4.16}$$

where p_ν denotes the pressure level at which the maximum weighting function is located and $\Delta_\nu \ln p$ is the differential of the pressure at the ν^{th} level and is defined as the effective width of the weighting function for wavenumber ν. Let the guess temperature at level p_ν be $T'(p_\nu)$ and subsequent upwelling radiance as I_ν. Dividing and noting that the dependence of the Planck function on temperature variations is much stronger than that of the weighting function, we obtain

$$\frac{R_\nu - B_\nu(T_S)\tau_\nu(p_S)}{I_\nu - B_\nu(T_S)\tau_\nu(p_S)} \approx \frac{B_\nu(T(p_\nu))}{B_\nu(T'(p_\nu))} \tag{4.17}$$

When the surface contribution to the upwelling radiance is negligible or dominant, the equation may be approximated in the iteration form by

$$\frac{R_\nu}{I_\nu^{old}} \approx \frac{B_\nu(T^{new}(p_\nu))}{B_\nu(T^{old}(p_\nu))} \tag{4.18}$$

Since most of the upwelling radiance at the strong absorption bands arise from the upper parts of the atmosphere, whereas the radiance from the less attenuating bands comes from the progressively lower levels, it is possible to select a set of wavenumbers to recover the atmospheric temperature at different pressure levels. The size of a set of sounding

wavenumbers is defined by the degree of the vertical resolution required and is obviously limited by the capacity of the sounding instrument.

4.4.2 The Smith Numerical Iteration Method

Smith (1970) developed an iterative solution for the temperature profile retrieval, which differs somewhat from that of the relaxation method introduced by Chahine. As before, let R_ν denote the observed radiance and $I_\nu^{(n)}$ the computed radiance in the nth iteration. Then the upwelling radiance expression may be written as:

$$I_\nu^{(n)} = B_\nu^{(n)}(T_s)\tau_\nu(p_s) + \int_{p_s}^{0} B_\nu^{(n)}(T(p))\frac{d\tau_\nu(p)}{d\ln p}d\ln p \tag{4.19}$$

Further, for the (n+1) step we set

$$\begin{aligned} R_\nu &= I_\nu^{(n+1)} \\ &= B_\nu^{(n+1)}T_s\tau_\nu(p_s) + \int_{p_s}^{0} B_\nu^{(n+1)}(T(p))\frac{d\tau_\nu(p)}{d\ln p}d\ln p \end{aligned} \tag{4.20}$$

Upon subtracting, we obtain

$$B_\nu^{(n+1)}(T(p)) = B_\nu^{(n)}(T(p)) + (R_\nu - I_\nu^{(n)}) \tag{4.21}$$

This is the iteration equation developed by Smith (1970). Moreover, for each wavenumber we have

$$T_\nu^{(n+1)}(p) = B_\nu^{-1}\left[B_\nu(T^{(n+1)}(p))\right] \tag{4.22}$$

Since the temperature inversion problem now depends on the sounding wavenumber ν, the best approximation of the true temperature at any level p, would be given by a weighted mean of independent estimates so that

$$T^{(n+1)}(p) = \sum_{\nu=1}^{M} T_\nu^{(n+1)}(p)W_\nu(p) \Big/ \sum_{\nu=1}^{M} W_\nu(p) \tag{4.23}$$

Where the proper weights should be approximately

$$W_\nu(p) = \left\{ \frac{d\tau_\nu(p), p < p_s}{\tau_\nu(p), p = p_s} \right\} \tag{4.24}$$

It should be noted that the numerical technique presented above makes no assumptions about the analytical form of the profile imposed by the number of radiance observations available.

4.5 Variational Analysis

Some difficulties were experienced in exploiting satellite sounding data in the form of retrieved temperature and humidity profiles in numerical weather prediction models. A method capable of extracting information from the satellite radiances in the presence of all analysis data directly is a scheme referred to as variational analysis. The one-dimensional analysis method is based on variational principles applied to the analysis of the atmospheric profile at a single location, using a forecast profile and its error covariance as constraints. This technique has also been used in two, three, and four dimensions.

It is assumed that the error distributions for both the model state and observation (x and y respectively) are Gaussian, with zero mean and that the background and observation errors are uncorrelated. The most probable atmospheric state can be obtained by minimizing the cost function $J(x)$ (e.g., Lorenc, 1986), which can be written as:

$$J(x) = \frac{1}{2}(x - x_b)^T B^{-1}(x - x_b) + \frac{1}{2}(y - H(x))^T R^{-1}(y - H(x)) \tag{4.25}$$

where x_b is an initial estimate given by the model state vector, x is the model state solution which is sought, H is the observation operator (or forward model) that provides estimated of the observations from the model fields, B is the background error matrix

and R is the observational error covariance matrix. The background profile x_b is obtained from the NWP model. The background error covariance matrix B is derived from estimating the differences between the background field and observations (e.g., Derber and Bouttier, 1999). The minimum is found by an iterative process. During each iteration, the descent direction is determined using the value of the cost function gradient:

$$\nabla_x J(x) = B^{-1}(x - x_b) + H^T R^{-1}(H(x) - y) \tag{4.26}$$

Where H^T is the adjoint operator of the Jacobian matrix H .

4.6 The use of Satellite Observations in Numerical Weather Prediction

Shortly after the NIMBUS-3 satellite was launched with the SIRS, Smith et al. (1970) developed the first algorithms to derive temperature and geopotential height profiles. This method was statistical and based on an objective analysis of radiosonde data with corrections derived for clouds, high terrain and hot terrain. Although the SIRS was flown as an experiment, its successful performance has permitted its data to be utilized conservatively, but routinely, in the Northern Hemisphere numerical analysis and forecast operation (Smith et al. 1970).

The major benefit from satellite soundings is to improve the analysis over areas with sparse conventional data coverage, and subsequently improve the forecast. When the National Meteorological Center (NMC) (now the National Centers for Environmental Prediction) used the SIRS data in its operational objective analyses, several cases were found where the SIRS soundings were significantly different from the first guess used by the analysis. Several experiments were conducted by Smith et al. (1970) to assess the impact of satellite data on the forecast. The first experiment generated analyses with and

without the SIRS retrievals. Smith et al. (1970) concluded that the 3-day forecast for the United States based on the analysis with the satellite data more closely resembled the observed situation. Other experiments were conducted in the Southern Hemisphere and Tropics with mixed results. The poorer performance in these regions was attributed to cloud contamination and instrument noise (Smith et al. 1970).

With NIMBUS-6 and a new Satellite Infra-Red Spectrometer (SIRS-B) came upgrades to the retrieval algorithms. The new technique used the NMC 12-hour forecast for the first guess profile and has hybrid characteristics as explained in Smith et al. (1972). The advantage of using the 12-hour forecast as a first guess is that the calculated profiles only differ from the forecast profiles when the error in the forecast exceeds the SIRS-B instrument noise. This technique was implemented by NESS on 14 June 1970. Verification statistics derived by Smith et al. (1972) indicate that in most cases the SIRS-B retrievals were significantly better than the 12-hour forecast. Using the NMC 12-hour forecast as the first guess was eventually replaced by statistical methods because it was concluded that the satellite soundings retained too much first guess information.

A technique for using eigenvectors of covariance matrices to retrieve atmospheric parameters was developed by Smith and Woolf (1976). This technique was statistical. Regression coefficients were derived from a dependent sample of measured radiances and radiosonde comparisons and updated weekly. Smith and Woolf (1976) also improved on the Smith (1968) and Smith et al. (1974) technique of "cloud clearing" soundings by using microwave channels. They were then able to generate three types of soundings, clear, partly cloudy (N*), and cloudy as explained in Smith et al. (1979) and Phillips et al. (1979).

Ghil et al. (1979) using a global, primitive equation, general circulation model (Somerville et al. 1974) found small but statistically significant positive impact from using satellite soundings by using the NOAA-4 and NIMBUS-6 retrievals generated using Smith and Woolf (1976). Their results were highly dependent on the data assimilation techniques. Ghil et al. (1979) also found that impact increased with quantity of satellite data. If both NOAA-4 and NIMBUS-6 data were used, the forecasts were better than using data from only one satellite. Tests conducted at the Australian Numerical Meteorology Research Centre by Kelly et al. (1978) identified improvement of more than 5 skill score points by using NIMBUS-6 temperature soundings. Kelly et al. (1978) also found a significant reduction of root-mean-square (RMS) temperature errors in the 24 hour forecasts. Tracton et al. (1980) tested the impact that satellite soundings had on an existing, operational, numerical weather prediction model. Their data assimilation scheme and model were the NMC operational version of the time. Tracton et al. (1980) found that the SAT (with satellite soundings) and NOSAT (without satellite soundings) impacts were generally small and of inconsistent sign. It was later discovered that there were errors in the way the MSU data were assimilated. Ohring (1979) reviewed various data assimilation experiments from different countries, using this same data. He concluded that, on average, the satellite soundings produce small improvements in the forecasts. This small average positive impact is not based on consistent small positive impacts in each forecast, but on an average of forecasts with positive, negative and no impact. Halem et al. (1982) used the Goddard laboratory for Atmospheric Sciences analysis/forecast system to assess the First GARP Global Experiment (FGGE) satellite observing system during the first Special Observing Period (SOP-1) and showed large impacts in the Southern Hemisphere and some

impact in the Northern Hemisphere from using satellite data. Using the NMC Limited-area Fine Mesh (LFM) model, Koehler et al. (1983) found the satellite only analyses depicted realistic atmospheric patterns, accurately locating upper level trough and ridge features. They also found that the satellite only analyses exhibited weaker thermal gradients than those found in the operational LFM analyses. These weaker thermal gradients, consistent with the satellite soundings, ultimately led to poorer forecasts.

In an attempt to alleviate the problems identified in the statistical approach, a "one-step" physical retrieval method was developed by Smith and Woolf (1984). This means that the atmospheric temperatures, surface temperature, and water vapor mixing ratios are retrieved iteratively as a single solution vector. The relationship between temperature and radiance is modeled by the RTE and the model is inverted to obtain the temperature profile from the radiances. This technique is referred to as the Minimum Variance Simultaneous technique. Details of later updates can be found in Fleming et al. (1986, 1988); Goldberg et al. (1988) and Dey et al. (1989).

Two real-time impact studies were conducted by Dey et al. (1989) where statistical derived soundings were compared to physical derived soundings. Results from the first study showed the physical satellite soundings performed consistently better in the Southern Hemisphere. However, the statistical derived soundings outperformed the physical derived soundings in the forecasts in the Northern Hemisphere. It was also found that the cloudy soundings had a higher bias and contained more noise than the clear and partly cloudy soundings. Problems in the selection criteria for the cloudy soundings were discovered. After several improvements were made, a second impact study was conducted. In this second study, the physical soundings performed better in both hemispheres, although the

improvement in the Southern Hemisphere was less pronounced. A similar study between statistical and physical simultaneous soundings was also conducted by Le Marshall (1988). He found that the physical soundings showed significant improvements in the moisture field over the statistical soundings. Given the importance of moisture distribution in both nowcasting and numerical weather prediction, the physical soundings were superior (Le Marshall, 1988).

As the assimilation systems and forecast models improved, the quality of the satellite soundings was again questioned. Quality control experiments conducted by Kelly et al. (1991) showed that the physical derived satellite soundings had large departures from their first guess fields. They (Kelly et al. 1991) cited specific problems in the lowest layer, near fronts, in the Polar Regions, and with subtropical inversions. Problems with the type of retrievals were also noted with those generated from cloudy radiances being of poorest quality. Andersson et al. (1991) reported on developments made to the ECMWF system analysis and forecast model which produced forecast improvements whether or not satellite soundings were used but improvements were larger when the satellite soundings were removed. Possible reasons for the negative impacts are discussed in Eyre et al. (1993).

To try to reduce the need for error characterization in the satellite soundings, the NWP centers started considering the use of radiances directly in their data assimilation systems. Early examples are Lorenc (1986), Le Dimet and Talagrand (1986), Pailleux (1990) and Eyre (1990) which outline the process of radiance assimilation in variational schemes (1D, 3D and 4D-VAR). Eyre et al. (1993) outline a 1D-VAR technique which generates satellite soundings using a 6-hour forecast for a first guess and the TOVS cloud cleared radiances. Using these satellite soundings from their 1D-VAR technique Eyre et al.

(1993) produced significant forecast improvements in both the Northern and Southern Hemispheres when compared to forecasts did and did not use NESDIS satellite soundings. Eyre et al. (1993) also outlined the weaknesses of the 1D-VAR technique and how a 3D- or 4D-VAR system would be superior.

Development of operational 3D-VAR assimilation systems soon followed (Parrish and Derber 1992; Derber et al. 1991; Courtier et al. 1993). With the development of the NCEP Spectral Statistical Interpolation (SSI) analysis system (Parrish and Derber 1992) the use of radiances directly into their assimilation and analysis system became practical. On 25 October 1995 the direct use of radiances replaced the use of the NESDIS retrievals in the operational NCEP global analysis and assimilation system (Derber and Wu 1998).

Several impact studies of satellite radiances using NCEP's operational regional and global model have shown generally positive results (Zapotocny et al. 2002; Zapotocny et al. 2005a; Zapotocny et al. 2007) with AMSU data contributing the most to forecast skill (Zapotocny et al. 2008).

Chapter 5: Analysis / Forecast System Design

Observing System Experiments (OSEs) are frequently used to assess the impact of new and existing data types and new assimilation methodologies. Observing system experiments of the type described here have been performed using NWP operational models including those using the ECMWF global model by Kelly (1997), NCEP's Eta Data Assimilation System by Zapotocny et al. (2000, 2002, 2005a and 2005b), and NCEP's Global Data Assimilation System by Zapotocny et al. (2007). The assimilation/forecast system used for the experiments described herein is the NCEP GDAS. This system consists of four main parts: the Data Pre-processing section, the Analysis or data assimilation section, the forecast model or GFS section and the Diagnostics and Forecast Verification section.

5.1 The Global Forecast System (GFS) Design

The two parts to the NCEP assimilation system, early and late, are shown in Fig 5.1. The early cycle has an observation window of -3 hours to +2.5 hours and is started at 2.75 hours after synoptic time. The analyses for the early cycle are followed by a 384 hour forecast. Consistent with the operational GDAS/GFS of the time, the model resolution starts at T254L64 then is reduced to T170L42 at 84 hours and finally to T126L28 at 180 hours. For this study, only the 00 UTC forecasts were run out to 384 hours. The late cycle has an observation window of -3 hours to +3 hours and is started 6 hours after synoptic time. The late cycle analysis includes data which were not yet available for the early cycle. The late cycle analysis is followed by a 6 hour forecast which is used as the background for the next early and late cycle.

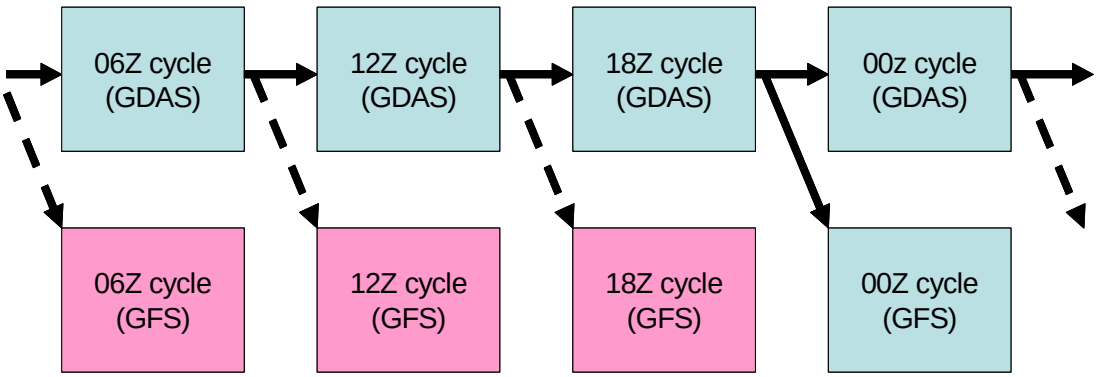

Figure 5.1 Flow diagram of NCEP's operational early, referred to as GFS, and late, referred to as GDAS, analysis cycles. The cycles in blue were used for these experiments. Each cycle consists of the pre-processing, analysis, forecast and post-process/verification steps. The GDAS cycle contains the analysis and a 6 hour forecast, the GFS cycle contains the analysis and a 384 hour forecast.

5.2 Data Pre-processing

As the data from various sources becomes available, the data pre-processing (prep) stage collects, prepares data for the appropriate assimilation cycle, performs super-obing on appropriate wind data types and performs the initial quality control. A solar correction is added to rawinsondes and they are checked for gross errors. All data types except satellite radiances are processed in this step. Any information not used by the assimilation system is removed to save disk space, computer memory and analysis processing time. Keyser (2001a, 2001b, 2003) provide an overview of data types available to NCEP on a daily basis and used operationally for the work of this study.

5.3 Analysis/ Data Assimilation

During the course of these experiments, NCEP changed the data assimilation scheme used in its operational GDAS. The system was, of course, kept constant during each experiment. The Spectral Statistical Interpolation (SSI) was used for the initial

experiments. When the Gridpoint Statistical Interpolation (GSI) matured to where NCEP started *operational* testing to replace the SSI, these experiments switched to using the GSI.

The SSI analysis scheme was a three-dimensional variational (3D-VAR) analysis scheme cast in spectral space (Derber et al. 1991: Parrish and Derber 1992). With this type of analysis system, the incorporation of the radiances directly in an analysis and assimilation system has become practical. The analysis is a 3 dimensional estimate of mass, momentum and moisture fields derived from all available data including the radiances. In October 1995 the direct use of clear and cloud-cleared satellite radiances in the construction of mass, momentum and moisture fields was first introduced (Caplan et al. 1997). The methodology for using the radiance data (including the bias correction, ozone analysis, skin temperature, and quality control) are described in Derber and Wu (1998) with the latest upgrades described in Derber et al. (2003).

Both the SSI and GSI use a thinning routine which identifies the optimal radiance profile for each satellite sensor type (Infrared, Microwave, Microwave Water vapor) in a pre-designated grid box (180 km^2, 160 km^2, and 240 km^2 respectively). The optimal radiance profile is selected based on minimizing its departure from the background temperature, its distance from the center of the grid box, its temporal departure from the assimilation time and its surface features (ocean, land, ice). All satellite sensor types, except AIRS, are sorted at their full spectral and horizontal resolution. In the case of AIRS, NCEP initially used the 281 channel, 1 of 18 FOV AIRS dataset available for operational use.

The optimal selected radiance profile could still contain contaminates such as clouds or dust and may not be entirely suitable for assimilation. The infrared radiance

profiles were then subject to a cloud detection algorithm similar to McNally and Watts (2003) which identified the clear channels within the profile. The channels which pass this final test are then used by the assimilation system.

5.3.1 Radiative Transfer Model

The radiative transfer calculations are performed using the JCSDA Community Radiative Transfer Model (CRTM). The CRTM simulates the infrared and microwave radiances observed by instruments on board various satellites which determine the state of the Earth's atmosphere and surface. For many satellite radiance applications, not only is the forward model essential, but also the capabilities to rapidly compute the radiance sensitivities with respect to the state variables. The CRTM includes the forward, tangent-linear, adjoint and K-Matrix models (Han et al. 2006). It is an essential component of the SSI and, more recently, the GSI data assimilation system at NCEP. Nearly all of the present day microwave and infrared sensors are supported by the CRTM.

The development of the CRTM has been advanced by recent community research activities in the area of radiative transfer modelling (Weng et al. 2005). For example, to fully utilize the information of satellite measurements under all weather conditions, research activities have been conducted to improve the forward modelling capabilities to include both scattering and polarization processes of microwave instruments. Although cloud affected infrared satellite radiances contain considerable information, they have not been assimilated into operational NWP. The use of cloudy infrared radiances in NWP (e.g. Le Marshall et al. 2008) will ultimately enhance the impacts that have been demonstrated through clear radiance assimilation and add to the knowledge of clouds, the surface and the hydrological cycle. Another important purpose in the development of the CRTM is that it

is designed to be used by research groups and developers to implement their results into a common framework, which can be directly tested and evaluated in an operational environment, thereby to accelerating the transition from research to operational applications.

The earlier RTMs used at the JCSDA were emission-based, applicable only to clear sky conditions (Kleespies et al., 2004). There was also no built-in component to compute the surface emissivity and reflectivity. The software, although well designed, was not flexible to meet NWP developmental requirements. The CRTM has improved on the earlier models in both the scientific and software aspects.

The CRTM now takes into account the absorption and scattering from various clouds and precipitation. It also includes a comprehensive model for computing surface emissivity and reflectivity over land, ocean, ice and snow surfaces. The software is redesigned with a balance between the computational efficiency and the flexibility for future improvement and extension (Han et al., 2006).

The transmittance model used by the CRTM estimates the channel transmittance, which is defined as the convolution of the monochromatic transmittance with the spectral response function. Currently it is implemented with a special version of the Optical Path TRANsmittance (OPTRAN) (McMillin et al., 1995). A distinct characteristic of the OPTRAN model is that the transmittances are estimated in absorber space, not in pressure space (Saunders, et al. 1999). One of the advantages of using the absorber space is that transmittances can be predicted accurately with fewer predictors than using the pressure space.

Two versions of OPTRAN are now being developed simultaneously. One version, referred to as OPTRAN-v7, adopts a new technique to take the polychromatic effects into account when computing the radiances with finite bandwidth (Xiong and McMillin, 2005). The other version referred to as Compact OPTRAN (so named due to its high efficiency in using computer memory resources) improves vertical structures of the Jacobian profiles by constraining the variations of the transmittance regression coefficients between different vertical levels. The Compact OPTRAN is the one currently implemented in the SSI. It was primarily developed by Dr. Yoshikiko Tahara, a visiting scientist from JMA and is explained in detail by Han et al. (2006).

The CRTM employs a suite of infrared and microwave surface emissivity and reflectivity models covering land, ocean, ice and snow surfaces. Some of the models are physically based while others are empirical or semi-empirical. The CRTM also has an option allowing the users to incorporate their own emissivity and reflectivity model.

The Infrared Sea Surface Emissivity model (IRSSE, van Delst 2003) is a parameterized version of the emissivity model for rough sea surfaces after Wu and Smith (1997). The sea surface is modelled by numerous small facets whose slopes approximately follow the normal and isotropic distribution (Cox and Munk, 1954), generated solely by the wind speed. Each of the facets is treated as a specular surface and its emission at the observation angle is computed with the geometrical optics. The wave shadowing effects and the surface reflection of surface emission have also been taken into account.

The infrared surface emissivity over land, snow and ice is given by the emissivity database as described in Carter et al. (2002). The database contains surface reflectance measurements as a function of wavelength in both the visible and infrared spectral regions

for the 24 surface types listed in Table 5.1. The emissivity is calculated as one minus the reflectance under the assumption of a Lambertian surface in the infrared.

Table 5.1 Surface types included in the CRTM infrared emissivity database

Surface Types	
Compacted soil	Grass scrub
Tilled soil	Oil grass
Sand	Urban concrete
Rock	Pine brush
Irrigated low vegetation	Broadleaf brush
Meadow grass	Wet soil
Scrub	Scrub soil
Broadleaf forest	Broadleaf(70)/Pine(30)
Pine Forest	Water
Tundra	Old snow
Grass soil	Fresh snow
Broadleaf /Pine forest	New ice

The microwave emissivity over ocean is computed using FASTEM-1 (English and Hewison, 1998). The model treats the surface emissivity in three categories: specular reflection and the modulation from large and small scales depending on wind speed and frequency of the electromagnetic wave. FASTEM-1 takes the satellite zenith angle, water temperature, surface wind speed, and frequency as model inputs and computes surface emissivity at vertical and horizontal polarizations.

The microwave land emissivity model used by the CRTM computes the land surface emissivity over various surface conditions including snow, deserts and vegetation using the two-stream radiative approximation (Weng et al. 2001). The vegetation canopy the optical parameters are derived using geometric optics. For a medium with a higher

fractional volume of particles such as snow and deserts, the scattering and absorption coefficients are approximated using the dense medium theory. The microwave land emissivity model takes satellite zenith angle, microwave frequency, soil moisture content, vegetation fraction, soil temperature, land surface temperature and snow depth as input and computes surface emissivity at vertical and horizontal polarizations.

An empirical approach is taken to compute the microwave emissivity for snow and ice. It is done by correlating satellite window channel observations and ground-based microwave instrument measurements. These ground-based measurements contain a set of emissivity spectral data measured at a zenith angle of 50^{o} for various surface types. Currently there are separate databases established, one for snow and one for ice. The window channel observations are used to identify the snow or ice surface type (Yan et al. 2004) which then uses the appropriate database to determine the surface emissivity.

5.4 The Global Forecast System

Comprehensive documentation of the global forecast model was completed by the National Meteorological Center (now NCEP) Development Division (1988) and can be found at http://wwt.emc.ncep.noaa.gov/gmb/wd23ja/doc/web2/tocold1.html. Subsequent model developments have been summarized by Kanamitsu (1989), Kalnay et al. (1990), and Kanamitsu et al. (1991). Updates to the radiation, surface layer, vertical diffusion, gravity wave drag, convective precipitation, shallow convection and non-convective precipitation can be found at http://sgi62.wwb.noaa.gov:8080/research/SONGYU/doc/physmrf1.html. The most recent information about the GFS atmospheric model (2003) is in NCEP Office Note #442 or http://emc.ncep.noaa.gov/officenotes/newernotes/OF442.pdf. A summary of GFS changes

and references are at http://www.emc.ncep.noaa.gov/gmb/moorthi/gam.html and at http://www.emc.ncep.noaa.gov/gmb/STATS/html/model_changes.html and are listed in appendix A and B.

For many of these AIRS radiance assimilation experiments, the latest operational version and resolution of the GFS was used. A horizontal resolution of 254 spectral triangular waves (T254) was used with a Gaussian grid of 768 X 384 or approximately equal to 0.5^o X 0.5^o latitude and longitude. The vertical domain ranges from the surface to approximately 0.27 hPa and is divided into 64 unequally spaced sigma layers with enhanced resolution near the bottom and top. There are 15 layers below 800 hPa and 24 layers above 100 hPa. On 5/31/2005 NCEP upgraded their GFS and changed resolution to T382L64.

5.5 Diagnostics and Verification

The diagnostics used here to verify forecast improvement include statistics commonly used by NCEP and other NWP centers. Anomaly correlations, root mean square error (RMS) and Forecast Impact are among those used.

The anomaly correlation is designed to detect similarities in the patterns of departures (i.e. anomalies) from the climatological mean field (Wilks, 1995). The computation of anomaly correlations for the forecasts produced by the GFS is by a standard method used by NWP centers world-wide. They are computed using code developed and maintained at NCEP. The anomaly correlations are evaluated using:

$$AC = \frac{\sum (F - C)(O - C)}{\sqrt{\sum (F - C)^2}\sqrt{\sum (O - C)^2}} \qquad (5.1)$$

The variables F, C, and O are the forecast, climatology and analysis field respectively. The NCEP reanalysis (Kistler et al. 2001) data are used for the climatology for determination of these anomaly correlations. Lahoz (1999) and Wilks (1995) present an overall description of what the anomaly correlation is typically used for. WMO (1999) NWS (2005a) provides a description of the standardized methods adopted by most NWP centers. The fields being evaluated by anomaly correlations are truncated to spectral wave numbers 1 through 20 from 2.5^{o} X 2.5^{o} pressure surface grids as defined in NWS (2005a). The verification domains are divided into 3 regions, the mid-latitudes (20^{o}-80^{o}) of the Northern and Southern Hemisphere and the tropical belt (20^{o}N – 20^{o}S). Anomaly correlations of geopotential height are evaluated at 1000 and 500 hPa.

Other diagnostics used here are to evaluate the RMS difference and the Forecast Impact (FI), as discussed further by Zapotocny et al. (2005a and 2007). For this study, a series of two-dimensional FI results are presented as the positive/negative impact provided by the addition of AIRS data. The geographic distributions of FI for a specific pressure level at a forecast time period are evaluated using:

$$FI(x,y) = 100\mathrm{X}\left\{\left(\sqrt{\frac{\sum_{i=1}^{N}(\mathrm{C}i-\mathrm{A}i)^2}{\mathrm{N}}}-\sqrt{\frac{\sum_{i=1}^{N}(\mathrm{D}i-\mathrm{A}i)^2}{\mathrm{N}}}\right)\Bigg/\sqrt{\frac{\sum_{i=1}^{N}(\mathrm{D}i-\mathrm{A}i)^2}{\mathrm{N}}}\right\} \quad (5.2)$$

The variables C and D are the control and AIRS added forecasts, respectively. The variable A is the 00-hr GDAS verifying control analysis containing all data types, except AIRS, which is valid at the same time as the forecasts. N is the number of diagnostic days. All FI diagnostics were computed from the 1x1 degree grids generated by NCEP's post processing package.

The first term on the right hand side enclosed by parentheses in (5.2) can be considered the error in the control forecast. The second term enclosed by parentheses in (5.2) can be considered the error in the AIRS forecast. Dividing by the error of the AIRS forecast normalizes the results. Multiplying by 100 provides a percent improvement/degradation with respect to the RMS error of the AIRS forecast. A positive forecast impact means the forecast compares more favorably to its corresponding analysis with AIRS included than without it.

Forecast impact and anomaly correlations are evaluated for the control and AIRS simulations. Forecast impact of conventional meteorological terms evaluated includes mean sea-level pressure, precipitable water, temperature, both components of the wind, and relative humidity. Comparisons are made on multiple pressure levels extending from near the earth's surface to the lower stratosphere.

5.6 The Operational Data

For these experiments, the complete NCEP operational database of conventional and satellite data are used. The observations assimilated in this work include upper-air rawinsonde observations of temperature, horizontal wind and specific humidity; operational Advanced TIROS-N (Reale 1995; NOAA 2000), Operational Vertical Sounder (Smith et al. 1979) radiances from the HIRS, MSU sensor (Spencer et al. 1990), AMSU-A and AMSU-B sensors (NOAA 2005), ozone information from the SBUV sensors (Miller et al. 1997); DMSP SSM/I surface wind speed (Alishouse et al. 1990); derived surface winds from Quikscat (Yu and McPherson 1984); Atmospheric Motion Vectors (AMV) from geostationary satellites (Menzel et al. 1998); aircraft observations of wind and temperature; land surface reports of surface pressure; and oceanic reports of surface pressure,

temperature, horizontal wind and specific humidity. Keyser (2001a, 2001b, 2003) provides an overview of data types provided to NCEP on a daily basis and used operationally for the experiments of this study. The conventional data and satellite data used in these experiments are summarized in Tables 5.2 and 5.3, respectively.

The case studies chosen consist of 45-day periods during two seasons, the Northern Hemisphere summer and winter. During these periods, an operational or near operational version of NCEP's global spectral model is used for the control, and for the AIRS assimilation experiments. The control run utilizes all the conventional (Table 5.2) and satellite data (Table 5.3) types routinely used in the GDAS during the two seasons tested with the real-time data cut-off constraints. Differences between the control and AIRS experimental runs are accumulated over the 45-day periods and analyzed to demonstrate the forecast impact of these data types through 168 hours.

Table 5.2 Conventional data used within the NCEP Global Data Assimilation System. Mass observations (temperature and moisture) are shown in the left column, wind observations are shown in the right column.

Rawinsonde temperature and humidity	Rawinsonde u and v component of wind
AIREP and PIREP aircraft temperatures	AIREP and PIREP aircraft u and v component of wind
ASDAR aircraft temperatures	ASDAR aircraft u and v component of wind
Flight-level reconnaissance and dropsonde temperature, humidity and station pressure	Flight-level reconnaissance and dropsonde u and v component of wind
MDCARS aircraft temperatures	MDCARS aircraft u and v component of wind
Surface marine ship, buoy and c-man temperature, humidity and station pressure	Surface marine ship, buoy and c-man u and v component of wind
Surface land synoptic and METAR temperature, humidity and station pressure	Surface land synoptic and METAR u and v component of wind
Ship temperature, humidity and station pressure	Wind Profiler u and v component of wind
	NEXRAD Vertical Azimuth Display u and v component of wind
	PIBAL u and v component of wind

Table 5.3 Satellite data used within the NCEP Global Data Assimilation System.

HIRS sounder radiances	SBUV ozone radiances
MSU radiances	QuikSCAT surface u and v component of wind
AMSU-A radiances	GOES atmospheric motion vectors
AMSU-B radiances	Atmospheric motion vectors from GMS-5 until May 2003 then GOES-9
GOES sounder radiances	METEOSAT atmospheric motion vectors
SSM/I precipitation rate	SSM/I surface wind speed
TRMM precipitation rate	

Chapter 6: AIRS Database

6.1 Introduction

AIRS data are received from ground station overpasses within 22 min at the Earth Data Operating System. They are then sent to the NOAA/NESDIS server and the Goddard Space Flight Center / Distributed Active Archive Center as high-rate buffered data (or Level 0). At NOAA/NESDIS, the Level 0 data are converted to Level 1b and are quality-controlled using software supplied by the Jet Propulsion Laboratory Team Leader Science Computing Facility. Each AMSU FOV has a spatial resolution of approximately 42 km near nadir and coincides with a 3 X 3 array of AIRS FOVs, which have a spatial resolution of approximately 14 km. The data are thinned by sub-sampling horizontally to the center FOV of each 3 X 3 array or golf ball (see Fig. 3.1). These data are then distributed to numerical weather prediction centers using the Binary Uniform Format for the Representation of meteorological data (BUFR). To further aid the distribution of AIRS data, two files are generated, each containing 1 of 18 FOV or every other golf ball (Goldberg et al. 2003). Data distribution is explained in greater detail by Goldberg et al. (2003). The first AIRS dataset used in operations by NCEP was the 281 channel, 1 of 18 FOV AIRS dataset in operations. Appendix C lists the 281 channels being sent to NCEP for assimilation. Once received at NCEP the AIRS data are processed into files specific to the early (GFS) and late (GDAS) cycles of the analysis. Both of these analyses accept data within three hours of the synoptic time. The cutoff time for the early analysis is 2:45 after synoptic time, and the cutoff time for the late analysis is 5:50 after synoptic time. All AIRS data meeting these two constraints are used by the analysis system. Figure 6.1 is an example of the AIRS orbits which were used in a 06 UTC analysis cycle.

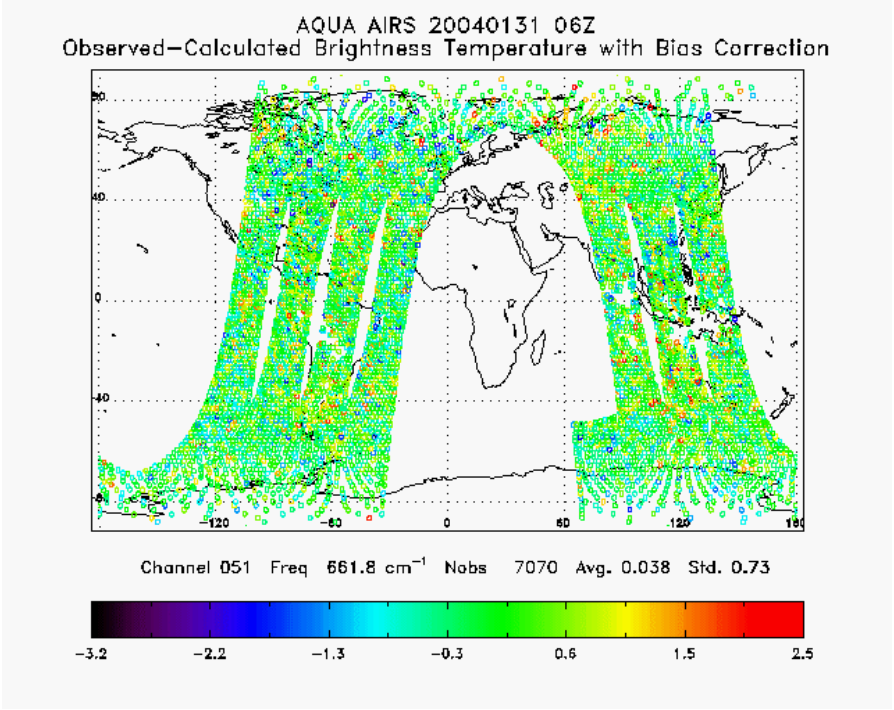

Figure 6.1 AIRS data coverage at 06 UTC on 31 January 2004. Geographical distribution of observation -background brightness temperatures at 661.8 cm^{-1} are shown.

6.2 Channel Selection

The AIRS instrument has 2378 channels. It is difficult to use all the channels in the data assimilation process because of computing and communication limitations. The information content of these channels is highly correlated. Computational time can be decreased by limiting the number of channels. It is also desirable to use channels with sharp localized weighting functions as it reduces the correlation between channels. For NWP centers, the AIRS data are spectrally thinned to 281 channels. These channels were selected as being optimal using the method of channel selection described in detail by Suskind et al. (2003). The 281 channels are shown with respect to the full set of 2378 channels in Fig. 6.2.

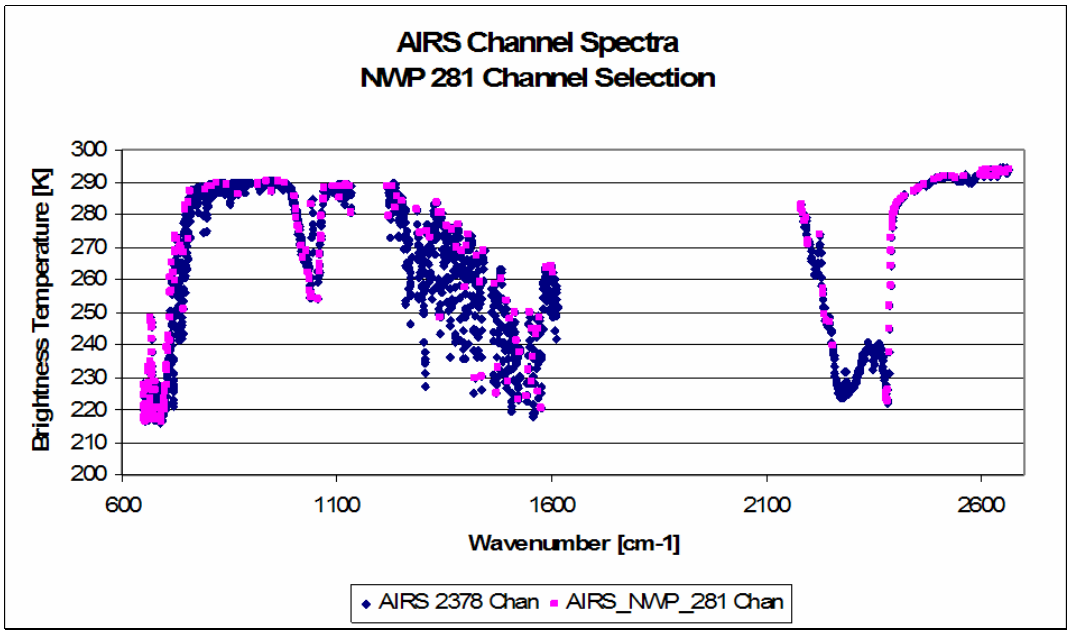

Figure 6.2 AIRS channel spectra by wavenumber for the 2378 channels (blue diamonds) and the 281 channels (magenta squares) for a mid-latitude atmosphere. A more detailed description of the AIRS channels including these used in NWP is seen in Appendix C. Courtesy of Chris Barnett.

In the NCEP operational AIRS 281 channel dataset, 30 channels are not assimilated in the GDAS for a number of reasons. The 667.27 – 670.57 cm^{-1} channels were removed because their weighting function peaks above the top of the present version of the model. The 2248.56 – 2388.15 cm^{-1} channels were removed due to local thermal equilibrium (LTE) effects. The 2640.04 cm^{-1} channel was removed due to large innovation differences. As such, 251 channels were considered usable for NCEP's operational assimilation system. The number of channels was further reduced to 152 due to the penalty function being dominated by AIRS data. The 152 channels are shown in Fig 6.3 with respect to the full 2378 channel set and are listed in Appendix C.

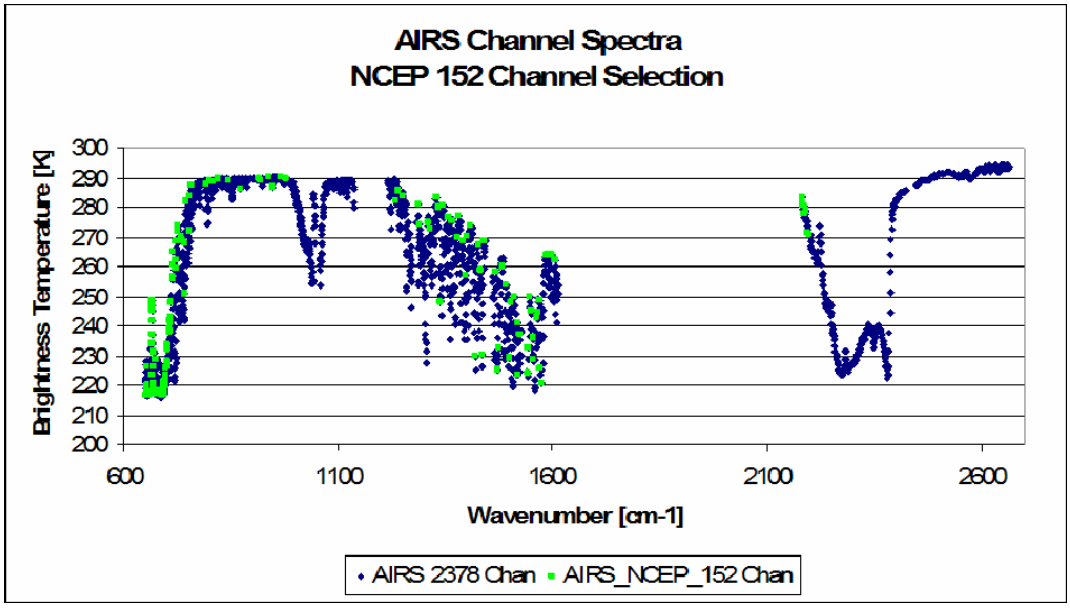

Figure 6.3 AIRS channel spectra by wavenumber for the 2378 channels (blue diamonds) and the 152 channels (green squares) for a mid-latitude atmosphere. A more detailed description of the AIRS channels including these used in NWP is seen in Appendix C. Courtesy of Chris Barnett.

For the studies reported here, a number of enhanced data sets were also generated and used, including every FOV with 281 channels and every FOV with 2378 channels. In particular, data sets comprising of every AIRS field of view were constructed and put into BUFR format. These were used in the studies reported in Chapters 7-10. The AIRS every field of view and 281 channels data set are now available in real time and are a part of the NCEP operational data base.

6.3 Assimilation Weights

The assimilation weights for AIRS are determined in a similar method as those for other types of radiances. Statistics of the brightness temperature standard deviation to the model background are collected over a several week period with the assimilation system set to monitor the values. Tests are done within the assimilation system to adjust the weights for other parameters such as surface type and solar reflection to provide an appropriate weighting for the data in comparison with other data types in the analysis.

The shortwave channels are difficult to assimilate during the day (solar zenith angle $< 90^{o}$) due to errors in modeling the reflection from the surface of the earth. To allow for the solar modeling shortcomings, the shortwave channels with wavenumbers between 2000 and 2500 cm^{-1} are down weighted and channels with wavenumbers longer than 2500 cm^{-1} are rejected when the solar zenith angle is less than 90^{o}.

6.4 Radiance Bias Corrections

Deriving the radiance bias correction for AIRS was similar to the procedures used for other instruments. Within the SSI and GSI the air mass portion of the radiance bias correction adjusts during each outer loop of the assimilation. At the end of the assimilation, the air mass and fixed predictors are recomputed and updated for the next cycle. The fixed predictors, latitude, surface temperature, temperature laps rate, temperature lapse rate squared and satellite zenith angle are computed as a 30 day running mean.

The initial computation of the bias corrections is accomplished by running the analysis system and monitoring the new sensor radiances for approximately 30 days. The statistics for these 30 days are then used to derive the fixed bias corrections. The assimilation system is then started at the beginning of the experiment, with identical bias correction files, and the bias corrections are allowed to adjust as the experiment proceeds.

Chapter 7: The AIRS Assimilation Experiment

7.1 Introduction

The AIRS instrument presents opportunities for significant improvements in numerical weather prediction from the assimilation of hyperspectral infrared data. The increase in spectral resolution available from the AIRS sensor, for example, will make it possible to more accurately determine temperature and moisture fields. Second generation sounders such as HIRS/3, AMSU-A, and AMSU-B have vertical resolutions of the order of 3km and as a result measure temperature to between 1.5K to 2.0K RMS (dependent on the first guess temperature profile). The new hyperspectral sounders such as AIRS measure temperature to within 1.0K in layers of 1.0km thickness. In relation to moisture profiles the accuracy of second generation sounder is typical of the order of 25% to 30% accuracy in relative humidity (dependent on first guess) while the specification for AIRS derived humidity was 15% in 1.0km layers. The considerably improved capability of the AIRS instrument relative to the second generation sounders are expected to provide improvement in analyzed temperature and moisture fields as a result of improved prognosis (Susskind et al. 2003).

This AIRS data assimilation experiment was designed in a way that renders it feasible for operational use of the methodology. This experiment involved using as many of the temperature and moisture channels as possible of the 281 channel AIRS subset chosen for operational distribution. There were 30 temperature channels which were not suitable for assimilation by the NCEP GDAS, and hence 251 were used for this experiment. These 251 channels are identified with the 2378 possible channels in Fig 7.1.

The analysis methodology was also similar to the current analysis practice, with particular consideration given to time limitations. As a result of the success of this experiment, operational application of these AIRS data followed the current NCEP operational upgrade of June 2005, being enabled by the enhanced computing resources.

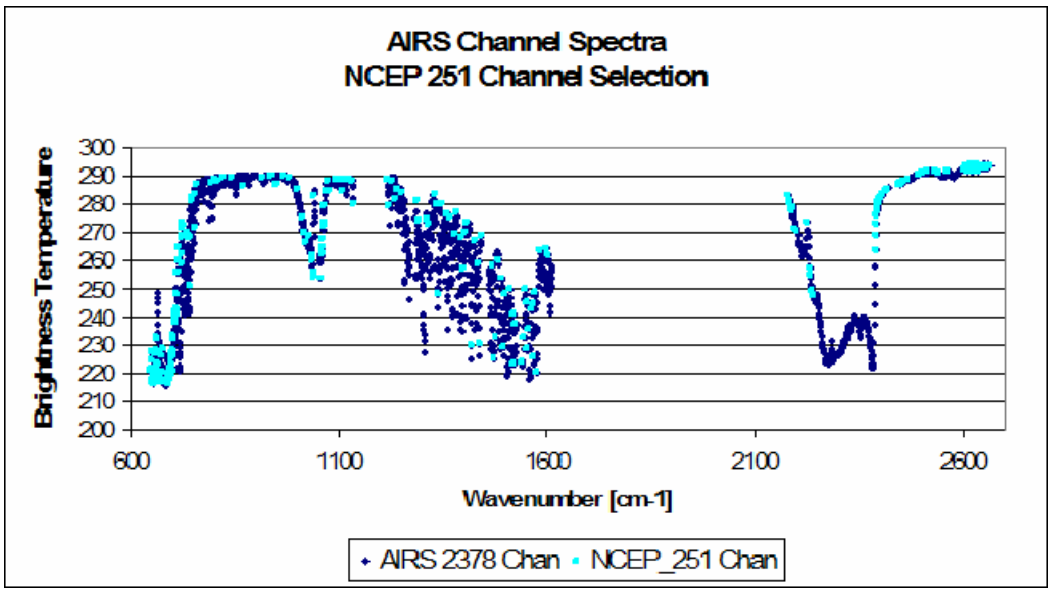

Figure 7.1 AIRS channel spectra by wavenumber for the 2378 channels (dark blue diamonds) and the 251 channels (light blue squares) for a mid-latitude atmosphere. Courtesy of Chris Barnett.

7.2 Assimilation of full spatial and spectral resolution data available to NWP

In order to improve the impact of AIRS data in NWP, the information content of the data set needed to be improved. This was accomplished by use of the full spectral and spatial AIRS data. The impact studies conducted so far have used the 1 of 18 FOV datasets, the low spatial resolution data, with 152 or 251 channels. Because of the sub-sampling scenario, it was suspected that there would be limited availability of clear data. Use of an AIRS dataset which has every FOV should increase the number of clear radiances used by the assimilation system.

The assimilation system would have difficulty assimilating all 2378 AIRS channels in the time allowed in this potential operational system. However, the information content in all of these channels is highly correlated and somewhat redundant. Computational time and convergence to observations within the analysis can be improved by limiting the number of channels. It is also desirable to use channels with sharp localized weighting functions as it reduces the correlation between channels. For NWP centers, the AIRS data are spectrally thinned to 281 channels. These channels were selected as being optimal for temperature and moisture, using a method of channel selection described in detail by Suskind et al. (2003). Of the 281 channels, the 251 suitable for use by the GDAS were assimilated. It was clear that full use of the available sub-sampled channels would improve the information content of the data used in the operational 3D-VAR system.

7.3 Experiment Design

The NCEP operational version of the GDAS/GFS (November 2003) was used at the operational resolution of T254, with 64 levels. For the control experiment, the NCEP operational database of conventional and satellite data, with the real-time cutoff constraints was used. A summary of the available data is detailed in Tables 5.2 and 5.3 where both the conventional and satellite components of the operational database are listed respectively.

The AIRS data was not a part of the operational data base during January – February 2004. These experiments were supported by the AIRS Science Team who reprocessed the AIRS data for the period 1 January – 15 February 2004 into files containing 281 channels and every FOV. These data were reformatted into BUFR by NESDIS. The radiances from the Aqua AMSU-A instrument were not included in the

control or AIRS experiment as these data were not part of the operational database at the time.

7.3.1 Determining Clear Radiance Profiles

The GDAS only uses radiances which are free from cloud effects. These radiances may be from cloud free areas, between clouds or from above the clouds. Finding FOVs with the most cloud free channels is critical to obtaining forecast impact. Knowledge of the surface temperature is a major component in determining if a FOV is clear. Typically, if a surface sensing channel is colder than the model surface temperature, the FOV is considered cloudy. The standard operational test for determining the clearest FOV for infrared sensors is to use a single channel which has a significant surface contribution. This channel surface-Brightness Temperature (BT) is compared to the GDAS surface temperature. If all surface-BTs are colder than the GDAS surface temperature, the spectral profile with the warmest surface-BT FOV is selected for assimilation. If more than one FOV is warmer than the GDAS surface temperature, the FOV closest to the center of the thinning box is selected.

The AIRS Science Team developed a Sea Surface Temperature (SST) algorithm (AST-SST) specific to AIRS which used 4 infrared channels (Mitch Goldberg, personal communication) and is calculated by:

$$\text{AST-SST} = 8.28206 - 0.97957*BT(10.89) + 0.60529*BT(11.29) + 1.74444*BT(9.19) - 0.4037*BT(7.44). \quad (7.1)$$

This SST algorithm is an improvement on the single channel estimates over the sea, but may under estimate the surface temperature over land, snow and ice. The channels in the 8μm region may lead to colder temperatures due to the surface emissivity of land and ice

being less than that of water. This may result in the FOV being treated as cloudy data and result in less clear data being assimilated.

A test which is typically used for detecting cloud contaminated profiles in the infrared region is the longwave/shortwave test or more commonly known as the BT(4.0) – BT(11.0) test. This test is used over land and ocean when the solar zenith angle is greater than 90^o (at night). It was used as criteria in the SSI thinning routine to determine the optimal radiance profile to assimilate. The AIRS channels closest to these wavelengths are BT(3.91) and BT(10.90). Radiance profiles which have a (BT(3.91) - BT(10.90)) between -1.5^oK and 1.0^oK are typically considered clear.

To determine the clearest FOV, equation (7.1) was used to determine the surface temperature. For FOVs over land and ocean at night, the following criteria must be met for the radiance profile to be considered clear:

$$(\text{AST-SST}) - (\text{Model Surface Temp}) > -0.80$$
$$\text{and}$$
$$-1.5 < (\text{BT}(3.91) - \text{BT}(10.90)) < 1.0$$

For FOVs during the day, the AIRS-SST must meet the following criteria:

$$(\text{AST-SST}) - (\text{Model Surface Temp}) > -0.20$$

If more than one FOV passed these tests in a specific thinning box, the spectral profile with the FOV closest to the center of the thinning box was selected. In the 6-hour assimilation time window, approximately 7450 thinning boxes are used. Once the best FOV was chosen for each thinning box, the AIRS data were then subjected to a test similar to that of McNally and Watts (2003). This test takes into account the variance of each channel along with the model derived channel BT. If the channel BT is sufficiently close to the model derived BT based on the channel variance, it is used by the assimilation system. Of the

7450 FOVs, almost all (7450) are used in the Stratosphere and this decreases to about 1000 at the surface. Figure 7.1 is an example of a histogram of AIRS channels which pass the quality control procedures for one assimilation cycle.

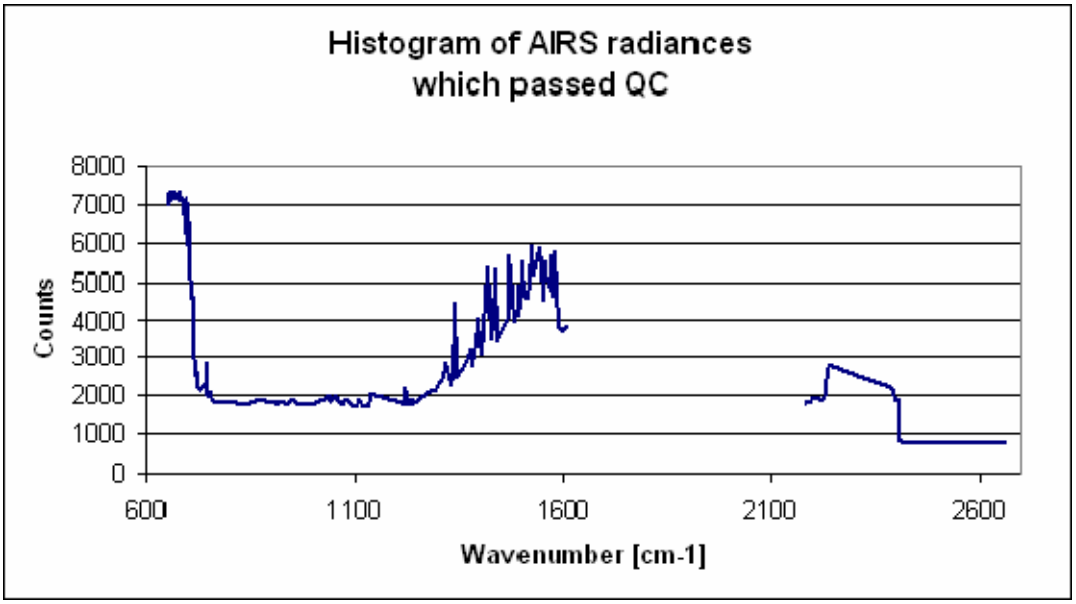

Figure 7.2 Histogram of AIRS clear radiances which passed all the quality control procedures in one assimilation cycle by wavenumber.

The total number of radiances available in a 6-hour assimilation is typically about 2.0×10^8. These are reduced to using only one FOV in a thinning box (7450 boxes * 281 channels = 2.1×10^6). Of those radiances in the thinning box, approximately 8.5×10^5 pass the quality control and are used by the assimilation system. The AIRS data usage is summarized in Table 7.1.

Table 7.1 AIRS data usage per analysis cycle in the full spatial and spectral resolution experiments.

Total AIRS data available to the analysis	2.0×10^8 radiances
Total selected for possible use	2.1×10^6 radiances
Data used by the analysis (clear)	8.5×10^5 radiances

7.4 Results

This experiment was run for the period 1 January to 27 January 2004 at which time NCEP ASP super-computer was terminated. The output was processed using the

operational NCEP verification software. Figures 7.3 and 7.4 present the waves 1-20 anomaly correlations for days 0 to 7 for the Control and AIRS experiment. The blue line is the control simulation which closely replicates NCEP operations at that time and includes all data routinely used by the GDAS/GFS. The magenta line is the anomaly correlation diagnosed from including AIRS data into the operational data stream. Figure 7.3 shows that AIRS has a consistent and beneficial effect on the 1000 hPa forecast anomaly correlations of geopotential height at mid-latitude for the (a) Northern and (b) Southern Hemispheres out to day 7. The mid-latitude 500 hPa geopotential height anomaly correlation (Fig. 7.4) are higher on average for the AIRS experiment for every forecast period. Another noticeable characteristic is that the Southern Hemisphere anomaly correlations have a consistently greater improvement than in the Northern Hemisphere. This is expected due to the extra land mass where less satellite data are used and the large number of conventional observations taken in the Northern Hemisphere.

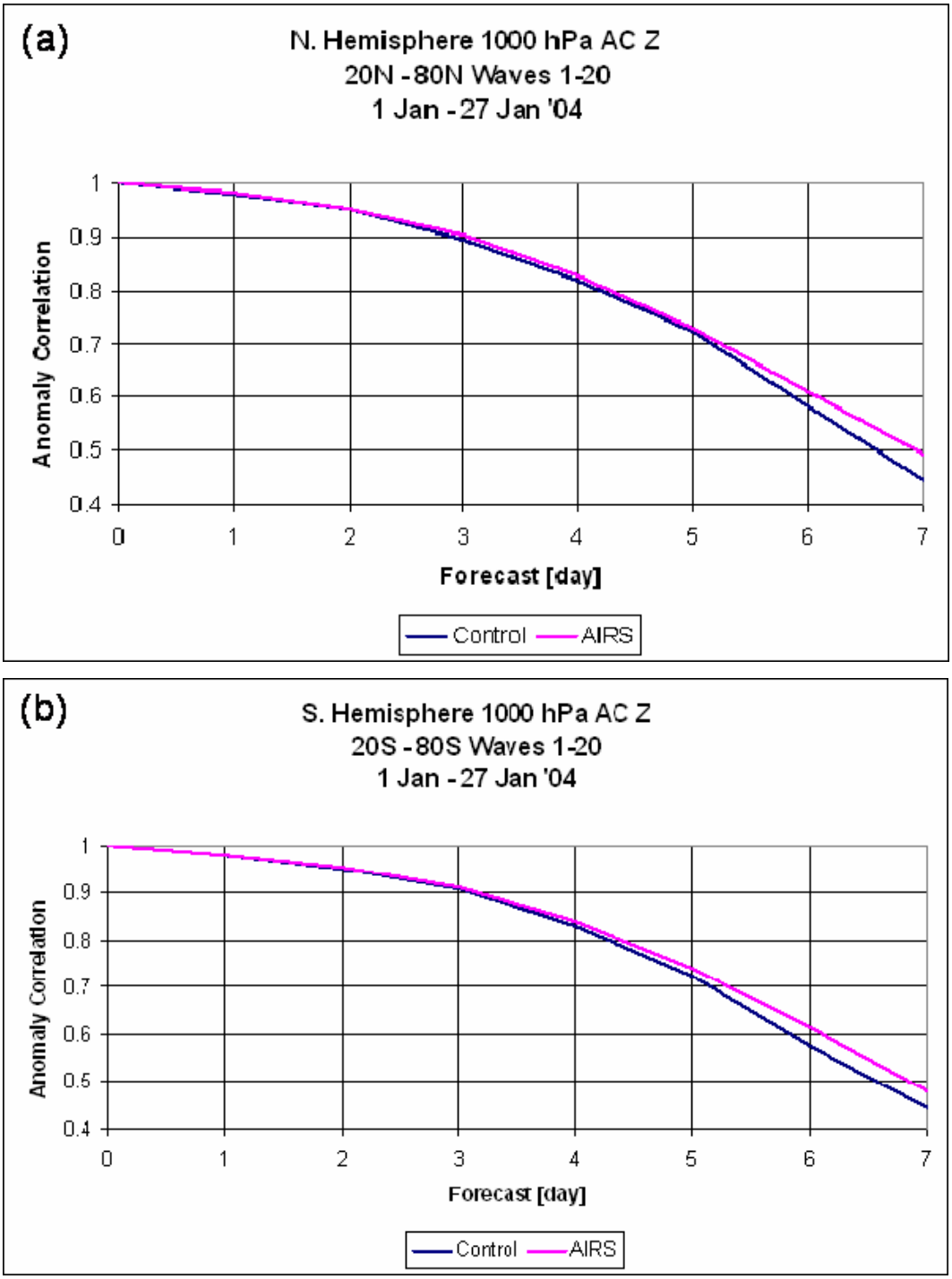

Figure 7.3 Anomaly correlations for waves 1 – 20 at 1000 hPa for the (a) Northern and (b) Southern Hemisphere. AIRS radiances (AIRS) are magenta and without AIRS (Control) are blue, for 1 January to 27 January 2004.

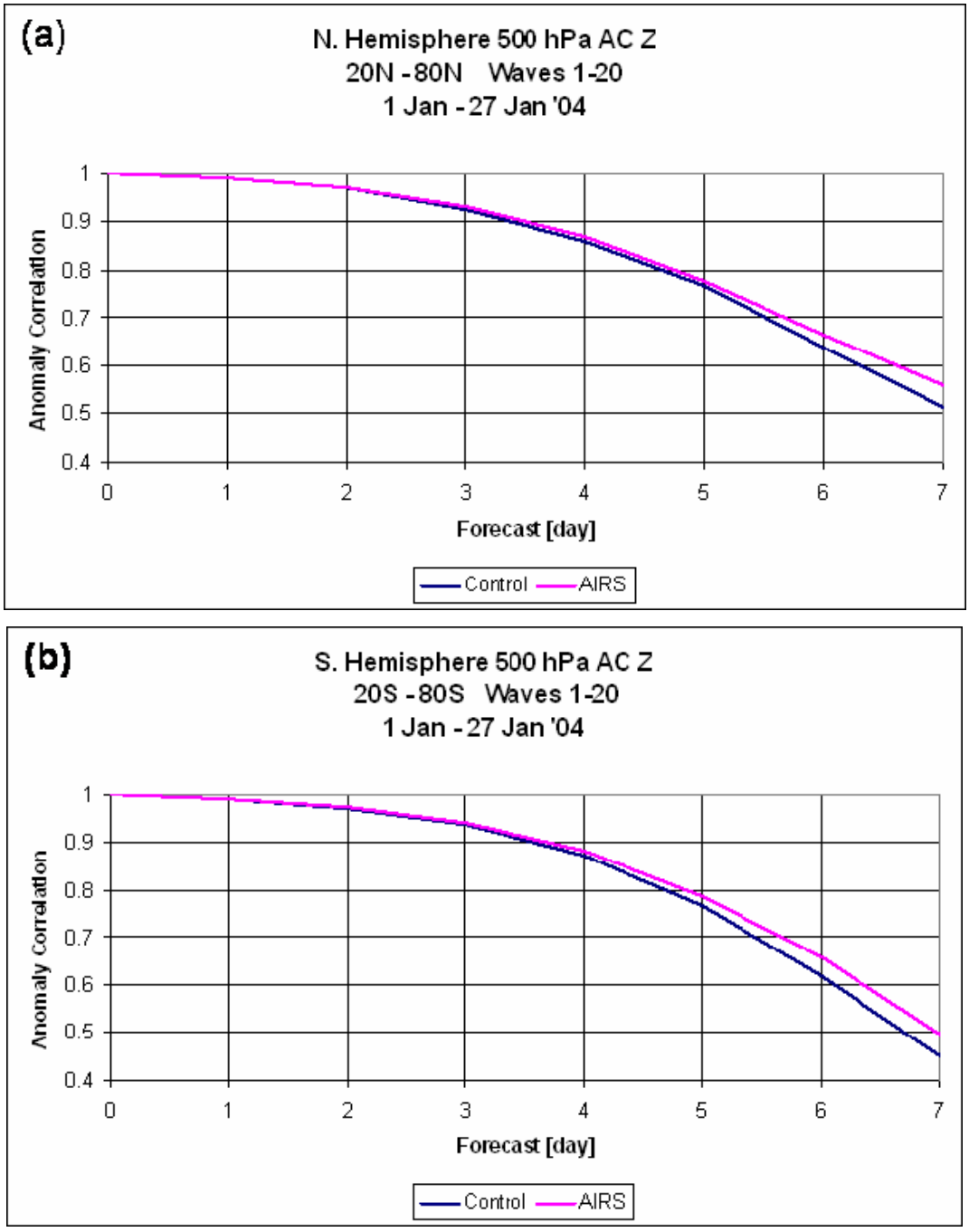

Figure 7.4 Anomaly correlations for waves 1 – 20 at 500 hPa for the (a) Northern and (b) Southern Hemisphere. AIRS radiances (AIRS) are magenta and without AIRS (Control) are blue, for 1 January to 27 January 2004.

Figures 7.5 and 7.6 display the time series variations of the day 5 forecast anomaly correlation at 1000 and 500 hPa respectively. Among the considerable daily variations, the time series shows more days with positive impact than negative. The standard deviations

of the anomaly correlations for the Northern Hemisphere at 500 hPa are almost equal at 0.0727 and 0.0736 for the Control and AIRS respectively. The standard deviations of the anomaly correlations for the Southern Hemisphere at 500 hPa show a decrease for AIRS, with the values being 0.0827 and 0.0761 for the Control and AIRS respectively. The standard deviations for both hemispheres at 1000 hPa are smaller with AIRS data. The values for 1000 hPa are 0.0793 and 0.0752 in the Northern Hemisphere and 0.0917 and 0.0823 in the Southern Hemisphere for the Control and AIRS respectively.

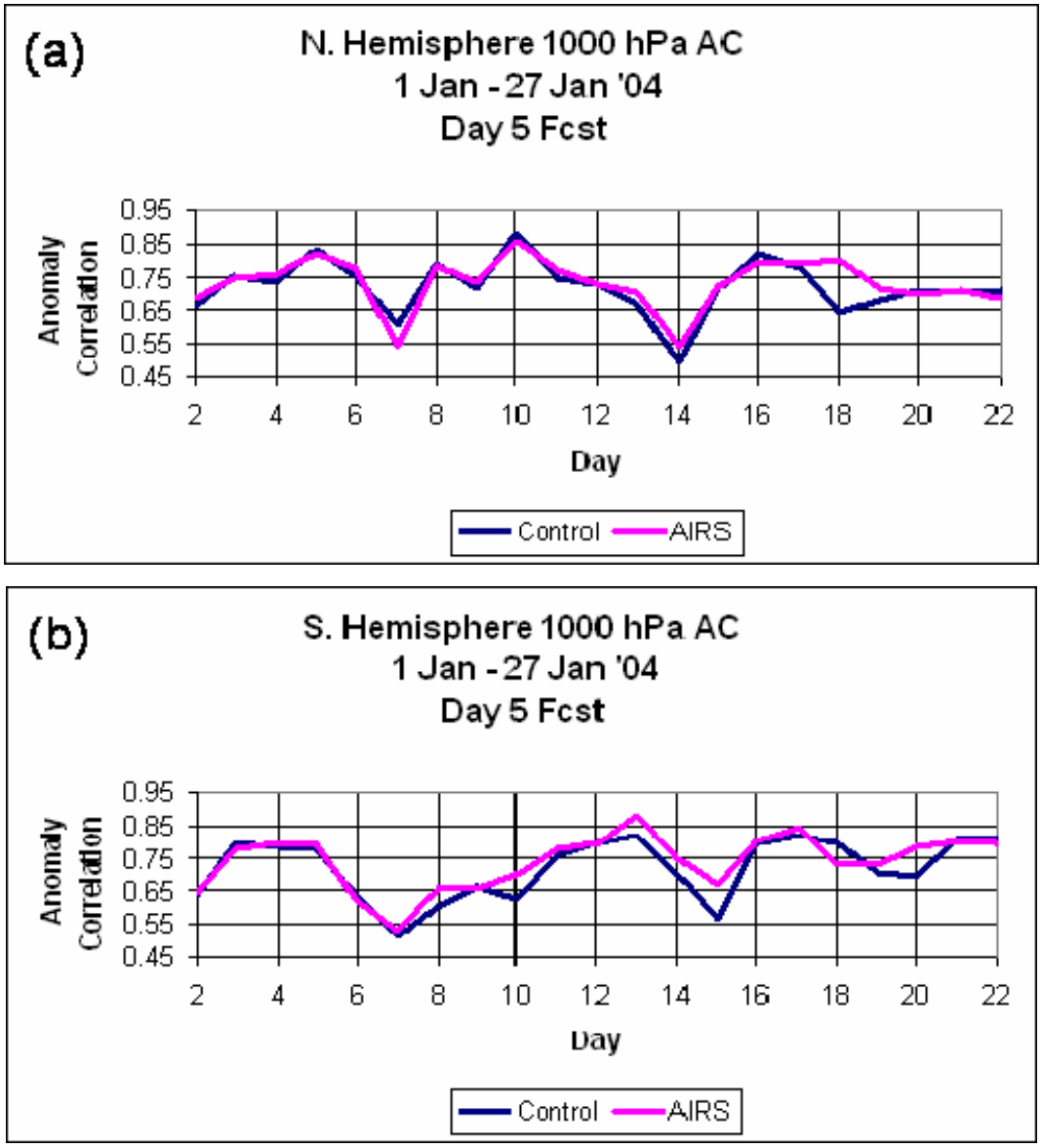

Figure 7.5 Time series of day 5 anomaly correlations for waves 1 – 20 at 1000 hPa for the (a) Northern and (b) Southern Hemisphere. AIRS radiances (AIRS) are magenta and without AIRS (Control) are blue, for 1 January to 27 January 2004.

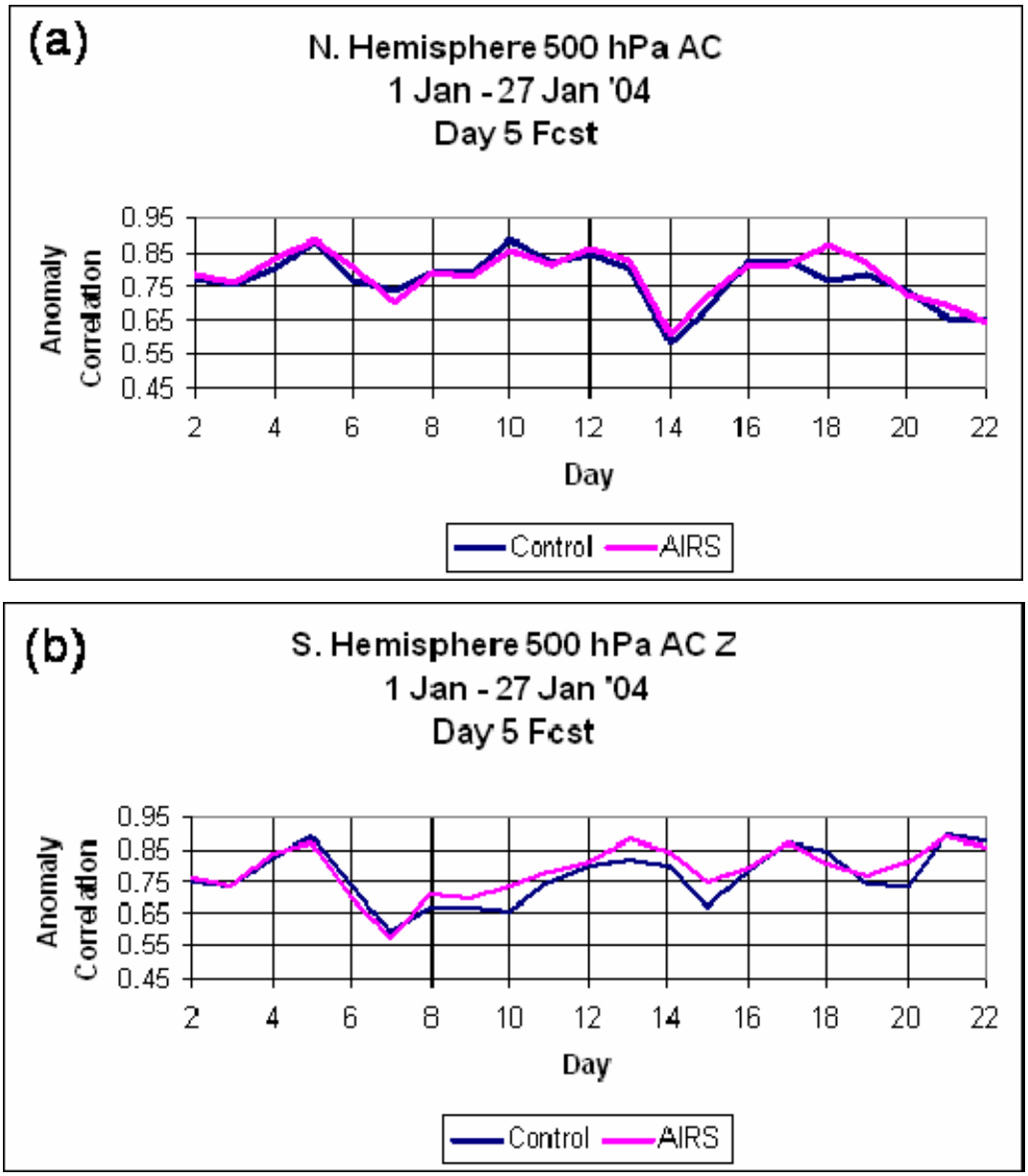

Figure 7.6 Time series of day 5 anomaly correlations for waves 1 – 20 at 1000 hPa for the (a) Northern and (b) Southern Hemisphere. AIRS radiances (AIRS) are magenta and without AIRS (Control) are blue, for 1 January to 27 January 2004.

Impacts on the wind field in the tropics for this experiment were near neutral with some showing small improvements. Anomaly Correlations for the V-component of wind (Fig. 7.7a) and wind vector RMS (Fig. 7.7b) are displayed at 850 hPa for the tropical region (20°N to 20°S). The GDAS/GFS forecast errors increase rapidly in the first day then

increase at a slower rate throughout the rest of the forecast in the tropics. This is a well know characteristic of the GDAS/GFS.

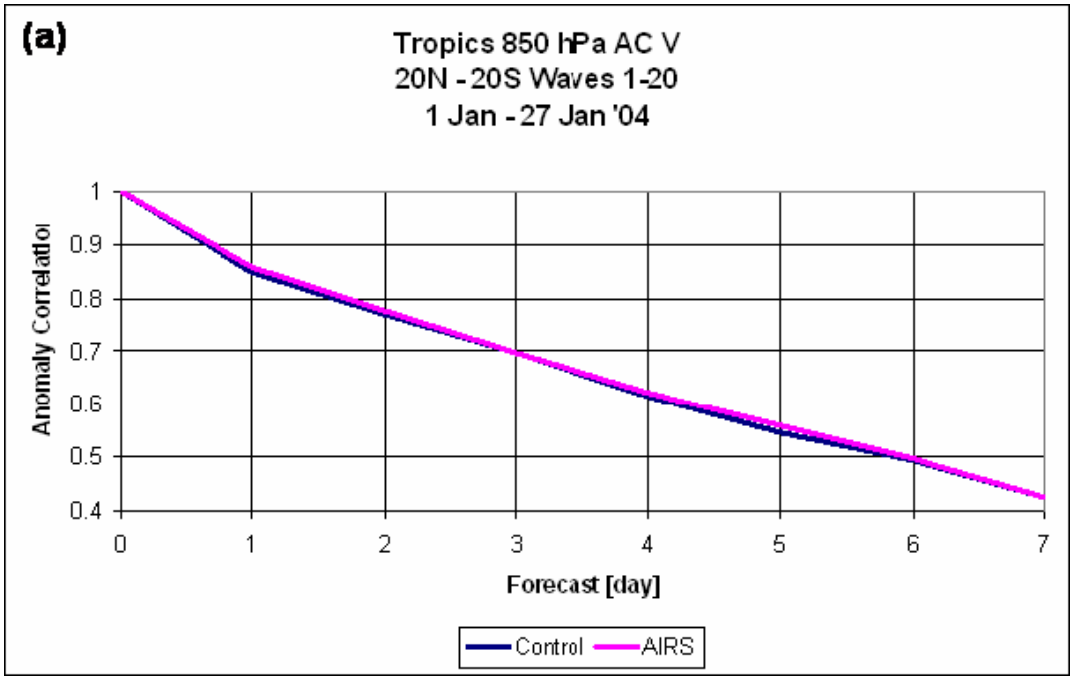

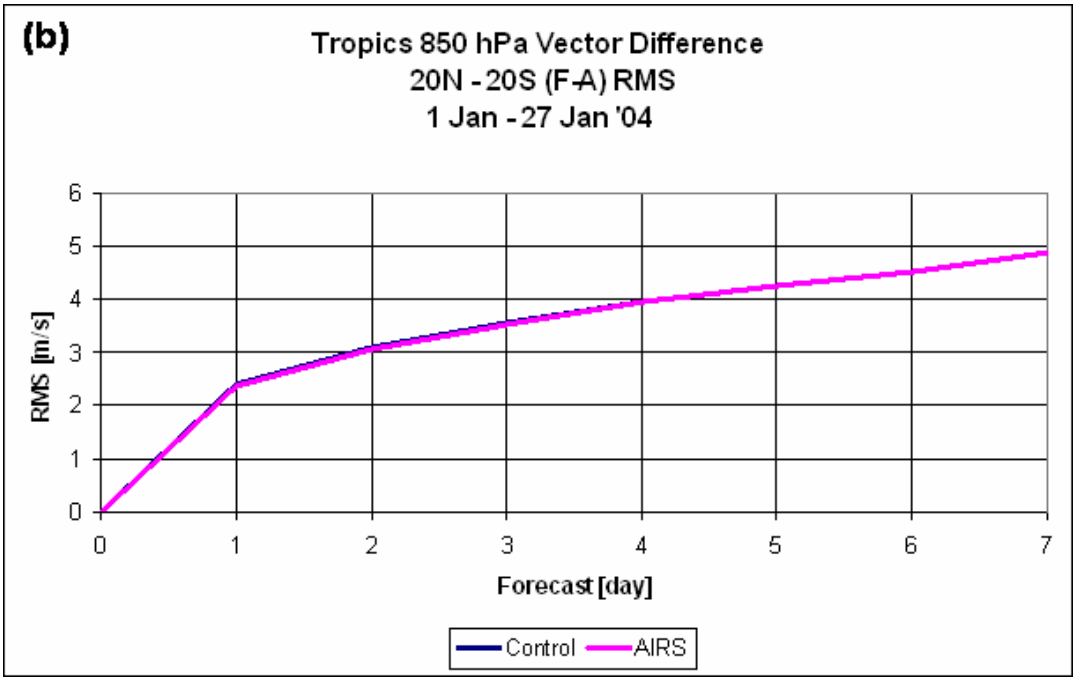

Figure 7.7 Anomaly correlations for the tropical region (20°N – 20°S). V-Component of wind (a) for waves 1 – 20 at 850 hPa. Wind vector RMS errors (b) at 850 hPa. AIRS radiances (AIRS) are magenta and without (Control) are blue for 1 January to 27 January 2004.

In the case of moisture, the impact is clearly positive. Figure 7.8 presents the 24-hour geographical distributions of forecast impact for (a) 850 hPa relative humidity and (b) 500 hPa temperature. The low level relative humidity impacts (Fig. 7.8a) are almost entirely positive. The greatest impacts are in the Polar Regions and over the land masses in the Southern Hemisphere. The large impacts in the Polar Regions can be explained by the low water vapor concentration and low temperatures creating large differences in relative humidity. The temperature impacts at 500 hPa (Fig. 7.8b) are also almost entirely neutral or positive.

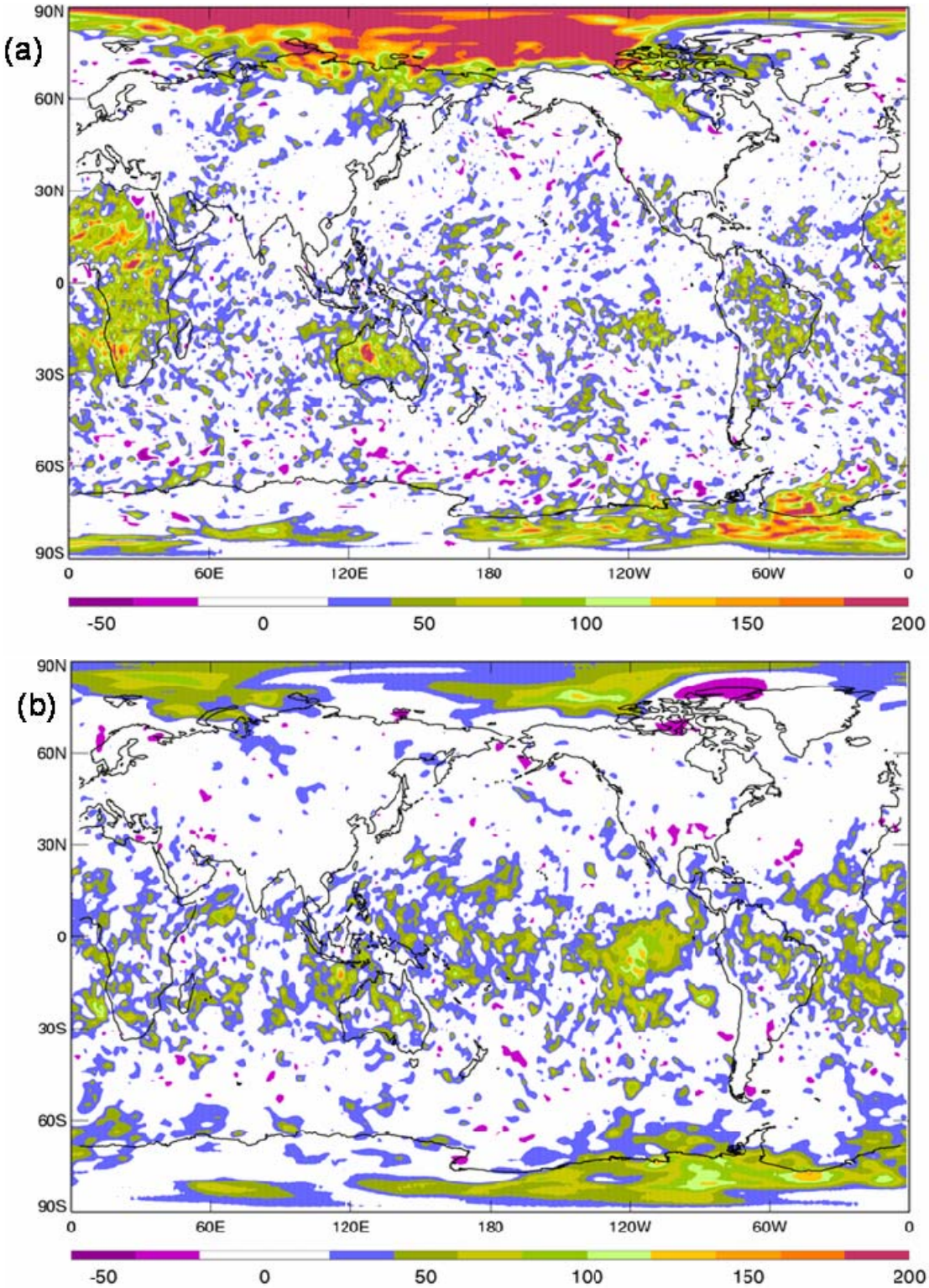

Figure 7.8 Geographical distribution of 24-hour forecast impact for (a) 850 hPa relative humidity and (b) 500 hPa temperature for 1 January to 27 January 2004.

7.5 Summary

The AIRS data present opportunities for significant improvements in numerical weather prediction. The increase in spectral resolution available from the AIRS sensor, for example, makes it possible to more accurately determine temperature and moisture fields. The new hyperspectral sounders such as AIRS measure temperature to within 1.0K in layers of 1.0km thickness. In relation to moisture profiles, the accuracy of AIRS is 15% in 1.0km layers, a 40% improvement over the second generation HIRS sounders. The considerably improved capability of the AIRS instrument, relative to the second generation sounders, results in improvements in analyzed temperature and moisture fields as a result of improved prognosis.

This was the first AIRS experiment which used the full spatial (every FOV) and 251 channel AIRS data. This experiment was designed in a way that rendered them feasible for operational application. The NCEP operational version of the GDAS/GFS (November 2003) was used at the operational resolution of T254, with 64 levels. For the control experiment, the NCEP operational database of conventional and satellite data, with the real-time cutoff constraints was used. This experiment was run from 1 January to 27 January 2004 when availability of the NCEP ASP super-computer was terminated.

In general the AIRS data improved most of NCEP's forecast skill benchmarks. AIRS data had a consistent and beneficial effect on the 1000 hPa forecast anomaly correlations of geopotential height at mid-latitude for the Northern and Southern Hemispheres out to day 7. The mid-latitude 500 hPa the average geopotential height anomaly correlations are higher for every forecast day (1-7) of the AIRS experiment. Another noticeable characteristic is that the Southern Hemisphere anomaly correlations

have a consistently greater improvement than in the Northern Hemisphere. Among the considerable daily variations, the time series shows more days with positive impact than negative. Impacts on the wind field in the tropics for this experiment were near neutral with some places showing small improvements. In the case of moisture, the impact was clearly positive. The greatest impacts are in the Polar Regions and over the land masses in the Southern Hemisphere.

AIRS hyperspectral data (from one orbital instrument), used within current stringent operational constraints, shows significant positive impacts in forecast skill over both the Northern and Southern Hemisphere for January 2004. The results indicate a considerable opportunity to improve operational analyses and forecasts with hyperspectral data.

7.6 Conclusion

The introduction of AIRS hyperspectral data into environmental analysis and prognosis centers was anticipated to provide improvements in forecast skill. We have demonstrated that AIRS hyperspectral data, used within stringent current operational constraints, has significant positive impact in forecast skill over both the Northern and Southern Hemispheres for 1 January to 27 January 2004. Figure 7.9 is a summary of the day 5 anomaly correlations in both the Northern and Southern Hemispheres highlighting the forecast improvement realized in NCEP's GDAS. Given the opportunities for future enhancement of the assimilation system, the results indicate a considerable opportunity to improve current analysis and forecast systems through the application of hyperspectral data. It is anticipated current results will be further enhanced through improved physical modeling, a less constrained operational environment allowing use of higher spectral and spatial resolution and cloudy data, the use of complementary data such as MODIS

radiances and the effective exploitation of the new hyperspectral data which will become available from the IASI, CrIS and Geosynchronous Imaging Fourier Transform Spectrometer (GIFTS) instruments.

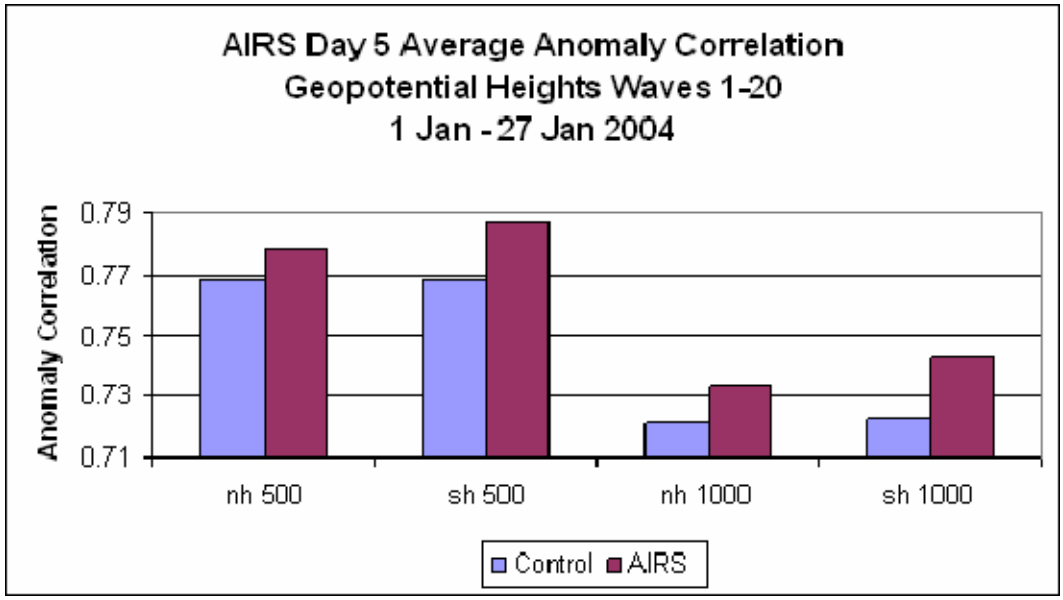

Figure 7.9 Bar chart of day 5 anomaly correlations of waves 1-20 at 500 and 1000 hPa for the mid-latitude regions during 1 January to 27 January 2004.

It is clear that the AIRS data have had a significant effect on forecast skill over both Hemispheres during this period. Not unexpectedly, the impacts are reduced in the Northern Hemisphere as a result of many influences, including greater data coverage from conventional surface-based observations, limited use of the AIRS data in the lower troposphere over land, and use of the data at less than full spatial and spectral resolution. The accuracy improvement shown in this sample of experimental forecasts is equivalent to a significant increase in operational forecast skill. The extent of the forecast improvement when compared, for example, with the rate of improvement in the United States through the 1990s, represents several years of development work at NCEP. In this case, the gain has come from adding data from a single instrument in conjunction with the many other operational data sources.

As a result of these experiments, the AIRS center FOV radiances, using 152 channels were incorporated into the operational dataset.

Chapter 8: Full Spatial Resolution Experiment

8.1 Introduction

In the impact studies using full spatial and spectral resolution AIRS data with the NCEP GDAS/GFS, cloud free AIRS radiance data were identified and used. The results of this previous experiment show that the AIRS data have a large beneficial effect on forecast skill over the Northern and Southern Hemisphere during January 2004. With the significant impact of the full spatial and spectral resolution experiment (Le Marshall et al. 2005a, Le Marshall et al. 2005b) in both the Northern and Southern Hemispheres, several questions were raised. Were the results due to the increased spatial resolution, spectral resolution or both? The design of this full spatial resolution experiment was to isolate and quantify the impacts of using every AIRS footprint.

8.2 Experiment design

The original operational AIRS BUFR files generated by NESDIS contained only the AIRS FOV from the center of every other AMSU FOV or 1 of 18 AIRS FOVs (see Fig. 3.1) which were transmitted to the NWP centers. In selecting the center FOV, no consideration was given to the FOV quality or cloud content for assimilation. The radiance thinning routine would then search through the AIRS BUFR dataset for the warmest BT(10.36) in the designated thinning box. This warmest field of view is considered to be the clearest/best for assimilation. This technique had limited success as stated by McNally et al. (2003) and Auligne et al. (2003).

The full spatial resolution dataset is used in both the center spot (AIRS Center) and the all AIRS FOVs (AIRS_SFOV) experiment. In the full spatial resolution datasets, all

footprints from the AIRS instrument, were generated and put into BUFR format by NESDIS for these experiments. The center of every other AIRS/AMSU golf ball was selected for use by the AIRS Center experiment (AIRS_Center). The AIRS Center experiment then used the original selection technique for infrared radiances of assimilating the warmest BT(10.36) in the thinning box. The AIRS_SFOV looked at every FOV and used the cloud characterization methods outlined in Chapter 7 to determine which FOV was the clearest (least cloud contaminated).

This experiment was designed in such a way that the methodology was suitable for operational application. This constraint includes using the 281 channel subset of AIRS data chosen for operational distribution. The analysis methodology was also similar to the current analysis practice, with particular consideration given to time limitations. Operational application of these AIRS data followed the current NCEP operational upgrade, being enabled by the enhanced computing resources. The operational GFS (November 2004), was run at the operational resolution of T254 with 64 levels. For the AIRS Center experiment, the NCEP operational database of conventional and satellite data, with the real-time cutoff constraints was used. A summary of the available data is found in Tables 5.2 and 5.3 where both the conventional and satellite components of the operational database are listed respectively. The full observational database was used including AQUA AMSU-A. Both the AIRS Center and the AIRS_SFOV experiment used 251 of the possible 281 AIRS channels. The table listing the 251 AIRS channels used for these experiments are in Appendix C.

8.3 Results

Typical AIRS data usage by the analysis, per analysis cycle, for the AIRS_SFOV and AIRS Center experiments are shown in Table 8.1. The total data available to the analysis was increased by more than an order of magnitude in the AIRS_SFOV experiment. The total number selected by the thinning routine remained the same because the total areal coverage of the AIRS data remained the same. Approximately 6% more data were used by the AIRS_SFOV experiment over the AIRS Center experiment. This 6% are considered the "extra" clear radiances found from using the full resolution dataset over the 1 of 18 dataset.

Table 8.1 AIRS radiance data usage per analysis cycle in the full spatial resolution experiments.

	AIRS_SFOV	AIRS Center
Total data input to analysis	$2.0x10^8$	$1.1x10^7$
Data selected for possible use	$2.1x20^6$	$2.1x10^6$
Data used in analysis	$8.5x10^5$	$8.0x10^5$

Figures 8.1 and 8.2 presents the waves 1-20 anomaly correlations of geopotential height at 1000 and 500 hPa respectively for days 0 to 7 of the AIRS_SFOV and AIRS Center experiment in the (a) Northern and (b) Southern Hemispheres during 1 January to 15 February 2004. Figures 8.3 and 8.4 are similar to Fig. 8.1 and 8.2 but are for 10 August to 20 September 2004. The blue line is the AIRS Center simulation which closely replicates NCEP operations and includes all data routinely used by the GDAS/GFS. The magenta line is the anomaly correlation derived from including AIRS SFOV data into the operational data stream. The AIRS had a consistent and beneficial effect on the 1000 hPa (Fig 8.1) and 500 hPa (Fig 8.2) forecast anomaly correlations for the (a) Northern and (b) Southern Hemispheres out to the day 7 for January-February 2004. The mid-latitude 500

hPa geopotential height anomaly correlation are higher for the AIRS_SFOV experiment for all (1-7) forecast days. The Southern Hemisphere anomaly correlations have a consistently greater improvement than in the Northern Hemisphere during January- February. During August-September (Fig 8.3 and 8.4) however, the Northern Hemisphere anomaly correlations show a greater improvement over the Southern Hemisphere. In these cases the AIRS_SFOV data have improved the summer forecasts more than the winter. The assimilation of AIRS_SFOV data in the tropical region shows neutral to small improvements at both levels in the V-component of wind and the wind Vector RMS for both January-February and August-September.

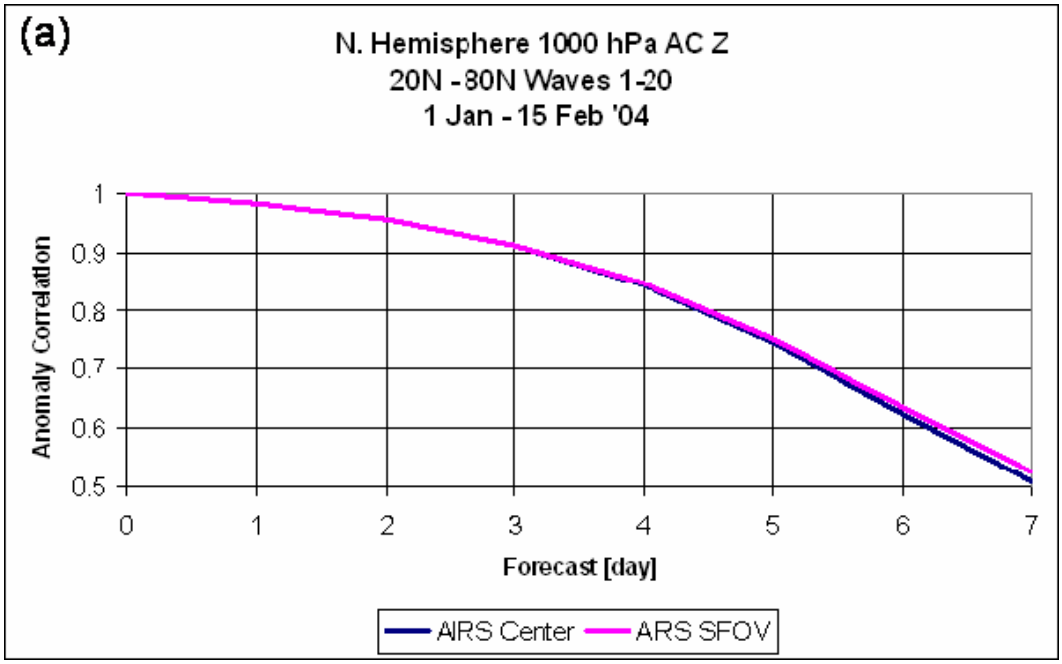

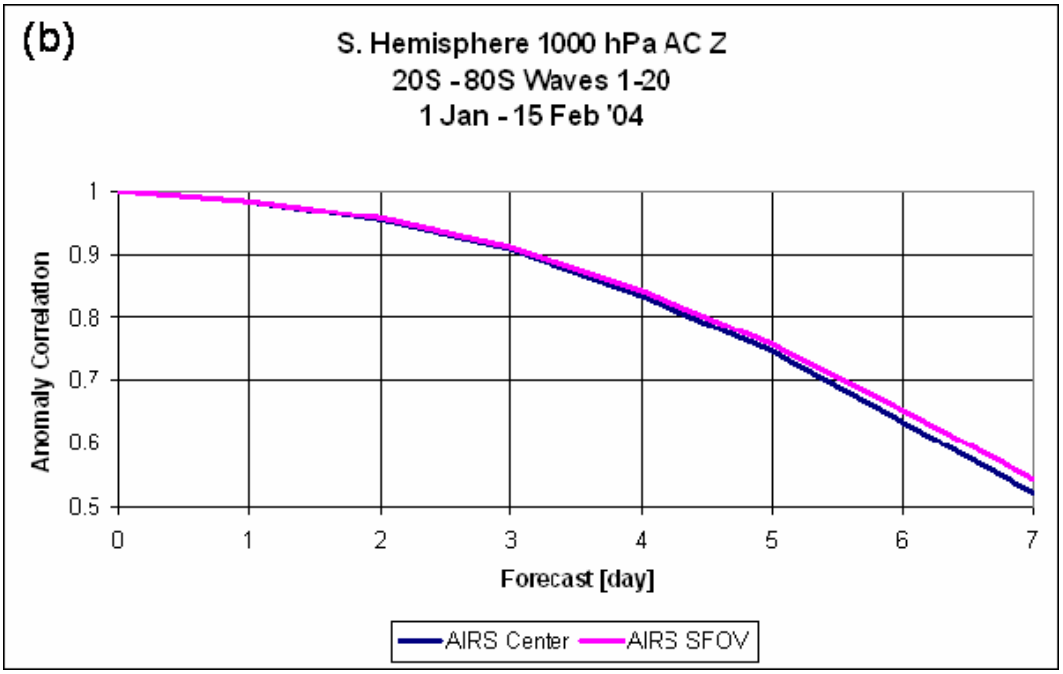

Figure 8.1 Anomaly correlations for waves 1 – 20 at 1000 hPa for the (a) Northern and (b) Southern Hemisphere. The single field of view (AIRS_SFOV) radiances are magenta, the 1 of 18 (AIRS Center) radiances are blue for 1 January to 15 February 2004.

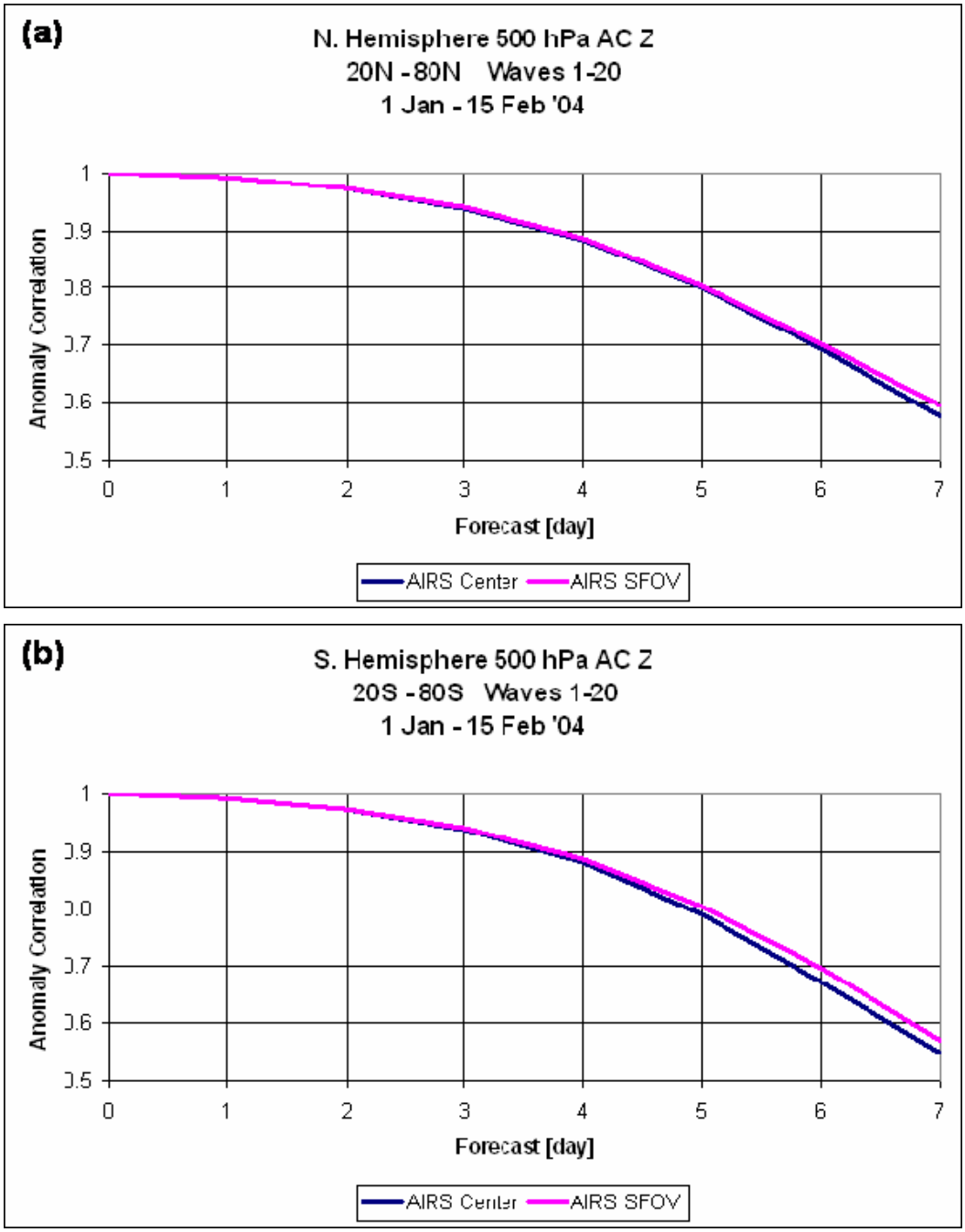

Figure 8.2 Anomaly correlations for waves 1 – 20 at 500 hPa for the (a) Northern and (b) Southern Hemisphere. The single field of view (AIRS_SFOV) radiances are magenta, the 1 of 18 (AIRS Center) radiances are blue for 1 January to 15 February 2004.

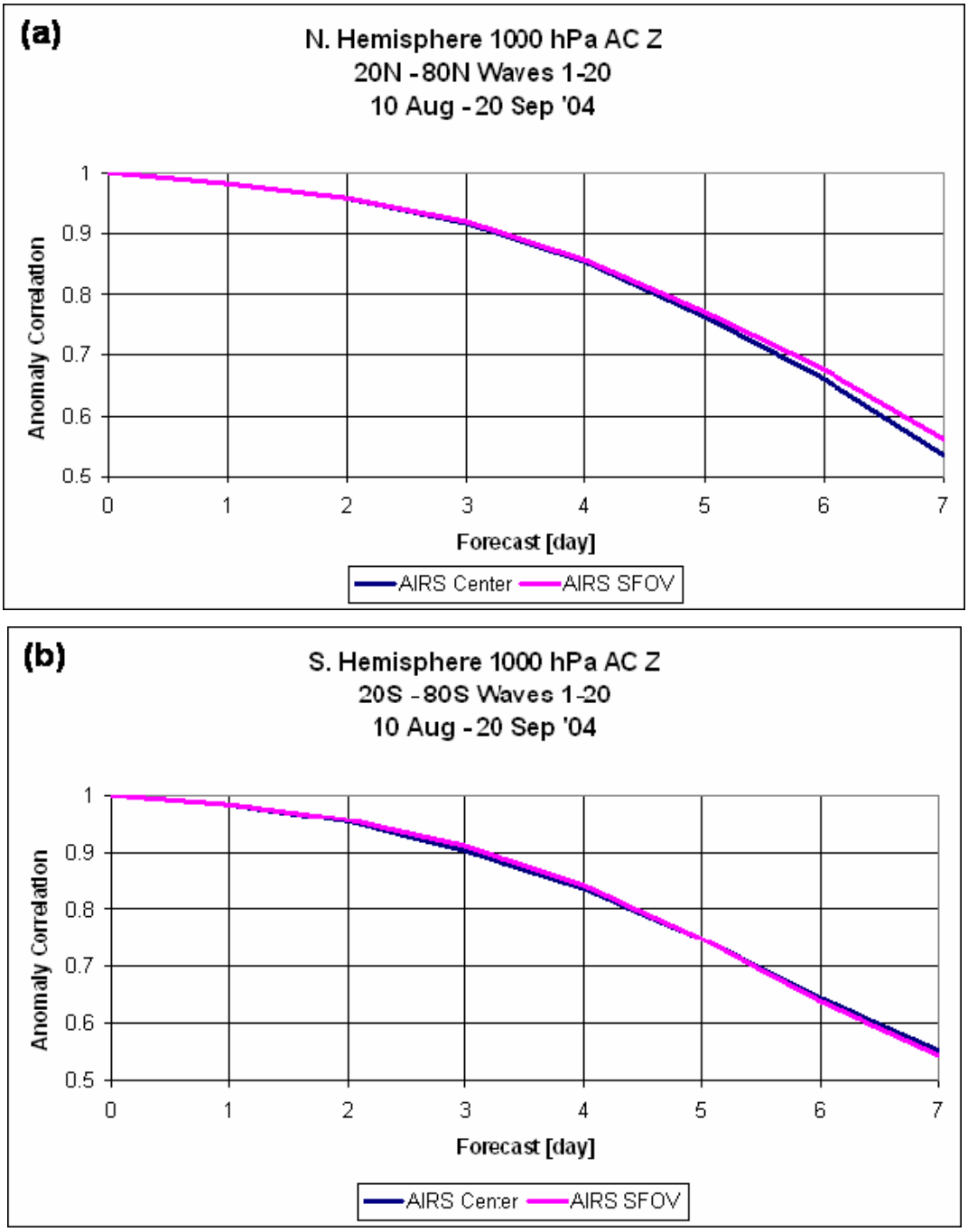

Figure 8.3 Anomaly Correlations for waves 1 – 20 at 1000 hPa for the (a) Northern and (b) Southern Hemisphere. The single field of view (AIRS_SFOV) radiances are magenta, the 1 of 18 (AIRS Center) radiances are blue for 10 August to 20 September 2004.

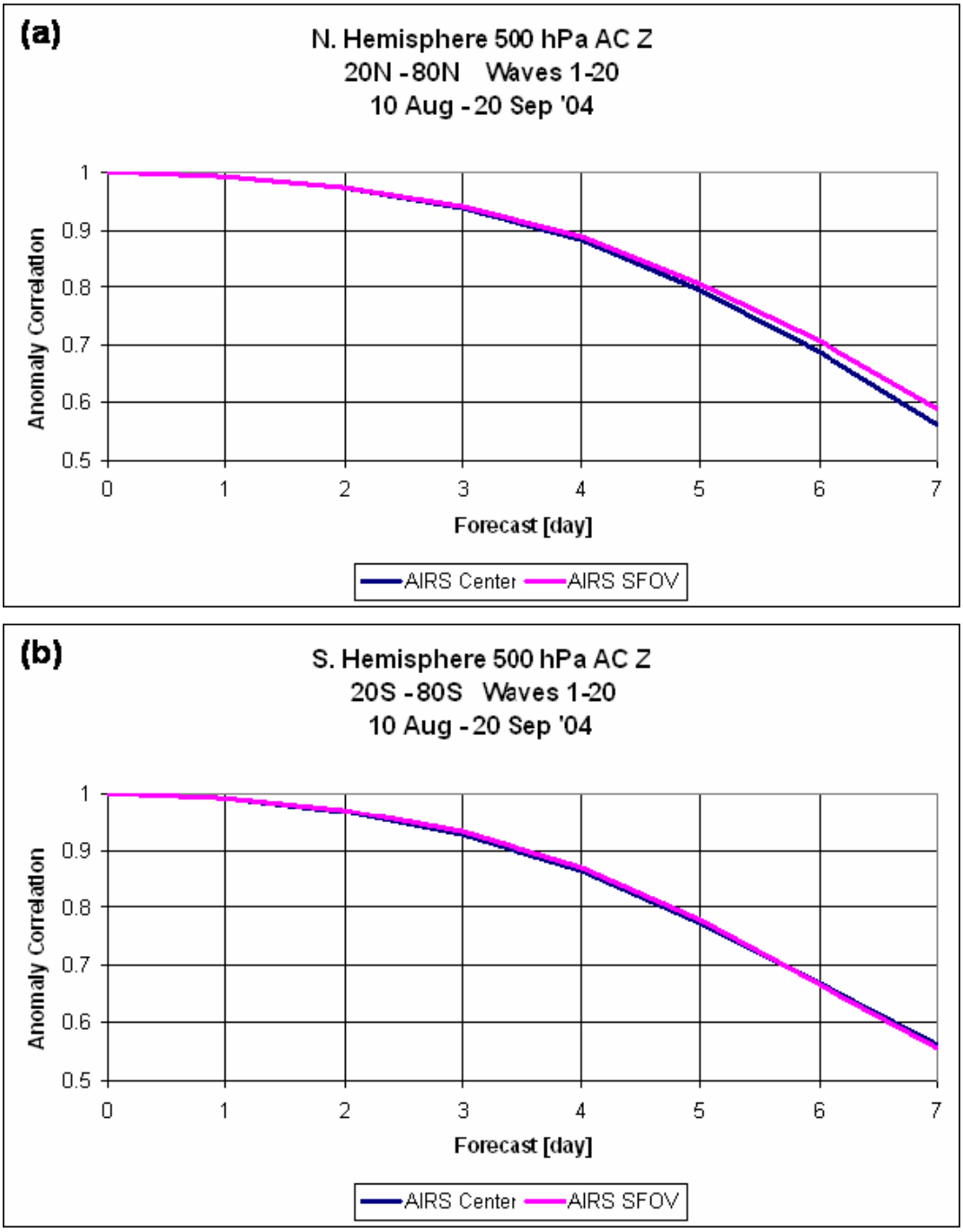

Figure 8.4 Anomaly Correlations for waves 1 – 20 at 500 hPa for the (a) Northern and (b) Southern Hemisphere. The single field of view (AIRS_SFOV) radiances are magenta, the 1 of 18 (AIRS Center) radiances are blue for 10 August to 20 September 2004.

Figures 8.5 and 8.6 display the time series variations of the day 5 forecast anomaly correlation in the (a) Northern and (b) Southern Hemispheres at 1000 and 500 hPa respectively for 1 January to 15 February 2004. Figures 8.7 and 8.8 are similar to Figs 8.5

and 8.6 except that these are for 10 August to 20 September 2004. Among the considerable daily variations, the time series shows more days with improved scores for the AIRS_SFOV than not. The standard deviations of the day 5 forecasts also suggest there is less variability in the forecast when using the full spatial resolution AIRS. Figure 8.9 is a bar chart of the day 5 forecast standard deviations for (a) 1 January to 15 February and (b) 10 August to 20 September 2004. This figure shows that, in general, using the AIRS_SFOV data generates a more consistent forecast. Only the AIRS_SFOV anomaly correlation for the Southern Hemisphere at 500 hPa during August-September displays a greater variability than the AIRS Center.

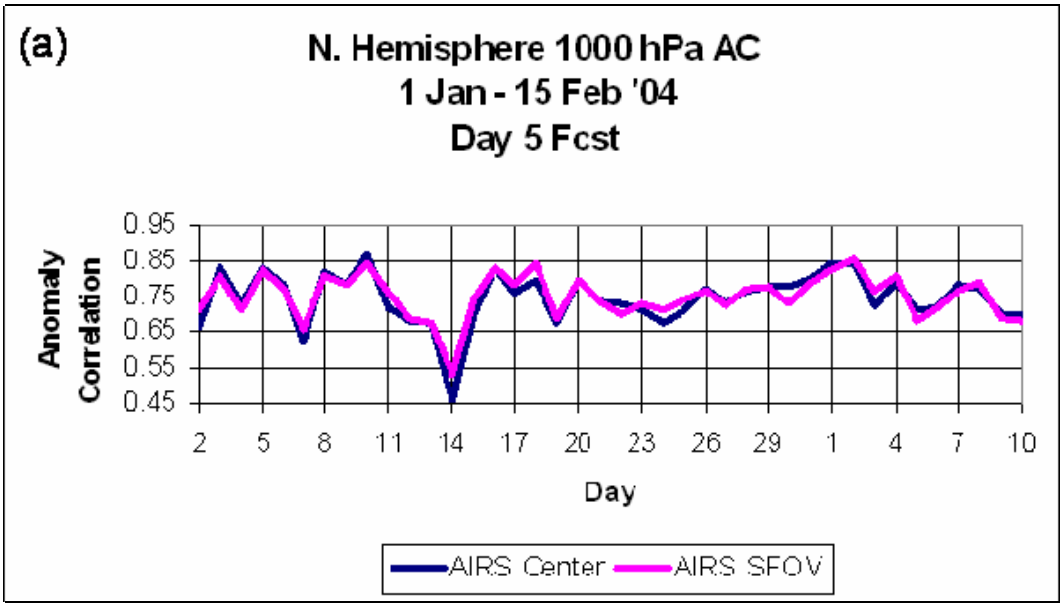

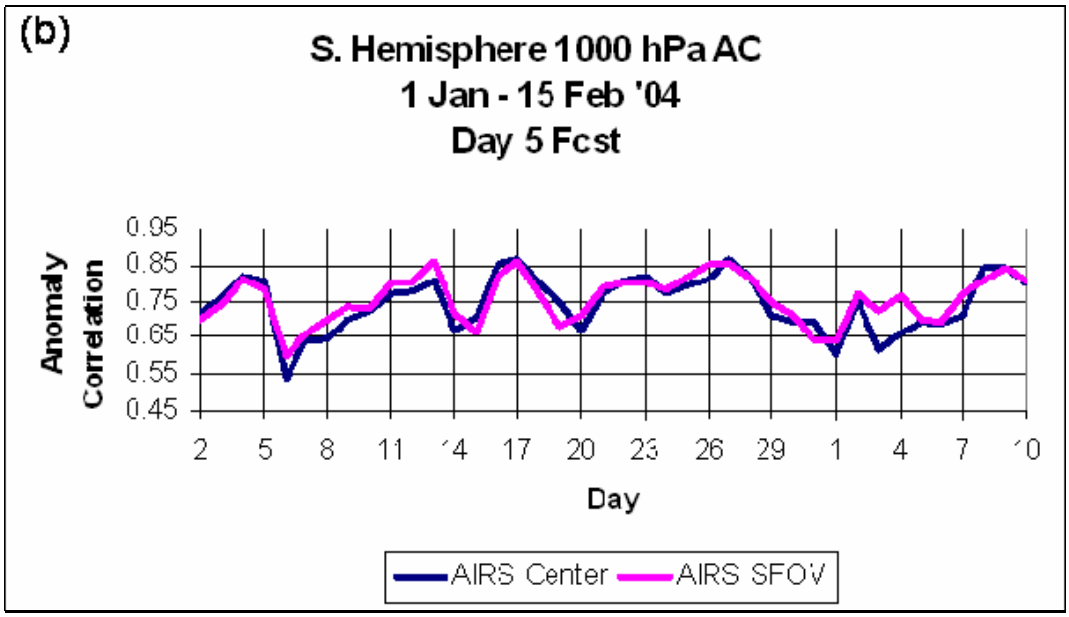

Figure 8.5 Time series of day 5 anomaly correlations for waves 1 – 20 at 1000 hPa for the (a) Northern and (b) Southern Hemisphere. The single field of view (AIRS_SFOV) radiances are magenta, the 1 of 18 (AIRS Center) radiances are blue for 1 January to 15 February 2004.

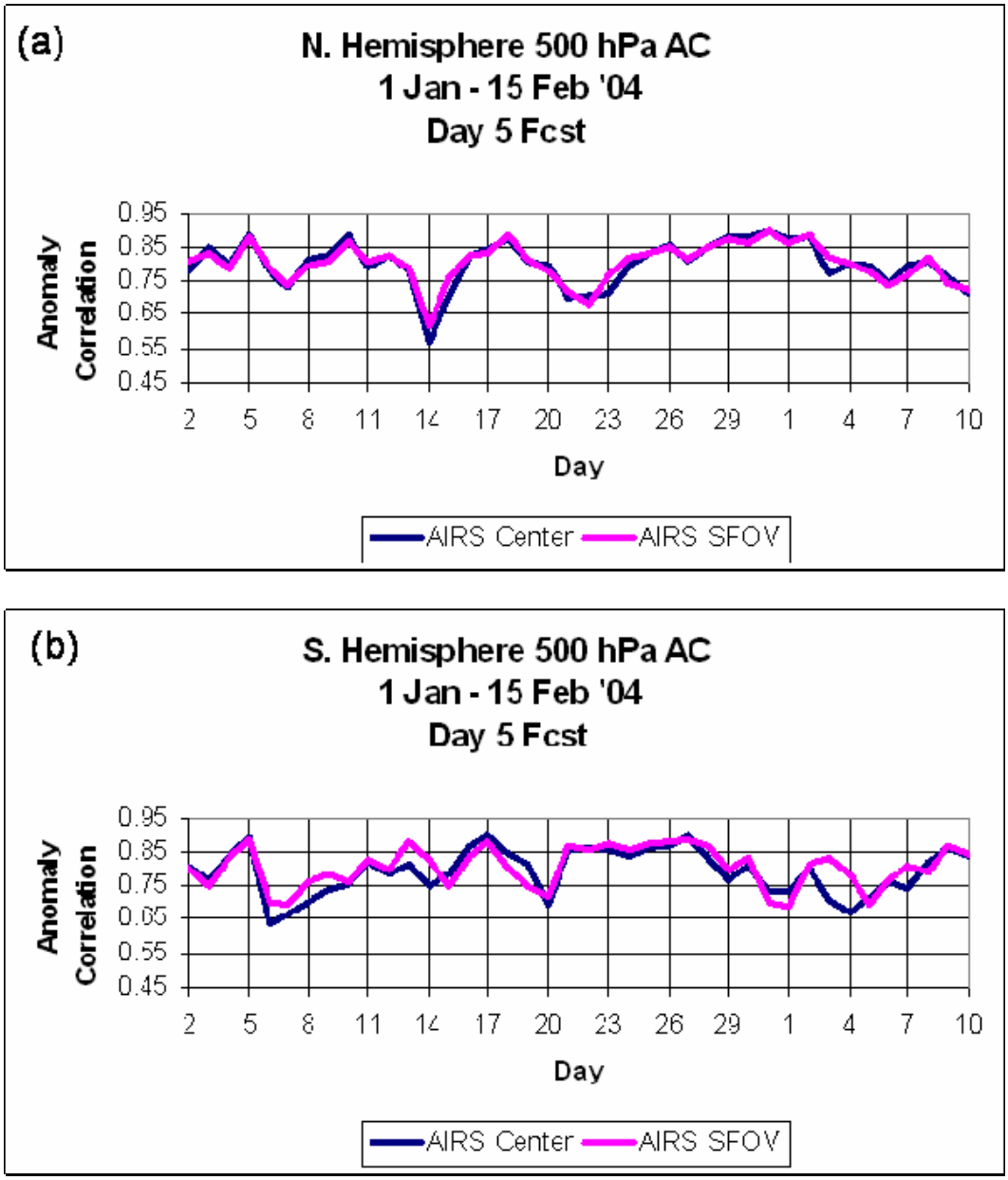

Figure 8.6 Time series of day 5 anomaly correlations for waves 1 – 20 at 500 hPa for the (a) Northern and (b) Southern Hemisphere. The single field of view (AIRS_SFOV) radiances are magenta, the 1 of 18 (AIRS Center) radiances are blue for 1 January to 15 February 2004.

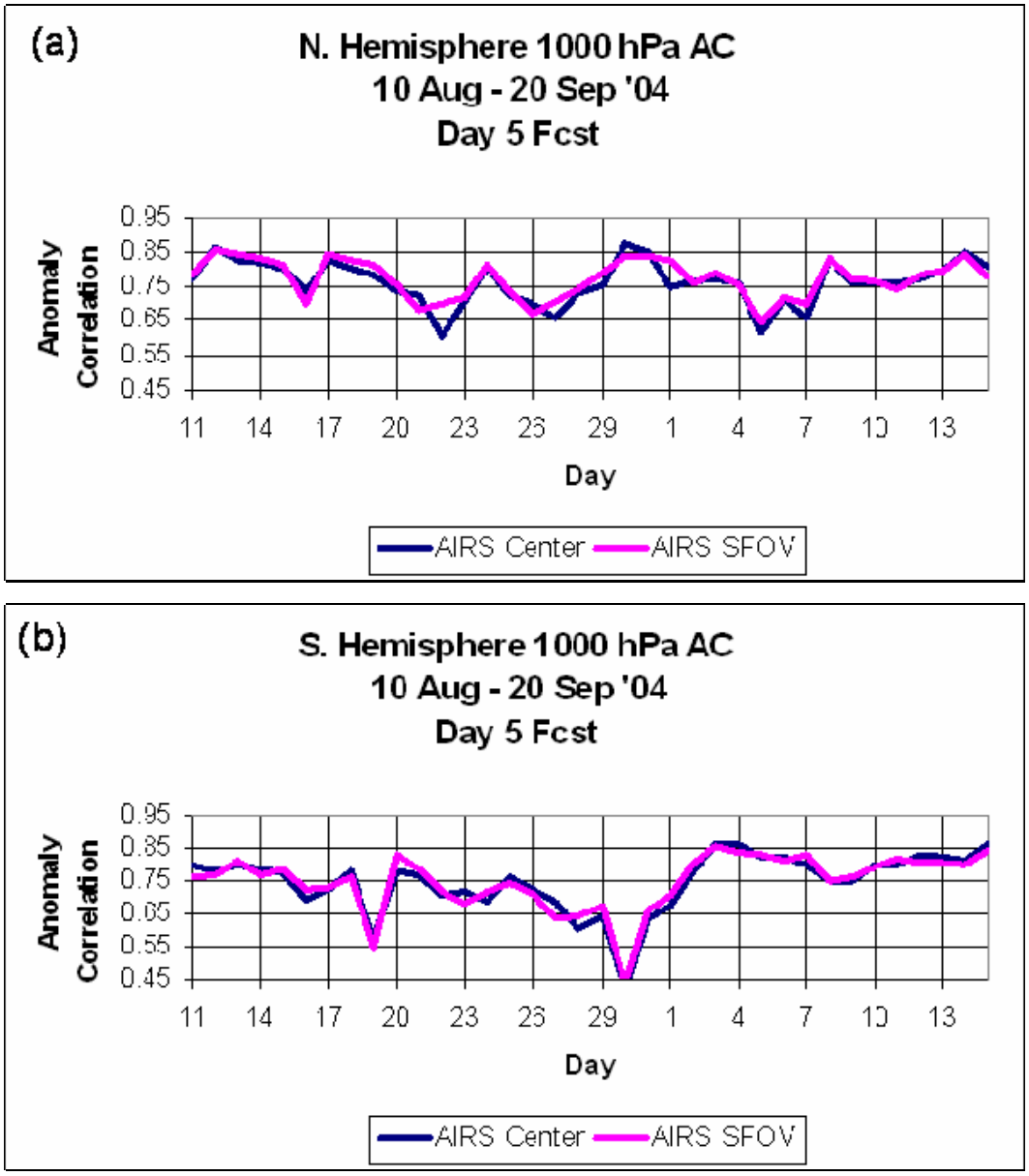

Figure 8.7 Time series of day 5 anomaly correlations for waves 1 – 20 at 1000 hPa for the (a) Northern and (b) Southern Hemisphere. The single field of view (AIRS_SFOV) radiances are magenta, the 1 of 18 (AIRS Center) radiances are blue for 10 August to 20 September 2004.

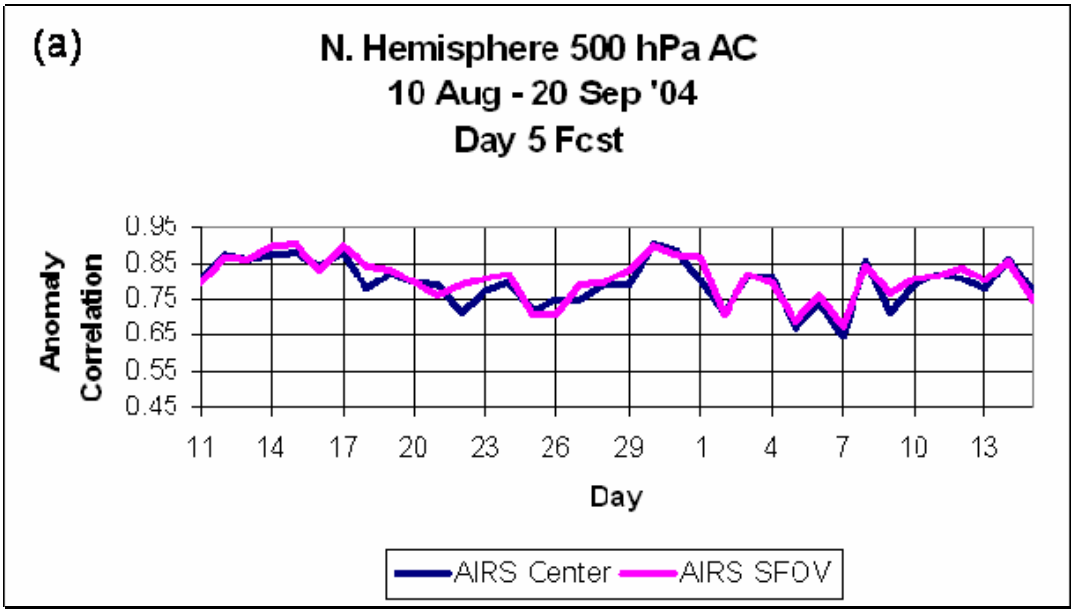

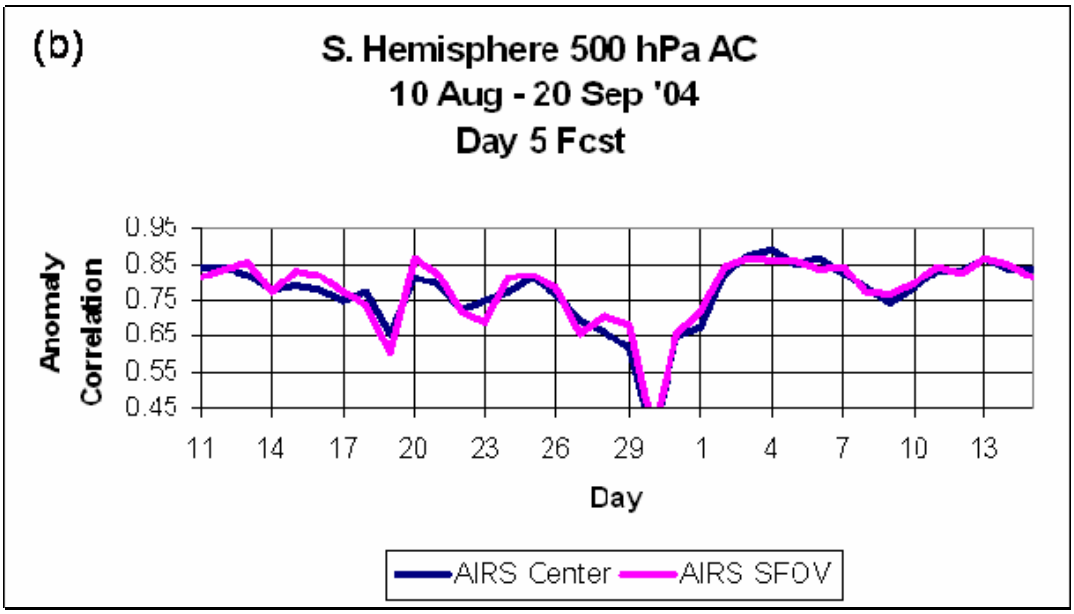

Figure 8.8 Time series of day 5 anomaly correlations for waves 1 – 20 at 500 hPa for the (a) Northern and (b) Southern Hemisphere. The single field of view (AIRS_SFOV) radiances are magenta, the 1 of 18 (AIRS Center) radiances are blue for 10 August to 20 September 2004.

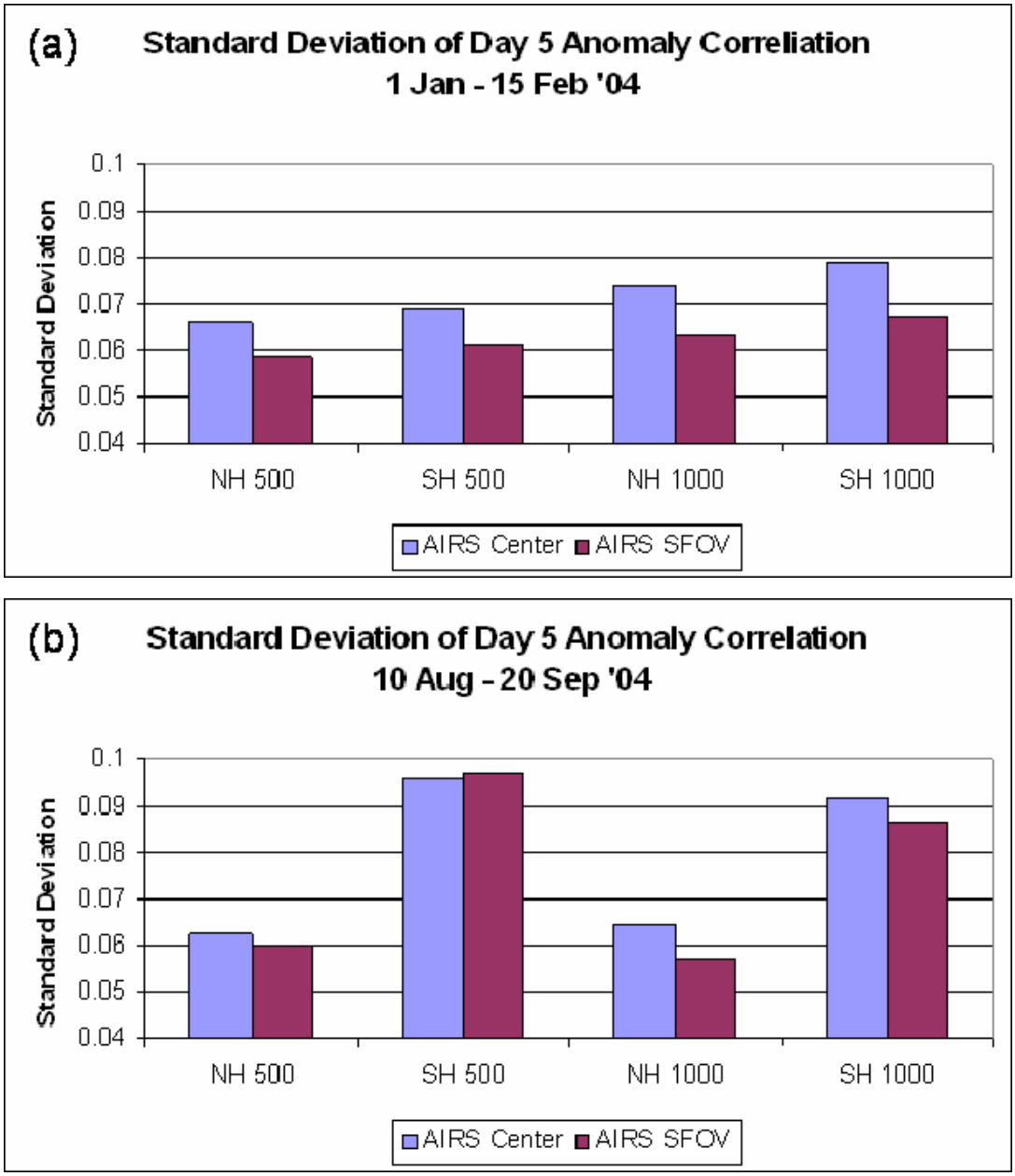

Figure 8.9 Standard deviation of day 5 anomaly correlations in the Northern and Southern Hemispheres at 500 and 1000 hPa for (a) 1 January to 15 February and (b) 10 August to 20 September 2004.

Figures 8.10 and 8.11 present the 24-hour geographical distributions of forecast impact for (a) vertically integrated precipitable water, (b) 500 hPa temperature and (c) 250 hPa U-component of wind for 1 January to 15 February 2004 and 10 August to 20 September 2004 respectively. The results for vertically integrated precipitable water are

small and mostly positive with the greatest impact occurring in the summer Hemisphere. Both the 500 hPa temperature and 250 hPa U-component of wind show small positive impacts with the greatest impacts occurring in the tropics.

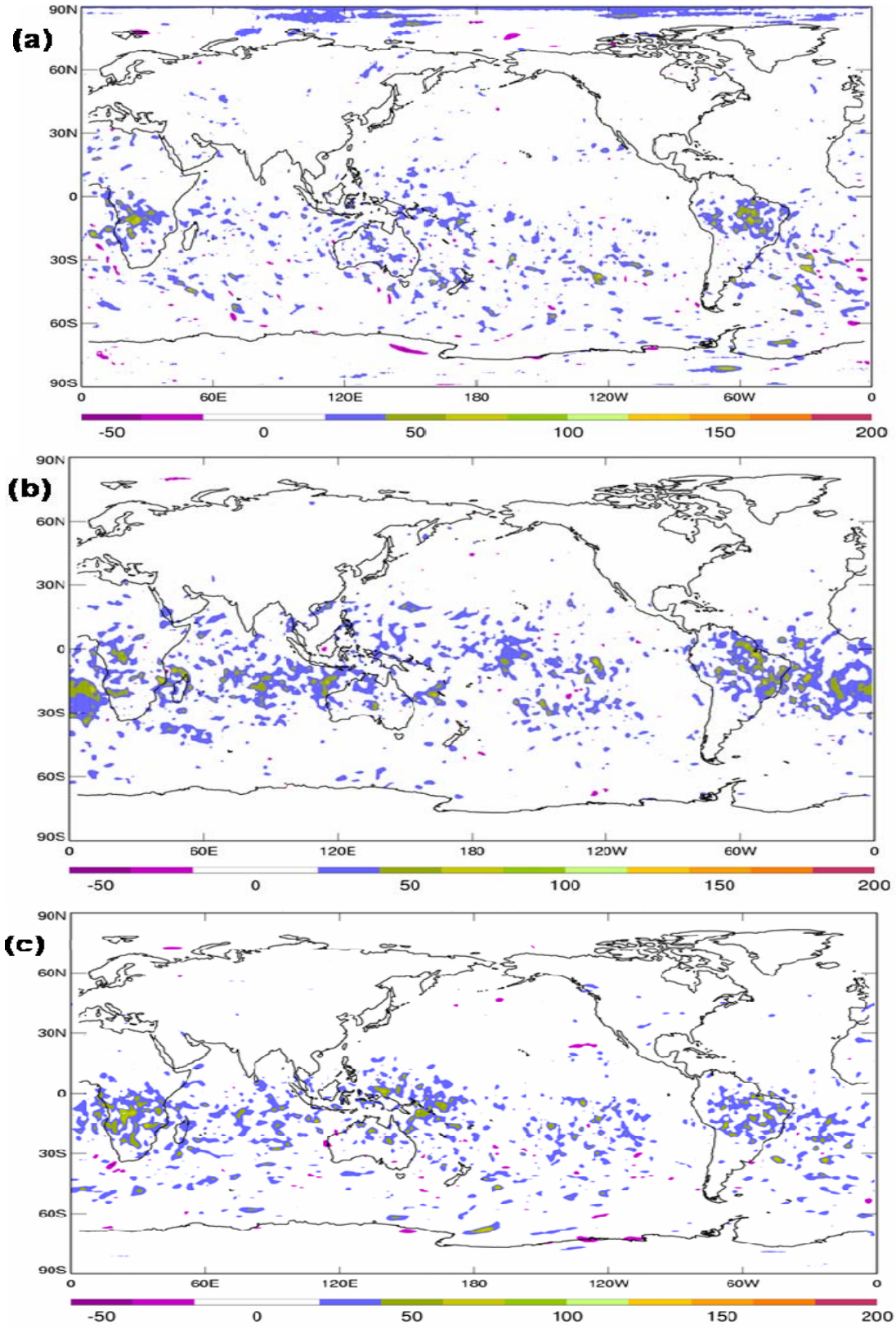

Figure 8.10 Geographical distribution of 24-hour forecast impact of (a) vertically integrated precipitable water, (b) 500 hPa temperature, (c) and 250 hPa U-component of wind for 1 January to 15 February 2004.

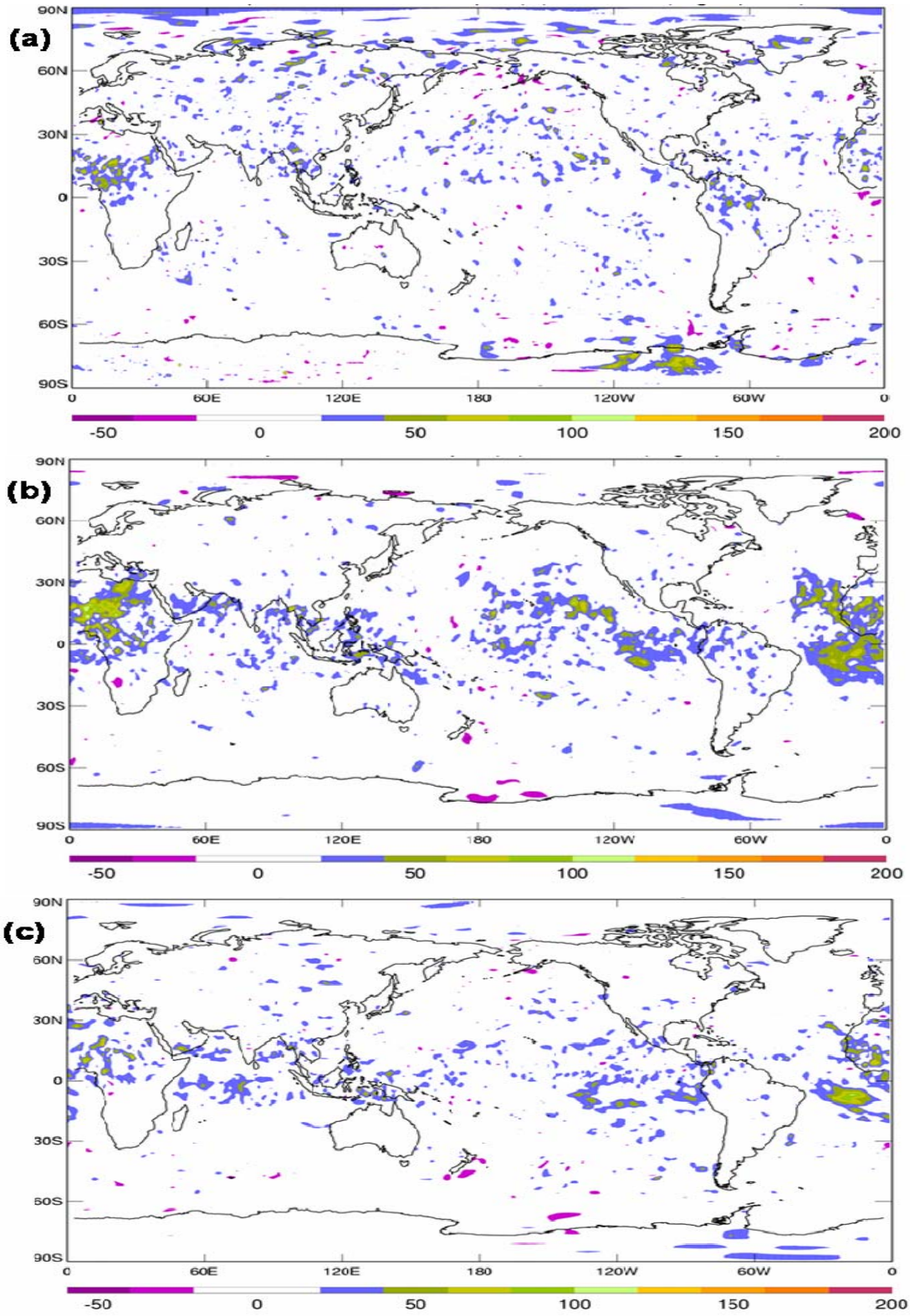

Figure 8.11 Geographical distribution of 24-hour forecast impact of (a) vertically integrated precipitable water, (b) 500 hPa temperature, (c) and 250 hPa U-component of wind for 10 August to 20 September 2004.

8.4 Summary

This AIRS experiment compared the full spatial resolution of AIRS (every FOV) to using the center spot of every other golf ball (1 in 18 FOV). Both experiments used 251 channel AIRS data which are available to NWP centers. These experiments were designed in a way that renders them feasible for operational application. The NCEP operational version of the GDAS/GFS (November 2003) was used at the operational resolution of T254, with 64 levels. For both the AIRS Center and AIRS SFOV experiments, the NCEP operational database of conventional and satellite data, with the real-time cutoff constraints was used. These experiments also included the AQUA AMSU-A microwave radiances.

In general, the AIRS data improved the forecasts with respect to NCEP's forecast skill benchmarks. AIRS data had a consistent and beneficial effect on the 1000 hPa forecast anomaly correlations of geopotential height at mid-latitude for the Northern and Southern Hemispheres. The mid-latitude 500 hPa average geopotential height anomaly correlations are higher for every forecast day (1-7) of the AIRS experiment. Another noticeable characteristic is that the summer Hemisphere anomaly correlations have a consistently greater improvement than in the winter Hemisphere. In relation to the significant daily variations, the time series shows more days with positive impact than negative. The standard deviations of the 1000 and 500 hPa geopotential height anomaly correlations were consistently smaller for the AIRS_SFOV experiment indicating more consistent forecasts. Impacts on the wind field in the tropics for this experiment were mostly neutral with some showing small improvements. In the case of moisture, the impact is clearly positive, especially in the summer Hemisphere.

Overall, AIRS hyperspectral data, used within current stringent operational constraints, shows significant positive impacts in forecast skill over both the Northern and Southern Hemisphere for 1 January to 15 February and 10 August to 20 September 2004. The results indicate a considerable opportunity to improve operational analyses and forecasts with hyperspectral data.

8.5 Conclusion

We have demonstrated that AIRS_SFOV hyperspectral data, used within stringent current operational constraints, has positive impact on the forecast skill of NCEP's GDAS over both the Northern and Southern Hemispheres during two seasons. Figure 8.12 is a summary of the day 5 anomaly correlations in both the Northern and Southern Hemispheres for both 1 January – 15 February 2004 and 10 August – 20 September 2004, highlighting the forecast improvements. It is clear that the AIRS data have had a significant effect on forecast skill over both Hemispheres during both time periods. Given the opportunities for future enhancement of the assimilation system, the results indicated opportunities to improve the then current analysis and forecast systems through the application of using every footprint of the AIRS hyperspectral data. This methodology was adopted at NCEP and a related selection process for warmest FOVs was later included in the data processing methodology at NESDIS. This led to the distribution of the warmest FOV and every FOV datasets to operational NWP centers rather than using the 1 in 18 FOVs.

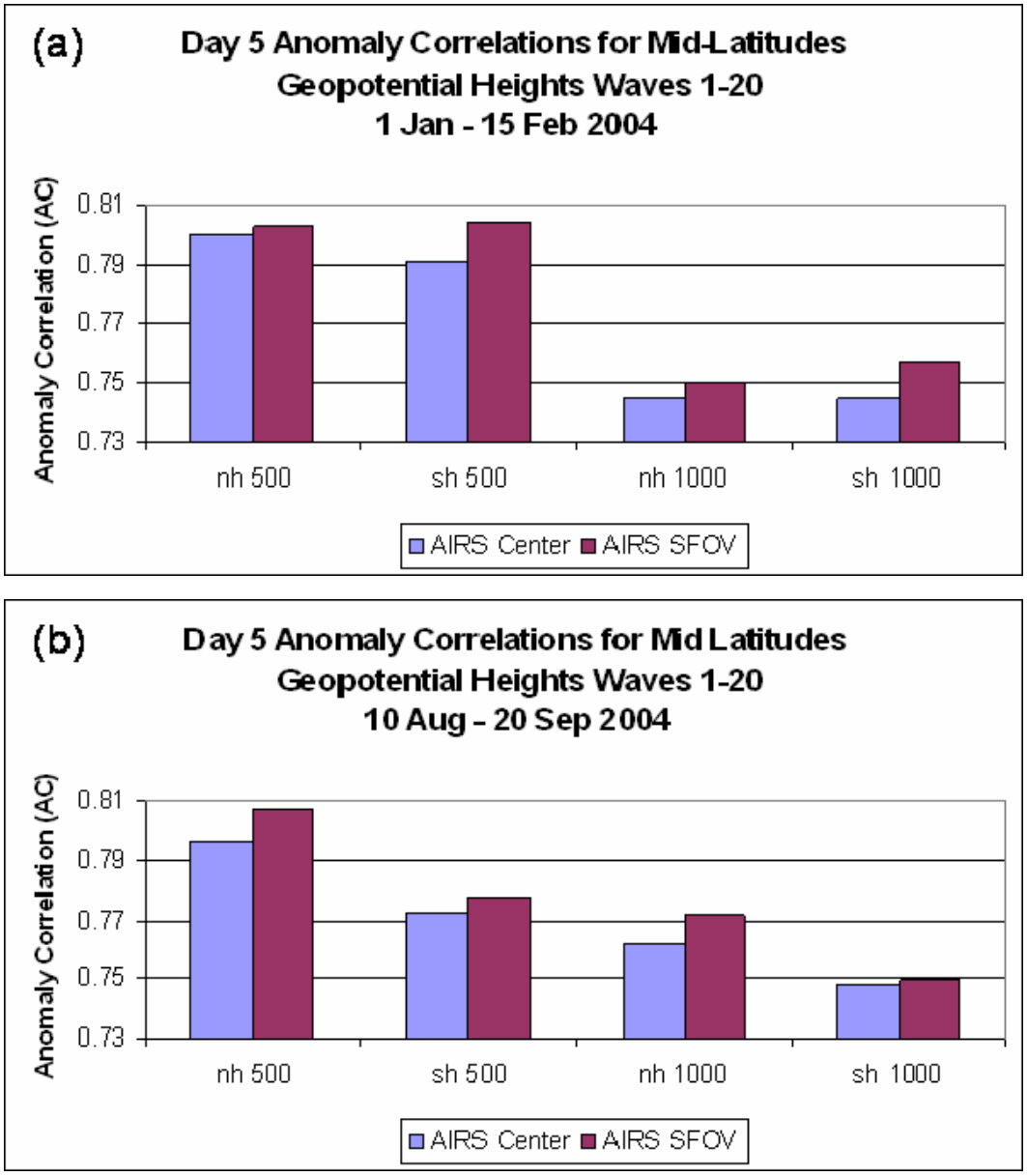

Figure 8.12 The day 5 anomaly correlations of waves 1-20 at 500 and 1000 hPa for the mid-latitude regions during (a) 1 January to 15 February and (b) 10 August to 20 September 2004.

Chapter 9: The Spectral Resolution Experiments

9.1 Introduction

The results of the spatial resolution AIRS experiment showed that the AIRS data have a beneficial effect on forecast skill over the Northern and Southern Hemisphere during January 2004. With the significant impact of this full spatial and spectral resolution experiment in both the Northern and Southern Hemispheres, several questions were raised concerning the contribution of the increased spectral resolution. The design of this spectral resolution experiment, in this chapter, is to isolate the impacts of using different combinations of AIRS channels. The impact studies here used the full spectral resolution AIRS BUFR data with the NCEP GDAS/GFS. Cloud free AIRS radiance data were identified and used by methods described in Chapter 7.

9.2 Experiment Design

Using the full spatial resolution dataset (every field of view), the impact of various spectral resolution combinations of AIRS data was investigated. A control and three experiments were conducted. The first experiment used the AIRS water vapor and shortwave channels only (Short_AIRS). The Short_AIRS experiment includes the AIRS observations whose central wavelengths are between 3.74 – 4.61μm, 6.20 – 8.22μm and 8.8 - 9.3μm ranges which consisted of 115 channels. The second experiment used the operational channels (Ops_AIRS) and covers the full spectral range from 15.4 – 3.74μm but was thinned to 152 channels. The third experiment uses the full spectrum of AIRS data available which are practical for assimilation and consists of 251 channels (All_AIRS). The channels used for each experiment are listed in appendix C. Channels shorter than

5.0μm have reduced weights and channels shorter than 4.0μm are rejected by the assimilation system during the day. The operational warmest FOV and thinning routine was used to determine the clearest FOVs. These experiments are compared to a control simulation using the same operational dataset except that all AIRS data was removed. Since the same dataset and all of the channels were used in determining the clearest FOV for the three experiments, the same number of thinning boxes resulted. This is why the total data input and data selected for possible use are identical in Table 9.1. The data were subject to the same quality control, again using all channels. The total number of channels used has changed based on the number of channels allowed to be used by each experiment. A summary of the conventional and satellite data in the operational database and used for these experiments are listed in Tables 5.2 and 5.3.

Table 9.1 AIRS data usage per analysis cycle in the spectral resolution experiments.

	All AIRS	Short AIRS	Ops AIRS
Total data input to analysis	2.0×10^8	2.0×10^8	2.0×10^8
Data selected for possible use	2.1×10^6	2.1×10^6	2.1×10^6
Data used in analysis	8.5×10^5	2.5×10^5	5.9×10^5

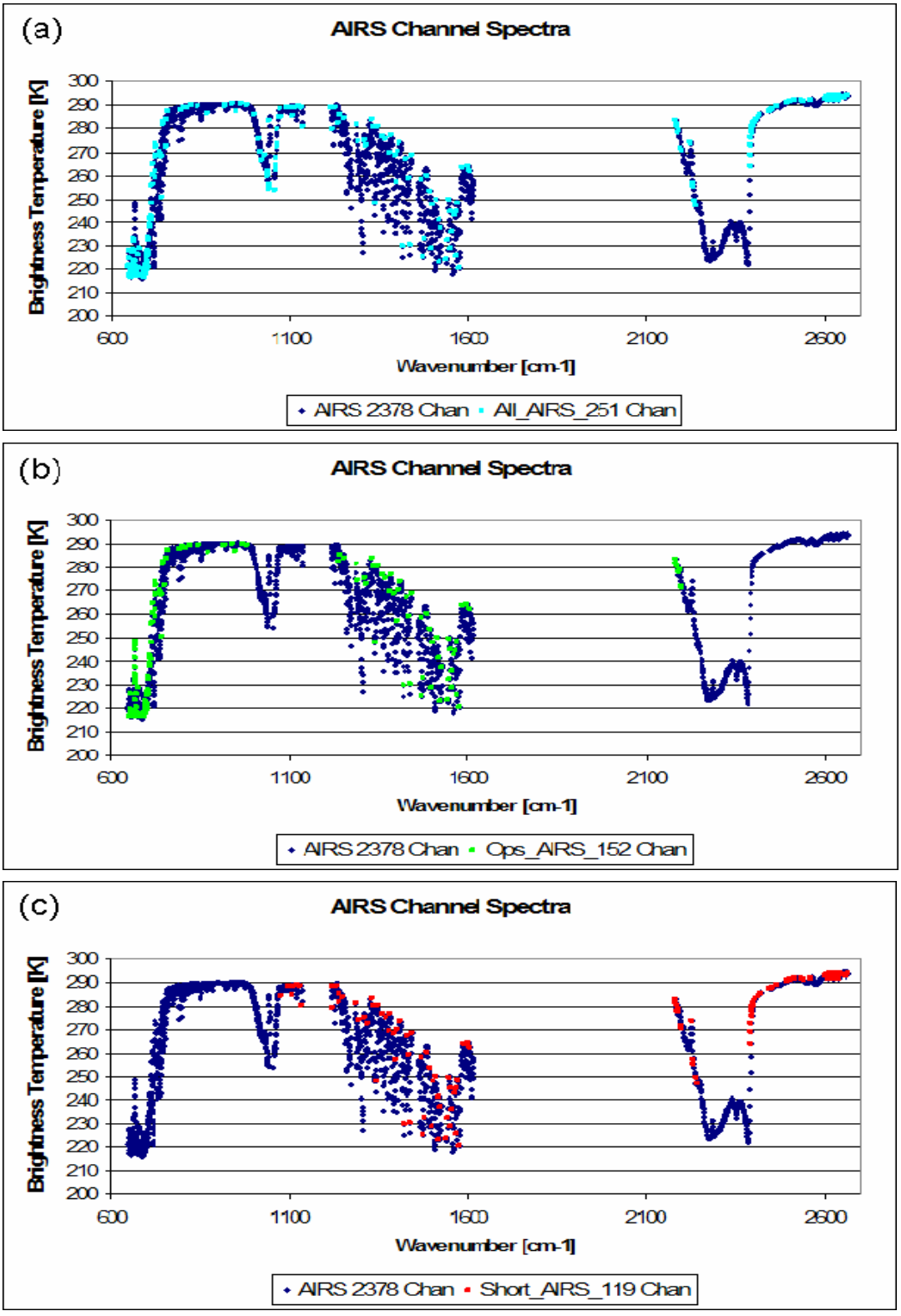

Figure 9.1 AIRS channel spectra by wavenumber for the 2378 channels (dark blue diamonds) for (a) All_AIRS 251 channels (light blue squares), (b) Ops_AIRS (green squares) and (c) Short_AIRS (red squares) for a mid-latitude atmosphere. Courtesy of Chris Barnett.

The current operational GFS (June 2005 version), including the full observation database with real-time cutoff constraints, was used except that the full spatial resolution AIRS BUFR was substituted for the operational dataset when appropriate. After the initial experiments were completed, the AQUA AMSU-A microwave radiances became operational. To be consistent with the current operational data stream, the AQUA AMSU-A microwave radiances were included in all of these experiments.

9.3 Results

Figure 9.2 shows the 1000 and 500 hPa geopotential height day 5 forecast anomaly correlations in the Northern and Southern Hemispheres for (a) 1 January to 15 February 2004 and (b) 10 August to 20 September 2004. It was apparent in this trial that the addition of the short wave channels (Short_AIRS) to the operational observation database generally provided a positive increment with a larger improvement being seen in the Southern Hemisphere 1000 hPa fields. While the operational AIRS channels (Ops_AIRS) provided a greater positive impact than the Short_AIRS, the addition of all the AIRS channels (All_AIRS) provided the greatest increase in forecast skill.

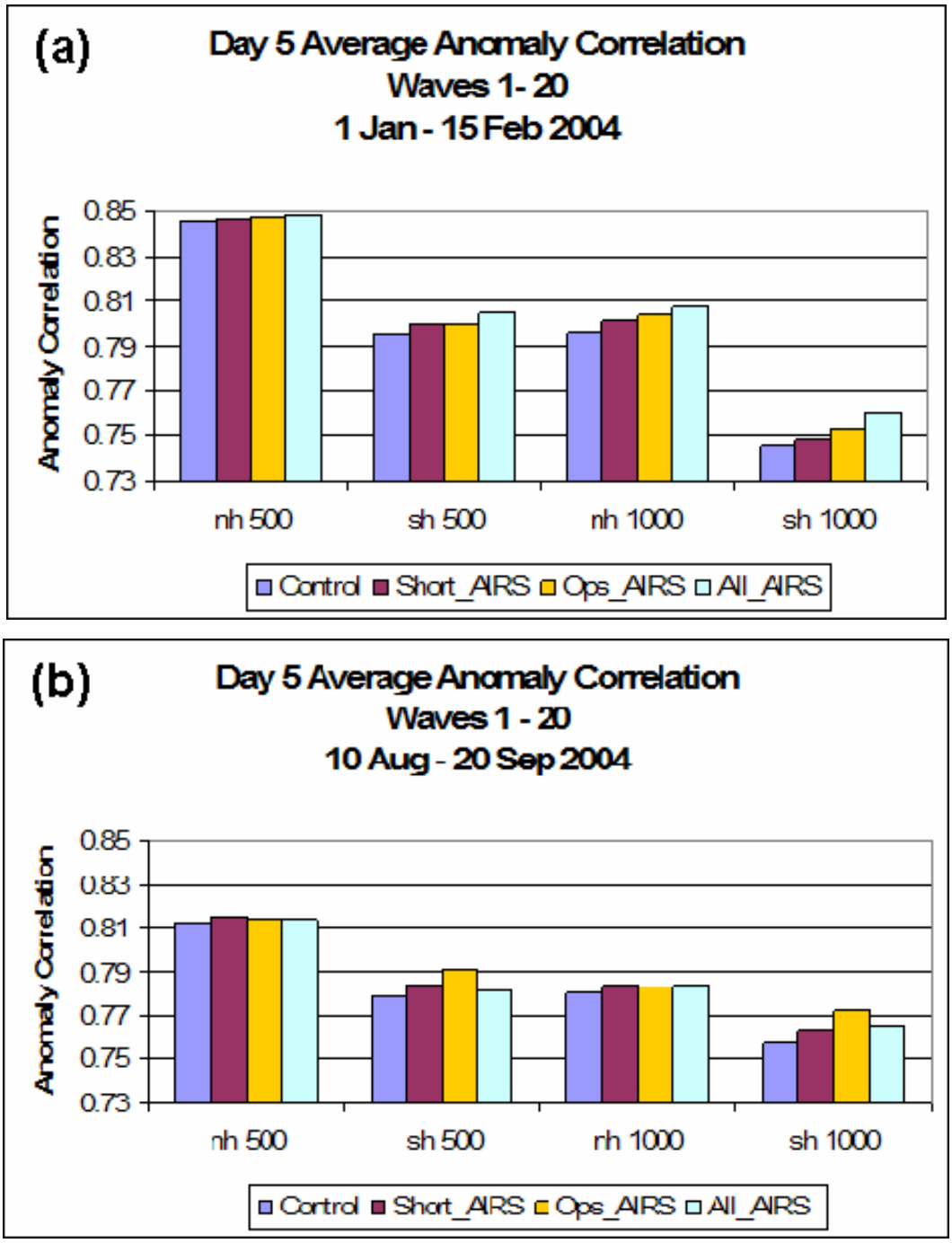

Figure 9.2 Anomaly correlations at day 5 for the Northern and Southern Hemisphere at 1000 and 500 hPa for no AIRS (Control), 115 channels (Short_AIRS), 152 channels (Ops_AIRS) and 251 channels (All_AIRS) during (a) 1 January to 15 February 2004 and (b) 10 August to 20 September 2004.

Figure 9.3 is a bar chart of the 5 day forecast standard deviations. The results are not as clear cut as in the spatial resolution experiments. To rank the various experiments, a weighted average was calculated based on the number of days in each category. The

results from worst to best standard deviations are Control (0.0646), Short_AIRS (0.0624), Ops_AIRS (0.0623) and All_AIRS (0.0614) however the differences are generally small.

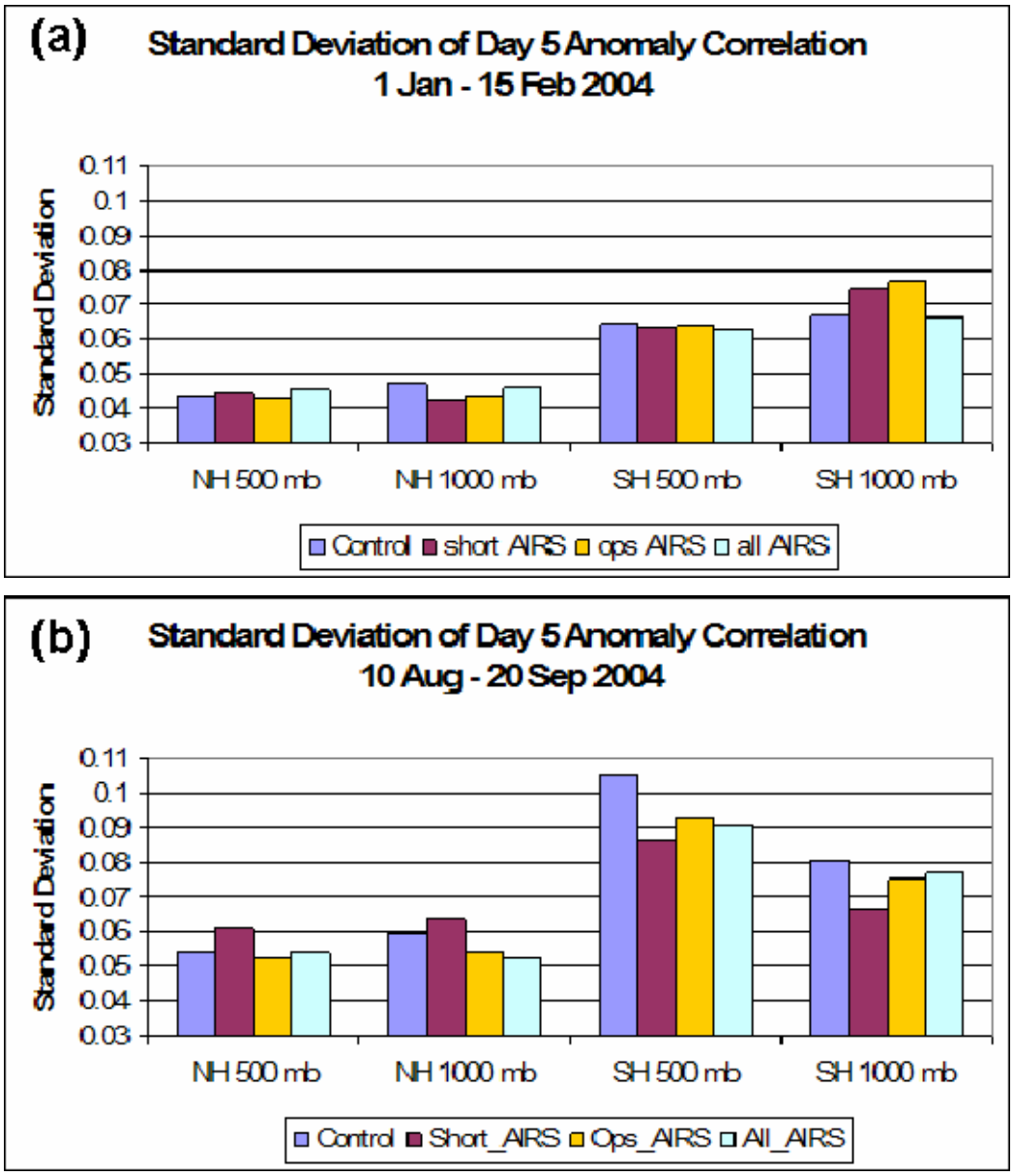

Figure 9.3 Standard deviation of day 5 anomaly correlations in the Northern and Southern Hemispheres at 500 and 1000 hPa for no AIRS (Control), 115 channels (Short_AIRS), 152 channels (Ops_AIRS) and 251 channels (All_AIRS) during (a) 1 January to 15 February and (b) 10 August to 20 September 2004.

All three experiments share similar water vapor channels. As such there are very few differences between the geographical forecast impacts of precipitable water from each of the three experiments as shown in Fig. 9.4. There are, however, large differences

between the control and the various experiments, suggesting a large positive impact from using the water vapor channels. Similar results to Fig. 9.4 were noted for the 10 August to 20 September 2004 experiments and are not shown here.

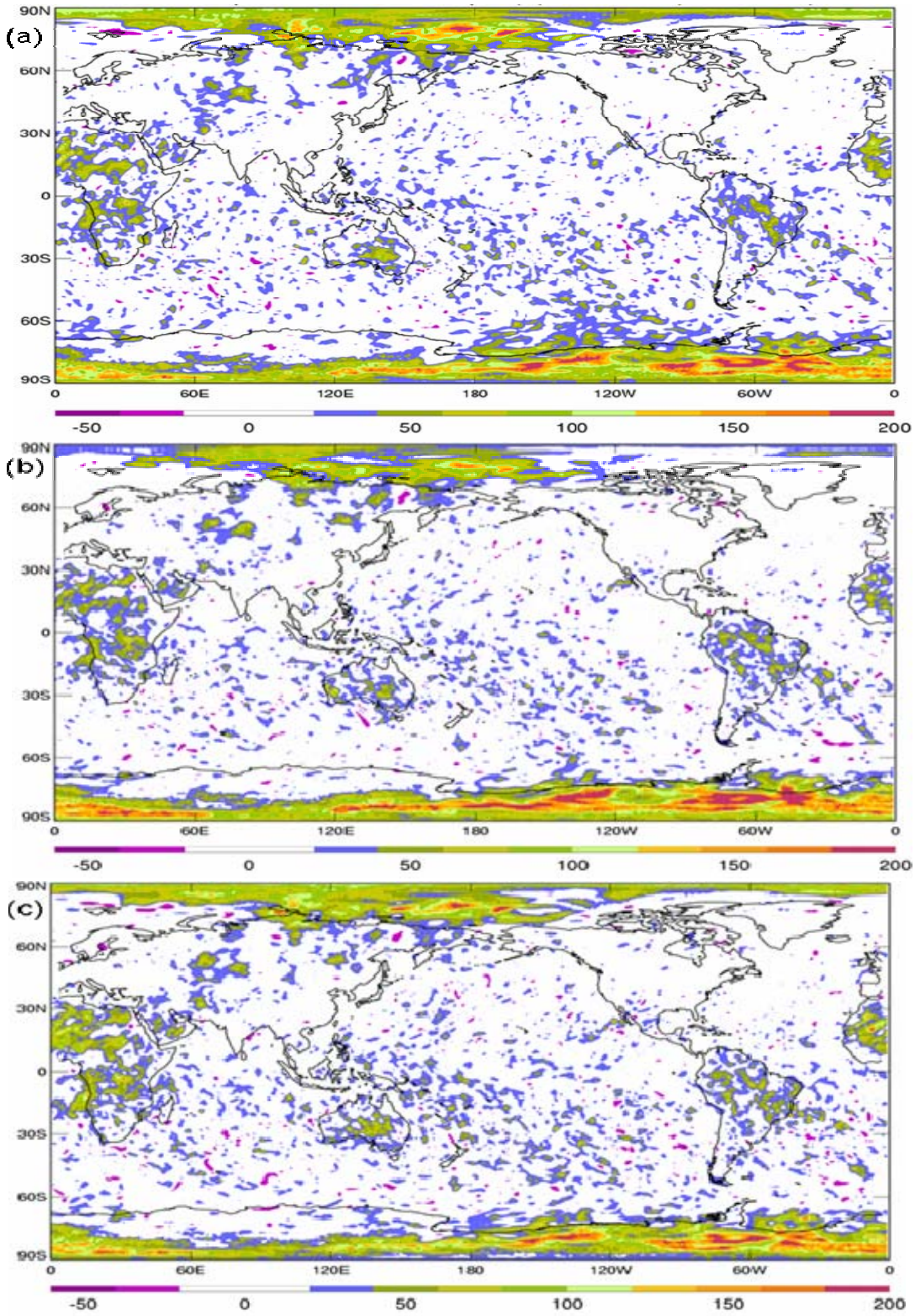

Figure 9.4 Geographical distribution of 24-hour forecast impact for integrated precipitable water during 1 January to 15 February 2004 for (a) Short_AIRS, (b) Ops_AIRS, and (c) All_AIRS.

The geographical distribution of 24-hour forecast impact for 500 hPa temperature is also large when compared to the control as shown in Fig. 9.5. A difference in the forecast impact observed between experiments can be seen in the Atlantic and Pacific Oceans near South America. In these regions the addition of more AIRS temperature channels has made a difference with the Short_AIRS (Fig. 9.5a) having the least forecast impact while the Ops_AIRS and All_AIRS (Fig 9.5 b and c) have progressively greater positive forecast impacts. Similar results were also noted in the 10 August to 20 September 2004 experiments thus are not shown here.

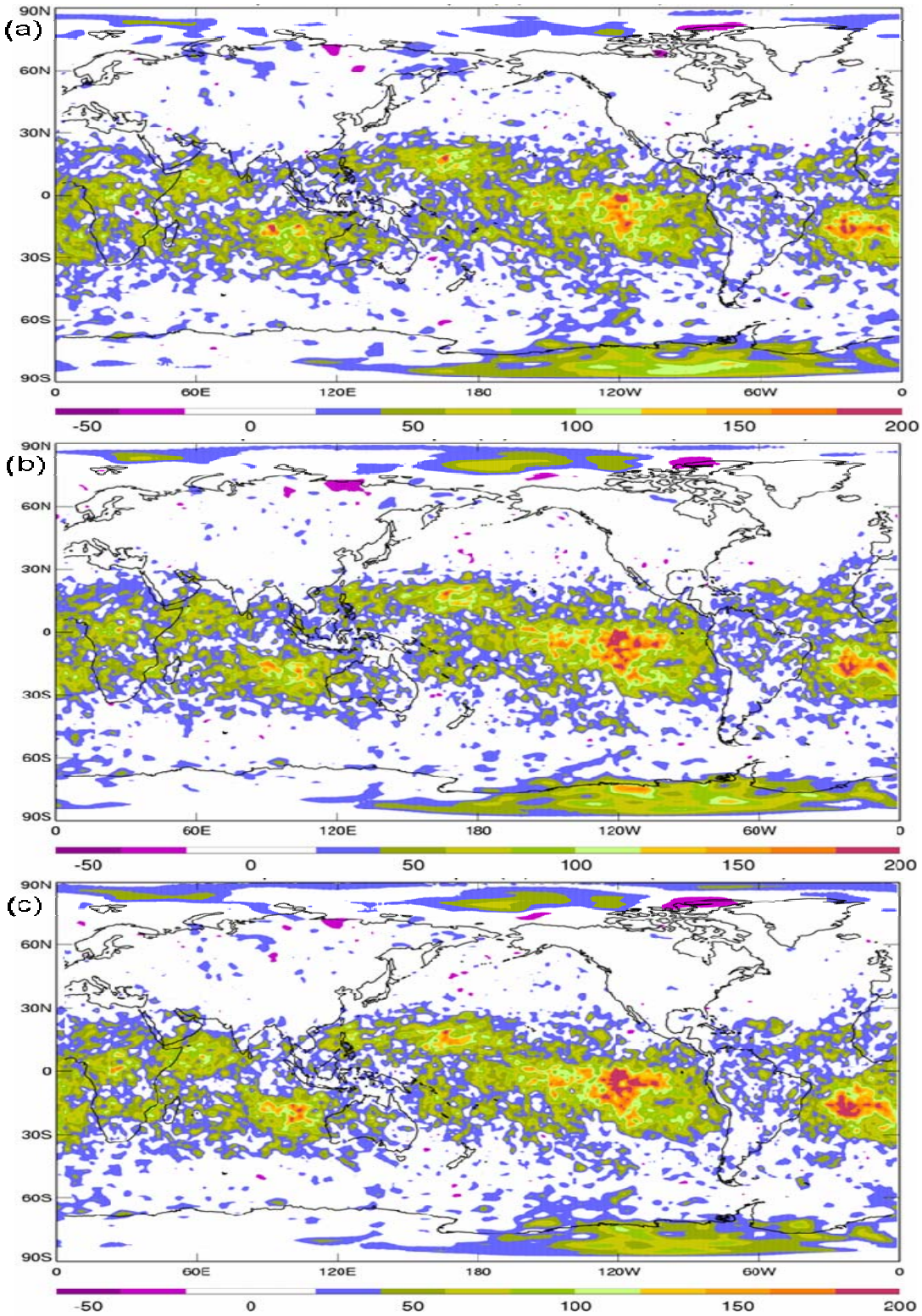

Figure 9.5 Geographical distribution 24-hour forecast impact for 500 hPa temperature during 1 January to 15 February 2004 for (a) Short_AIRS, (b) Ops_AIRS, and (c) All_AIRS.

9.4 Summary

This AIRS experiment compared various combinations of spectral resolutions of AIRS data from using no AIRS channels (Control) to using 115 of the water vapor and short wave (Short_AIRS) to using a limited set of 152 channels (Ops_AIRS) to using the full complement of 251 channels (All_AIRS). These experiments were also designed in a way that renders them feasible for operational application. The NCEP operational version of the GDAS/GFS (June 2005) was used at the operational resolution of T254, with 64 levels. For the three AIRS experiments and the control, the NCEP operational database of conventional and satellite data, with the real-time cutoff constraints was used. These experiments also included the AQUA AMSU-A microwave radiances.

The results show that the 1000 and 500 hPa anomaly correlations of geopotential height in both the Northern and Southern Hemisphere at mid-latitudes are generally improved from the Control to Short_AIRS to Ops_AIRS to All_AIRS. The results are very consistent for 1 January to 15 February that more AIRS channels improves the forecast skill. The standard deviation of the geopotential height anomaly correlations also decrease with the addition of more AIRS channels, with the All_AIRS experiment being the best.

The forecast impact on the 500 hPa temperature field also improves with the addition of more AIRS channels, especially in the oceanic region around South America. The greatest impact comes from the initial use of the AIRS channels (Control vs. Short_AIRS) with minor improvements realized from adding more channels. Similar results were noted in the precipitable water field.

AIRS hyperspectral data (from one orbital instrument), used within current stringent operational constraints, shows significant positive impacts in forecast skill over both the

Northern and Southern Hemisphere for 1 January to 15 February and 10 August to 20 September 2004. The results indicate a considerable opportunity to improve operational analyses and forecasts with hyperspectral data.

9.5 Conclusion

We have demonstrated that AIRS SFOV hyperspectral data, used within stringent current operational constraints, has positive impact on the forecast skill of NCEP's GDAS over both the Northern and Southern Hemispheres during two seasons. The results show that the 1000 and 500 hPa anomaly correlations of geopotential height in both the Northern and Southern Hemisphere at mid-latitudes are generally improved from the Control to Short_AIRS to Ops_AIRS to All_AIRS. The results are very consistent for 1 January to 15 February that more AIRS channels improves the forecast skill. The standard deviation of the geopotential height anomaly correlations also decrease with the addition of more AIRS channels, with the All_AIRS experiment being the best.

The forecast impact on the 500 hPa temperature field also improves with the addition of more AIRS channels, especially in the oceanic region around South America. The greatest impact comes from the initial use of the AIRS channels (Control vs. Short_AIRS) with minor improvements realized from adding more channels. Similar results were noted in the precipitable water field.

It is clear that the AIRS data have had a significant effect on forecast skill over both Hemispheres during both time periods. In general, the positive impacts are less in the Northern Hemsiphere as a result of many influences, including greater data coverage from conventional surface-based observations and the limited use of the AIRS data in the lower troposphere over land.

Chapter 10: Cloud Detection and Surface Emissivity Experiments

10.1 Introduction

The use of weather satellite data over land is reduced by its limited ability to sound the lowest levels of the atmosphere and to separate the effect of surface temperature from natural variations in surface emissivity. The next generations of infrared sounders, like AIRS, are able to improve profiles of atmospheric temperature and water vapor with their nearly continuous coverage of the 8 – 14μm window region. These high spectral resolution sounders have the advantage of being able to resolve individual absorption lines of water vapor and carbon dioxide and use a number of transparent microwindows. These microwindows require smaller atmospheric corrections than the previous generation broad-band instruments. This allows a surface temperature to be determined simultaneously with the land surface emissivity. One method for determining the surface temperature and surface emissivity using high spectral resolution infrared observations is explained in Knuteson et al. (2003) and Knuteson et al. (2004).

Being able to derive and use surface temperature and update surface emissivity within a data assimilation system, will improve the use of radiances near the surface and also improve the analysis, especially near the surface. Assimilation techniques used by NWP could benefit from using these techniques both by improved analyses and forecasts. To date, this methodology has not been investigated for use in NWP data assimilation.

10.2 Determining Clear Radiance Profiles

This technique of deriving surface skin temperature and surface emissivity is particularly sensitive to cloud and other contaminants, which may be in the radiance data.

Extra care must be taken to prevent these contaminated radiances from being used in the determination of surface temperature and emissivity. If these contaminated radiances are not screened out, unrealistic values may occur.

Cloud detection from remote sensing data has been an area of active research for years. The International Satellite Cloud Climatology Project (ISCCP) uses a combination of spectral, temporal, and spatial tests to estimate clear-sky radiances and values of cloud forcing (Key and Barry, 1989; Rossow and Garder, 1993; Rossow and Schiffer, 1991; Rossow et al. 1993). Statistical classification procedures, including maximum likelihood and Euclidean distance methods, have also been applied in cloud detection algorithms (Ebert, 1989; Key, 1990; Key et al. 1989; Welch et al. 1992). Although these techniques may have worked well for the various satellites, they are not easily modified for use with the reduced AIRS dataset. The main reason is that channels with similar spectral response functions are not present in this 281 channel AIRS dataset. Similar channels are available in the 2378 channel AIRS dataset.

The surface temperature is a major component in determining if a FOV is clear. Typically if a surface sensing channel is colder than the model surface temperature, the FOV is considered cloudy. The operational SSI and GSI use a single channel brightness temperature, BT(10.36), for comparison to the GDAS surface temperature. The warmest FOV is selected for assimilation if all BT(10.36)s are colder than the GDAS surface temperature. If more than one FOV is warmer than the GDAS surface temperature, the FOV closest to the center of the thinning box is selected.

10.2.1 Determining clear radiances over ocean

The AIRS science team developed a Sea Surface Temperature (SST) algorithm (AST-SST) specific to AIRS which uses 4 infrared channels and is calculated by:

$$SST = 8.28206 - 0.97957*BT(10.89) + 0.60529*BT(11.29) + 1.74444*BT(9.19) - 0.4037*BT(7.44).$$

This SST algorithm under estimates the surface temperature over land and ice although not to the extent that the operational single channel brightness temperature does. The channels in the 8μm region are one cause of the colder temperatures due to the surface emissivity being significantly less than over water.

10.2.2 Determining clear radiances at night

A test which is typically used for detecting cloud contaminated profiles in the infrared region is the longwave/shortwave test or more commonly known as the BT(4.0) – BT(11.0) test. This test is used over land and ocean at night. It can be used in conjunction with the SSI/GSI thinning routine to determine the optimal radiance profile to assimilate. The AIRS channels closest to these wavelengths are BT(3.91) and BT(10.90). Radiance profiles which have brightness temperature differences between -1.5^{o}K and 1.0^{o}K are typically considered clear fields of view. The BT(4.0) – BT(11.0) test for AIRS is:

$$-1.5 < (BT(3.91) - BT(10.90)) < 1.0$$

This test is useful but allows a significant number of cloudy FOVs to be mis-classified as clear. Li et al. (2000) used a 3 channel technique for cloud detection for the HIRS/3 instrument. It consists of differencing the BT(11.11), BT(4.0) and BT(3.76) channels. Tests were conducted with similar AIRS channels to determine if they were viable. The FOVs that were warmer than the model were chosen as training data to minimize cloud contamination. Histograms of BT(10.9) – BT(4.0), BT(10.9) – BT(3.76), and BT(4.0) –

BT(3.76) were generated over land and ocean at night for the BT(10.9) channel temperatures greater than the model surface temperature. These histograms are shown in Figs. 10.1-10.2. The data were also stratified by land and ocean as surface emissivities are different for these channels. These histograms do not have a normal distribution which is most likely due to cloud contamination. Brightness temperature differences that are negative have possible cirrus contamination. Brightness temperature differences which are positive may have stratus or low cloud contamination. The distributions are also not centered at zero. This was expected due to the fact that the surface emissivity is different for each channel. Removing the tails as still being cloud contaminated, the following thresholds were derived for selecting AIRS FOVs with the most uncontaminated information.

Over ocean:

$$\text{Abs}(BT(10.9) - BT(4.0) - 0.10) < 0.75$$
$$\text{Abs}(BT(10.9) - BT(3.76) + 0.39) < 0.55$$
$$\text{Abs}(BT(4.0) - BT(3.76) + 0.49) < 0.50$$

Over land:

$$\text{Abs}(BT(10.9) - BT(4.0) - 0.39) < 0.75$$
$$\text{Abs}(BT(10.9) - BT(3.76) + 0.13) < 0.70$$
$$\text{Abs}(BT(4.0) - BT(3.76) + 0.52) < 0.55$$

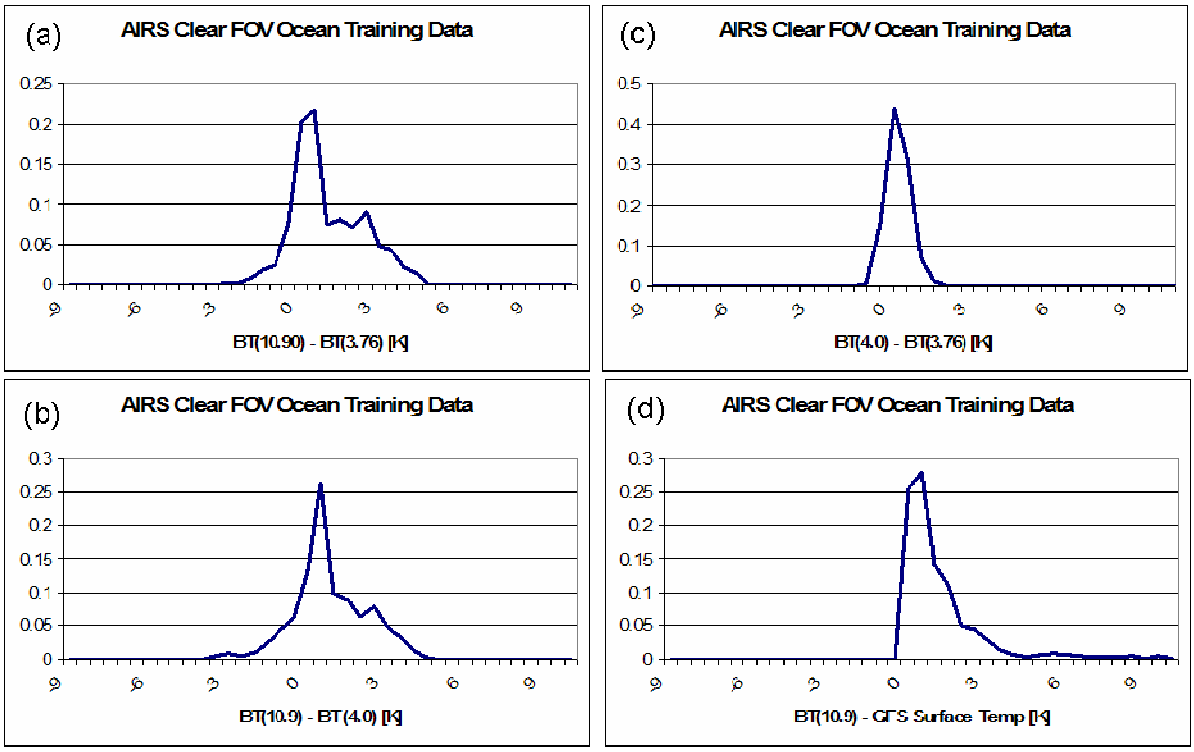

Figure 10.1 Ocean training data histograms. The tests include (a) the BT(10.9)-BT(3.76), (b) the BT(4.0)-BT(3.76), (c) the BT(10.9)-BT(4.0) and (d) the BT(10.9)-GFS Surface Temperature. These data are selected from points in which the BT(10.9) was warmer than the GFS Surface Temperature.

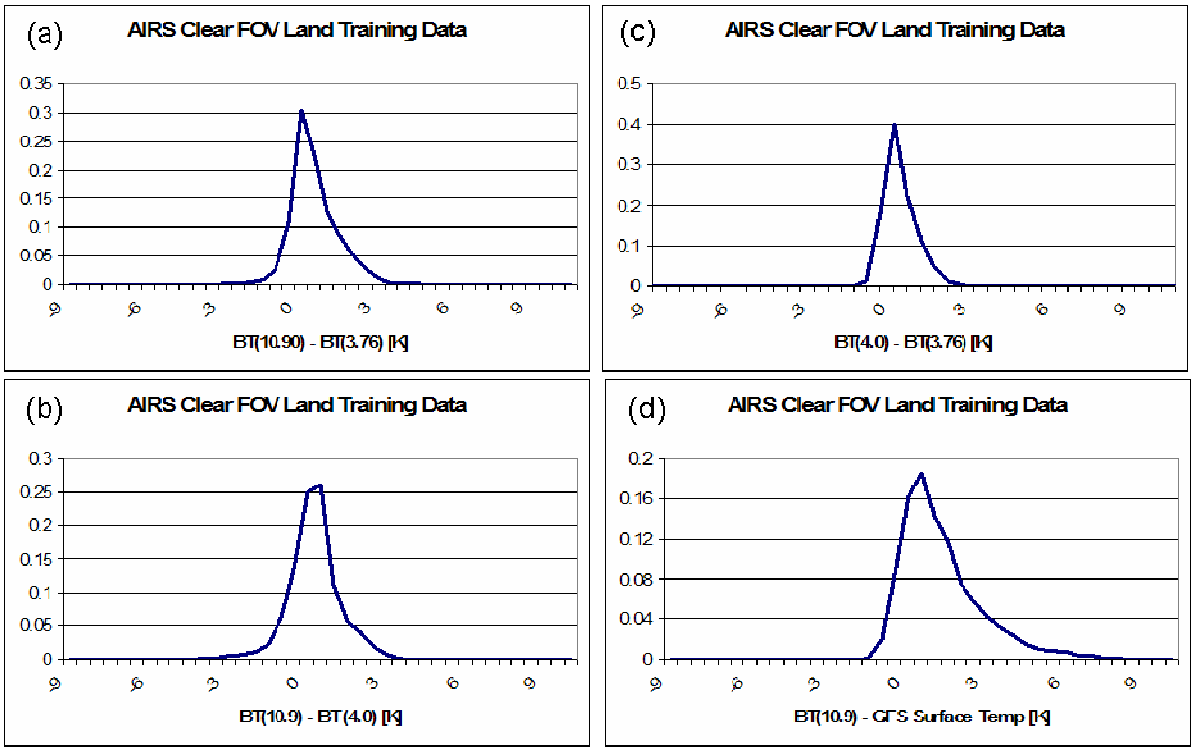

Figure 10.2 Land training data histograms. The tests include (a) the BT(10.9)-BT(3.76), (b) the BT(4.0)-BT(3.76), (c) the BT(10.9)-BT(4.0) and (d) the BT(10.9)-GFS Surface Temperature. These data are selected from points in which the BT(10.9) was warmer than the GFS Surface Temperature.

All three tests must be met for a FOV to be considered clear. Ocean and land Histograms of each of the tests for the FOVs that passed all three tests from all the possible FOVs are shown in Figs 10.1 and 10.2 respectively. It was discovered that FOVs can pass these three tests and yet the BT(10.9) be considerably colder than the GFS surface temperature. These FOVs are randomly distributed throughout the histograms. Adjusting the cutoff criteria will not identify and reject these FOVs. An arbitrary threshold of BT(10.9) - (GFS surface temp.) of less than -6.0K was set to be a rejection criteria for the FOV being cloudy. All FOVs must be:

$$BT(10.9) - GFS\ Surface\ Temp > -6$$

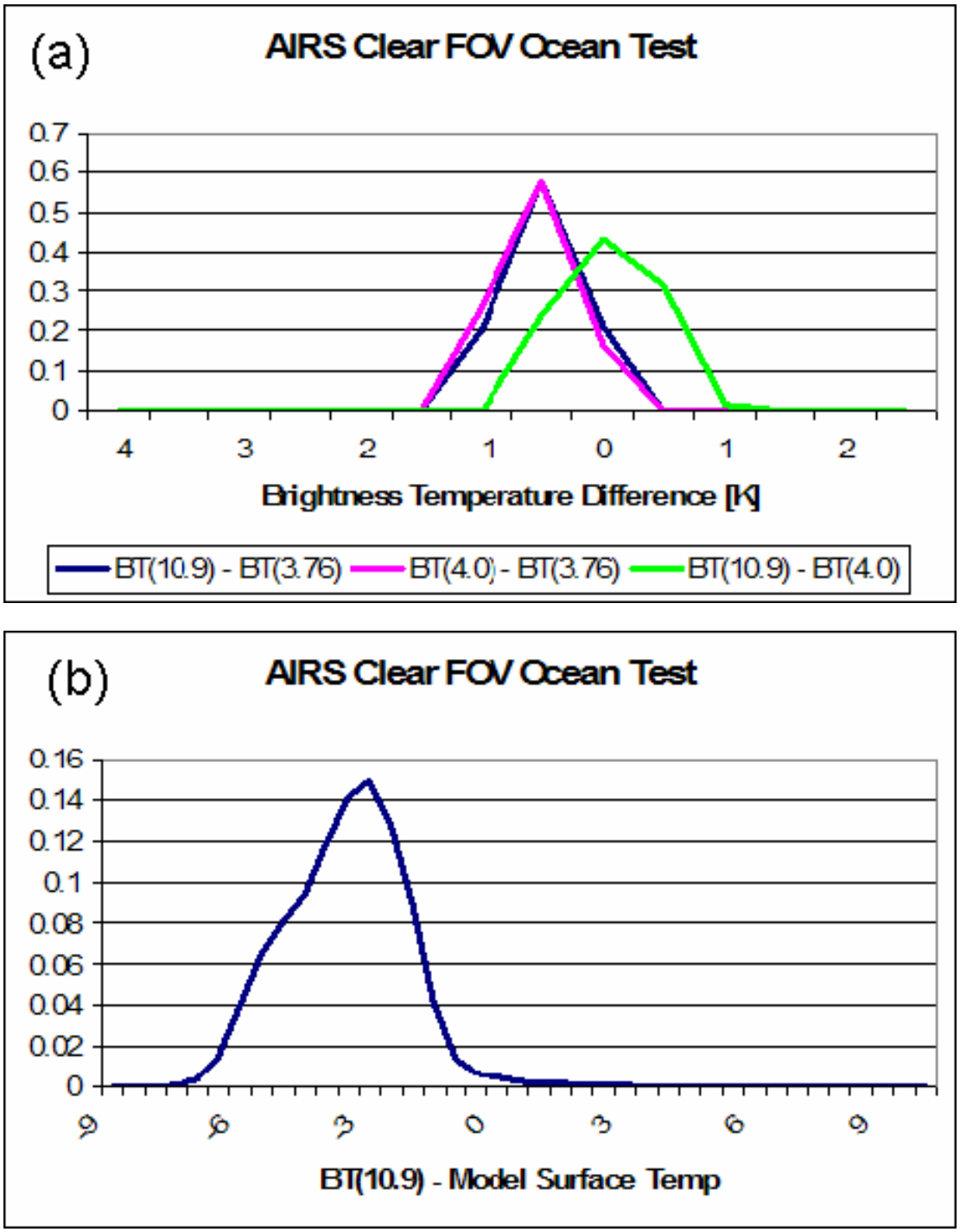

Figure 10.3 Ocean histograms of the cloud tests for those FOVs which pass the three selection criteria. Panel (a) is the histograms of the selection criteria in which all FOVs pass the three tests. Panel (b) is the histogram of BT(10.9) –Model Surface Temperature in which all of the FOVs pass the three cloud tests.

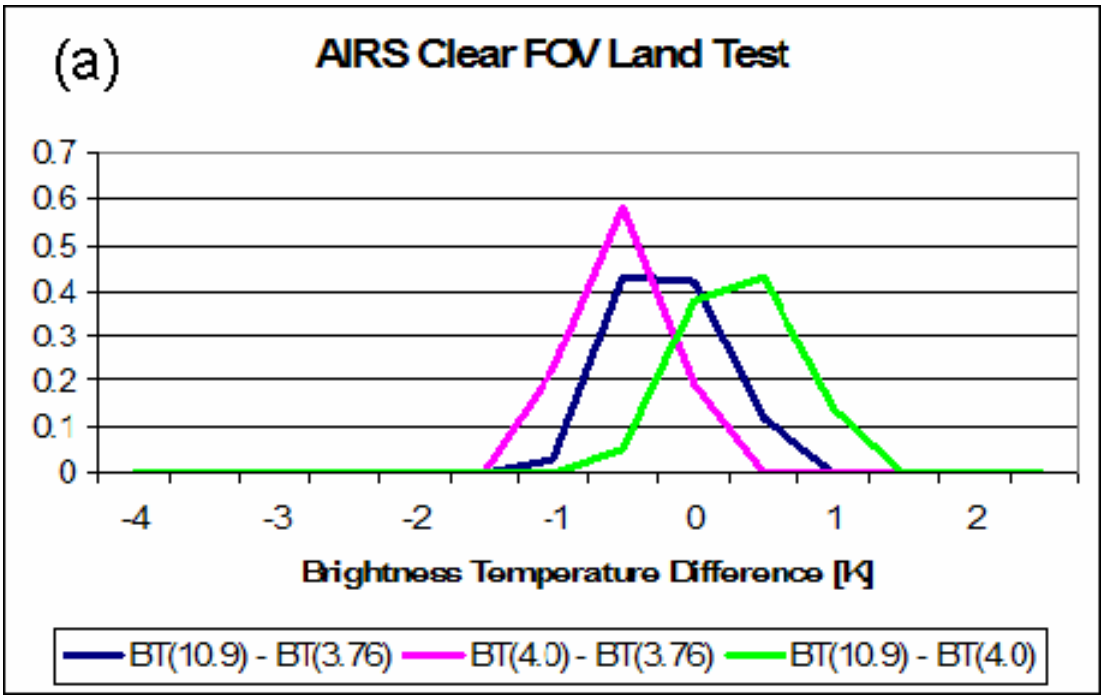

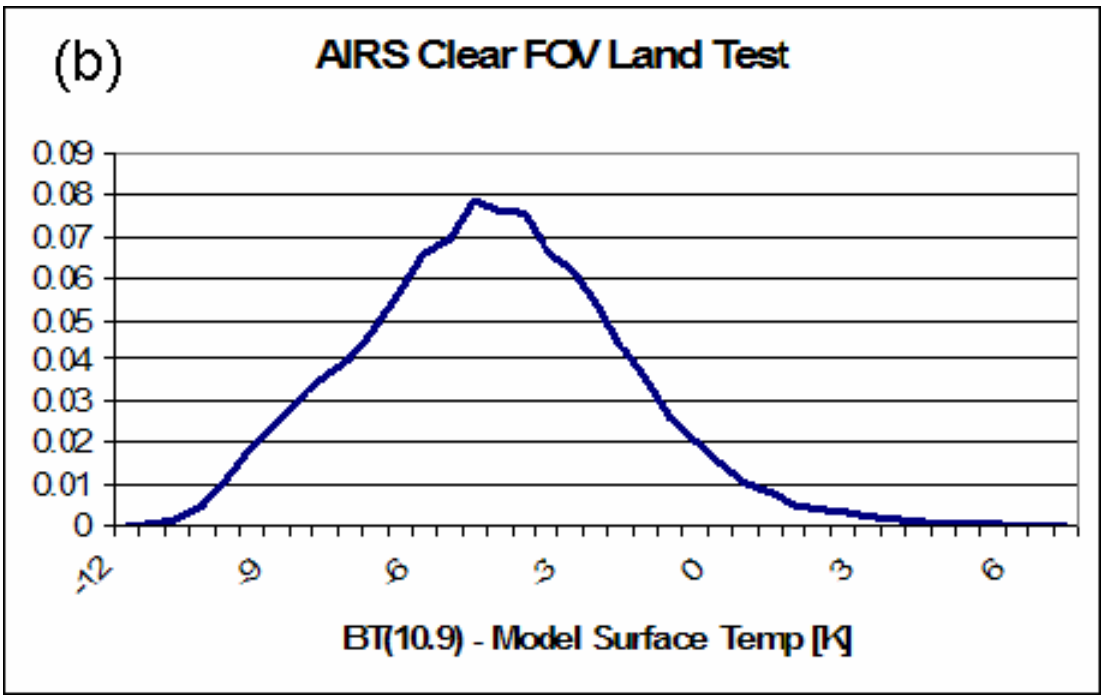

Figure 10.4 Land histograms of the cloud tests for those FOVs which pass the three selection criteria. Panel (a) is the histograms of the selection criteria in which all FOVs pass the three tests. Panel (b) is the histogram of BT(10.9) –Model Surface Temperature in which all of the FOVs pass the three cloud tests.

10.2.3 Determining clear radiance profiles for snow and ice.

Determining clear FOVs over snow and ice is very difficult. In the infrared region, snow and ice have similar properties as clouds. Holz and Ackerman (2006) determined that the absorption coefficients for ice and water are significantly different near 12.5μm with ice having the higher absorption coefficient. Clouds with similar microphysical characteristics, except for phase, will result in the ice cloud having a warmer measured BT than water at 12.5μm. Holz and Ackerman (2006) also noted that ice surface emissivity has a significant spectral dependence between 9.1 and 12.5μm. The emissivity differences between 9.1 and 12.5μm can result in a brightness temperature difference of 2.5^{o}K at 250.0^{o}K (Holz and Ackerman, 2006). Holz an Ackerman (2006) also found that the sensitivity to the cloud effective radius can also be used in a cloud mask. The difference in sensitivity between 10.4 and 9.1μm can help to improve the cloud mask. Based on these findings, Holz and Ackerman (2006) developed four BT channel tests for clear AIRS FOVs.

$$(BT(12.5) - BT(9.1)) > -0.05$$
$$(BT(12.5) - BT(9.1)) < 1.0$$
$$(BT(10.4) - BT(9.1)) > -0.05$$
$$(BT(10.4) - BT(9.1)) < 1.0$$

The BT(12.5) – BT(9.1) will be negative for ice clouds and greater than 1 for water clouds. A BT(10.4) – BT(9.1) difference of less than -.05 and greater than 1.0 indicates the presence of clouds.

Since inversions are common over snow and ice, choosing the FOVs warmer than the model has too many false alarms to be valid. Instead the shape of the BT(10.55) – GDAS surface temperature histogram is used to determine how well the test does. In the process of generating the histogram statistics it was noted that the test did not do well at temperatures near and above 273K. An arbitrary threshold of observation temperatures of

263K was established to improve the test. It is speculated that at temperatures above 263K, water may be present at the surface nullifying the emissivity and radius difference tests. As shown in Fig. 10.5 these tests do a reasonable job of producing a normal distribution.

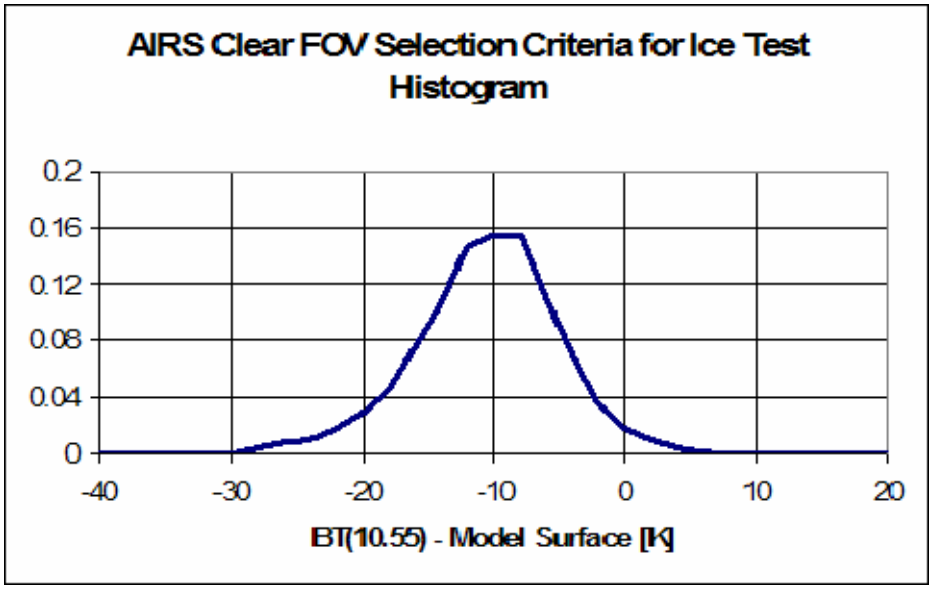

Figure 10.5 Ice and Snow histogram of the cloud tests for those FOVs which pass the four selection criteria and are colder than 263K.

10.2.4 Detecting surface inversions with AIRS radiances in Polar Regions.

Another method of determining clear radiances over snow and ice would be to check for inversions. Ackerman (1996) found that large negative BT(6.7) – BT(11.0) differences occur in the presence of strong, low-level temperature inversions over Antarctica with the Advanced Very High Resolution Radiometer (AVHRR) and HIRS/2. Ackerman (1996) also noted that clouds inhibit the formation of the inversion and obscure it from Infrared satellite sensor detection. The BT(6.7) - BT(11.0) test should be able to identify clear sky conditions when strong inversions exist.

Liu et al. (2004) found that using the MODIS 7.2-μm water vapor channel could also be used to identify low level inversions in cloud free regions of the Arctic. Under clear-sky conditions, the 7.2-μm channel is sensitive to temperatures near 800 hPa. Using

the MODIS BT(11) surface channel and BT(7.2) water vapor channel, Liu et al. (2004) determined that the BT(7.2) – BT(11.0) difference is related to the temperature difference between 800 hPa and the surface.

Similar channels were identified and tested within the AIRS reduced dataset. The tests cited here were conducted using HIRS or HIRS like instruments with much broader spectral response functions which contained water vapor absorption lines. Similar AIRS channels with the broad spectral response functions are not present in the 281 channel dataset. The two AIRS channels which are close to the water vapor absorption lines used by Liu et al. (2004) were found to be relatively insensitive and caused a considerable number of false alarms.

10.2.5 Water vapor lines inversion test

The sharper spectral response functions of the AIRS data allows for a new technique to be used to determine inversions. The water vapor lines which usually cause the brightness temperature to be colder than the corresponding off water vapor line brightness temperatures will become warmer for an inversion. Figure 10.6 is an example of the AIRS spectra with and without a surface inversion.

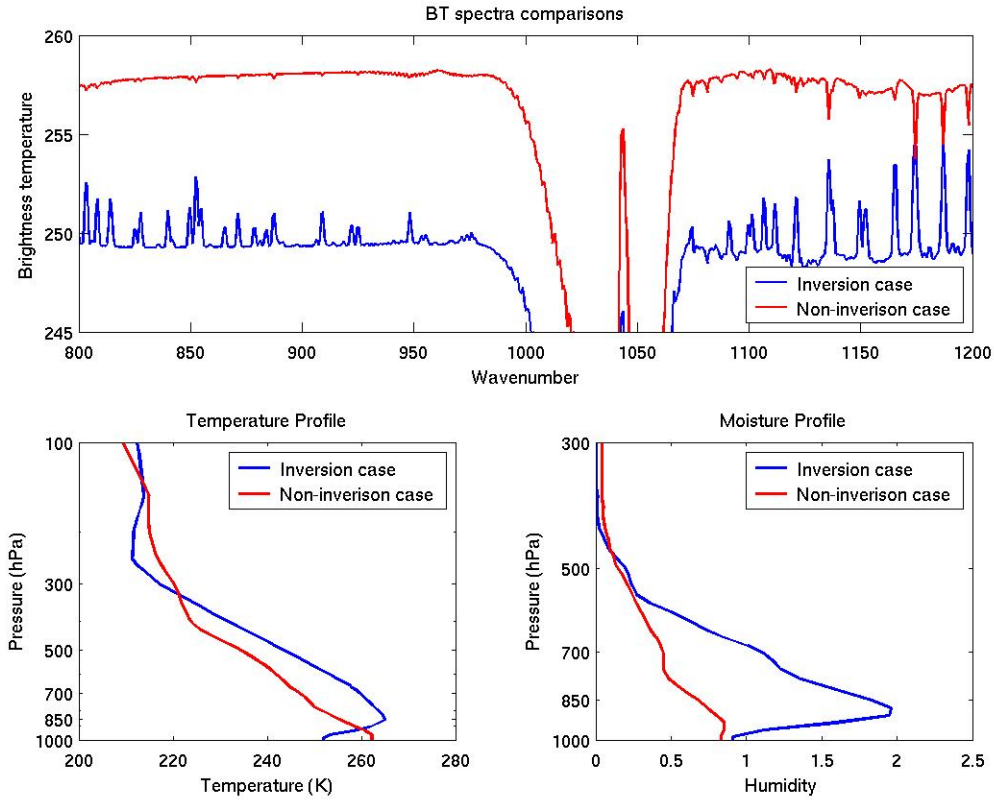

Figure 10.6 AIRS spectra with and without a surface inversion (Jun Li, personal communication).

Four channel pairs were found that seem to contain enough of the water vapor absorption lines to make a valid test. The on-line channels are listed in the left column and the off-line pairs are listed in the right column of Table 10.1. When all of the on-line channels are warmer than their off-line pair, an inversion is anticipated. A final check looks for the warmest brightness temperature from 10.90 to 14.15 μm. If a FOV passes all four of the water vapor absorption line test, and the warmest brightness temperature between 10.0 and 13.0 μm is 5.0K warmer than the BT(10.90), an inversion is assumed. Better on-line / off-line pairs exist to detect inversions in the full 2378 channel data but they are not included in the spectrally reduced (281 channels) dataset delivered to NWP centers.

Table 10.1 On-line / off-line channels used to detect polar inversions. If all on-line channels are warmer than their off-line pairs, an inversion is anticipated.

On-line wavelength (μm)		Off-line wavelength (μm)
13.594	>	13.598
13.604	>	13.376
7.1831	>	7.2400
6.6969	>	6.6713

10.3 Deriving Surface Temperature and Emissivity within the Analysis System

The long-wave / short-wave difference tests, the ice emissivity tests and the polar inversion test are incorporated into the recent version of NCEP's SSI. The long-wave / short-wave tests are used at night over land and ocean to help screen both high cirrus and low stratus cloud contaminated pixels. The warmest BT(10.36) FOV test was replaced by the AST-SST algorithm over land and ocean. At night and over land or ocean, the FOV with the warmest SST value which passed the BT(3.91) – BT(10.90) test was chosen first. If all FOVs failed the BT(3.91) – BT(10.90) test, then the FOV with the warmest SST is chosen. During the day, the FOV with the warmest AST-SST was chosen. If more than one FOV is warmer than the model surface temperature, the FOV closest to the center of the thinning box is used. Over snow and ice and surface temperatures colder than 263K, the clear radiance profile test (for snow and ice) is used first. If a FOV does not pass this test, the water vapor lines inversion test was used. If all the points in a specific thinning box failed these tests, the warmest BT(10.36) is chosen.

Once the best FOV is chosen in the thinning box, the AIRS data is then subject to the McNally and Watts (2003) profile test. Only the channels which passed these tests are

assimilated. There are approximately 7450 thinning boxes with AIRS data in an assimilation cycle. Of these 7450 AIRS FOVs, almost all are used in the stratosphere and decreases to about 1000 which are considered clear at the surface. Figure 10.7 is an example of a histogram of AIRS channels which pass the quality control procedures for one assimilation cycle.

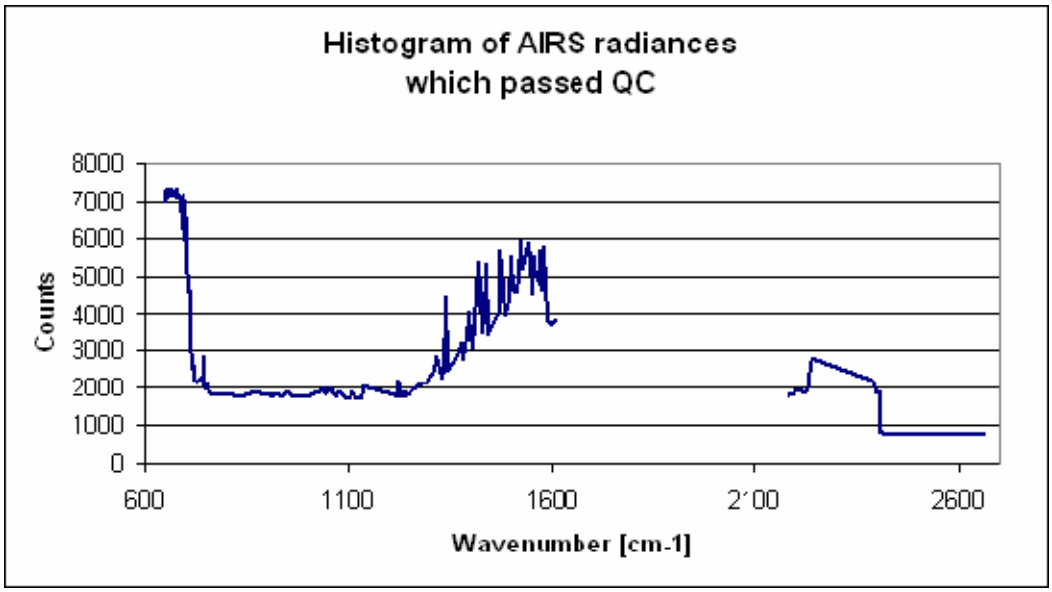

Figure 10.7 Histogram of AIRS clear radiances which passed all the quality control procedures in one assimilation cycle by wavenumber.

10.3.1 Defining Surface Skin Temperature

Once the clear profiles were identified, the radiative transfer equation was used to derive the surface temperature from the AIRS radiances. The cloud-free radiative transfer equation, neglecting solar radiation and scattering effects, for a down-looking infrared sensor viewing a homogeneous surface used in this technique is given by:

$$R_v = \int_0^Z B_v[T(z)]\frac{\delta\tau_v(z,Z)}{\delta z}dz + \varepsilon_v \cdot B_v(T_s)\cdot\tau_v(0,Z) + (1-\varepsilon_v)\cdot\tau_v(0,Z)\int_\infty^0 B_v[T(z)]\frac{\delta\tau_v(z,Z)}{\delta z}dz \quad (10.1)$$

Where R_v, ε_v, B_v, T_s, $\tau_v(z,Z)$, Z, and T(z) are observed spectral radiance, spectral emissivity, spectral Planck function, surface temperature, spectral transmittance at wavenumber *v* from altitude z to Z, sensor altitude and air temperature at altitude z respectively. The first term of the equation is the emission from the atmosphere above the surface, the second term is the direct emission from the surface that reaches the sensor, and the third term is the down-welling atmospheric emission reflected off the ground.

Solving the radiative transfer equation for emissivity, equation (10.1) becomes:

$$\varepsilon_v = \frac{[R_v - N_v \uparrow] - \tau_v N_v \downarrow}{\tau_v B_v(T_s) - \tau_v N_v \downarrow} \tag{10.2}$$

Where:

$$N_v \uparrow = \int_0^Z B_v[T(z)] \frac{\delta \tau_v(z,Z)}{\delta z} dz$$

$$N_v \downarrow = \int_\infty^0 B_v[T(z)] \frac{\delta \tau_v(z,Z)}{\delta z} dz$$

Where R_v is the observed up-welling spectral radiance, N↑ represents the up-welling only emission from the atmosphere and N↓ represents the down-welling flux at the surface.

Fractional changes in emissivity are observed from the spectral emission lines when varying the surface temperature. This is due to the reflected infrared radiance from water vapor spectral emission lines. Figure 10.8 shows the spectral changes in emissivity when the surface temperature (T_s) is varied by up to 2K. The AIRS channels between 13.0 to 10.0μm, 9.25 to 8.33μm and 4.0 to 3.76μm with the water vapor emission lines are paired with the nearest off-line window channel and are listed in Table 10.2. The shortwave

channels (4.0 – 3.76μm) are used only at night. The variance in emissivity is calculated by summing the differences between the on-line and off-line pair.

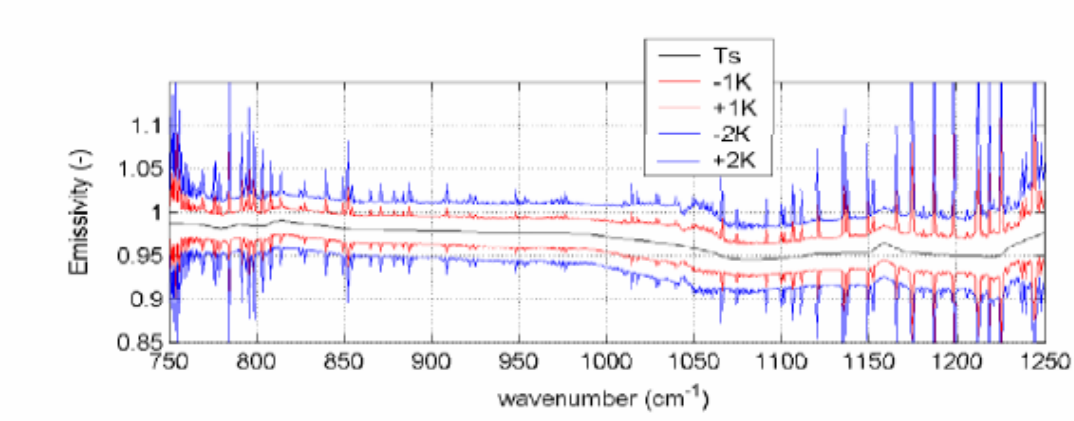

Figure 10.8 Derived emissivity vs. wavenumber for a range of surface temperatures (from Knuteson et al. 2003)

Table 10.2 On-line / off-line AIRS channel pairs used to derive surface temperature.

On-line wavelength	Off-line wavelength
12.61	12.48
12.43	12.48
12.36	12.18
11.48	10.90
10.55	10.36
9.03	8.97
3.83	3.84
3.82	3.83
3.78	3.765
3.763	3.75

The surface temperature is iterated with equation (10.2) using just the channel pairs in Table 10.2. The upper and lower bounds of the iteration are set at +/- 2K from the GFS surface temperature to find the minimum variance in emissivity. Where the minimum variance is defined as:

$$\sum \left(\varepsilon_{\text{online}} - \varepsilon_{\text{offline}}\right)^2 = MIN$$

An example of how the sum of the emissivity variance changes with surface temperature is shown in Figure 10.9. The optimum surface temperature will have the least variance in

emissivity. Equation (10.2) is then iterated through the channels with a significant surface component to calculate their surface emissivity.

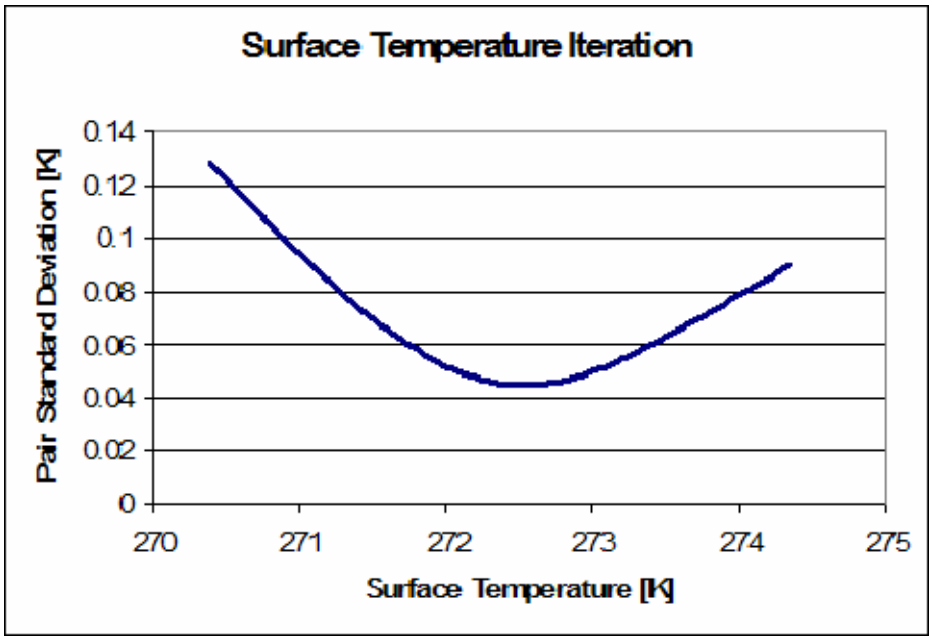

Figure 10.9. The change in standard deviation for changes in surface temperature. The minimum standard deviation is the optimum surface temperature for calculating surface emissivity.

After the optimum surface temperature is derived, Eq. (10.2) is used with the appropriate AIRS channels to determine the surface emissivity. Three types of quality control were included to help remove unrealistic emissivity profiles. The first step is to require the derived surface temperature to be within 1.0K of the GDAS analysis surface temperature. This ensures the atmospheric component ($N_v\uparrow$) does not deviate significantly from the radiance measurements and the model profile is reasonable. The second step is to require the standard deviation of the channel pair emissivity difference to be less than 0.1. The third step is to require the calculated emissivity value to be within +/- 0.03 of commonly accepted ocean emissivity values. These AIRS derived surface emissivity values over ocean are compared to the surface emissivity algorithm used in the CRTM Van Delst (2003) and are shown in Fig 10.10.

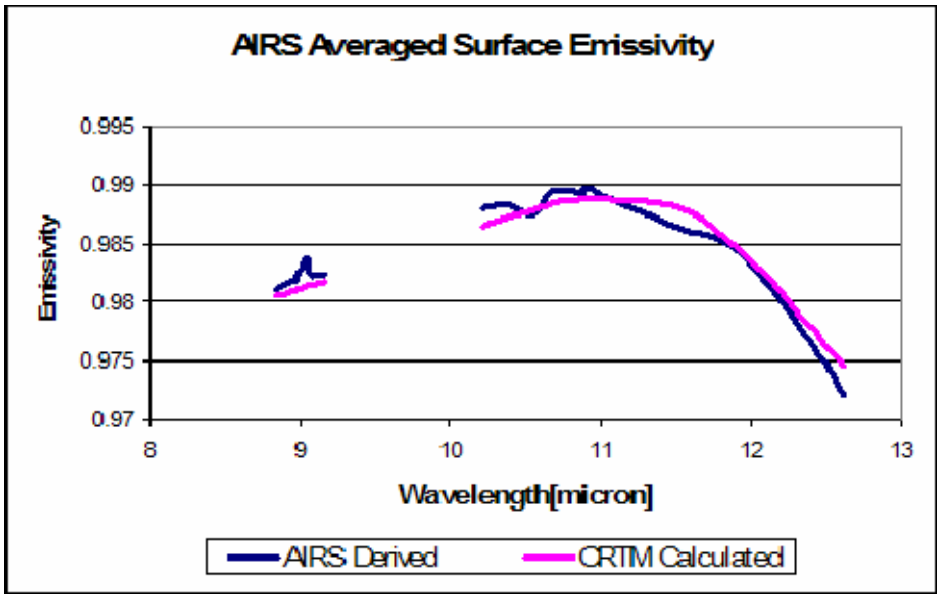

Figure 10.10 Ocean surface emissivities derived from the AIRS surface channels and those calculated within the CRTM.

The ocean surface emissivity has scan angle dependencies. In measuring the quality of the emissivity derived from AIRS, the results are also compared to the CRTM model at the various scan angles. Figure 10.11 shows the values of the emissivity for the AIRS surface channel spectra for selected scan angles. In general, the emissivity decreases with increasing scan angle. It is also more sensitive to scan angle at longer wavelengths. Figure 10.12 shows the comparison of the AIRS derived emissivity at 12.18μm to the CRTM. The relatively good agreement between the AIRS derived and CRTM ocean emissivities at this wavelength and others (not shown) are encouraging.

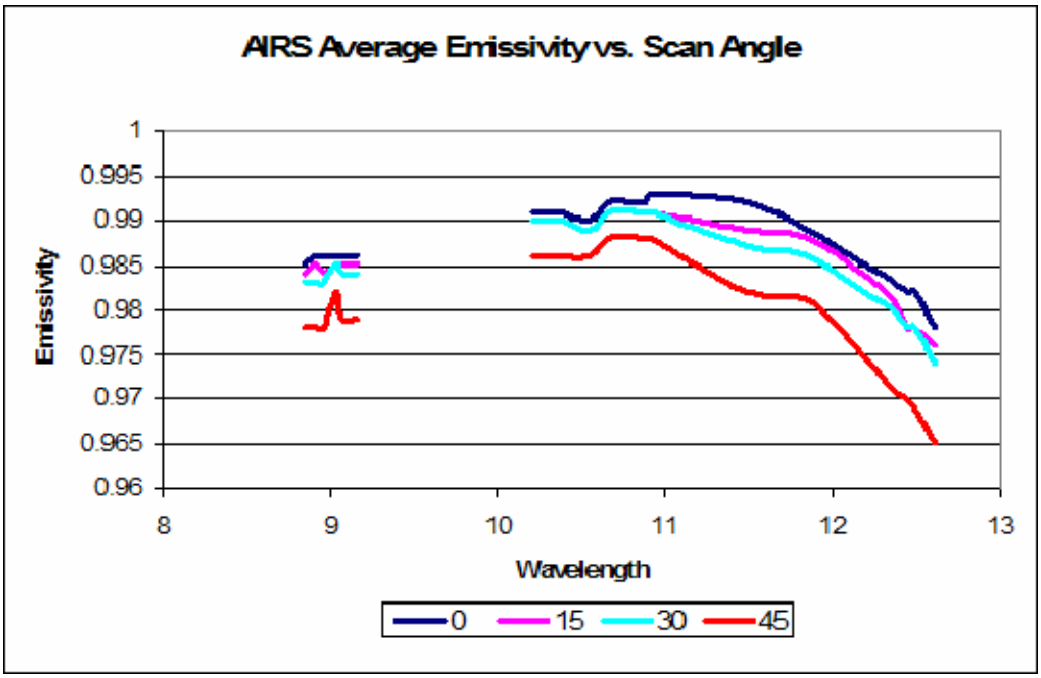

Figure 10.11 Ocean emissivity derived from AIRS at selected scan angles.

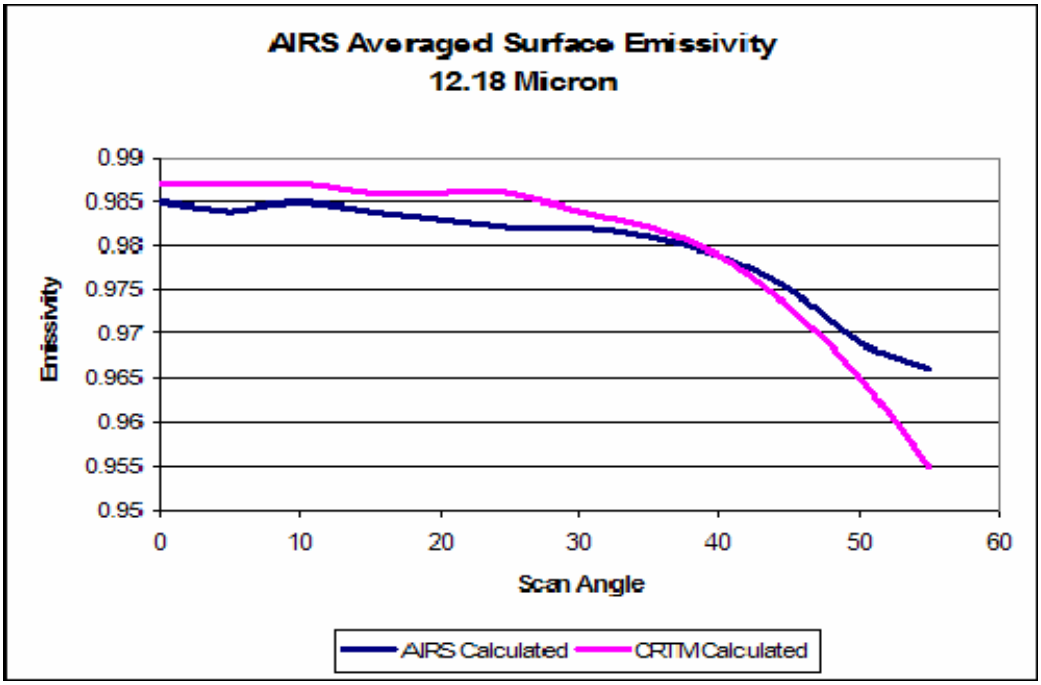

Figure 10.12 Comparison of the ocean emissivity derived from AIRS to the emissivity model used by the CRTM for 12.18μm.

The infrared surface emissivity over land, snow and ice used by the CRTM is described in Carter et al. (2002). The database contains surface reflectance measurements as a function of wavelength in both the visible and IR spectral regions for the 24 surface

types listed in Table 5.1, of these 24 surface types, the GDAS uses snow, ice and 11 land types listed in Table 10.3.

Table 10.3 Surface types defined by the GDAS

Surface Types	
Compacted soil	Pine brush
Tilled soil	Broadleaf brush
Broadleaf forest	Scrub soil
Pine Forest	Broadleaf(70)/Pine(30)
Scrub	New snow
Broadleaf /Pine forest	Old Snow
Tundra	Ice

The same technique for deriving the ocean emissivity was used to derive the surface emissivity for the various land types. Our comparisons over land showed less agreement with the values used by the CRTM, however the accuracy of the CRTM emissivities over land are less than over ocean. Differences in emissivity between the CRTM and those derived from AIRS data for each land type category can be large. Comparisons of the emissivity values for three surface types used by the CRTM are shown in Fig. 10.13. There are several reasons the land surface emissivities deviate considerably; the natural variability of surface emissivities is considerably more over land than ocean, the accuracy of the land type categories and related emissivity in the CRTM still need improvement, and seasonal variations in emissivity are not taken into account, the GDAS forecast surface temperature forecast may be inadequate, and the instrument noise and channel pairs in the provided AIRS dataset may not be adequate to capture the spectral variability in the emissivity.

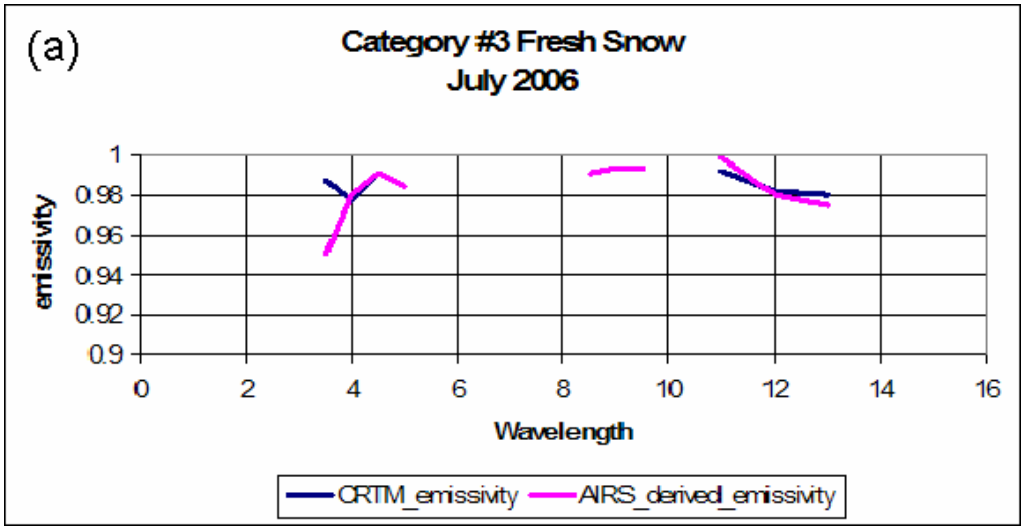

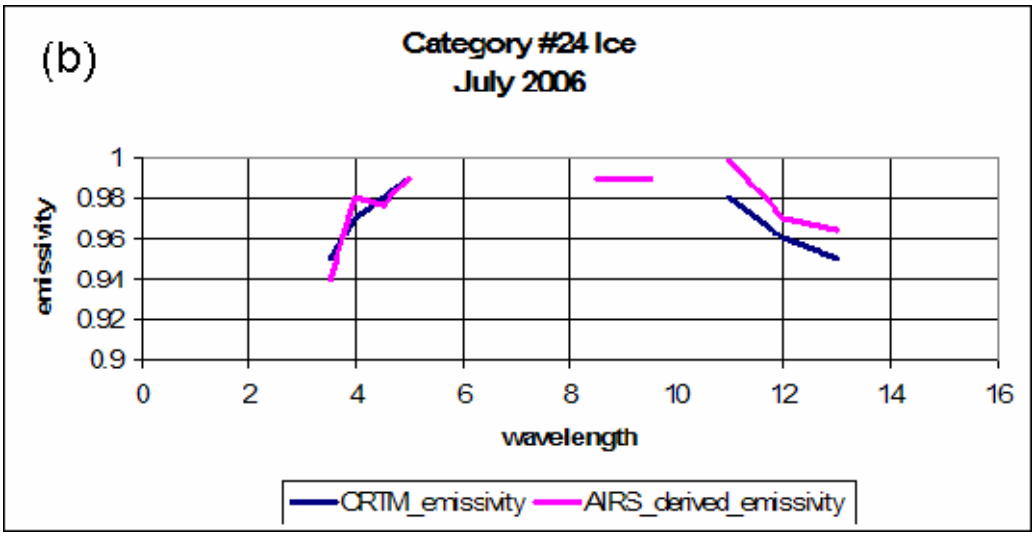

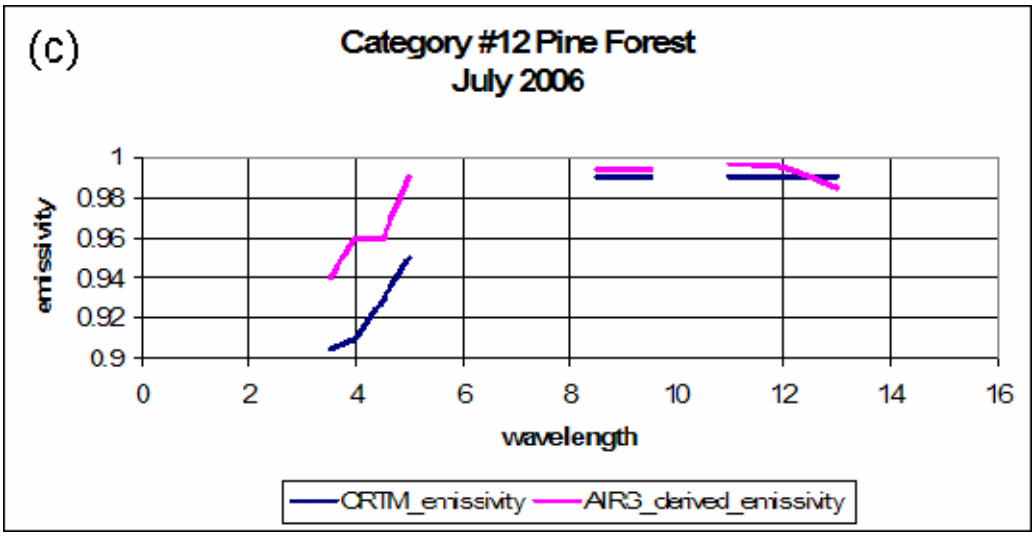

Figure 10.13 Surface emissivity derived from using AIRS surface channels compared to values used in the CRTM during July 2006 for (a) New Snow, (b) Ice and (c) Pine Forest.

This technique, when using the NWP AIRS reduced channel set tends to be noisy for a single observation. The limited number of on-line / off-line pairs in the NWP AIRS dataset lessens the accuracy in deriving the surface temperature. Increasing the number of surface channels and using emissivity Eigen vectors would be expected to reduce the noise and may allow updating of the background emissivity field.

10.4 Summary

The use of weather satellite data over land is limited by its inability to separate the effect of surface temperature from natural variations in surface emissivity. The next generations of hyperspectral infrared sounders, like AIRS, are able to improve profiles of atmospheric temperature and water vapor with their nearly continuous coverage of the 8 – 14μm window region. This allows an effective surface temperature to be determined simultaneously with an effective land surface emissivity. Being able to derive surface temperature and emissivity (with good a priori data) within a data assimilation system will improve the use of radiances near the surface which should improve the analysis, especially near the surface.

This technique is particularly sensitive to cloud and other contaminants which may be in the radiance data. Extra care must be taken to prevent these contaminated radiances from being used in the determination of surface temperature and emissivity. If these contaminated radiances are not screened out, unrealistic values may occur. Several tests to determine clear profiles such as long-wave / short-wave tests, detecting inversions, and detecting on-line/off-line water vapor differences over snow and ice have been incorporated into the GDAS thinning routine.

The surface temperature and emissivity was derived from as many on-line / off-line pairs as possible within the reduced NWP AIRS dataset to calculate surface temperature. The radiative transfer equation was solved for emissivity and iterated through a range of temperature to find the minimum variance in emissivity. The temperature, at which this minimum variance occurs, is the surface temperature. This surface temperature is then used to derive the surface emissivity for each channel.

The AIRS derived surface emissivity values over ocean were compared to the surface emissivity algorithm used in the CRTM. The ocean surface emissivity has scan angle dependencies which were successfully derived from the AIRS surface channels. In measuring the quality of the emissivity derived from AIRS, the results are also compared to the CRTM model at the various scan angles.

Our comparisons over land showed less agreement with the values provided by the CRTM. Differences in emissivity between the CRTM and those derived from AIRS data for each land type category can be large. There are several reasons the land surface emissivities deviate considerably. The natural variability of surface emissivities over land is considerably more over land than ocean. Seasonal variation in emissivity was not taken into account. The GDAS surface temperature forecast may be inadequate. The instrument noise and channel pairs in the AIRS dataset may not be adequate to capture the spectral variability in the emissivity.

10.5 Conclusion

Using on-line / off-line channel pairs from the AIRS hyperspectral instrument, the surface emissivity can be derived within NCEP's GDAS. We have demonstrated that the relatively spatially uniform ocean emissivity can be derived from AIRS surface channels.

The satellite scan angle dependence is also estimated with reasonable accuracy using this technique.

This technique is particularly sensitive to cloud and other contaminants which may be in the radiance data. Extra care must be taken to prevent these contaminated radiances from being used in the determination of surface temperature and emissivity variance parameters. If these contaminated radiances are not screened out, unrealistic values may occur. Special care must be taken to ensure the profiles used to generate the surface emissivity are clear. The model surface temperature must also be close to the skin temperature.

The AIRS derived surface emissivity values over ocean were compared to the surface emissivity algorithm used in the CRTM with relatively good agreement. The ocean surface emissivity has scan angle dependencies which were also successfully derived from the AIRS surface channels. Our comparisons of the CRTM emissivity to the AIRS derived values for the various land categories were not as definitive. In some cases the differences in the emissivity values between those derived from AIRS and those in the CRTM for a given land type category were large. Continued research in this area is needed to help resolve these differences.

Chapter 11: Summary and Conclusions

The object of this research was to effectively assimilate the information content of hyperspectral infrared radiances from the AIRS instrument. Initial impacts of AIRS data in global NWP were positive but modest. Here we approached the problem by adding to the information content available to the analysis by increasing the spatial and spectral coverage of the AIRS observations. We improved the selection of radiances free from the effects of clouds. As a result the impact of AIRS was greatly enhanced. In addition studies such as using all fields of view has led to the warmest FOV being distributed as the operational AIRS dataset and other changes to the operational assimilation of AIRS data at NCEP.

Hyperspectral infrared radiance data present opportunities for significant improvements in data assimilation and Numerical Weather Prediction (NWP). The increase in spectral resolution available from the Atmospheric Infrared Sounder (AIRS) sensor, for example, makes it possible to more accurately determine temperature and moisture fields. Improved accuracy of the analyses and forecasts are a result. The spatial and spectral resolution of AIRS data used by NWP centers was initially based on theoretical calculations and logistic constraints. Several problems were not fully addressed. These problems include cloud characterization, surface related issues, aerosols, and temperature inversions.

Until the present work, data assimilation methods used for AIRS have been similar to those used by the HIRS and AMSU, and as yet have not taken full advantage of the unique hyperspectral properties of AIRS. Initially, NWP centers tested the assimilation of AIRS data and showed limited benefit. At ECMWF, McNally et al. (2003) used

assimilation techniques similar to those used to assimilate HIRS and AMSU radiances over land and ocean. The average impact of AIRS in 100 cases studied was positive but small (McNally et al. 2003). Similar AIRS assimilation studies conducted with the Meteo-France numerical weather prediction model also produced small positive results (Auligne et al. 2003).

The introduction of AIRS hyperspectral data into NWP centers was anticipated to provide significant improvements in forecast skill. Here, we have noted results where AIRS hyperspectral data, used at higher spectral and spatial resolution than initially used at NWP centers, have shown significant positive impact in forecast skill in both the Northern and Southern Hemisphere. The magnitude of the improvement is quite significant and would normally take several years to achieve at an operational weather center. We have also noted the improvement gained from using AIRS at a spatial density greater than that initially used by NWP Centers. In addition, we have completed studies which look at the impact of spectral coverage and found for the period studied, use of fuller AIRS spectral coverage and the full AIRS spectral range provided superior forecasts. The efficacy of using higher spatial and spectral resolution data for depicting the moisture field has also been shown.

It is anticipated current results will be further enhanced through improved physical modeling, a less constrained operational environment allowing use of higher spectral and spatial resolution and cloudy data, the use of complementary data such as MODIS radiances and the effective exploitation of the new hyperspectral data which will become available from the IASI, CrIS and Geosynchronous Imaging Fourier Transform Spectrometer (GIFTS) instruments.

11.1 The AIRS Assimilation Experiment

This was the first AIRS experiment which used the full spatial (every FOV) and 251 channel AIRS data. This experiment was designed in a way that rendered them feasible for operational application. The NCEP operational version of the GDAS/GFS (November 2003) was used at the operational resolution of T254, with 64 levels. For the control experiment, the NCEP operational database of conventional and satellite data, with the real-time cutoff constraints was used. This experiment was run from 1 January to 27 January 2004 when availability of the NCEP ASP super-computer was terminated.

In general the AIRS data improved the majority of NCEP's forecast skill benchmarks. AIRS data had a consistent and beneficial effect on the 1000 hPa forecast anomaly correlations of geopotential height at mid-latitude for the Northern and Southern Hemispheres out to day 7. The mid-latitude 500 hPa average geopotential height anomaly correlations are higher for every forecast day (1-7) of the AIRS experiment. Another noticeable characteristic is that the Southern Hemisphere anomaly correlations have a consistently greater improvement than in the Northern Hemisphere. Among the considerable daily variations, the time series shows more days with positive impact than negative. Impacts on the wind field in the tropics for this experiment were near neutral with some places showing small improvements. In the case of moisture, the impact was clearly positive. The greatest impacts are in the Polar Regions and over the land masses in the Southern Hemisphere.

AIRS hyperspectral data (from one orbital instrument), used within current stringent operational constraints, shows significant positive impacts in forecast skill over both the Northern and Southern Hemisphere for January 2004. The results indicate a considerable

opportunity to improve operational analyses and forecasts with hyperspectral data. As a result of these experiments, the AIRS center FOV radiances were incorporated into the NCEP operational dataset initially, and was later expanded to using every field of view.

11.2 Full Spatial Resolution Experiment

The AIRS full spatial resolution experiment compared the full spatial resolution of AIRS (every FOV) to using the center spot of every other golf ball (1 in 18 FOV). These experiments were designed in a way that renders them feasible for operational application. For both the AIRS Center and AIRS SFOV experiments, the NCEP operational database of conventional and satellite data, with the real-time cutoff constraints was used.

In general, the AIRS data improved almost all of NCEP's forecast skill benchmarks. AIRS data had a consistent and beneficial effect on the 1000 hPa forecast anomaly correlations of geopotential height at mid-latitude for the Northern and Southern Hemispheres. The mid-latitude 500 hPa the average geopotential height anomaly correlations are higher for every forecast day (1-7) of the AIRS experiment. Another noticeable characteristic is that the summer Hemisphere anomaly correlations have a consistently greater improvement than in the winter Hemisphere. The standard deviations of the anomaly correlations were consistently smaller for the AIRS_SFOV experiment indicating more consistent forecasts. In the case of moisture, the impact is clearly positive, especially in the summer Hemisphere.

This methodology was later adopted at NCEP and a related selection process for warmest FOVs was later included in the data processing methodology at NESDIS and led to the distribution of the warmest FOV to operational NWP rather than using the 1 in 18 FOVs.

11.3 Full Spectral Resolution Experiment

The spectral resolution AIRS experiments compared various combinations of spectral resolution of AIRS from using no AIRS channels (Control) to using 115 of the water vapor and short wave (Short_AIRS) to using a limited set of 152 channels (Ops_AIRS) to using the full complement of 251 channels (All_AIRS). For the three AIRS experiments and the control, the NCEP operational database of conventional and satellite data, with the real-time cutoff constraints was used.

The results show that the 1000 and 500 hPa anomaly correlations of geopotential height in both the Northern and Southern Hemisphere at mid-latitudes are generally improved from the Control to Short_AIRS to Ops_AIRS to All_AIRS. The results are very consistent for 1 January to 15 February that more AIRS channels improves the forecast skill. The standard deviation of the geopotential height anomaly correlations also decrease with the addition of more AIRS channels, with the All_AIRS experiment being the best.

The forecast impact on the 500 hPa temperature field also improves with the addition of more AIRS channels, especially in the oceanic region around South America. The greatest impact comes from the initial use of the AIRS channels (Control vs. Short_AIRS) with less improvement realized from adding more channels. Related results were noted in the precipitable water field.

11.4 Cloud Detection and Surface Emissivity Experiments

The use of weather satellite data over land is limited to a significant extent by the inability to separate the effect of surface temperature from natural variations in surface emissivity. Being able to derive surface temperature and emissivity within a data

assimilation system will improve the use of radiances near the surface which should improve the analysis near the surface.

This technique of determining surface temperature and emissivity is particularly sensitive to cloud and other contaminants which may be in the radiance data. Extra care must be taken to prevent these contaminated radiances from being used in the determination of surface temperature and emissivity. If these contaminated radiances are not screened out, unrealistic values may occur. Several tests to determine clear profiles such as long-wave / short-wave tests, detecting inversions, and detecting on-line/off-line water vapor differences over snow and ice were incorporated into the GDAS thinning routine.

The surface temperature and emissivity was derived from as many on-line / off-line pairs as possible within the reduced NWP AIRS dataset to calculate surface temperature. The radiative transfer equation was solved for emissivity and iterated through a range of temperature to find the minimum variance in emissivity. The temperature, at which this minimum variance occurs, is the surface temperature. This surface temperature is then used to derive the surface emissivity for each channel.

The AIRS derived surface emissivity values over ocean were compared to the surface emissivity algorithm used in the CRTM. The ocean surface emissivity has scan angle dependencies which were successfully derived from the AIRS surface channels. In measuring the quality of the emissivity derived from AIRS, the results were also compared to the CRTM model at the various scan angles and found to be consistent.

Our comparisons of the CRTM emissivity to the AIRS derived values over land were not as mutually supportive. Differences in the emissivity values between the CRTM

and AIRS derived emissivity were sometimes significant and require further investigation. There are several reasons the land surface emissivities deviate considerably; the natural variability of surface emissivities is larger over land than ocean, the accuracy of the land type categories in the CRTM and thus emissivities may not be consistent, and seasonal variations in emissivity were not taken into account. The GDAS surface temperature forecast may also be inadequate, and the instrument noise and channel pairs in the provided dataset may not be adequate to capture the full spectral variability in the emissivity.

11.5 Future Work

During the course of these experiments several research areas of development have presented themselves. Although the temperature and moisture fields within the GDAS are greatly improved, they appear to be short of the standards suggested by Suskind et al. (2003). Reducing the size of the thinning box and increasing the number of channels may improve the temperature and moisture fields of the analysis and the subsequent forecasts. The method of deriving the surface emissivity used in these studies has many weaknesses. Improving the on-line / off-line window channel pairs (both quality and quantity) and employing noise reduction techniques such as the use of Eigen vectors could improve the variability now associated with this technique.

A topic not covered in these studies but worthy of research is the assimilation of cloudy infrared radiances. If infrared radiances could be used where clouds are present, considerable information could be obtained about the cloud environment as well as the cloud properties.

APPENDIX A

The GFS Atmospheric Model

(status as of August 28, 2003)
(from http://www.emc.ncep.noaa.gov/gmb/moorthi/gam.html)

Model Documentation:

Comprehensive documentation of the 1988 version of the model was provided by the NMC (now NCEP) Development Division (1988), with subsequent model development summarized by Kanamitsu (1989), Kanamitsu et al. (1991), Kalnay et al. (1990).

The documentation NCEP MRF/RSM physics status as of August 1999 is located here. This document containing radiation, surface layer, vertical diffusion, gravity wave drag, convective precipitation, shallow convection, non-convective precipitation and references updates the old 1988 documentation. In addition Office Note # 424, New Global Orography Data Sets contains documentation of the higher resolution orography for the MRF. The documentation of the GFS atmospheric model as of 2003 is in NCEP Office Note # 442 .

Numerical/Computational Properties

- **Horizontal Representation**
  Spectral (spherical harmonic basis functions) with transformation to a Gaussian grid for calculation of nonlinear quantities and physics.

- **Horizontal Resolution**
  Spectral triangular 254 (T254); Gaussian grid of 768X384, roughly equivalent to 0.5 X 0.5 degree latitude/longitude.

- **Vertical Domain**
  The vertical domain is from the earth's surface (sigma=1) to the top of the atmosphere (sigma=0). This domain is divided into 64 layers with enhanced resolution near the bottom and the top. For a surface pressure of 1000 hPa, the lowest atmospheric level is at a pressure of about 997.3 hPa and the top level is at about 0.27 hPa.

- **Vertical Representation**
  Sigma coordinate. Lorenz grid. Quadratic-conserving finite difference scheme by Arakawa and Mintz (1974).

- **Vertical Resolution**
  64 unequally-spaced sigma levels. For a surface pressure of 1000 hPa, 15 levels are below 800 hPa, and 24 levels are above 100 hPa.

- **Computer/Operating System**

IBM RS/6000 SP (Class VIII) in an AIX environment.

- **Computational Performance**
  About 12 minutes computation time on the IBM per one-day forecast at T254.

- **Initialization**
  Initialization is not necessary because the statistical spectral interpolation analysis scheme eliminates the unbalanced initial state.

- **Time Integration Scheme(s)**
  The main time integration is leapfrog for nonlinear advection terms, and semi implicit for gravity waves and for zonal advection of vorticity and moisture. An Asselin (1972) time filter is used to reduce computational modes. The dynamics and physics are split. The physics are written in the form of an adjustment and executed in sequence. For physical processes, implicit integration with a special time filter (Kalnay and Kanamitsu, 1988) is used for vertical diffusion. In order to incorporate physical tendencies into the semi-implicit integration scheme, a special adjustment scheme is performed (Kanamitsu et al., 1991). The time step is 7.5 minutes for computation of dynamics and physics, except that the full calculation of longwave radiation is done once every 3 hours and shortwave radiation every hour (but with corrections made at every time step for diurnal variations in the shortwave fluxes and in the surface upward longwave flux).

- **Smoothing/Filling**
  Mean orographic heights on the Gaussian grid are used (see Orography). Negative atmospheric moisture values are not filled for moisture conservation, except for a temporary moisture filling that is applied in the radiation calculation.

Dynamical/Physical Properties

- **Atmospheric Dynamics**
  Primitive equations with vorticity, divergence, logarithm of surface pressure, specific humidity virtual temperature, and cloud condensate as dependent variables.

- **Horizontal Diffusion**
  Scale-selective, second-order horizontal diffusion after Leith (1971) is applied to vorticity, divergence, virtual temperature, and specific humidity and cloud condensate. The diffusion of temperature, specific humidity, and cloud condensate are performed on quasi-constant pressure surfaces (Kanamitsu et al. 1991).

- **Vertical Diffusion**
  See Planetary Boundary Layer

- **Gravity-wave Drag**

Gravity-wave drag is simulated as described by Alpert et al. (1988). The parameterization includes determination of the momentum flux due to gravity waves at the surface, as well as at higher levels. The surface stress is a nonlinear function of the surface wind speed and the local Froude number, following Pierrehumbert (1987). Vertical variations in the momentum flux occur when the local Richardson number is less than 0.25 (the stress vanishes), or when wave breaking occurs (local Froude number becomes critical); in the latter case, the momentum flux is reduced according to the Lindzen (1981) wave saturation hypothesis. Modifications are made to avoid instability when the critical layer is near the surface, since the time scale for gravity-wave drag is shorter than the model time step (see also Time Integration Schemes and Orography). The treatment of the gravity-wave drag parameterization in the lower troposphere is improved by the use of the Kim and Arakawa (1995) enhancement. Included is a dependence of variance on wind direction relative to the mountain as well as subgrid statistical details of mountain distribution. This improves the prediction of lee cyclogenesis and the accompanying movement of cold outbreaks.

- **Radiation**

  The longwave (LW) radiation in NCEP's operational GFS employs a Rapid Radiative Transfer Model (RRTM) developed at AER (Mlawer et al. 1997). The parameterization scheme uses a correlated-k distribution method and a linear-in-tau transmittance table look-up to achieve high accuracy and efficiency. The algorithm contains 140 unevenly distributed intervals (g-point) in 16 broad spectral bands. In addition to the major atmospheric absorbing gases of ozone, water vapor, and carbon dioxide, the algorithm also includes various minor absorbing species such as methane, nitrous oxide, oxygen, and up to four types of halocarbons (CFCs). In water vapor continuum absorption calculations, RRTM-LW employs an advanced CKD_2.4 scheme (Clough et al. 1992). A maximum-random cloud overlapping method is used in the GFS application. Cloud liquid/ice water path and effective radius for liquid water and ice are used for calculation of cloud-radiative properties. Hu and Stamnes' method (1993) is used to treat liquid water clouds, while Ebert and Curry's method (1992) is used for ice cloud. Atmospheric aerosol effect is not included in the current model.

  The shortwave (SW) radiative transfer parameterization (Hou et al., 2002) is based on Chou's work (1992) and his later improvements (Chou and Lee, 1996; Chou and Suarez, 1999). The parameterization uses a correlated-k distribution method for water vapor and transmission function look-up tables for carbon dioxide and oxygen absorptions. The model contains eight broad spectral bands covering ultraviolet (UV) and visible region (< 0.7 Ã¦), and choices of one or three spectral bands in the near infrared (NIR) region (> 0.7 Ã¦). (Currently one NIR band is used in GFS for computational economy, but may be switched to three bands in the future.) Ten correlated-k values are used in each NIR spectral band. The model includes atmospheric absorbing gases of ozone, water vapor, carbon dioxide, and oxygen. A delta- Eddington approximation method is used in multi-scattering calculations. Random cloud overlapping is assumed in the operational GFS. Cloud liquid/ice water path and effective radius for cloud liquid water and ice are used for calculation of cloud-radiative properties. For liquid water clouds, cloud-optical property coefficients

are derived based on Slingo (1989), and coefficients for ice clouds are based on Fu (1996). Atmospheric aerosol effect is included in the SW radiation calculation. A global distributed seasonal climatology data from Koepke et al. (1997) is used to form a mixture of various tropospheric aerosol components. Aerosol optical properties and vertical profile structures are established based on Hess et al. (1998). Horizontal distribution of surface albedo is a function of Matthews (1985) surface vegetation types in a manner similar to Briegleb et al. (1986). Monthly variation of surface albedo is derived in reference to Staylor and Wilbur (1990).

For both LW and SW, the cloud optical thickness is calculated from the predicted cloud condensate path. The cloud single-scattering albedo and asymmetry factor are as functions of effective radius of the cloud condensate. The effective radius for ice is taken as a linear function of temperature decreasing from a value of 80 microns at 263.16 K to 20 microns at temperatures at or below 223.16K. For water droplets with temperatures above 273.16 K an effective radius of 5 microns is used and for supercooled water droplets between the melting point and 253.16 K, a value between 5 and 10 microns is used. (See also Cloud Fraction). Effects from rain drops and snow are not included in the operational GFS but may be included in the future.

- **Convection**

  Penetrative convection is simulated following Pan and Wu (1994), which is based on Arakawa and Schubert(1974) as simplified by Grell (1993) and with a saturated downdraft. Convection occurs when the cloud work function exceeds a certain threshold. Mass flux of the cloud is determined using a quasi-equilibrium assumption based on this threshold cloud work function. The cloud work function is a function of temperature and moisture in each air column of the model gridpoint. The temperature and moisture profiles are adjusted towards the equilibrium cloud function within a specified time scale using the deduced mass flux. A major simplification of the original Arakawa-Shubert scheme is to consider only the deepest cloud and not the spectrum of clouds. The cloud model incorporates a downdraft mechanism as well as the evaporation of precipitation. Entrainment of the updraft and detrainment of the downdraft in the sub-cloud layers are included. Downdraft strength is based on the vertical wind shear through the cloud. The critical cloud work function is a function of the cloud base vertical motion. As the large-scale rising motion becomes strong, the cloud work function (similar to CAPE) is allowed to approach zero (therefore approaching neutral stability). Mass fluxes induced in the updraft and the downdraft are allowed to transport momentum. The momentum exchange is calculated through the mass flux formulation in a manner similar to that for heat and moisture. In order to take into account the pressure gradient effect on momentum, a simple parameterization using entrainment is included for the updraft momentum inside the cloud. The entrainment rate, tuned to ensure that the tropical easterly jet strength in the Indian monsoon flow maintains the least drift in the forecast is set to 10^{-4} m^{-1}. This addition to the cumulus parameterization has reduced the feedback between heating and circulation in sheared flows.

In addition, we have made a change in the cloud top selection algorithm in the convection parameterization. In the current SAS scheme, the cloud top level is determined by the parcel method. The level where the parcel becomes stable with respect to the environment is the cloud top. When the prognostic cloud water scheme is tested with this scheme, there is evidence that cloud top detrainment is too concentrated in the upper troposphere. In order to provide a more even detrainment of cloud water in the tropics, we are making a change to the selection algorithm. Once the highest possible cloud top has been determined by the parcel method, we make a random selection of the actual cloud top between the highest possible cloud top and the level where environmental moist static energy is a minimum. The proper entrainment rate is computed to ensure that the parcel becomes neutral at the new cloud top. This is very similar to the Relaxed Arakawa-Schubert (RAS) scheme developed by S. Moorthi. Cloud top detrained water is separated in to condensate and vapor with the condensate used as a source of prognostic cloud condensate.

- **Shallow convection**
  Following Tiedtke (1983), the simulation of shallow (nonprecipitating) convection is parameterized as an extension of the vertical diffusion scheme. The shallow convection occurs where convective instability exist but no convection occurs. The cloud base is determined from the lifting condensation level and the vertical diffusion is invoked between the cloud top and the bottom. A fixed profile of vertical diffusion coefficients is assigned for the mixing process.

- **Cloud Fraction**
  The fractional area of the grid point covered by the cloud is computed diagnostically following the approach of Xu and Randall (1996). The saturation specific humidity is calculated with respect to water phase or ice phase depending on the temperature. Unlike the operational model, the new model has only one type of cloud cover. In the tropics the cloudiness is primarily due to convective anvils, the result of cumulus detrainment, whereas in the extratropics, cloudiness is mainly through grid-scale condensation.

  The fractional cloud cover is available at all model levels. There is no cloud cover if there is no cloud condensate. Clouds in all layers are assumed to be randomly overlapped. Other options will be explored in the future. (See also Radiation)

- **Grid-scale Condensation and Precipitation**
  The prognostic cloud condensate has two sources, namely convective detrainment (see convection) and grid-scale condensation. The grid-scale condensation is based on Zhao and Carr(1997), which in turn is based on Sundqvist et al. (1989). The sinks of cloud condensate are grid-scale precipitation which is parameterized following Zhao and Carr (1997) for ice, and Sundqvist et al. (1989) for liquid water, and evaporation of the cloud condensate which also follows Zhao and Carr (1997). Evaporation of rain in the unsaturated layers below the level of condensation is also taken into account. All precipitation that penetrates the bottom atmospheric layer is allowed to fall to the surface (see also Snow Cover).

- **Planetary Boundary Layer**
  A new scheme based on the Troen and Mahrt (1986) paper was implemented on 25 October, 1995. The scheme is still a first-order vertical diffusion scheme. There is a diagnostically determined planetary boundary layer height that uses the bulk-Richardson approach to iteratively estimate a planetary boundary layer height starting from the ground upward. Once the planetary boundary layer height is determined, the profile of the coefficient of diffusivity is specified as a cubic function of the planetary boundary layer height. The actual values of the coefficients are determined by matching with the surface-layer fluxes. There is also a counter-gradient flux parameterization that is based on the fluxes at the surface and the convective velocity scale. (See Hong and Pan(1996) for a description of the scheme as well as a description of the convection scheme in the model).

- **Orography**
  New orography data sets are constructed based on a United States Geological Survey (USGS) global digital elevation model (DEM) with a horizontal grid spacing of 30 arc seconds (approximately 1 km). Orography statistics including average height, mountain variance, maximum orography, land-sea-lake masks are directly derived from a 30-arc second DEM for a given resolution. See NCEP Office Note 424 (Hong, 1999) for more details. (see also Gravity-wave Drag).

- **Ocean**
  A daily OI sea surface temperature analysis that assimilates observations from past seven days is used (Reynolds and Smith, 1994, available here). The sea surface temperature anomaly is damped with an e-folding time of 90 days during the course of the forecast.

- **Sea Ice**
  Sea-ice is obtained from the analysis by the marine Modeling Branch, available daily. The sea ice is assumed to have a constant thickness of 3 meters, and the ocean temperature below the ice is specified to be 271.2 K. The surface temperature of sea ice is determined from an energy balance that includes the surface heat fluxes (see Surface Fluxes) and the heat capacity of the ice. Snow accumulation does not affect the albedo or the heat capacity of the ice.

- **Snow Cover**
  Snow cover is obtained from an analysis by NESDIS (the IMS system) and the Air Force, updated daily. When the snow cover analysis is not available, the predicted snow in the data assimilation is used. Precipitation falls as snow if the temperature at sigma=.85 is below 0 C. Snow mass is determined prognostically from a budget equation that accounts for accumulation and melting. Snow melt contributes to soil moisture, and sublimation of snow to surface evaporation. Snow cover affects the surface albedo and heat transfer/capacity of the soil, but not of sea ice. See also Sea Ice, Surface Characteristics, Surface Fluxes, and Land Surface Processes.

- **Surface Characteristics**
  Roughness lengths over oceans are determined from the surface wind stress after the method of Charnock (1955). Over sea ice the roughness is a uniform 0.01 cm. Roughness lengths over land are prescribed from data of Dorman and Sellers (1989) which include 12 vegetation types. Note that the surface roughness is not a function of orography. Over oceans the surface albedo depends on zenith angle. The albedo of sea ice is a function of surface skin temperature and nearby atmospheric temperature as well as snow cover (Grumbine, 1994), with values ranging from 0.65-0.8 for snow-covered sea ice and from 0.45-0.65 for bare sea ice. Albedos for land surfaces are based on Matthews (1985) surface vegetation distribution (See Radiation). Longwave emissivity is prescribed to be unity (black body emission) for all surfaces. Soil type and Vegetation type data base from GCIP is used. Vegetation fraction monthly climatology based on NESDIS NDVI 5-year climatology is used.

- **Surface Fluxes**
  Surface solar absorption is determined from the surface albedos, and longwave emission from the Planck equation with emissivity of 1.0 (see Surface Characteristics). The lowest model layer is assumed to be the surface layer (sigma=0.996) and the Monin-Obukhov similarity profile relationship is applied to obtain the surface stress and sensible and latent heat fluxes. The formulation was based on Miyakoda and Sirutis (1986) and has been modified by P. Long in the very stable and very unstable situations. A bulk aerodynamic formula is used to calculate the fluxes once the turbulent exchange coefficients have be obtained. Roughness length over ocean is updated with a Charnock formula after surface stress has been obtained. Thermal roughness over the ocean is based on a formulation derived from TOGA COARE(Zeng et al, 1998). Land surface evaporation is comprised of three components: direct evaporation from the soil and from the canopy, and transpiration from the vegetation. The formulation follows Pan and Mahrt (1987).

- **Land Surface Processes**
  Soil temperature and soil volumetric water content are computed in two layers at depths 0.1 and 1.0 meters by a fully implicit time integration scheme (Pan and Mahrt, 1987). For sea ice, the layer depths were specified as 1.5 and 3 meters. Heat capacity, thermal and hydraulic diffusivity and hydraulic conductivity coefficients are strong functions of the soil moisture content. A climatological deep-soil temperature is specified at the third layer of 4 meters for soil and a constant value of 272 K is specified as the ice-water interface temperature for sea ice. The vegetation canopy is allowed to intercept precipitation and re-evaporation. Runoff from the surface and drainage from the bottom layer are also calculated.

- **Chemistry**
  Ozone is a prognostic variable that is updated in the analysis and transported in the model. The sources and sinks of ozone are computed using zonally averaged seasonally varying production and destruction rates provided by NASA/GSFC.

References

Alpert, J.C., M. Kanamitsu, P.M. Caplan, J.G. Sela, G.H. White, and E. Kalnay, 1988: Mountain induced gravity wave drag parameterization in the NMC medium-range model. Preprints of the Eighth Conference on Numerical Weather Prediction, Baltimore, MD, American Meteorological Society, 726-733.

Arakawa, A. and W. H. Shubert, 1974: Interaction of a Cumulus Ensemble with the Large-Scale Environment, Part I. J. Atmos. Sci., 31, 674-704.

Asselin, R., 1972: Frequency filter for time integrations. Mon. Wea. Rev., 100, 487-490.

Betts, A.K., S.-Y. Hong and H.-L. Pan, 1996: Comparison of NCEP-NCAR Reanalysis with 1987 FIFE data. Mon. Wea. Rev., 124, 1480-1498

Briegleb, B. P., P. Minnus, V. Ramanathan, and E. Harrison, 1986: Comparison of regional clear-sky albedo inferred from satellite observations and model computations. J. Clim. and Appl. Meteo., 25, 214-226.

Charnock, H., 1955: Wind stress on a water surface. Quart. J. Roy. Meteor. Soc., 81, 639-640.

Chen, F., K. Mitchell, J. Schaake, Y. Xue, H.-L. Pan, V. Koren, Q. Y. Duan, M. Ek, and A. Betts, 1996: Modeling of land surface evaporation by four schemes and comparison with FIFE observations. J. Geophys. Res., 101, D3, 7251-7268.

Chou, M-D, 1990: Parameterizations for the absorption of solar radiation by O2 and CO2 with application to climate studies. J. Climate, 3, 209-217.

Chou, M-D, 1992: A solar radiation model for use in climate studies. J. Atmos. Sci., 49, 762-772.

Chou, M-D and K-T Lee, 1996: Parameterizations for the absorption of solar radiation by water vapor and ozone. J. Atmos. Sci., 53, 1204-1208.

Chou, M.D., M. J. Suarez, C. H. Ho, M. M. H. Yan, and K. T. Lee, 1998: Parameterizations for cloud overlapping and shortwave single scattering properties for use in general circulation and cloud ensemble models. J. Climate, 11, 202- 214.

Clough, S.A., M.J. Iacono, and J.-L. Moncet, 1992: Line-by-line calculations of atmospheric fluxes and cooling rates: Application to water vapor. J. Geophys. Res., 97, 15761-15785.

Dorman, J.L., and P.J. Sellers, 1989: A global climatology of albedo, roughness length and stomatal resistance for atmospheric general circulation models as represented by the Simple Biosphere model (SiB). J. Appl. Meteor., 28, 833-855.

Ebert, E.E., and J.A. Curry, 1992: A parameterization of ice cloud optical properties for climate models. J. Geophys. Res., 97, 3831-3836.

Fu, Q., 1996: An accurate parameterization of the solar radiative properties of cirrus clouds for climate models. J. Climate, 9, 2058-2082.

Hess, M., P. Koepke, and I. Schult, 1998: Optical properties of aerosols and clouds: The software package OPAC. Bull. Am. Meteor. Soc., 79, 831-844.

Grell, G. A., 1993: Prognostic Evaluation of Assumprions Used by Cumulus Parameterizations. Mon. Wea. Rev., 121, 764-787.

Grumbine, R. W., 1994: A sea-ice albedo experiment with the NMC medium range forecast model. Weather and Forecasting, 9, 453-456.

Hong, S.-Y. and H.-L. Pan, 1996: Nonlocal boundary layer vertical diffusion in a medium-range forecast model. Mon. Wea. Rev., 124, 2322-2339.

Hong, S.-Y., 1999: New global orography data sets. NCEP Office Note #424.

Hou, Y-T, K. A. Campana and S-K Yang, 1996: Shortwave radiation calculations in the NCEP's global model. International Radiation Symposium, IRS-96, August 19-24, Fairbanks, AL.

Hou, Y.-T., S. Moorthi, and K.A. Campana, 2002: Parameterization of solar radiation transfer in the NCEP models. NCEP Office Note 441.

Hu, Y.X., and K. Stamnes, 1993: An accurate parameterization of the radiative properties of water clouds suitable for use in climate models. J. Climate, 6, 728-742.

Joseph, D., 1980: Navy 10' global elevation values. National Center for Atmospheric Research notes on the FNWC terrain data set, 3 pp.

Kalnay, E. and M. Kanamitsu, 1988: Time Scheme for Strongly Nonlinear Damping Equations. Mon. Wea. Rev., 116, 1945-1958.

Kalnay, M. Kanamitsu, and W.E. Baker, 1990: Global numerical weather prediction at the National Meteorological Center. Bull. Amer. Meteor. Soc., 71, 1410-1428.

Kanamitsu, M., 1989: Description of the NMC global data assimilation and forecast system. Wea. and Forecasting, 4, 335-342.

Kanamitsu, M., J.C. Alpert, K.A. Campana, P.M. Caplan, D.G. Deaven, M. Iredell, B. Katz, H.-L. Pan, J. Sela, and G.H. White, 1991: Recent changes implemented into the global forecast system at NMC. Wea. and Forecasting, 6, 425-435.

Kim, Y-J and A. Arakawa, 1995: Improvement of orographic gravity wave parameterization using a mesoscale gravity wave model. J. Atmos. Sci. 52, 11, 1875-1902.

Koepke, P., M. Hess, I. Schult, and E.P. Shettle, 1997: Global aerosol data set. MPI Meteorologie Hamburg Report No. 243, 44 pp.

Leith, C.E., 1971: Atmospheric predictability and two-dimensional turbulence. J. Atmos. Sci., 28, 145-161.

Lindzen, R.S., 1981: Turbulence and stress due to gravity wave and tidal breakdown. J. Geophys. Res., 86, 9707-9714.

Matthews, E., 1985: "Atlas of Archived Vegetation, Land Use, and Seasonal Albedo Data Sets.", NASA Technical Memorandum 86199, Goddard Institute for Space Studies, New York.

Mitchell, K. E. and D. C. Hahn, 1989: Development of a cloud forecast scheme for the GL baseline global spectral model. GL-TR-89-0343, Geophysics Laboratory, Hanscom AFB, MA.

Mlawer, E.J., S.J. Taubman, P.D. Brown, M.J. Iacono, and S.A. Clough, 1997: Radiative transfer for inhomogeneous atmospheres: RRTM, a validated correlated-k model for the longwave. J. Geophys. Res., 102, 16663-16682.

Miyakoda, K., and J. Sirutis, 1986: Manual of the E-physics. [Available from Geophysical Fluid Dynamics Laboratory, Princeton University, P.O. Box 308, Princeton, NJ 08542.]

NMC Development Division, 1988: Documentation of the research version of the NMC Medium-Range Forecasting Model. NMC Development Division, Camp Springs, MD, 504 pp.

Pan, H-L. and L. Mahrt, 1987: Interaction between soil hydrology and boundary layer developments. Boundary Layer Meteor., 38, 185-202.

Pan, H.-L. and W.-S. Wu, 1995: Implementing a Mass Flux Convection Parameterization Package for the NMC Medium-Range Forecast Model. NMC Office Note, No. 409, 40pp. [Available from NCEP, 5200 Auth Road, Washington, DC 20233]

Pierrehumbert, R.T., 1987: An essay on the parameterization of orographic wave drag. Observation, Theory, and Modeling of Orographic Effects, Vol. 1, Dec. 1986, European Centre for Medium Range Weather Forecasts, Reading, UK, 251-282.

Ramsay, B.H., 1998: The interactive multisensor snow and ice mapping system. Hydrol. Process. 12, 1537-1546.

Reynolds, R. W. and T. M. Smith, 1994: Improved global sea surface temperature analyses. J. Climate, 7, 929-948.

Roberts, R.E., J.A. Selby, and L.M. Biberman, 1976: Infrared continuum absorption by atmospheric water vapor in the 8-12 micron window. Appl. Optics., 15, 2085-2090.

Schwarzkopf, M.D., and S.B. Fels, 1985: Improvements to the algorithm for computing CO2 transmissivities and cooling rates. J. Geophys. Res., 90, 10541-10550.

Schwarzkopf, M.D., and S.B. Fels, 1991: The simplified exchange method revisited: An accurate, rapid method for computation of infrared cooling rates and fluxes. J. Geophys. Res., 96, 9075-9096.

Sela, J., 1980: Spectral modeling at the National Meteorological Center, Mon. Wea. Rev., 108, 1279-1292.

Slingo, A., 1989: A GCM parameterization for the shortwave radiative properties of water clouds. J. Atmos. Sci.,46, 1419-1427.

Slingo, J.M., 1987: The development and verification of a cloud prediction model for the ECMWF model. Quart. J. Roy. Meteor. Soc., 113, 899-927.

Slingo, A., 1989: A GCM parameterization for the shortwave radiative properties of water clouds. J. Atmos. Sci.,46, 1419-1427.

Stephens, G. L., 1984: The parameterization of radiation for numerical weather prediction and climate models. Mon. Wea. Rev., 112, 826-867.

Staylor, W. F. and A. C. Wilbur, 1990: Global surface albedos estimated from ERBE data. Preprints of the Seventh Conference on Atmospheric Radiation, San Francisco CA, American Meteorological Society, 231-236.

Sundqvist, H., E. Berge, and J. E. Kristjansson, 1989: Condensation and cloud studies with mesoscale numerical weather prediction model. Mon. Wea. Rev., 117, 1641- 1757.

Tiedtke, M., 1983: The sensitivity of the time-mean large-scale flow to cumulus convection in the ECMWF model. ECMWF Workshop on Convection in Large-Scale Models, 28 November-1 December 1983, Reading, England, pp. 297-316.

Troen, I. and L. Mahrt, 1986: A simple model of the atmospheric boundary layer; Sensitivity to surface evaporation. Bound.-Layer Meteor., 37, 129-148

Xu, K. M., and D. A. Randall, 1996: A semiempirical cloudiness parameterization for use in climate models. J. Atmos. Sci., 53, 3084-3102.

Zeng, X., M. Zhao, and R.E. Dickinson, 1998: Intercomparison of bulk aerodynamical algorithms for the computation of sea surface fluxes using TOGA COARE and TAO data. J. Climate, 11, 2628-2644.

Zhao, Q. Y., and F. H. Carr, 1997: A prognostic cloud scheme for operational NWP models. Mon. Wea. Rev., 125,1931-1953.

APPENDIX B

Global Forecast System Modification History

(from http://www.emc.ncep.noaa.gov/gmb/STATS/html/model_changes.html)

MRF/AVN/GDAS changes since 1991

Many of the more recent changes (TPB > 442) are documented in Global Modeling Branch Technical Procedures Bulletins(TPB)
Another source of information is the Parallel run home page

- Pre-1991
  - 08/80: R30L12
  - 10/83: R40L12
  - 04/85: MRF85 R40L18 - GFDL physics
  - 06/86: MRF86 R40L18 - convection to tropopause
  - 08/87: MRF87 T80L18 - diurnal cycle, moisture all layers
  - 01/88: MRF88 T80L18 - interactive clouds
- 03/91: T80L18 to T126L18, silhouette to mean orog, new SST, marine stratus, reduced horizontal diffusion
- 06/91: SSI analysis
- 08/93: Arakawa-Schubert convection, 28 layers
- 01/95: SSM/I PW over sea; analysis changes; various physics changes (TPB 417 (not on Web))
- 10/95: Satellite radiances instead of T retrievals; ERS-1 winds; physics changes (TPB 428 (not on Web))
- 06/96: Adjustments to PBL and convection
- 02/97: SSM/I water vapor discontinued
- 11/97: Elimination of "valley snow" and other small changes (TPB 443)
- 01/98: TOVS-1b radiances; vertical diffusion inc in free atmosphere (TPB 445)
- 06/15/98: T170L42 to day 3.5; physics changes; 3D ozone; analysis changes (See TPB 449)
- 07/22/98: First emergency implementation: fix to convection, horizontal diffuse, plant evap: see last section of TPB 449 above.
- 10/06/98: Second emergency implementation: Back to T126L28, better fits to data, more iterations in analysis, physics changes (TPB 450)
- 12/01/98: Snow resolution increased from 2.0 to 0.5 degrees; snow depth field added; snow depth no longer estimated by model
- 01/08/99: Use of VAD winds eliminated due to problems with light wind speeds
- 03/08/99: Introduction of high-resolution data from the NOAA-15 satellite. The data are radiances from the AMSU-A and HIRS-3 instruments. The NOAA-11 Satellite is no longer providing AMSU data and will soon be unable to provide HIRS data.
- 01/24/2000: Resolution upgraded from T126L28 to T170L42, restoring the resolution used from June 15 through Oct 5, 1998. No other changes in the forecast/analysis

system. The MRF is run at T170L42 through day 7, then at T62L28 through day 16. The AVN is run at T170L42 out to 84 hours four times a day. (See TPB 452)

- 05/17/2000: AVN available out to 126h at full (T170) resolution at 00Z and 12Z.
- 06/27/2000: Resolution of ensemble members increased from T62 to T126 for first 60 hours of forecast.
- 07/06/2000: Hurricanes and tropical storms in the model's guess field are relocated to the official Tropical Prediction Center position in each 6-hour analysis cycle. (TPB 472)
- 08/29/2000 18Z: Data cutoff time for the 06Z and 18Z final analysis (FNL) extended from 4 hours to 6 hours.
- 10/01/2000 06Z: Package of minor changes:
  Observations and analysis: New obs error diagnosis, rawinsonde radiation correction, effects of balloon drift in time and space included
  Forecast and post processing: Improved orography, reduced Gaussian grid over polar regions, new surface albedo climatology, single scattering albedo adjusted
- 11/01/2000 12Z: ERA wind data erratic; turned off.
- 02/13/2001 12Z: Satellite radiance and moisture analysis changes plus smoothed output MSLP.
- 05/15/01 12Z: (See TPB 484).
  - Inclusion of cloud condensate as a history variable
  - Use of the cloud condensate in the calculation of radiative transfer
  - Stronger quality control for AMSU radiances
  - Momentum mixing included in deep convection
  - Refinement of hurricane relocation algorithm
  - SST anomaly damped toward climatology during forecast, with 90-day relaxation time
- 06/27/01 12Z: Minor increase in vegetation fraction.
- 07/24/01 12Z: The data source for the daily 1-degree sea surface temperature analysis is changed from NOAA-14 to NOAA-16 due to instrument drift.
- 08/15/2001 06Z: Package of minor changes:
  Observations and analysis: Higher resolution sea ice mask
  Forecast and post processing: Bug corrections in gravity wave drag, randomization of convective cloud tops, land surface evaporation with trace snow cover; minor adjustments in effective radius for ice crystals, autoconversion rate for ice, evaporation of falling precip, and critical RH for condensation
- 10/09/2001: Snow depth is updated daily at 00Z from observations; at 06Z, 12Z and 18Z the model guess is used. Formerly the same 00Z update was reinserted in each of the day's cycles.
- 01/15/2002 12Z: Quikscat surface winds included.
- 03/05/2002 : AVN runs four times a day out to 384 hours. Resolution is T170L42 to 180h, thereafter T62L28.
- 04/23/2002 00Z: MRF is replaced by the 00Z AVN. Look-alike MRF grids will still be available daily for several months on the ftp server at ftp://ftpprd.ncep.noaa.gov/pub/data/nccf/com/mrf/para/
- Sept-Oct 2002: Name changes: The AVN will be referred to as the Global Forecast System model (GFS).

- 10/29/02 12Z:(See draft TPB)
  - Resolution change
    old: T170L42 to 180h, T62L28 to 384h
    new: T254L64 to 84h, T170L42 to 180h, T126L28 to 384h
  - Analysis and observation changes: background error recomputed, AMSU-A channels 12 and 13 from NOAA-15 and NOAA-16 and HIRS from NOAA-16 used, METAR surface pressure observations used, divergence tendency constraint in tropics turned off.
- 03/11/03 12Z: NOAA 17 1B radiances assimilated, NOAA-16 AMSU-A radiances restored, QuikSCAT winds superobbed at 0.5 degrees.
- 08/28/03 12Z: RRTM longwave radiation from AER installed: More trace gases (CH_4, N_2O, CFC's) and better tropospheric water vapor absorption.
- 10/28/03 12Z: NOAA-17 AMSU-A radiances turned off
- 11/20/03 12Z: Package of minor analysis changes (see description)
- 12/09/03 12Z: Vertical diffusion added to ozone
- 02/24/04 12Z: Mountain blocking: Parameterization of the separation of airflow in the vertical with passage over mountainous terrain.
- 03/09/04 12Z: Ensemble run 4 times daily. Resolution T126 0-180 h, then T62 to 384 h.
- 05/25/04 12Z: Turn off NOAA-16 HIRS/3 observations
- 05/31/05 12Z:
  - Resolution change:
    old: T254L64 to 84h, T170L42 to 180h, T126L28 to 384h
    new: T382L64 to 180h, T190L64 to 384h
  - Increase mountain blocking, decrease vertical diffusion and modify sea ice.
- 06/14/05 12Z: Increase canopy resistance of vegetation
- 07/07/05 12Z: Correct error in temperature near top of model

APPENDIX C

AIRS Channels used by NWP

airs channel property file:
L2.chan_prop.2003.11.19.v8.0.0.anc
idx1 = index in 281 set
idx2 = index in original AIRS set
freq = most recent frequency assessment
T1 = used for temperature retrievals before water ret
T2 = used for temperature retrievals after water ret
STR = used for stratospheric temperature (never sensitive to clouds
SRF = used for surface retrievals
H2O = used for water retrievals
O3 = used for ozone retrievals
fixed = surface to space transmittance for fixed gases, US STD
water = surface to space transmittance for water, US STD
ozone = surface to space transmittance for ozone, US STD
nedt = NEDT at T=250K, K, from AIRS BB measurements
rtafit = RTA fitting error, K, as computed by UMBC
tuning = Tuning values, K, as determined by GSFC
moderr = Empirical model error, K, as determined by GSFC
Cij = % spatial correlation (1.0 = perfect)
comment = why chl is considered BAD by AIRS Science Team
comment = * = 251 channels, # = 152 operational channels, & = 119 shortwave channels

idx1	idx2	freq	...TEMP...		SRF	H2O	O3	fixed	water	ozone	nedt	rtafit	tuning	moderr	Cij	comment
1	1	649.61	T1	T2	U	.	.	0.0000	0.2939	0.9784	0.6490	0.0190	0.1769	1.2263	-0.0288	*
2	6	650.81	T1	T2	U	.	.	0.0000	0.2161	0.9685	0.6540	0.0150	0.2774	0.7779	-0.0284	*
3	7	651.05	T1	T2	.	.	.	0.0000	0.2163	0.9605	0.6850	0.0180	0.2298	1.7215	-0.0287	*
4	10	651.77	T1	T2	.	.	.	0.0000	0.3802	0.9789	0.6480	0.0180	1.2889	0.8911	-0.0258	*
5	11	652.01	T1	T2	U	.	.	0.0000	0.3806	0.9812	0.6780	0.0160	1.1173	0.7912	-0.0274	*
6	15	652.97	T1	T2	.	.	.	0.0000	0.3073	0.9849	0.6360	0.0130	0.4672	2.0574	-0.0260	*#
7	16	653.21	T1	T2	.	.	.	0.0000	0.3055	0.9781	0.6720	0.0130	0.9485	1.2029	-0.0262	*
8	17	653.45	T1	T2	U	.	.	0.0000	0.3059	0.9820	0.6230	0.0160	1.1705	0.7017	-0.0285	*
9	20	654.17	T1	T2	.	.	.	0.0000	0.3070	0.9868	0.5830	0.0150	0.4444	1.4967	-0.0288	*#
10	21	654.42	T1	T2	.	.	.	0.0000	0.3056	0.9870	0.6230	0.0080	0.4470	1.9196	-0.0269	*#
11	22	654.66	T1	T2	U	.	.	0.0000	0.2903	0.9795	0.6050	0.0100	0.8785	1.3168	-0.0257	*#
12	24	655.14	T1	T2	.	.	.	0.0000	0.2912	0.9760	0.5850	0.0160	0.9366	0.7124	-0.0249	
13	27	655.87	T1	T2	.	.	.	0.0000	0.2921	0.9482	0.5810	0.0130	0.2250	1.7352	-0.0259	*#
14	28	656.12	T1	T2	.	.	.	0.0000	0.3054	0.9563	0.5660	0.0090	0.6245	1.5538	-0.0245	*#
15	30	656.60	T1	T2	U	.	.	0.0000	0.5801	0.9618	0.5470	0.0160	1.1753	0.6125	-0.0286	*
16	36	658.07	T1	T2	U	.	.	0.0000	0.6158	0.9841	0.5190	0.0180	1.3036	0.6810	-0.0282	*
17	39	658.81	T1	T2	.	.	.	0.0000	0.6650	0.9784	0.4980	0.0110	0.5177	1.6366	-0.0307	*
18	40	659.05	T1	T2	.	.	.	0.0000	0.6695	0.9756	0.5030	0.0090	0.5630	1.0642	-0.0299	*#
19	42	659.54	T1	T2	U	.	.	0.0000	0.5028	0.9644	0.4810	0.0180	1.4061	0.5226	-0.0301	*
20	51	661.77	T1	T2	.	.	.	0.0000	0.5142	0.9123	0.4830	0.0120	0.4267	1.0369	-0.0292	*
21	52	662.02	T1	T2	.	.	.	0.0000	0.5197	0.9017	0.4780	0.0150	0.2825	1.0730	-0.0302	*#
22	54	662.51	T1	T2	U	.	.	0.0000	0.5150	0.9102	0.4790	0.0240	0.2612	0.5150	-0.0289	*
23	55	662.76	T1	T2	U	.	.	0.0000	0.5175	0.9200	0.4690	0.0170	0.2311	0.4455	-0.0298	*
24	56	663.01	T1	T2	U	.	.	0.0000	0.5156	0.9283	0.4650	0.0160	0.1318	0.5555	-0.0307	*
25	59	663.76	T1	T2	.	.	.	0.0000	0.5101	0.9753	0.4510	0.0240	0.1194	1.1321	-0.0321	*
26	62	664.51	T1	T2	.	.	.	0.0000	0.5083	0.9375	0.4470	0.0160	0.6351	0.8687	-0.0333	*
27	63	664.76	T1	T2	.	.	.	0.0000	0.5083	0.9378	0.4520	0.0180	0.2665	0.8006	-0.0331	*
28	68	666.01	T1	T2	.	.	.	0.0000	0.5103	0.9272	0.4510	0.0110	0.6972	0.7366	-0.0301	*

29	69	666.26	T1	T2	.	.	.	.	0.0000	0.5104	0.9334	0.4450	0.0060	0.4642	0.8417	-0.0306	*#
30	71	666.77	T1	T2	.	.	.	.	0.0000	0.5113	0.9303	0.4290	0.0130	0.4095	0.4311	-0.0329	*
31	72	667.02	T1	T2	.	.	.	.	0.0000	0.5116	0.9158	0.4240	0.0090	0.5803	0.5681	-0.0330	*#
32	73	667.27	T1	T2	U	.	.	.	0.0000	0.5119	0.9129	0.4260	0.0330	1.0005	0.5654	-0.0282	
33	74	667.52	T1	T2	U	.	.	.	0.0000	0.5121	0.9232	0.4240	0.0240	0.4619	0.5632	-0.0245	
34	75	667.78	T1	T2	U	.	.	.	0.0000	0.5125	0.9280	0.4270	0.0270	0.5730	0.2634	-0.0235	
35	76	668.03	T1	T2	U	.	.	.	0.0000	0.5129	0.9276	0.4190	0.0330	0.8853	0.4054	-0.0252	
36	77	668.28	T1	T2	U	.	.	.	0.0000	0.5132	0.9275	0.4140	0.0320	0.7975	0.3598	-0.0282	
37	78	668.53	T1	T2	U	.	.	.	0.0000	0.5136	0.9273	0.4130	0.0370	0.7410	0.3542	-0.0285	
38	79	668.79	T1	T2	U	.	.	.	0.0000	0.5141	0.9277	0.4290	0.0360	0.8186	0.3811	-0.0274	
39	80	669.04	T1	T2	U	.	.	.	0.0000	0.5143	0.9291	0.4230	0.0290	1.0237	0.4046	-0.0288	
40	82	669.55	T1	T2	U	.	.	.	0.0000	0.5152	0.9279	0.3930	0.0290	1.1738	0.4540	-0.0333	
41	83	669.80	T1	T2	U	.	.	.	0.0000	0.5157	0.9277	0.4100	0.0260	1.0249	0.4353	-0.0319	
42	84	670.06	T1	T2	U	.	.	.	0.0000	0.5161	0.9325	0.4990	0.0330	0.5355	0.1216	-0.0224	
43	86	670.57	T1	T2	.	.	.	.	0.0000	0.5126	0.9356	0.4280	0.0280	0.3483	0.2062	-0.0306	
44	92	672.10	T1	T2	.	.	.	.	0.0000	0.5216	0.9065	0.4190	0.0140	0.1515	0.1744	-0.0319	*#
45	93	672.36	T1	T2	.	.	.	.	0.0000	0.5220	0.9060	0.4210	0.0110	0.4863	0.2051	-0.0316	*#
46	98	673.64	T1	T2	.	.	.	.	0.0000	0.5692	0.9295	0.4230	0.0120	0.5050	0.2549	-0.0307	*#
47	99	673.90	T1	T2	.	.	.	.	0.0000	0.5700	0.9668	0.4110	0.0080	0.5976	0.2752	-0.0327	*#
48	101	674.41	T1	T2	.	.	.	.	0.0000	0.5616	0.9642	0.4260	0.0200	1.1247	0.1393	-0.0278	
49	104	675.19	T1	T2	.	.	.	.	0.0000	0.6010	0.9394	0.4300	0.0090	0.3891	0.2540	-0.0269	*#
50	105	675.45	T1	T2	.	.	.	.	0.0000	0.5909	0.9282	0.4530	0.0090	0.7016	0.2480	-0.0240	*#
51	108	676.23	T1	T2	.	.	.	.	0.0000	0.5928	0.9314	0.4280	0.0170	0.7167	0.1293	-0.0268	*
52	110	676.74	T1	T2	.	.	.	.	0.0000	0.0000	0.9621	0.4450	0.0090	0.3726	0.2936	-0.0243	*#
53	111	677.01	T1	T2	.	.	.	.	0.0000	0.0000	0.9229	0.4470	0.0080	0.5201	0.2883	-0.0244	*#
54	113	677.53	T1	T2	U	.	.	.	0.0000	0.0000	0.9216	0.4020	0.0190	1.2921	0.1264	-0.0296	*
55	116	678.31	T1	T2	.	.	.	.	0.0000	0.1398	0.9602	0.4340	0.0110	0.3583	0.2540	-0.0263	*#
56	117	678.57	T1	T2	.	.	.	.	0.0000	0.2264	0.9328	0.4490	0.0110	0.4854	0.2538	-0.0248	*#
57	123	680.14	T1	T2	.	.	.	.	0.0000	0.5712	0.9169	0.4060	0.0100	0.3647	0.2641	-0.0300	*#
58	124	680.40	T1	T2	.	.	.	.	0.0000	0.5721	0.9123	0.4290	0.0110	0.7168	0.2260	-0.0269	*
59	128	681.46	T1	T2	.	.	.	.	0.0000	0.5665	0.8505	0.4400	0.0140	0.3772	0.2121	-0.0262	*#
60	129	681.72	T1	T2	.	.	.	.	0.0000	0.5419	0.9353	0.4270	0.0140	0.3237	0.3608	-0.0276	*#
61	138	689.49	T1	T2	.	.	.	.	0.0000	0.7252	0.9593	0.3500	0.0350	0.2385	0.2200	-0.0392	*#
62	139	689.76	T1	T2	.	.	.	.	0.0000	0.7053	0.9538	0.3520	0.0300	0.1276	0.2290	-0.0372	*#
63	144	691.12	T1	T2	.	.	.	.	0.0000	0.6884	0.9019	0.3160	0.0120	0.1359	0.2454	-0.0429	*#
64	145	691.39	T1	T2	.	.	.	.	0.0000	0.6571	0.9175	0.3620	0.0170	0.1312	0.2601	-0.0333	*#
65	150	692.76	T1	T2	.	.	.	.	0.0000	0.3030	0.8608	0.3690	0.0120	0.1496	0.2126	-0.0328	*#
66	151	693.03	T1	T2	.	.	.	.	0.0000	0.3897	0.9109	0.3680	0.0190	0.1108	0.2517	-0.0317	*#
67	156	694.40	T1	T2	.	.	.	.	0.0000	0.0516	0.9166	0.3180	0.0150	0.1135	0.2231	-0.0411	*#
68	157	694.67	T1	T2	.	.	.	.	0.0000	0.2290	0.9550	0.3310	0.0130	0.0851	0.1905	-0.0370	*#
69	159	695.22	T1	T2	.	.	.	.	0.0000	0.2478	0.9545	0.3080	0.0140	0.6981	0.2130	-0.0419	*
70	162	696.05	T1	T2	.	.	.	.	0.0000	0.2186	0.9270	0.3300	0.0270	0.1711	0.2323	-0.0359	*#
71	165	696.88	T1	T2	.	.	.	.	0.0000	0.2006	0.9412	0.3160	0.0150	0.5148	0.2111	-0.0390	*
72	168	697.71	T1	T2	.	.	.	.	0.0000	0.3007	0.9256	0.3190	0.0230	0.1492	0.2346	-0.0383	*#
73	169	697.99	T1	T2	.	.	.	.	0.0000	0.6667	0.9398	0.2830	0.0210	0.0376	0.2073	-0.0493	*#
74	170	698.27	T1	T2	.	.	.	.	0.0000	0.6030	0.9478	0.2860	0.0150	0.4924	0.1952	-0.0482	*
75	172	698.82	T1	T2	.	.	.	.	0.0000	0.6132	0.9495	0.2810	0.0250	0.2479	0.2264	-0.0490	*#
76	173	699.10	T1	T2	.	.	.	.	0.0000	0.6309	0.9539	0.2800	0.0290	0.3282	0.1957	-0.0508	*#
77	174	699.38	T1	T2	.	.	.	.	0.0000	0.6940	0.9550	0.2980	0.0160	0.1909	0.2018	-0.0446	*#
78	175	699.66	T1	T2	.	.	.	.	0.0000	0.6914	0.9381	0.2900	0.0100	0.1094	0.2576	-0.0458	*#
79	177	700.22	T1	T2	.	.	.	.	0.0000	0.6870	0.9517	0.2880	0.0130	0.5118	0.1904	-0.0462	*
80	179	700.78	T1	T2	.	.	.	.	0.0000	0.6871	0.9554	0.2810	0.0460	0.2062	0.1623	-0.0495	*#
81	180	701.06	T1	T2	.	.	.	.	0.0000	0.7039	0.9451	0.2790	0.0190	0.0974	0.1789	-0.0494	*#
82	182	701.62	T1	T2	.	.	.	.	0.0000	0.7343	0.9340	0.2920	0.0170	0.3218	0.2211	-0.0464	*
83	185	702.46	T1	T2	.	.	.	.	0.0000	0.6759	0.9357	0.2910	0.0280	0.2126	0.1934	-0.0441	*#
84	186	702.74	T1	T2	.	.	.	.	0.0000	0.5732	0.9437	0.2960	0.0190	0.1383	0.1637	-0.0442	*#

85	190	703.87	T1	T2	.	.	.	.	0.0000	0.6739	0.9572	0.2780	0.0520	0.3350	0.1511	-0.0444	*#
86	192	704.44	T1	T2	.	.	.	.	0.0000	0.7062	0.9305	0.2850	0.0590	0.2084	0.1635	-0.0451	*#
87	198	706.14	T1	T2	.	.	.	.	0.0002	0.6194	0.9448	0.2560	0.0250	0.2828	0.1408	-0.0606	*#
88	201	706.99	T1	T2	.	.	.	.	0.0001	0.5940	0.9224	0.2600	0.0410	0.2941	0.1409	-0.0558	*#
89	204	707.85	T1	T2	.	.	.	.	0.0007	0.4563	0.9306	0.2650	0.0420	0.2439	0.1621	-0.0518	*#
90	207	708.71	T1	T2	.	.	.	.	0.0002	0.6550	0.8260	0.2940	0.0800	0.3618	0.1613	-0.0425	*#
91	210	709.57	T1	T2	.	.	.	.	0.0015	0.7110	0.9357	0.3000	0.0550	0.3561	0.1584	-0.0414	*#
92	215	711.01	T1	T2	.	.	.	.	0.0060	0.6842	0.9430	0.2600	0.0400	0.1992	0.1367	-0.0507	*#
93	216	711.29	T1	T2	.	.	.	.	0.0035	0.6743	0.9429	0.2680	0.0520	0.2452	0.1520	-0.0469	#
94	221	712.74	T1	T2	.	.	.	.	0.0387	0.6643	0.9224	0.2590	0.0490	0.2211	0.1664	-0.0481	*#
95	226	714.19	T1	T2	.	.	.	.	0.0688	0.4849	0.9051	0.2380	0.0510	0.3075	0.1592	-0.0639	*#
96	227	714.48	T1	T2	.	.	.	.	0.0751	0.5501	0.9220	0.2410	0.0740	0.2580	0.1396	-0.0653	*#
97	232	715.94	T1	T2	.	.	.	.	0.1268	0.7609	0.9110	0.2610	0.0320	0.1736	0.1498	-0.0555	*#
98	252	721.84	T1	T2	.	.	.	.	0.0652	0.7437	0.9473	0.2560	0.0290	0.1610	0.1320	-0.0694	*#
99	253	722.14	T1	T2	.	.	.	.	0.0897	0.7680	0.9462	0.2430	0.0510	0.1353	0.1364	-0.0750	*#
100	256	723.03	T1	T2	.	.	.	.	0.2375	0.7920	0.8857	0.2440	0.0440	0.0168	0.1714	-0.0789	*#
101	257	723.33	T1	T2	.	.	.	.	0.2521	0.7920	0.8760	0.2430	0.0300	0.0097	0.1935	-0.0789	*#
102	261	724.52	T1	T2	.	.	.	.	0.2850	0.7957	0.9585	0.2460	0.0370	-0.0245	0.1890	0.0067	*#
103	262	724.82	T1	T2	.	.	.	.	0.2770	0.7937	0.9764	0.2460	0.0600	-0.0293	0.1637	-0.0845	*#
104	267	726.33	T1	T2	.	.	.	.	0.2807	0.7934	0.9702	0.2640	0.0310	0.0029	0.1720	-0.0817	*#
105	272	727.83	T1	T2	.	.	.	.	0.2747	0.7699	0.9668	0.2780	0.0200	0.0845	0.1979	-0.0599	*#
106	295	734.15	T1	T2	.	.	.	.	0.2174	0.7957	0.9740	0.3480	0.0300	0.1138	0.2497	0.0404	*#
107	299	735.38	T1	T2	.	.	.	.	0.1728	0.7971	0.9665	0.2420	0.0470	0.0966	0.1685	0.0401	*#
108	300	735.69	T1	T2	.	.	.	.	0.2178	0.8041	0.9662	0.2380	0.0260	0.0821	0.1517	0.0404	*#
109	305	737.24	T1	T2	.	.	.	.	0.2144	0.8037	0.9366	0.3840	0.0240	bad	bad	0.0402	*#
110	310	738.79	T1	T2	.	.	.	.	0.2101	0.7858	0.9694	0.3690	0.0240	0.0213	0.1685	0.0408	*#
111	321	742.23	T1	T2	.	.	.	.	0.0543	0.5592	0.9669	0.5050	0.0790	0.1012	0.2711	0.0403	*#
112	325	743.48	T1	T2	.	.	.	.	0.3402	0.6753	0.9392	0.3220	0.0620	-0.0421	0.2054	0.0423	*#
113	333	746.01	T1	T2	.	.	.	.	0.5241	0.7657	0.9838	0.2450	0.0260	-0.2129	0.2446	0.0436	*#
114	338	747.60	T1	T2	.	.	.	.	0.6030	0.7339	0.9890	0.3640	0.0270	-0.1540	0.2299	0.0446	*#
115	355	753.06	.	.	.	.	.	.	0.2913	0.7410	0.9734	0.3130	0.0620	-0.0527	0.1989	0.0448	*#
116	362	755.33	T1	. T2	.	.	.	.	0.7829	0.6264	0.9828	0.2330	0.0160	-0.1592	0.2414	0.0454	*#
117	375	759.57	.	T2	S	.	.		0.8896	0.8333	0.9837	0.2330	0.0070	-0.4946	0.3357	0.0475	*#
118	453	793.17	.	.	.	S	H2O	.	0.9238	0.7920	0.9954	0.2580	0.0080	-0.4314	0.2656	0.0326	*#
119	475	801.10	.	.	.	S	.	.	0.9850	0.8352	0.9978	0.2730	0.0040	-0.5382	0.3144	0.0327	*#
120	484	804.39	.	.	.	.	H2O	.	0.9716	0.7996	0.9986	0.3820	0.0070	-0.4839	0.3339	0.0311	*#
121	497	809.18	.	.	.	.	H2O	.	0.9601	0.8393	0.9987	0.3350	0.0050	-0.4490	0.3119	0.0374	*#
122	528	820.83	.	.	.	S	.	.	0.9920	0.8817	0.9993	0.4140	0.0040	-0.5473	0.2850	0.0335	*#
123	587	843.91	.	.	.	S	.	.	0.9773	0.8935	0.9999	0.2990	0.0010	-0.4656	0.2714	0.0305	*#
124	672	871.29	.	.	.	.	H2O	.	0.9929	0.5170	1.0000	0.2060	0.0120	-0.1984	0.2083	0.0444	*#
125	787	917.31	.	.	.	S	.	.	0.9774	0.9203	1.0000	0.1100	0.0010	-0.4310	0.2981	0.1517	*#
126	791	918.75	.	.	.	S	.	.	0.9746	0.8547	1.0000	0.1250	0.0060	-0.3491	0.2810	0.1609	*#
127	843	937.91	.	.	.	S	H2O	.	0.9922	0.9261	1.0000	0.1280	0.0020	-0.4581	0.2858	0.2245	*#
128	870	948.18	.	.	.	S	.	.	0.9526	0.6151	0.9999	0.1420	0.0140	-0.2780	0.3022	0.2475	*#
129	914	965.43	.	.	.	S	.	.	0.9860	0.9334	0.9989	0.1210	0.0060	-0.4188	0.3242	0.2869	*#
130	950	979.13	.	.	.	S	.	.	0.9835	0.9376	0.9868	0.0900	0.0220	-0.4913	0.3422	0.2589	*#
131	1003	1001.38	.	.	.	.	.	O3	0.9997	0.9398	0.8662	0.1140	0.0450	-0.5177	0.3731	0.3044	*
132	1012	1005.26	.	.	.	.	.	O3	0.9996	0.9481	0.7565	0.0810	0.0590	-0.5249	0.3451	0.2970	
133	1019	1008.30	.	.	.	.	.	O3	0.9987	0.9490	0.7006	0.0970	0.0610	-0.5436	0.3416	0.3050	
134	1024	1010.48	.	.	.	.	.	O3	0.9990	0.8148	0.6718	0.0940	0.0680	-0.3823	0.3436	0.2782	
135	1030	1013.11	.	.	.	.	.	O3	0.9981	0.9473	0.6260	0.1270	0.0550	-0.2510	0.3159	0.2864	*
136	1038	1016.64	.	.	.	.	.	O3	0.9969	0.9464	0.5163	0.1170	0.0620	-0.3396	0.2824	0.2787	*
137	1048	1021.08	.	.	.	.	.	O3	0.9935	0.9528	0.4304	0.1120	0.0740	-0.4576	0.2826	0.2408	*
138	1069	1030.53	.	.	.	.	.	O3	0.9972	0.8959	0.4819	0.0920	0.1320	-0.4069	0.2988	0.2236	*
139	1079	1035.09	.	.	.	.	.	O3	0.9826	0.9550	0.3417	0.0960	0.0750	-0.7899	0.2519	0.1973	*
140	1082	1036.46	.	.	.	.	.	O3	0.9953	0.9566	0.3481	0.1260	0.0740	-0.6603	0.2355	0.1912	*

```
141 1083  1036.92  . . . . . O3       0.9887 0.9563 0.3207  0.1350  0.0620 -0.8797  0.2379  0.1823  *
142 1088  1039.23  . . . . . O3       0.9504 0.9226 0.2722  0.1330  0.0810 -1.1885  0.2556  0.1706  *
143 1090  1040.15  . . . . . O3       0.9881 0.9321 0.2462  0.0940  0.0870 -1.2808  0.2099  0.1689  *
144 1092  1041.08  . . . . . O3       0.9490 0.9564 0.2335  0.1610  0.1090    bad      bad    0.1652  *
145 1095  1042.47  . . . . . O3       0.9916 0.8999 0.7739  0.2340  0.0490    bad      bad    0.1478  *
146 1104  1056.07  . . . . . O3       0.9351 0.8500 0.2329  0.1750  0.1170    bad      bad    0.3221  *
147 1111  1059.42  . . . . . O3       0.9527 0.9372 0.3586  0.2350  0.0720  0.2686  0.2633  0.3535  *
148 1115  1061.33  . . . . . O3       0.9841 0.9523 0.3890  0.2270  0.0860  0.2527  0.2381  0.3405  *
149 1116  1061.81  . . . . . O3       0.9814 0.9478 0.4396  0.2130  0.0830  0.2305  0.2548  0.3501  *
150 1119  1063.26  . . . . . O3       0.9928 0.9189 0.5553  0.1270  0.1120 -0.0248  0.2697  0.3412  *
151 1120  1063.74  . . . . . O3       0.9932 0.9498 0.5616  0.3140  0.1100    bad      bad    0.3099  *
152 1123  1065.19  . . . . . O3       0.9876 0.9252 0.6996  0.1210  0.0800 -0.2137  0.3173  0.3311  *
153 1130  1068.58  . . . . . O3       0.9648 0.9552 0.8653  0.1180  0.0270 -0.6153  0.3238  0.3389  *
154 1138  1072.48  . . . S  . .       0.9475 0.8929 0.9749  0.1620  0.0200 -0.3843  0.3380  0.3177  *
155 1142  1074.45  . . . . H2O  .     0.9128 0.6520 0.9646  0.1370  0.0510 -0.3121  0.3314  0.3211  * &
156 1178  1092.42  . . .  S  . .      0.9708 0.9465 0.9736  0.1370  0.0080 -0.5452  0.2939  0.2898  * &
157 1199  1103.17  . . .  S  . .      0.9717 0.9433 0.9828  0.2190  0.0050 -0.4837  0.2878  0.2620  * &
158 1206  1106.80  . . . . H2O  .     0.9774 0.4981 0.9799  0.1650  0.0230 -0.2435  0.3194  0.2437  * &
159 1221  1114.64  . . .  S  . .      0.9859 0.9506 0.9748  0.1870  0.0090 -0.6562  0.2740  0.2368  * &
160 1237  1123.13  . . .  S  . .      0.9928 0.9478 0.9727  0.3950  0.0090 -0.6159  0.2685  0.1858  * &
161 1252  1131.20  . . .  S  . .      0.9926 0.9552 0.9594  0.3400  0.0090 -0.4537  0.2688  0.1416  * &
162 1260  1135.54  . . . . H2O  .     0.9889 0.3217 0.9705  0.2660  0.0360 -0.0962  0.2680  0.1195  * &
163 1263  1216.97  . . .  S  . .      0.9406 0.8677 1.0000  0.0850  0.0100 -0.4809  0.2944  0.4301  * &
164 1266  1218.50  . . . . H2O  .     0.9354 0.2297 1.0000  0.1080  0.0270 -0.0789  0.2131  0.4341  * &
165 1285  1228.22  . . .  S  . .      0.9580 0.8959 1.0000  0.0870  0.0150 -0.5476  0.2466  0.4490  * &
166 1301  1236.54  . . .  SH2O  .     0.6803 0.7313 1.0000  0.0810  0.0390 -0.3274  0.2125  0.4805  *#&
167 1304  1238.11  .    T2  H2O  .    0.8048 0.8577 1.0000  0.0800  0.0240 -0.5359  0.2455  0.4872  *#&
168 1329  1251.36  .    T2  H2O  .    0.8354 0.5746 1.0000  0.0880  0.0120 -0.3353  0.2219  0.4542  *#&
169 1371  1285.47  .    T2  H2O  .    0.7823 0.4032 1.0000  0.1040  0.0080 -0.3862  0.2257  0.4447  *#&
170 1382  1291.71  . . . . H2O  .     0.5026 0.4873 1.0000  0.1150  0.0190 -0.3753  0.2200  0.4500  *#&
171 1415  1310.77  . . . . H2O  .     0.6047 0.1929 1.0000  0.1280  0.0230 -0.3313  0.1488  0.4111  *#&
172 1424  1316.06  . . . . H2O  .     0.7461 0.0078 1.0000  0.1330  0.0340 -0.1048  0.1468  0.4013  *#&
173 1449  1330.98  .    T2  H2O  .    0.9052 0.2198 1.0000  0.1630  0.0170 -0.3083  0.1733  0.3472  *#&
174 1455  1334.60  .    T2  H2O  .    0.8833 0.0619 1.0000  0.1700  0.0090 -0.2059  0.1397  0.3379  *#&
175 1466  1339.69  . . . . H2O  .     0.9021 0.0002 1.0000  0.1340  0.0320  0.7912  0.2398  0.4585  *#&
176 1477  1345.31  . . . . H2O  .     0.8982 0.0704 1.0000  0.1420  0.0090 -0.0763  0.1723  0.5101  *#&
177 1500  1357.24  . . . . H2O  .     0.7903 0.0129 1.0000  0.1210  0.0150  0.0366  0.1704  0.5408  *#&
178 1519  1367.25  . . . . H2O  .     0.9593 0.0014 1.0000  0.1100  0.0090  0.2322  0.1518  0.6048  *#&
179 1538  1377.43  . . . . H2O  .     0.9049 0.0000 1.0000  0.1090  0.0170  0.4076  0.1761  0.6360  *#&
180 1545  1381.21  .    T2  H2O  .    0.9341 0.0031 1.0000  0.1020  0.0120  0.0787  0.1510  0.6585  *#&
181 1565  1392.15  . . . . H2O  .     0.9785 0.0000 1.0000  0.0990  0.0070  0.5526  0.2157  0.6669  *#&
182 1574  1397.14  . . . . H2O  .     0.9655 0.0000 1.0000  0.0760  0.0150  0.9768  0.2480  0.6400  *#&
183 1583  1402.15  . . . . H2O  .     0.9786 0.0000 1.0000  0.0760  0.0050  0.4853  0.2043  0.6628  *#&
184 1593  1407.77  . . . . H2O  .     0.9712 0.0000 1.0000  0.1090  0.0050  0.2463  0.1726  0.6527  *#&
185 1614  1419.72  . . . . H2O  .     0.9649 0.0000 1.0000  0.0810  0.0770  0.4073  0.2110  0.5787  *#&
186 1627  1427.23  . . . . H2O  .     0.9581 0.0000 1.0000  0.0800  0.0040  0.6410  0.2296  0.6665  *#&
187 1636  1432.47  . . . . H2O  .     0.9499 0.0000 1.0000  0.1190  0.0140  0.8167  0.2508  0.6511  *#&
188 1644  1437.16  . . . . H2O  .     0.9439 0.0000 1.0000  0.1300  0.0820  0.4721  0.2353  0.5705  *#&
189 1652  1441.89  . . . . H2O  .     0.9274 0.0000 1.0000  0.1220  0.0040  0.4749  0.2134  0.6074  *#&
190 1669  1468.83  . . . . H2O  .     0.8876 0.0000 1.0000  0.0940  0.0020  1.0400  0.2705  0.6669  *#&
191 1674  1471.91  . . . . H2O  .     0.8749 0.0000 1.0000  0.0730  0.0470  0.0703  0.2320  0.6225  *#&
192 1681  1476.25  . . . . H2O  .     0.8709 0.0000 1.0000  0.0710  0.0650  0.4540  0.2096  0.6585  *#&
193 1694  1484.37  . . . . H2O  .     0.8432 0.0000 1.0000  0.0920  0.0040  0.9191  0.2651  0.7137  *#&
194 1708  1493.21  . . . . H2O  .     0.8274 0.0000 1.0000  0.0710  0.0030  1.1689  0.2725  0.7197  *#&
195 1717  1498.96  . . . . H2O  .     0.8273 0.0000 1.0000  0.0740  0.0530  0.2855  0.2280  0.6752  *#&
196 1723  1502.81  . . . . H2O  .     0.8108 0.0000 1.0000  0.1120  0.0030  1.1662  0.2790  0.6942  *#&
```

197	1740	1513.83	. . . . . H2O .	0.7995	0.0000	1.0000	0.1090	0.0030	1.1891	0.2874	0.6666	*#&
198	1748	1519.07	. . . . . H2O .	0.7875	0.0000	1.0000	0.0910	0.0050	0.9717	0.2847	0.6265	*#&
199	1751	1521.05	. . . . . H2O .	0.7833	0.0000	1.0000	0.0920	0.0440	-0.0650	0.2662	0.5321	*#&
200	1756	1524.35	. . . . . H2O .	0.7746	0.0000	1.0000	0.0950	0.0180	0.7282	0.2609	0.6058	*#&
201	1763	1542.45	. . . . . H2O .	0.6769	0.0000	1.0000	0.1170	0.0550	0.0385	0.2653	0.5420	*#&
202	1766	1544.48	. . . . . H2O .	0.6740	0.0000	1.0000	0.1220	0.0260	0.4208	0.2709	0.5745	*#&
203	1771	1547.88	. . . . . H2O .	0.6490	0.0000	1.0000	0.1220	0.0040	1.0092	0.2625	0.6234	*#&
204	1777	1551.98	. . . . . H2O .	0.6509	0.0000	1.0000	0.1200	0.0030	1.0483	0.2853	0.6132	*#&
205	1780	1554.04	. . . . . H2O .	0.6387	0.0000	1.0000	0.1230	0.0470	0.2774	0.2549	0.5485	*#&
206	1783	1556.10	. . . . . H2O .	0.6459	0.0000	1.0000	0.1260	0.0080	0.6988	0.2948	0.6118	*#&
207	1794	1563.71	. . . . . H2O .	0.6634	0.0000	1.0000	0.1500	0.0050	1.0130	0.2806	0.5616	*#&
208	1800	1567.89	. . . . . H2O .	0.6810	0.0000	1.0000	0.1470	0.0070	1.0520	0.2810	0.5430	*#&
209	1803	1569.99	. . . . . H2O .	0.6900	0.0000	1.0000	0.1980	0.0520	0.2207	0.3187	0.4872	*#&
210	1806	1572.09	. . . . . H2O .	0.6984	0.0000	1.0000	0.1520	0.0040	1.1064	0.2802	0.5209	*#&
211	1812	1576.32	. . . . . H2O .	0.7047	0.0000	1.0000	0.3640	0.0490	0.1148	0.4711	0.4057	*#&
212	1826	1586.26	. . . . . H2O .	0.7292	0.0000	1.0000	0.1870	0.0050	0.8066	0.2466	0.4630	*#&
213	1843	1598.49	. . . . . H2O .	0.7288	0.0000	1.0000	0.2290	0.0030	0.5199	0.2636	0.4054	*#&
214	1852	1605.05	. . . . . H2O .	0.7340	0.0000	1.0000	0.2740	0.0020	0.7665	0.2770	0.3539	*#&
215	1865	2181.49	. . . S . .	0.5981	0.8278	0.9959	0.1210	0.1000	-0.3103	0.1775	0.8342	*#&
216	1866	2182.40	. . . S . .	0.5245	0.8853	0.9960	0.1200	0.0470	-0.0962	0.1967	0.8353	*#&
217	1868	2184.21	. . . S . .	0.4326	0.9424	0.9963	0.1190	0.0340	-0.0983	0.1782	0.8469	*#&
218	1869	2185.12	. . . S . .	0.4789	0.8265	0.9957	0.1210	0.0470	-0.1469	0.1540	0.8473	*#&
219	1872	2187.85	. . . S . .	0.3605	0.8139	0.9969	0.0880	0.0530	-0.0730	0.1541	0.8456	*#&
220	1873	2188.76	. . . S . .	0.3807	0.9412	0.9967	0.0870	0.0310	-0.1202	0.1561	0.8504	*#&
221	1876	2191.50	. . . S . .	0.3876	0.9561	0.9977	0.0880	0.0360	-0.1806	0.1601	0.8511	*#&
222	1881	2196.07	. . . . . .	0.2172	0.9837	0.9978	0.0890	0.0410	0.0432	0.1292	0.8394	*#&
223	1882	2196.99	. . . . . .	0.1993	0.9858	0.9974	0.0910	0.0400	0.0569	0.1276	0.8343	*#&
224	1883	2197.91	. . . . . .	0.1912	0.9615	0.9977	0.0920	0.0320	0.0979	0.1289	0.8376	* &
225	1911	2223.94	. . . . . .	0.2448	0.9808	0.9982	0.1010	0.0720	-0.0897	0.1269	0.8391	*#&
226	1917	2229.59	T1 T2	0.0398	0.9780	0.9977	0.1040	0.0280	0.1152	0.1079	0.8284	*#&
227	1918	2230.54	T1 T2	0.0337	0.9592	0.9986	0.1060	0.0350	0.1195	0.1017	0.8323	*#&
228	1924	2236.23	T1 T2	0.0109	0.9555	0.9984	0.1120	0.0310	0.0202	0.1153	0.8179	*#&
229	1928	2240.03	T1 T2	0.0078	0.9848	0.9986	0.1130	0.0230	0.1069	0.0950	0.8068	*#&
230	1937	2248.65	T1 T2	0.0041	0.9838	0.9986	0.1290	0.0240	0.1892	0.1145	0.7872	
231	1941	2252.50	T1 T2	0.0007	0.9683	0.9984	0.1220	0.0170	0.2106	0.1128	0.7800	
232	2099	2378.43	T1 T2	0.0005	0.9959	0.9999	0.1850	0.0260	1.4626	0.3255	0.9833	
233	2100	2379.40	T1 T2	0.0005	0.9959	0.9999	0.1880	0.0320	1.3784	0.3816	0.9818	
234	2101	2380.36	T1 T2	0.0006	0.9960	0.9999	0.1470	0.0400	1.3787	0.2959	0.9890	
235	2103	2382.31	T1 T2	0.0008	0.9960	0.9999	0.1390	0.0450	0.8310	0.2640	0.9889	
236	2104	2383.28	T1 T2	0.0009	0.9959	0.9999	0.1390	0.0480	0.5276	0.2368	0.9901	
237	2106	2385.23	T1 T2	0.0012	0.9960	0.9999	0.1440	0.0470	0.3395	0.1704	0.9860	
238	2107	2386.20	T1 T2	0.0016	0.9960	0.9999	0.1860	0.0490	0.2628	0.1853	0.9896	
239	2108	2387.18	T1 T2	0.0030	0.9961	0.9999	0.1900	0.0470	0.2608	0.1529	0.9893	
240	2109	2388.15	T1 T2	0.0086	0.9967	0.9999	0.1430	0.0450	0.2942	0.1497	0.9915	
241	2110	2389.13	T1 T2	0.0278	0.9962	0.9999	0.1460	0.0440	0.2260	0.1639	0.9924	* &
242	2111	2390.11	T1 T2	0.0703	0.9968	0.9999	0.1460	0.0520	0.0692	0.1627	0.9925	* &
243	2112	2391.09	T1 T2	0.1324	0.9973	0.9999	0.1450	0.0560	0.0533	0.1537	0.9949	* &
244	2113	2392.07	T1 T2	0.2040	0.9973	0.9999	0.1460	0.0460	0.0453	0.1607	1.0000	* &
245	2114	2393.05	T1 T2	0.2685	0.9953	0.9999	0.1480	0.0350	0.0406	0.1618	0.9932	* &
246	2115	2394.03	T1 T2S . .	0.3145	0.9938	0.9999	0.1440	0.0310	-0.0567	0.1632	0.9916	* &
247	2116	2395.01	T1 T2	0.3435	0.9933	0.9999	0.1480	0.0300	-0.0872	0.1621	0.9924	* &
248	2117	2396.00	T1 T2S . .	0.3632	0.9948	0.9999	0.1540	0.0290	-0.0808	0.1646	0.9922	* &
249	2118	2396.98	T1 T2	0.3796	0.9965	0.9999	0.1520	0.0290	-0.0653	0.1649	0.9893	* &
250	2119	2397.96	T1 T2 S . .	0.3945	0.9970	0.9999	0.1570	0.0280	-0.0577	0.1681	0.9882	* &
251	2120	2398.95	T1 T2	0.4077	0.9973	0.9999	0.1570	0.0270	-0.1071	0.1672	0.9866	* &
252	2121	2399.94	T1 T2	0.4201	0.9971	0.9999	0.1530	0.0260	-0.1052	0.1697	0.9885	* &

253	2122	2400.92	T1	T2	.	.	.	.	0.4317	0.9969	0.9999	0.1550	0.0260	-0.1328	0.1732	0.9857	*	&
254	2123	2401.91	.	.	.	S	.	.	0.4428	0.9973	0.9999	0.2220	0.0250	-0.1295	0.1780	0.9795	*	&
255	2128	2406.86	T1	T2	.	.	.	.	0.4894	0.9950	1.0000	0.1540	0.0240	-0.1778	0.1809	0.9803	*	&
256	2134	2412.83	T1	T2	.	.	.	.	0.5326	0.9975	0.9999	0.1600	0.0220	-0.2296	0.1821	0.9773	*	&
257	2141	2419.83	.	.	.	S	.	.	0.5778	0.9973	0.9999	0.1710	0.0200	-0.2538	0.1828	0.9554	*	&
258	2145	2446.19	.	.	.	S	.	.	0.6814	0.9975	1.0000	0.1760	0.0160	-0.3601	0.2012	0.9377	*	&
259	2149	2450.30	T1	T2	.	.	.	.	0.6941	0.9974	1.0000	0.1830	0.0150	-0.3638	0.2023	0.9349	*	&
260	2153	2454.41	.	.	.	S	.	.	0.7196	0.9978	0.9999	0.2130	0.0140	bad	bad	0.8559	*	&
261	2164	2465.80	.	.	.	S	.	.	0.7744	0.9974	0.9999	0.1870	0.0110	-0.4114	0.2142	0.9253	*	&
262	2189	2492.08	.	.	.	S	.	.	0.8691	0.9980	1.0000	0.2240	0.0060	-0.4344	0.2295	0.8707	*	&
263	2197	2500.60	T1	T2	.	.	.	.	0.8990	0.9972	1.0000	0.2410	0.0050	-0.4608	0.2322	0.8418	*	&
264	2209	2513.49	.	.	.	S	.	.	0.9127	0.9973	1.0000	0.2940	0.0040	-0.4763	0.2421	0.7854	*	&
265	2226	2531.98	.	.	.	S	.	.	0.9146	0.9948	1.0000	0.3350	0.0060	-0.4694	0.2486	0.6974	*	&
266	2234	2540.77	.	.	.	S	.	.	0.8774	0.9966	1.0000	0.3870	0.0060	-0.4533	0.2515	0.6508	*	&
267	2280	2561.13	.	.	.	S	.	.	0.8945	0.9953	1.0000	0.3430	0.0060	-0.4918	0.2726	0.7534	*	&
268	2318	2600.50	.	.	.	S	.	.	0.9462	0.9519	1.0000	0.3170	0.0090	-0.4563	0.2851	0.8136	*	&
269	2321	2603.66	.	.	.	S	.	.	0.9650	0.9914	1.0000	0.3090	0.0060	-0.5070	0.2981	0.8148	*	&
270	2325	2607.89	.	.	.	S	H2O	.	0.9821	0.7983	1.0000	0.3480	0.0300	-0.3374	0.2829	0.8218	*	&
271	2328	2611.07	.	.	.	S	.	.	0.9875	0.9865	1.0000	0.3180	0.0020	-0.5196	0.2930	0.8244	*	&
272	2333	2616.38	.	.	.	S	H2O	.	0.9895	0.9942	1.0000	0.3100	0.0020	-0.5138	0.2903	0.8318	*	&
273	2339	2622.79	.	.	.	S	H2O	.	0.9814	0.7610	1.0000	0.3130	0.0370	-0.3406	0.2886	0.8310	*	&
274	2348	2632.47	.	.	.	S	H2O	.	0.9726	0.9907	1.0000	0.3150	0.0020	-0.5125	0.2931	0.8403	*	&
275	2353	2637.87	.	.	.	S	H2O	.	0.9828	0.7901	1.0000	0.3310	0.0470	-0.2375	0.2852	0.8276	*	&
276	2355	2640.04	.	.	.	S	.	.	0.9841	0.9054	1.0000	0.3200	0.0080	-0.4532	0.3044	0.8283	*	&
277	2357	2642.21	.	.	.	S	H2O	.	0.9849	0.8668	1.0000	1.3990	0.0250	-0.4804	bad	0.8322		
278	2363	2648.75	.	.	.	S	H2O	.	0.9898	0.9006	1.0000	0.3470	0.0210	-0.4025	0.2867	0.8052	*	&
279	2370	2656.42	.	.	.	S	.	.	0.9779	0.8565	1.0000	0.3520	0.0220	-0.3776	0.2850	0.7825	*	&
280	2371	2657.52	.	.	.	.	H2O	.	0.9847	0.8853	1.0000	0.3690	0.0170	-0.4382	0.2892	0.7798	*	&
281	2377	2664.14	.	.	.	S	.	.	0.9882	0.8610	1.0000	0.3860	0.0170	-0.3855	0.3005	0.7627	*	&

APPENDIX D

Publications

Reviewed Papers:

Jung, J. A. T. H. Zapotocny, J. F. Le Marshall and R. E. Treadon, 2008: A Two Season Impact Study of NOAA Polar Orbiting Satellites in the NCEP Global Data Assimilation System. Submitted to *Wea. Forecasting*.

Le Marshall, J., J. A. Jung, J. C. Derber, R. Treadon, S. Lord, M. Goldberg, W. Wolf, H. C. Liu, J. Joiner, J. Wollen, and R. Todling, 2005: AIRS Hyperspectral Data Improves Southern Hemisphere Forecasts. *Aust, Met. Mag*. **54**, 57-60.

Le Marshall, J., J. Jung, J. Derber, R. Treadon, S. J. Lord, M. Goldberg, W. Wolf, H. C. Liu, J. Joiner, J. Wollen, R. Todling, and G. Gelaro, 2005: Impact of Atmospheric Infrared Sounder Observations on Weather Forecasts. *EOS* **86**, Number 11, 15 March 2005.

Le Marshall, J., J. Jung, S. Lord, J. Derber, R.Treadon, J. Joiner, M. Goldberg, W. Wolf, and H. C. Liu, 2005: AIRS associated accomplishments at the JCSDA: First use of full spatial resolution hyperspectral data show significant improvements in global forecasts. *Proceedings of the SPIE, Atmospheric and Environmental Remote Sensing Data Processing and Utilization: Numerical Atmospheric Prediction and Environmental Monitoring*. Edited by Huang, Hung-Lung A.; Bloom, Hal J.; Xu, Xiaofeng; Dittberner, Gerald J. **5890**, 155-161.

Le Marshall, J., J. Jung, J. Derber, M. Chahine, R. Treadon, S. J. Lord, M. Goldberg, W. Wolf, H. C. Liu, J. Joiner, J. Wollen, R. Todling, P. Van Delst, and Y. Tahara 2006: Advanced Infrared Sounder (AIRS) observations improve global analysis and forecast capability. *Bull. Amer. Meteor. Soc.* **87**, 891-894.

Le Marshall, J., J. Jung, T. Zapotocny, J., Derber, R. Treadon, S. Lord, M. Goldberg, and W. Wolf, 2006: The Application of AIRS Radiances in Numerical Weather Prediction. *Aust. Meteor. Mag*., **55**, 213-217.

Le Marshall, J., L. Bi, J. Jung, T. Zapotocny, and M. Morgan, 2007: WindSat Polarimetric Microwave Observations Improve Southern Hemisphere Numerical Weather Prediction. *Aust. Meteor. Mag*. **56**, 35-40.

Schmit, T. J., W. F. Feltz, W. P. Menzel, J. A. Jung, A. P. Noel, J. N. Heil, J. P. Nelson, and G. S. Wade, 2002: Validation and Use of GOES Sounder Moisture Information. *Wea. Forecasting*, **17**, 139–154.

Zapotocny, T. H., S. J. Nieman, W. P. Menzel, J. P. Nelson, J. A. Jung, E. Rogers, D. F. Parrish, G. J. DiMego, M. Baldwin, and T. J. Schmit, 2000: A Case Study of the Sensitivity of the Eta Data Assimilation System. *Wea. Forecasting*, **15**, 603–622.

Zapotocny, T. H., W. P. Menzel, J. P. Nelson, and J. A. Jung, 2002: An Impact Study of Five Remotely Sensed and Five In Situ Data Types in the Eta Data Assimilation System. *Wea. Forecasting*, **17**, 263–285.

Zapotocny, T. H., W. P. Menzel, J. A. Jung, and J. P. Nelson, 2005: A Four-Season Impact Study of Rawinsonde, GOES, and POES Data in the Eta Data Assimilation System. Part I: The total Contribution. *Wea. Forecasting*, **20**, 161-177.

Zapotocny, T. H., W. P. Menzel, J. A. Jung, and J. P. Nelson, 2005: A Four-Season Impact Study of Rawinsonde, GOES, and POES Data in the Eta Data Assimilation System. Part II: Contribution of the Components. *Wea. Forecasting*, **20**, 178-198.

Zapotocny, T. H., J. A. Jung, J. F. Le Marshall, and R. E. Treadon 2007: A Two Season Impact Study of Satellite and In-Situ Data in the NCEP Global Data Assimilation System. *Wea. Forecasting*, **22**, 887-909.

Zapotocny, T. H., J. A. Jung, J. F. Le Marshall, and R. E. Treadon, 2008: A Two Season Impact Study of four Satellite Data Types and Rawinsonde Data in the NCEP Global Data Assimilation System. *Wea. Forecasting*, **23**, 80-100.

Non-Reviewed Papers

Boe, B. A., and J. A. Jung, 1990: The Application of Geostationary Satellite Imagery for Decision Making in Convective Cloud Seeding in North Dakota. *J. Wea. Mod.* **22**, 73-78.

Jung, J. A., and Snomax Technologies. 1990: Preliminary field experiments of Snowmax Super(T) on Cumulus Mediocris Clouds to Artificially Induce the Production of Ice Particles. *J. Wea. Mod*., **22**, 153-157.

Conference Papers and Posters

Bi, L., J. F. Le Marshall, T. H. Zapotocny, J. Jung, and M. C. Morgan 2007: Assessing the Forecast Impact Of WindSat/Coriolis Data In The NCEP GDAS/GFS. *Proc. 87th AMS Annual Meeting,* San Antonio, TX 14-18 January 2007.

Jung, J. A., R. M. Aune, T. J. Schmit, and T. H. Zapotocny, 2001: Assimilation of GOES Sounder Cloud Top Pressure in NCEP's 48km Eta Mesoscale Model. *Proc 11th AMS Conference on Satellite Meteorology and Oceanography*, Madison WI, 15-18 October 2001.

Jung, J. A., A. J. Schreiner, W. F. Feltz, S. M. Thomas, T. J. Schmit, and J. Daniels, J. 2004: Improvements to the GOES-12 Imager Cloud Product. *Proc. 13th AMS Conference on Satellite Meteorology and Oceanography*, Norfolk, VA, 20-23 September 2004.

Jung, J. A., T. H. Zapotocny, W. P. Menzel, and J. P. Nelson, 2004: Regional and Global NWP Observing System Data Denial Experiments using NCEP's Operational Models. *Proc. 13th AMS Conference on Satellite Meteorology and Oceanography*, Norfolk, VA, 20-23 September 2004.

Jung, J. A., T. H. Zapotocny, R. E. Treadon, J. F. Le Marshall 2006: Atmospheric Infrared Sounder Assimilation Experiments Using NCEP's GFS. *Proc 14th AMS Conference on Satellite Meteorology and Oceanography*, Atlanta, GA, 29 January – 2 February 2006.

Jung, J. A., T. H. Zapotocny, J. F. Le Marshall, and R. E. Treadon 2007: NOAA Polar Orbiting Satellite Observing System Experiments using the NCEP GDAS. *Proc. 87th AMS Annual Meeting,* San Antonio, TX 14-18 January 2007.

Le Marshall, J. F., J. Jung, S. Lord, J. Derber, R. Treadon, J. Joiner, M. Goldberg, W. Wolf, H. C. Liu, J. Woollen, and R. Todling, 2005: AIRS Associated Accomplishments at the JCSDA. *Proc. 14th International TOVS Study Conference*, Beijing, China, 25–31 May 2005.

Le Marshall, J. F., J. A. Jung, J. Derber, R. Treadon, M. Goldberg, W. Wolf and T. H. Zapotocny, 2006: Assimilation of Atmospheric Infrared Sounder (AIRS) Observations at the JCSDA. *Proc. 14th AMS Conference on Satellite Meteorology and Oceanography*, Atlanta, GA, 28 January-2 February 2006.

Le Marshall, J. F., J. Jung, S. Lord, J. Derber, M. Goldberg, W. Wolf, and S. Mango. 2006: Risk Reduction for NPOESS Using Heritage Sensors: AIRS, HIRS, MSU, SSM/I, AMSU, and MODIS. *Second Symposium: Toward a Global Earth Observation System of Systems—Future National Operational Environmental Satellite Systems 1.4*

Le Marshall, J.F., J. Jung, T. H. Zapotocny, W. L. Smith, D. K. Zhou, J. Derber, R. Treadon, S. Lord, M. Goldberg, and W. Wolf, 2007: The use of global AIRS hyperspectral observations in numerical weather prediction. *Proc. 87th AMS Annual Meeting,* San Antonio, Texas, 14-18 January 2007.

LeMarshall, J.F., S. Lord, M. Rienecker, P. Phoebus, J. Jung, J. Derber, M. Goldberg, F. Weng, L. P. Riishojgaard, and J. G. Yoe, 2007: The Joint Center for Satellite Data Assimilation (JCSDA) - Helping to Improve Climate, Weather, Ocean and Air Quality Forecasts and the Accuracy of Climate Data Sets. *Proc. 87th AMS Annual Meeting,* San Antonio, Texas, 14-18 January 2007.

Lord, S., T. Zapotocny, and J. Jung, 2004: Observing System Experiments with NCEP's Global Forecast System. *3rd WMO Workshop on the Impact of Various Observing Systems on Numerical Weather Prediction, World Meteorological Organization*, Alpbach, Austria

Santek, D., J. A. Jung, T. Zapotocny, J. Key, and C. Velden, 2006: Mechanisms that Propagate Polar Satellite-derived Atmospheric Motion Vector Information into Lower Latitudes. *Proc 14th AMS Conference on Satellite Meteorology and Oceanography*, Atlanta, GA, 29 January – 2 February 2006.

Schreiner, A. J., T. J. Schmit, C. Koepken, X. Su, C. Holland, J. A. Jung, 2003: Introducing the GOES Imager Clear-Sky Brightness Temperature (CSBT). *Proc 12thAMS Conference on Satellite Meteorology and Oceanography,* Long Beach, CA, 9-13 February 2003.

Schreiner, A. J., J. A. Jung, T. J. Schmit, C. W. Holland, J. P. Nelson, T. L. Olander, and W. P. Menzel, 2006: Introducing the Operational GOES Imager Clear-Sky Brightness Temperature (CSBT) Data Products. *Proc 14th AMS Conference on Satellite Meteorology and Oceanography*, Atlanta, GA, 29 January-2 February 2006.

Su, X., J. C. Derber, J. A. Jung, Y. Tahara, D. Keyser, and R. Treadon, 2003: Usage of the GOES Imager Clear-Sky Radiance in the NCEP Global Data Assimilation System. *Proc.12thAMS Conference on Satellite Meteorology and Oceanography*, Long Beach CA, 9-13 February 2003.

Zapotocny, T. H., W. P. Menzel, J. P. Nelson and J. A. Jung, 2001: An Impact Study of five Remotely Sensed and five In-situ Eta Data Types in the Data Assimilation System. *Proc. 11th AMS Conference on Satellite Meteorology and Oceanography*, Madison, WI, 15-18 October 2001.

Zapotocny, T. H., J. A. Jung, R. Treadon, and J. F. Le Marshall 2006: Recent MODIS Data Assimilation Experiments in the NCEP GFS. *Proc. 14th AMS Conference on Satellite Meteorology and Oceanography,* Atlanta, GA, 29 January – 2 February 2006.

Glossary

ABI	Advanced Baseline Imager
AIREP	Aircraft Report
AIRS	Atmospheric Infrared Sounder
AMSR-E	Advanced Microwave Scanning Radiometer for EOS
AMSU	Advanced Microwave Sounding Unit
AMV	Atmospheric Motion Vector
APT	Automatic Picture Transmission
ASDAR	Aircraft to Satellite Data Relay
AST	AIRS Science Team
ATMS	Advanced Technology Microwave Sounder
ATS	Application Technology Satellites
AVHRR	Advanced Very High Resolution Radiometer
BT	Brightness Temperature
BUFR	Binary Uniform Format for the Representation of meteorological data
CERES	Clouds and the Earth's Radiant Energy System
CMIS	Conical Microwave Imager/Sounder
CRTM	Community Radiative Transfer Model
CrIS	Cross-track Infrared Sounder
CZCS	Costal Zone Color Scanner
DMSP	Defense Meteorological Satellite Program
DOD	Department of Defense
DS	Dwell Sounding
ECMWF	European Center for Medium Range Forecast
EOS	Earth Observing System
ERBE	Earth Radiation Budget Experiment
ESSA	Environmental Science Services Administration
EUMETSAT	European Organization for the Exploitation of Meteorological Satellites
FGGE	First GARP Global Experiment
FI	Forecast Impact
FOV	Field of View
GDAS	Global Data Assimilation System
GFS	Global Forecast System
GIFTS	Geosynchronous Imaging Fourier Transform Spectrometer
GMS	Geostationary Meteorological Satellite
GOES	Geostationary Operational Environmental Satellite
GSFC	Goddard Space Flight Center
GSI	Gridpoint Statistical Interpolation
GVHRR	Geosynchronous Very High Resolution Radiometer
HES	Hyperspectral Environmental Sounder
HIRS	High Resolution Infrared Radiation Sounder
HSB	Humidity Sensor for Brazil
IASI	Infrared Atmospheric Sounding Interferometer

INPE	Brazil's National Institute for Space Research
IR	Infrared
IRIS	Infrared Interferometer Spectrometer
ISCCP	International Satellite Cloud Climatology Project
ITOS	Improved TIROS Operational System
ITPR	Infrared Temperature Profile Radiometer
JCSDA	Joint Center for Satellite Data Assimilation
K	Degrees Kelvin
LFM	Limited-area Fine Mesh
LTE	Local Thermal Equilibrium
MDCARS	Meteorological Data Collection and Reporting System
METAR	Meteorological Aerodrome Report
METEOSAT	Meteorological Satellite (Europe)
MODIS	Moderate-resolution Imaging Spectroradiometer
MRIR	Medium Resolution Infrared Radiometer
MSI	Multi-Spectral Imaging
MSR	Microwave Scanning Radiometer
MSU	Microwave Sounding Unit
NASA	National Aeronautics and Space Administration
NASDA	Japan's National Space Development Agency
NCEP	National Centers for Environmental Prediction
NEMS	NIMBUS Experimental Microwave Spectrometer
NESDIS	National Environmental Satellite, Data and Information Service
NESS	National Environmental Satellite Service
NEXRAD	Next Generation Radar
NMC	National Meteorological Center
NOAA	National Oceanographic and Atmospheric Administration
NPOESS	National Polar-orbiting Operational Environmental Satellite System
NWP	Numerical Weather Prediction
OMPS	Ozone Mapping and Profiler Suite
OPTRAN	Optical Path TRANsmittance
OSE	Observing System Experiment
PIBAL	Pilot Balloon
PIREP	Pilot Report
POES	Polar Orbiting Environmental Satellites
RMS	Root Mean Square (error)
RTE	Radiative Transfer Equation
SAR	Search and Rescue
SBUV	Solar Backscatter Ultraviolet
SCAMS	Scanning Microwave Spectrometer
SEM	Space Environment Monitor
SFOV	Single Field of View
SIRS	Satellite Infra-Red Spectrometer
SMMR	Scanning Multichannel Microwave Radiometer
SMS	Synchronous Meteorological Satellites
SOP-1	Special Observing Period

SSCC	Spin Scan Cloud-cover Camera
SSI	Spectral Statistical Interpolation
SSM/I	Special Sensor Microwave Imager
SMMR	Scanning Multichannel Microwave Radiometer
SSI	Spectral Statistical Interpolation
SST	Sea Surface Temperature
TIROS	Television Infrared Observational Satellite
TM	Thematic Mapper
TMI	TRMM Microwave Imager
TOVS	TIROS Operational Vertical Sounder
TRMM	Tropical Rainfall Measurement Mission
UTC	Universal Time Coordinates
VAR	Variational Assimilation Scheme
VAS	VISSR Atmospheric Sounder
VHRR	Very High Resolution Radiometer
VIIRS	Visible/Infrared Imager/Radiometer Suite
VISSR	Visible Infrared Spin Scan Radiometer
VTPR	Vertical Temperature Profile Radiometer
WSRP	Winter Storm Reconnaissance Program
Z	Geopotential Height

Bibliography

Ackerman, S. A., 1996: Global satellite observations of negative brightness temperature differences between 11 and 6.7μm. *J. Atmos. Sci*., **53**, 2803-2812.

Alishouse, J. C., S. Snyder, J. Vongsathorn, and R. R. Ferraro, 1990: Determination of oceanic total precipitable water from the SSM/I. *IEEE Trans. Geosci. Remote Sens*., **28**, 811-816.

Andersson, E., A. Hollingsworth, G. Kelly, P. Lonnberg, J. Pailleux and Z. Zhang, 1991: Global Observing System Experiments on Operational Statistical Retrievals of Satellite Sounding Data. *Mon. Wea. Rev*., **119**, 1851-1864.

Auligne, T., F. Rabier, L. Lavanant, and M. Dahoui, 2003: First results of the assimilation of AIRS data in Meteo-France Numerical Weather Prediction model. Proceedings of the 13th International TOVS Working Group Conference., St. Adele, Canada., 29 Oct – 4 Nov.

Aumann, H. H., M. T. Chahine, C. Gautier, M. D. Goldberg, E. Kalnay, L. M. McMillin, H. Revercomb, P. W. Rosenkranz, W. L. Smith, D. H. Staelin, L. L. Strow, and J. Suskind, 2003: AIRS/AMSU/HSB on the Aqua Mission: Design, Science Objectives, Data Products, and Processing System. *IEEE Trans. Geosci. Remote Sensing*, **41**, 253-264.

Barnes, W.L., T. S. Pagano and V. V. Salomonson, 1998: Prelaunch characteristics of the Moderate Resolution Imaging Spectroradiometer (MODIS) on EOS-AM1. *IEEE Trans. Geosci. Remote Sensing*, **36**, 1088-1100.

Caplan, P., J. C. Derber, W. Gemmill, S. Hong, H. Pan, and D. F. Parrish, 1997: Changes to the 1995 NCEP Operational Medium-Range Forecast Model Analysis-Forecast System. *Wea. Forecasting,* **12**, 581-594.

Carter, C., Q. Liu, W. Yang, D. Hommel, and W. Emery, 2002: Net heat flux, visible/infrared imager/radiometer suite algorithm theoretical basis document. http://npoesslib.ipo.noaa.gov/IPOarchive/SCI/atbd/msoFC63C.pdf

Chahine, M. T., 1970: Inverse Problems in Radiative Transfer: Determination of Atmospheric Parameters. *J. Atmos. Sci*., **27**, 960-967.

Courtier, P., and Coauthors, 1993: Variational Assimilation at ECMWF. ECMWF Tech. Memo. 194, 84 pp. [Available from European Centre for Medium Range Weather Forecasts, Shinfield Park, Reading, Perkshire R62 9AX, United Kingdom.]

Cox, C., and W. Munk, 1954: Statistics of the Sea Surface Derived from Sun Glitter. *J. Mar. Res*., **13**, 198-227.

Derber, J. C., and W.-S. Wu, 1998: The use of TOVS Cloud-Cleared Radiances in the NCEP SSI Analysis System. *Mon. Wea. Rev*., **126**, 2287-2299.

_____, F. Bouttier, 1999: A Reformation of the Background Error Covariance in the ECMWF Global Data Assimilation System., *Tellus*, **51A**, 195-221.

_____, P. Van Delst, X. Su, X. Li, K. Okamoto, and R. Treadon, 2003: Enhanced use of radiance data in the NCEP data assimilation system. Proceedings of the 13th International TOVS Conference. St. Adele, Canada., 20 Oct – 4 Nov.

_____, D. F. Parrish, and S. J. Lord, 1991: The new global operational analysis system at the National Meteorological Center. *Wea. Forecasting,* **6**, 538-547.

Dey, C. H., R. A. Petersen, B. A. Ballish, P. M. Caplan, L. L. Morone, H. J. Thiebaux, G. H. White, H. E. Fleming, A. L. Reale, D. G. Gray, M. D. Goldberg, and J. M. Daniels,1989: An Evaluation of NESDIS TOVS Physical Retrievals Using Data Impact Studies. *NOAA Tech. Memo. NWS NMC 69*, National Meteorological Center, Washington D.C., 25 pp.

Ebert, E. 1989: Analysis of polar clouds from satellite imagery using pattern recognition and a statistical cloud analysis scheme. *J. Appl. Meteor*., **28**, 382-399.

English, S. J. and T.J. Hewison, 1998: A fast generic millimeter wave emissivity model. Microwave Remote Sensing of the Atmosphere and Environment Proc. *SPIE*, **3503**, 22-30.

Eyre, J. R., 1990: Progress on Direct use of Satellite Soundings in Numerical Weather Prediction. Preprints, WMO INT. Symp. on Assimilation of Observations in Meteorology and Oceanography, Clermont-Ferrand, France, 117-121.

_____, G. A. Kelly, A. P. McNally, E. Andersson and A. Persson, 1993: Assimilation of TOVS Radiance Information Through One-Dimensional Variational Analysis. *Q. J. R. Meteorol. Soc*., **119**, 1427-1463.

Fleming, H. E., M. D. Goldberg, and D. Crosby, 1986: Minimum Variance Simultaneous Retrieval of Temperature and Water Vapor from Satellite Radiance Measurements. *Preprints: Second Conf. on Satellite Meteorology/Remote Sensing and Applications*. Amer. Meteor. Soc., Boston, MA, 20-23.

_____, M. D. Goldberg, and D. Crosby, 1988: Operational Implementation of the Minimum Variance Simultaneous Retrieval Method. *Preprints, Third Conf. on Meteorology and Oceanography*. Amer. Meteor. Soc., Boston, MA, 16-19.

Fritz, S., D. Q. Wark, H.E. Fleming, W. L. Smith, H. Jacobowitz, D. T. Hilleary, and J. C. Alishouse, 1972: Temperature Sounding from Satellites. NOAA Tech Rep. NESS 59 Washington, DC.

Gaiser, S. L., H. H. Aumann, L. L. Strow, S. E. Hannon, and M. Weiler, 2003: In-Flight Spectral Calibration of the Atmospheric Infrared Sounder. *IEEE Trans. Geosci. Remote Sensing*, **41**, 287-297.

Gautier, C., Y. Shiren, and M. D. Hofstadter 2003: AIRS/Vis Near IR instrument. *IEEE Trans. Geosci. Remote Sensing*, **41**, 330-342.

Ghil, M., M. Halem, and R. Atlas 1979: Time-continuous Assimilation of Remote-Sounding Data and its Effect on Weather Forecasting. *Mon. Wea. Rev*., **107**, 140-171.

Goldberg, M. D., J. M. Daniels, and H. E. Fleming, 1988: A Method for Obtaining an Improved Initial Approximation for the Temperature/Moisture Retrieval Problem. *Preprints, Third Conf. on Satellite Meteorology and Oceanography*. Amer. Meteor. Soc., Boston, MA, 20-23.

_____, Y. Qu, L. M. McMillin, W. Wolf, L. Zhou, and M. Divakarla, 2003: AIRS Near-Real-Time Products and Algorithms in Support of Numerical Weather Prediction. *IEEE Trans. Geosci. Remote Sensing*, **41**, 379-389.

Gurka, J. J., and G. J. Dittberner, 2001: The next generation GOES instruments: Status and potential impact. Preprints, *Fifth Symp. on Integrated Observing Systems*, Albuqueruqe, NM, Amer, Meteor. Soc.,

_____, and T. J. Schmit, 2004: Baseline Instruments Planned for the GOES-R Series, *Proc. 13th AMS Conference on Satellite Meteorology and Oceanography*, Norfolk, VA, 20-23 September 2004.

Hagan, D. E., and P. J. Minnett, 2003: AIRS Radiance Validation Over Ocean from Sea Surface Temperature Measurements. *IEEE Trans. Geosci. Remote Sensing*, **41**, 432-441.

Halem, M., E. Kalnay, W. E. Baker, and R. Atlas, 1982: An Assessment of the FGGE Satellite Observing System during SOP-1. *Bull. Amer. Meteor. Soc.*, **63**, 407-429.

Han, Y., P. van Delst, Q. Liu, F. Weng, B. Yan, R. Treadon, and J. Derber, 2006: JCSDA Community Radiative Transfer Model (CRTM) – Version 1, *NOAA Technical Report #122*, 33pp.

Holz, R. E., S. A. Ackerman 2006: Arctic Winter High Spectral Resolution Cloud Height Retrievals. *Proc. 14th AMS Conference on Satellite Meteorology and Oceanography*, Atlanta, Ga. 29 January – 2 February 2006.

Kalnay, E., M. Kanamitsu, and W.E. Baker, 1990: Global numerical weather prediction at the National Meteorological Center. *Bull. Amer. Meteor. Soc*., **71**, 1410-1428.

Kanamitsu, M., 1989: Description of the NMC global data assimilation and forecast system. *Wea. Forecasting*, **4**, 335-342.

_____, J.C. Alpert, K.A. Campana, P.M. Caplan, D.G. Deaven, M. Iredell, B. Katz, H.-L. Pan, J. Sela, and G.H. White, 1991: Recent changes implemented into the global forecast system at NMC. *Wea. Forecasting*, **6**, 425-435.

Kaplan, L. D., 1959: Inference of Atmospheric Structure from Remote Radiation Measurements. *J. Optical Soc. Am*., **49**, 1004-1007.

Kawanishi, T., T. Sezai, Y. Ito, K. Imaoka, T. Takeshima, Y. Ishido, a. Shibata, M. Miura, H. Inahata, and R. W. Spencer, 2003: The Advanced Microwave Scanning Radiometer for the Earth Observing System (AMSR-E), NASDA's Contribution to the EOS for Global Energy and Water Cycle Studies. *IEEE Trans. Geosci. Remote Sensing*, **41**, 184-194.

Kelly, G., G. Mills, and W. Smith, 1978: Impact of Nimbus-6 Temperature Soundings on Australian Region Forecasts. *Bull. Amer. Meteor. Soc*., **59**, 393-405.

Kelly, G., E. Andersson, A. Hollingsworth, P. Lonnberg, J. Pailleux and Z. Zhang, 1991: Quality Control of Operational Physical Retrievals of Satellite Sounding Data. *Mon. Wea. Rev*., **119**, 1866-1880.

_____, 1997: Influence of observations on the operational ECMWF system. Technical Proceedings of the Ninth International TOVS Study Conference. Igls, Austria, pp 239-244.

Key, J., and R. G. Barry, 1989: Cloud cover analysis with Arctic AVHRR data: 1. Cloud detection. *J. Geophys, Res*., **94**, 18521-18535.

_____, J. A., Maslanik and A. J.Schweiger, 1989: Classification of merged AVHRR and SMMR Arctic data with neutral networks. *Photo. Eng. and Rmt. Sens*., **55**, 1331-1338.

_____, 1990: Cloud cover analysis with Arctic advanced very high resolution radiometer data: 2. Classification with spectral and textural measures. *J. Geophys. Res*., **95**, 7661-7675.

Keyser, D., cited 2001a: Code table for PREPBUFR report types used by the ETA/3DVAR. [Available online from http://www.emc.ncep.noaa.gov/mmb/papers/keyser/prepbufr.doc/table_4.htm.

_____, cited 2001b: Summary of the current NCEP analysis system usage of data types that do not pass through PREPBUFR processing. [Available online from http://www.emc.ncep.noaa.gov/mmb/papers/keyser/prepbufr.doc/table_19.htm.]

_____, cited 2003: Observational data processing at NCEP. [Available online from http://www.emc.ncep.noaa.gov/mmb/papers/keyser/data_processing/.]

Kidder, S. Q., and T. H. Vonder Haar 1995: Satellite Meteorology, An Introduction. *Academic Press*, San Diego, CA, pp 466.

King, J. I. F., 1958: The Radiative Heat Transfer of Planet Earth. Scientific Uses of Earth Satellites. *Univ. of Michigan Press*, Ann Arbor, MI, pp. 133.

King, M. D., and R. Greenstone, 1999: *EOS Reference Handbook*. Greenbelt, MD: NASA Goddard Space Flight Center, pp. 1-361.

King, M. D., R. Greenstone, and W. Bandeen, 1999: *EOS Science Plan: The State of Science in the EOS Program*. Greenbelt, MD: NASA Goddard Space Flight Center, pp.1-397.

Kistler, R., E. Kalnay, W. Collins, S. Saha, G. White, J. Woollen, M. Chelliah, W. Ebisuzaki, M. Kanamitsu, V. Kousky, H. Van den Dool, R. Jenne and M. Fiorino,

2001: The NCEP-NCAR 50-Year Reanalysis: Monthly Means CD-ROM and Documentation. *Bull. Amer. Meteor. Soc.*, **82**, 247-267.

Kleespies, T. J., P. Van Delst, L. M. McMillin, and J. C. Derber, 2004: Atmospheric Transmittance of an Absorbing Gas. OPTRAN Status Report and Introduction to the NESDIS/NCEP Community Radiative Transfer Model. *Applied Optics*, **43**, 3103-3109.

Knuteson, R. O. B. J. Osborne, H. E. Revercomb, and D. C. Tobin, 2003: Validation of Satellite AIRS LST/LSE Products Using Aircraft Observations. Proceedings of the 13th International TOVS Conference., Ste. Adele, Canada, 29 Oct – 4 Nov.

_____, F. A. Best, D. H. DeSlover, B. J. Osborne, H. E. Revercomb, and W. L. Smith Sr., 2004: Infrared land surface remote sensing using high spectral resolution aircraft observations. *Adv. Space Res.*, **33**, 1114-1119.

Koehler, T. L., J. C. Derber, B.D. Schmidt, and L. H. Horn, 1983: An Evaluation of Soundings, Analyses and Model Forecasts Derived from TIROS-N and NOAA-6 Satellite Data. *Mon. Wea. Rev.*, **111**, 562-771.

Kunkee, D., 2002: NPOESS Conical Scanning Microwave Imager/Sounder (CMIS) Overview. pp 18. [Available online at

http://eic.ipo.noaa.gov/IPOarchive/SCI/sensors/cmis/Microwave_Imaging_CMIS.pdf].

Lahoz, W. A., 1999: Predictive skill of the UKMO unified model in the lower stratosphere. *Quart. J. Roy. Meteor. Soc*., **125**, 2205-2238.

Lambrigtsen, B. H., 2003: Calibration of the AIRS Microwave Instruments. *IEEE Trans. Geosci. Remote Sensing*, **41**, 369-378.

Lambrigtsen, B. H., and R. V. Calheiros, 2003: The Humidity Sounder for Brazil-An International Partnership. *IEEE Trans. Geosci. Remote Sensing*, **41**, 352-361.

Le Dimet, F. X. and O. Talagrand, 1986: Variational Algorithms for Analysis and Assimilation of Meteorological Observations: Theoretical Aspects. *Tellus*, **38A**, 97-110.

Le Marshall, J. F., W. L. Smith and G. M. Callan 1985: Hurricane Debby-An Illustration of the Complementary Nature of VAS Soundings and Cloud and Water Vapor Motion Winds. *Bull. Amer. Meteor. Soc*., **66**, 258-263.

_____, J. F., 1988: An Intercomparison of Temperature and Moisture Fields Derived from TIROS Operational Vertical Sounder Data by Different Retrieval Techniques. Part I: Basic Statistics., *J. Appl. Met.*, **27**, 1282-1293.

_____, J., J. Jung, J. Derber, R. Treadon, S. Lord, M. Goldberg, W. Wolf, H. C. Liu, J. Joiner, J. Wollen and R. Todling, 2005a: AIRS Hyperspectral Data Improves Southern Hemisphere Forecasts., *Aust. Meteor. Mag*., **54**, 57-60.

_____, J., J. Jung, J. Derber, R. Treadon, S. Lord, M. Goldberg, W. Wolf, H. C. Liu, J. Joiner, J. Wollen and R. Todling, 2005b: Impact of Atmospheric Infrared Sounder Observations on Weather Forecasts. EOS, 86, 109, 115, 116.

_____, J., 2006: Satellite Meteorology and Atmospheric Remote Sensing. pp 19.

_____, J., J. A. Jung, M. Goldberg, C. Barnet, W. Wolf, J. Derber, R. Treadon, and S. Lord, 2008: Using Cloudy AIRS Fields of View in Numerical Weather Prediction. Accepted *Aust. Meteor. Mag.*

Li, J., W. W. Wolf, W. P. Menzel, W. Zhang, H.-L. Huang and T. H. Achtor, 2000: Global Soundings of the Atmosphere from ATOVS Measurements: The Algorithm and Validation. *J. Appl. Met.*, **39**, 1248-1268.

Liu, Y., J. R. Key, R. A. Frey, S. A. Ackerman, and W. P. Menzel, 2004: Nighttime polar cloud detection with MODIS. *Rmt. Sens. Environ*., **92**, 181-194.

Lorenc, A. C., 1986: Analysis Methods for Numerical Weather Prediction. *Quart. J. Roy. Meteor. Soc*., **112**, 1177-1194.

McMillin, L. M. 1986: The use of Classification Procedures to Improve the Accuracy of Satellite Soundings of Temperature and Moisture. Preprints, Second Conference on Satellite Meteorology/Remote Sensing and Applications. Amer. Meteor. Soc., Boston, MA., 1-4.

_____, L. J. Crone, M. D. Goldberg, and T. J. Kleespies, 1995: Atmospheric Transmittance of an Absorbing Gas. 4. OPTRAN: a Computationally fast and Accurate Transmittance Model for Absorbing Gases with Fixed and Variable Mixing Ratios at Variable Viewing Angles. *Appl Opt*., **34**, 6269-6274.

McNally, A. P., and P. D. Watts, 2003: A Cloud Detection Algorithm for High-spectral-resolution Infrared Sounders. *Quart. J. Roy. Meteor. Soc*., **129**, 3411-3423.

_____, P. D. Watts and J. A. Smith, 2003: The Assimilation of AIRS Radiance data at ECMWF. *Proceedings of the 13th International TOVS Conference.*, St. Adele, Canada., 20 Oct – 4 Nov.

Menzel, W. P., F. C. Holt, T. J. Schmit, R. M. Aune, A. J. Schreiner, G. S. Wade, and D. G. Gray, 1998: Application of GOES-8/9 soundings to weather forecasting and nowcasting. *Bull. Amer. Meteor. Soc*., **79**, 2059-2077.

Miller, A.J., L.E. Flynn, S.M. Hollandsworth, J.J. DeLuisi, I.V. Petropavlovskikh, G.C. Tiao, G.C. Reinsel, D.J. Wuebbles, J. Kerr, R.M. Nagatani, L. Bishop, and C.H. Jackman, 1997: Information content of Umkehr and **SBUV**(2) satellite data for ozone trends and solar responses in the stratosphere. *J. Geophys. Res.*, **102**, 19,257-19,263.

Miller, S. D., J.D. Hawkins, J. Kent, F. J. Turk, T. F. Lee, A. P. Kuciauskas, K. Richardson, R. Wade, and C. Hoffman, 2006: NexSat: Previewing NPOESS/VIIRS Imagery Capabilities. Bull. *Amer. Meteor. Soc.*, **87**, 433-446.

Muth, C., P. S. Lee, S. Krimchansky, J. C. Shiue, and W. A. Webb, 2004: Advanced Technology Microwave Sounder on NPOESS and NPP. Pp 5. [Available online from http://140.90.86.6/IPOarchive/SCI/sensors/ATMSDraftBriefv4_AlanWebb.pdf].

NOAA, cited 2005: NOAA Polar Orbiter Data (POD) User's Guide, November 1998 revision. [Available online from http://www2.ncdc.noaa.gov/docs/klm/html/c3/sec3-3.htm .]

Ohring, G. 1979: Impact of Satellite Sounding Data on Weather Forecasts. *Bull. Amer. Meteor. Soc.*, **60**, 1141-1147.

Pailleux, J., 1990: A Global Variational Assimilation Scheme and its Application for Using TOVS Radiances. Preprints, WMO Int. Symp. On Assimilation of Observations in Meteorology and Oceanography, Clermont-Ferrand, France 315-328.

Pagano, T. S., H. H. Aumann, D. E. Hagan, and K. Overoye, 2003: Prelaunch and In-Flight Radiometric Calibration of the Atmospheric Infrared Sounder (AIRS). *IEEE Trans. Geosci. Remote Sensing*, **41**, 265-273.

Parkinson, C. L., and R. Greenstone, 2000: EOS Data Products Handbook. NASA Goddard Space Flight Center, Greenbelt MD, vol. 2 pp 1-253.

Parrish, D. F., and J. C. Derber, 1992: The National Meteorological Center's spectral statistical interpolation analysis system. *Mon. Wea. Rev.*, **120**, 1747-1763.

Phillips, N., L. McMillin, A. Gruber, and D. Wark, 1979: An evaluation of early operational temperature soundings from TIROS-N. *Bull. Amer. Meteor. Soc*., **60**, 1188-1197.

Reale, A. L., 1995: Departures between derived satellite soundings and numerical weather forecasts: Present and future. *Tech. Proc. Eighth Intl. TOVS Study Conf*., Queenstown, New Zealand, WMO, 395-404.

Rodgers, C. D. 1970: Remote Soundig of the Atmospheric Temperature Profile in the Presence of Cloud. *Quart. J. Roy. Meteor. Soc*., **96**, 654-666.

Rossow, W. B. and R. A. Schiffer 1991: ISCCP cloud data products. *Bull. Amer. Meteor. Soc*., **80**, 2261-2287.

_____, A. W. Walker, and L. C. Garder 1993: Comparison of ISCCP and other cloud amounts. *J. Climate*, **6**, 2394-2418.

_____, and L. C. Garder, 1993: Cloud detection using satellite measurements of infrared and visible radiances for ISCCP. *J. Climate*, **6**, 2341-2369.

Saunders, R. M., M. Matricardi, and P. Brunel, 1999: An Improved Fast Radiative Transfer Model for Assimilation of Satellite Radiance Observations, *Quart. J. Roy. Meteor. Soc*., **125**, 1407-1425.

Schmit, T. J., J. J. Gurka, W. P. Menzel, and J. Li, 2005a: Application of the GOES-R HES (Hyperspectral Environmental Suite) Infrared Measurements. Hyperspectral Imaging and Sounding of the Environment, Optical Society of America. 31 Jan – 2 Feb 2005, Alexandria, VA., pp 3. [Available online at ftp://ftp.ssec.wisc.edu/ABS/publications/Applications_of_the_GOES_HES_OSA_final.pdf].

_____, M. M. Gunshor, W. P. Menzel, J. Li, S. Bachmeier, J. J. Gurka, 2005b: Introducing the Next-generation Advanced Baseline Imager (ABI) on GOES-R, *Bull. Amer. Meteor. Soc.,* **86**, 1079-1096.

Smith, W. L. 1968: An Improved Method for Calculating Tropospheric Temperature and Moisture from Satellite Radiometer Measurements. *Mon. Wea. Rev*., **96**, 387-396.

_____, 1970: Iterative Solution of the Radiative Transfer Equation for Temperature and Absorbing Gas Profile of an Atmosphere. *Appl. Optics*, **9**, 1993-1999.

_____, H. M. Woolf and W. J. Jacob, 1970: A Regression Method for Obtaining Real Time Temperature and Geopotential Height Profiles from Satellite Spectrometer Measurements and its Application to Nimbus III "SIRS" Observations. *Mon. Wea. Rev*., **98**, 582-603.

_____, H. M. Woolf, and H. E. Fleming 1972: Retrieval of Atmospheric Temperature Profiles from Satellite Measurements for Dynamical Forecasting. *J. Appl. Meteor*., **11**, 113-122.

_____, H. M. Woolf, P. G. Abel, C. M. Hayden, M. Chalfant, and N. Grody, 1974: Nimbus-5 Sounder Data Processing System. Part I: Measurement Characteristics and Data Reduction Procedures. NOAA Tech. Memo. NESS 57, Washington, DC.

_____, and H. M. Woolf, 1976: The use of Eigenvectors of Statistical Covariance matrices for Interpreting Satellite Sounding Radiometer Observations. *J. Atmos. Sci*., **33**, 1127-1140.

_____, H. M. Woolf, C. M. Hayden, D. Q. Wark, and L. M. McMillin, 1979: The TIROS-N operational vertical sounder. *Bull. Amer. Meteor. Soc*., **60**, 1177-1187.

_____, and H. M. Woolf, 1984: Improved Vertical Soundings from an Amalgamation of Polar and Geostationary Radiance Observations. *Preprints: Conf. on Satellite Meteorology/Remote Sensing and Applications*, Amer. Meteor. Soc., Boston, MA, 45-48.

Somerville, R. C. J., P. H. Stone, M. Halem, J. E. Hansen, J. S. Hogan, L. M. Druyan, G. Russell, A. S. Lacis, W. J. Quirk and J. Tenenbaum, 1974: The GISS Model of the Global Atmosphere. *J. Atmos. Sci.*, **31**, 84-117.

Spencer, R.W., J.R. Christy and N. C. Grody, 1990: Global Atmospheric Temperature Monitoring with Satellite Microwave Measurements: Method and Results 1979-84., *J. Climate*, **3**, 1111-1128.

Strand, O. N., and E. R. Westwater 1968: Statistical Estimation of the Numerical Solution of a Fredholm Integral Equation of the First Kind. *J. Assoc Comp. Mach*., **15**, 100-114.

Strow, L. L.,S. E. Hannon, M. Weiler, K. Overoye, S. L. Gaiser, and H. H. Aumann, 2003: Prelaunch Spectral Calibration of the Atmospheric Infrared Sounder (AIRS). *IEEE Trans. Geosci. Remote Sensing*, **41**, 274-286.

Suskind, J., C. D. Barnett, and J. M. Blaisdell, 2003: Retrieval of Atmospheric and Surface Parameters from AIRS/AMSU/HSB Data in the Presence of Clouds. *IEEE Trans. Geosci. Remote Sensing*. **41**. 390-409.

Thompson, O. E., M. D. Goldberg, and D. A. Dazlich 1985: Pattern Recognition in the Satellite Temperature Problem. *J. Climate Appl. Meteor*., **24**, 30-48.

Tracton, M. S., A. J. Desmarais, R. J. Van Haaren, and R. D. McPherson, 1980 : The impact of Satellite Soundings on the National Meteorological Center's Analysis and Forecast System-the Data System Test Results. *Mon. Wea. Rev*., **108**, 543-586.

Uddstrom, M. J., and D. Q. Wark 1985: A Classification Scheme for Satellite Temperature Retrievals. J. *Climate Appl. Meteor*., **24**, 16-29.

Van Delst, P. 2003: JCSDA Infrared Sea Surface Emissivity Model. Proceedings of the 13th International TOVS Working Group Conference, St. Adele, Canada, 29 Oct – 4 Nov 2003.

Waters, J. W., K. F. Kunzi, R. L. Pettyjohn, R. K. L. Poon, and D. H. Staelin 1975: Remote Sensing of Atmospheric Temperature Profiles with the Nimbus 5 Microwave Spectrometer. *J. Atmos. Sci*., **32**, 1953-1969.

Wielicki, B. A., B. R. Barkstrom, E. F. Harrison, R. B. Lee III, G. L. Smith, and J. E. Cooper, 1996: Clouds and the Earth's Radiant Energy System (CERES): An Earth Observing System experiment, *Bull. Amer. Meteor. Soc*., **77**, 853-868.

Welch, R. M., S. K. Sengupta, A. K. Goroch, R. Rabindra, N. Rangaraj, and M. S. Navar, 1992: Polar cloud and surface classification using AVHRR imagery: An intercomparison of methods. *J Appl. Meteor*., **31**, 405-420.

Weng, F., B. Yan, and N. Grody, 2001: A microwave land emissivity model, *J. Geophys. Res*., **106**, 20115-20123.

_____, Y. Han, P. van Delst, Q. Liu, and B. Yan, 2005: JCSDA Community Radiative Transfer Model (CRTM), *Technical Proceedings of 14th International ATOVS Study Conference*, Beijing, China, 25 – 31 May 2005.

Wilks, D. S., 1995: Statistical Methods in the Atmospheric Sciences, Academic Press, Volume **59**, pp 467.

WMO, 1999: *Commission for Basic Systems Abridged Final Report with Resolutions and Recommendations*. Extraordinary Session Karlsruhe, 30 September – 9 October 1998, Report WMO-No. 893, Geneva, Switzerland. Also accessible online at http://www.wmo.ch/pages/prog/www/reports/CBS-Ext98.pdf.

Wu, X., and W. L. Smith 1997: Emissivity of Rough Sea Surface for 8 – 13 μm Modeling and Verification. *Appl. Optics*, **36**, 2609-2619.

Xiong, X., and L. M. McMillin, 2005: An Alternative to the Effective Transmittance Approach for Calculating Polychromatic Transmittances in Rapid Transmittance Models, *Appl. Opt*., **44**, 67-76.

Yan, B., F. Weng, and K. Okamoto, 2004: Improved Estimation of Snow Emissivity from 5 to 200 GHz. *8th Specialist Meeting on Microwave Radiometery and Remote Sensing Applications*, 24-27 February 2004, Rome, Italy.

Yu, T.-W., and R. D. McPherson, 1984: Global data assimilation experiments with scatterometer winds from Seasat-A. *Mon. Wea. Rev.*, **112**, 368-376.

Zapotocny, T. H., S. J. Nieman, W. P. Menzel, J. P. Nelson III, J. A. Jung, E. Rogers, D. F. Parrish, G. J. DiMego, M. Baldwin and T. J. Schmit, 2000: A Case Study of the Sensitivity of the Eta Data Assimilation System. *Wea. Forecasting,* **15**, 603-621.

_____, W. P. Menzel, J. P. Nelson III, and J. A. Jung, 2002: An Impact Study of the Five Remotely Sensed and Five In-Situ Data Types in the Eta Data Assimilation System. *Wea Forecasting*, **17**, 263-285.

_____, W. P. Menzel, J. A. Jung, and J. P. Nelson III, 2005a: A Four Season Impact Study of Rawinsonde, GOES and POES data in the Eta Data Assimilation System. Part 1: The Total Contribution. *Wea. Forecasting*, **20** 161-177

_____, W. P. Menzel, J. A. Jung, and J. P. Nelson III, 2005b: A Four Season Impact Study of Rawinsonde, GOES and POES data in the Eta Data Assimilation System. Part II: Contribution of the Components. *Wea. Forecasting*, **20** 178-198.

_____, J. A. Jung, J. F. Le Marshall, R. E. Treadon, 2007: A Two Season Impact Study of Satellite and In-Situ Data in the NCEP Global Data Assimilation System., *Wea. Forecasting*, **22**, 887-909.

_____, J. A. Jung, J. F. Le Marshall, and R. E. Treadon, 2008: A Two Season Impact Study of four Satellite Data Types and Rawinsonde Data in the NCEP Global Data Assimilation System., *Wea. Forecasting*, **23**, 80-100.